ADVANCES IN HEAT TRANSFER

Volume 35

James P. Hartnett

ADVANCES IN
HEAT TRANSFER

Volume 35

This Page Intentionally Left Blank

Advances in

HEAT
TRANSFER

Serial Editors

James P. Hartnett
Energy Resources Center
University of Illinois at Chicago
Chicago, Illinois

Thomas F. Irvine, Jr.
Department of Mechanical Engineering
State University of New York at Stony Brook
Stony Brook, New York

Serial Associate Editors

Young I. Cho
Department of Mechanical Engineering
Drexel University
Philadelphia, Pennsylvania

George A. Greene
Department of Advanced Technology
Brookhaven National Laboratory
Upton, New York

Volume 35

ACADEMIC PRESS

A Harcourt Science and Technology Company

San Diego   San Francisco   New York   Boston   London   Sydney   Tokyo

CONTENTS

Thermal Performance Testing of Industrial Heat Exchangers

Thomas Lestina and Kenneth Bell

Boiling Heat Transfer and Bubble Dynamics in Microgravity

Johannes Straub

Heat Transfer and Fluid Flow in Rotating Sealed Cavities

WEI SHYY AND MICHAEL P. EBERT

Recent Advances in the Modeling and Applications of Nonconventional Heat Pipes

Suresh V. Garimella and C. B. Sobhan

This Page Intentionally Left Blank

CONTRIBUTORS

Numbers in parentheses indicate the pages on which the authors' contributions begin

KENNETH BELL (1), School of Chemical Engineering, Oklahoma State University, Stillwater, Oklahoma.

MICHAEL P. EBERT (173), Department of Aerospace Engineering, Mechanics, and Engineering Science, University of Florida, Gainesville, Florida 32611.

SURESH V. GARIMELLA (249), Cooling Technologies Research Consortium, School of Mechanical Engineering, Purdue University, West Lafayette, Indiana 47907-1288.

THOMAS LESTINA (1), MPR Associates, Inc., Alexandria, Virginia.

WEI SHYY (173), Department of Aerospace Engineering, Mechanics, and Engineering Science, University of Florida, Gainesville, Florida 32611.

C. B. SOBHAN (249), Department of Mechanical Engineering, Regional Engineering College, Calicut, Kerala 673601, India.

JOHANNES STRAUB (57), Technische Universität München, Institute für Thermodynamiks, D-85748 Garching, Germany.

This Page Intentionally Left Blank

PREFACE

For over a third of a century this serial publication, *Advances in Heat Transfer*, has filled the information gap between regularly published journals and university-level textbooks. The series presents review articles on special topics of current interest. Each contribution starts from widely understood principles and brings the reader up to the forefront of the topic being addressed. The favorable response by the international scientific and engineering community to the thirty-five volumes published to date is an indication of the success of our authors in fulfilling this purpose.

In recent years, the editors have undertaken to publish topical volumes dedicated to specific fields of endeavor. Several examples of such topical volumes are Volume 22 (Bioengineering Heat Transfer), Volume 28 (Transport Phenomena in Materials Processing), and Volume 29 (Heat Transfer in Nuclear Reactor Safety). As a result of the enthusiastic response of the readers, the editors intend to continue the practice of publishing topical volumes as well as the traditional general volumes.

The editorial board expresses its appreciation to the contributing authors of Volume 35 who have maintained the high standards associated with *Advances in Heat Transfer*. Lastly, the editors acknowledge the efforts of the staff at Academic Press who have maintained the attractive presentation of the published volumes over the years.

This Page Intentionally Left Blank

Thermal Performance Testing of Industrial Heat Exchangers

THOMAS LESTINA

MPR Associates, Inc.
Alexandria, Virginia

KENNETH BELL

School of Chemical Engineering, *Oklahoma State University*
Stillwater, Oklahoma

Abstract

Methods to perform thermal performance tests and analyze the results for heat exchangers in industrial process streams are discussed. Industrial test practices and operating conditions are compared with experimental methods. A thorough review of sources of error and their contribution to overall test uncertainty is described. The analysis includes methods to estimate the uncertainty of predicted performance based on test data measured at different operating conditions. It is concluded that accurate industrial tests (as accurate as laboratory tests) are performed infrequently because the cost of temperature and flow instruments is high and it is difficult to control or adjust process conditions as needed. To overcome these limitations, future work is needed to implement cost effective smart sensors and online analysis methods along with continuing development of test standards. This chapter is of interest to personnel responsible for thermal testing of industrial heat exchangers and those implementing performance enhancements in industrial processes.

I. Introduction

Industrial facilities often monitor the process stream and heat exchanger performance by observing temperatures and assessing adverse trends. Experience with the adequacy of more detailed performance assessments is mixed. Some performance testing produces accurate and repeatable results. For some heat exchanger installations, accurate and repeatable test results are difficult and expensive to obtain. This chapter reviews test and analysis methods for thermal performance assessment of industrial heat exchangers, discusses capabilities and limitations, and identifies areas for future work. The discussion and data presented are of interest to personnel responsible for performing thermal performance testing of heat exchangers, designing process control and monitoring equipment and methods, and implementing thermal performance enhancements in industrial processes.

A. Overview of Testing Needs and Capabilities

The particular circumstances surrounding industrial heat exchanger testing are varied; however, the objectives of these assessments can be grouped into one or a combination of the following:

- Comparison of the measured performance with specifications or manufacturing design rating data
- Evaluation of the cause of degradation or malfunctioning
- Assessment of process improvements such as those due to enhancements or heat exchanger replacement

Manufacturers typically do not test new heat exchangers, as performance is reasonably assured by application of margins such as fouling factors and tube plugging allowances. During initial testing of a new process facility, effort is focused on startup of the production process and performance evaluation of the heat exchangers is usually not considered central to meeting these startup needs. After the production process has settled into baseline operation, operators often compare process data with the design values, and in rare instances, a controlled test is performed to determine if the performance of a process heat exchanger meets the original design requirements.

Open literature data are rarely available for industrial performance tests because of the ad hoc test practices and potential commercial implications. The most extensive study of heat exchanger performance data in the open literature is the research program carried out under ASME sponsorship from 1947 to 1963 at the University of Delaware [1–4]. The tests were conducted with clean heat exchangers under carefully controlled test condi-

tions. Test results have been used to develop a design method for shell-side heat transfer coefficient and pressure drop, which was first published in 1961 [4]. The Delaware Method remains the most accurate and comprehensive shell-and-tube design method in the open literature. Following the completion of the ASME program at the University of Delaware, carefully controlled heat exchanger tests have been performed under sponsorship from industry organizations such as Heat Transfer Research, Inc., and Heat Transfer and Fluid Flow Services. In general, these data are proprietary and not available in the open literature.

Reports of other test programs of industrial heat exchangers are intermittent and the scope is limited to particular applications. Kays and London [5] have assembled and discussed the performance data for a wide variety of compact test cores for gas heat transfer applications. The Nuclear Regulatory Commission has issued regulations requiring performance tests of cooling water heat exchangers [6]. Reports of test methods and results based on these regulatory requirements have been published [7–12]. The experience of these nuclear power utilities indicates that high-accuracy testing is possible (i.e., hot stream heat transfer rate is less than 2% different from cold stream heat transfer rate), but the results are sensitive to measurement and analysis practices. For other power plant applications, several descriptions of heat transfer tests are available in the open literature for condensing applications such the main condenser [13–16] and feedwater heater [17–19]. For petrochemical processes, very few reports of heat exchanger tests are available in the open literature [20, 21]. For air-to-air HVAC applications, a publication by Guo, Ciepliski, and Besant [22] provides a detailed description of test methods and some results. In general, industrial experience with in-process performance indicates that it is often difficult (and expensive) to interpret test results with sufficient accuracy to distinguish among fouling, instrumentation degradation, and variation in operating conditions.

To diagnose heat exchanger fouling, fouling monitors are sometimes used. Knudsen [23] provides a general discussion of the apparatus and techniques for the measurement of the fouling of heat transfer surfaces. Typical test section geometries and methods to reduce heat flux, flow rate, and temperature data are discussed. Chenoweth [24] describes the operation of research and commercial liquid fouling monitors. To obtain accurate trends of fouling, these monitors use idealized geometry to reduce uncertainty. Most commercial liquid fouling monitors are used in cooling water applications to evaluate the effectiveness of chemical injections. Marner and Henslee [25] have surveyed gas-side fouling monitoring devices applied to coal-fired boiler applications and heat recovery systems for gas combustion streams. They conclude that very few gas-side fouling probes have been developed

capable of measuring on-line fouling resistances as a function of time in industrial applications. In general, for all fouling monitors, it is observed that accurate fouling measurements are performed at localized heat transfer areas under idealized geometry and heat transfer conditions. As such, these monitors may not always provide a representative assessment of overall performance of a large heat transfer surface and may not provide a better assessment of the overall performance than the temperature and flow data for the heat exchanger.

Standards have been developed to provide guidance to the test engineer in planning and analyzing results. The American Institute of Chemical Engineers developed general test and analysis guidance 30 years ago [26] and is currently revising these guidelines. The Society of Automotive Engineers has developed recommended practices for laboratory testing heat transfer performance of vehicle and industrial heat exchangers [27]. The nuclear power industry has developed guidelines and standards to establish test programs for service water heat exchangers under sponsorship of EPRI and ASME [28, 29]. Continuing development and refinement of test methods under the guidelines of the ASME Board of Performance Test Codes (PTC) has developed comprehensive test methods for accurate performance assessments that include detailed discussions of test and analysis limitations and uncertainty evaluations [30]. The work to develop this latest industry standard has involved an extensive review of research and industry practices and is the basis of this manuscript. Based on industry test experience and the results of the more recent standards development, the following observations can be made:

- High-accuracy testing (necessary to determine if the heat exchanger has fouled to its design limit) is expensive and performed infrequently.
- The results are sensitive to the instrumentation, test practices and analysis methods.
- A large number of factors may contribute to test results that are different than expected, and it is difficult to pinpoint the cause of unexpected results.

With the development of industrial sensor technology, improvements in the current practices may be implemented at a reasonable cost. This chapter discusses test methods for heat exchanger thermal performance and discusses how improvements are possible with the implementation of new technology.

B. INDUSTRIAL OPERATING CONDITIONS

Because of practical economic considerations with the operating environment in an industrial facility, the test conditions may not be ideal for

performance assessment. The following factors are considered typical for industrial tests:

Nonideal Instrument Installations.   Industrial instrument installations are limited to key locations that are used for process control and reliability. The costs for the instrument installation are kept under control by reducing the number of instruments and ensuring that the instruments installed are highly reliable. Installation practices are determined by the need for high reliability and not high accuracy. Calibration intervals are long (1 year and greater) and often the instrument is not removed from service to perform the calibration so that a check against an independent reference measurement is often not performed.

Unknown and Varying Fouling Conditions.   Inspections of installed heat exchangers are often difficult to perform because of the impact on process operations (or outages) and limited access ports to internal heat transfer surfaces. Even if inspections are performed, the scope is often limited to a small fraction of the overall area and correlation between visual inspection results and fouling resistance is often not accurate. Even if the heat exchanger is new, clean conditions often cannot be assured because storage and shipping practices cannot be confirmed after the unit leaves the factory. In addition to unknown conditions, fouling conditions may increase and decrease on a day-to-day basis and some processes may undergo fouling changes during the test.

Off-Design and Changing Plant Operating Conditions.   The temperatures and flow rates of the process streams are typically different from design conditions. Furthermore, these operating conditions often change on day-to-day and month-to-month bases. As a result, it usually is not practical to test at design conditions, nor is it practical to test at the same operating conditions for a sequence of tests over a period of several years.

Inability to Adjust Process Operating Conditions.   Industrial processes are adjusted to maximize product output or maintain product quality. Changing process conditions to support a test is difficult to justify even if it is only a temporary change, since operating staff often considers the effort to be a research effort. Instead, the test engineer is often required to calculate estimated performance at design conditions based on test results at different operating conditions.

Uncertain Properties of Fluid Streams.   Except for a few common engineering fluids (such as air, steam, and water), the uncertainty of thermal physical properties of fluids may be substantial for industrial process

streams. The cost to obtain samples and measure their properties often is excessive for many situations. In addition, the composition of industrial process streams may vary on a day-to-day basis, and changes in process temperatures may be attributed to changes in cold or hot stream fluid properties rather than degradation in heat exchanger performance.

Variation in Process Conditions. During a period where test data is collected (from 15 minutes to several hours) variations in temperature and flow rate are expected. Modulating control valves and changes in operating conditions elsewhere in the facility may have an impact on the conditions directly affecting the heat exchanger under test. Laboratory conditions can be controlled more closely than industrial conditions even in situations where test procedures specify narrow operating limits.

C. DESCRIPTION OF A THERMAL MODEL

A thermal model for a heat exchanger is needed to analyze the test data. For heat exchanger design, comprehensive models have been developed and confirmed by years of operating experience and data from heat exchanger test units. Such computer models contain geometry data for the standard designs, thermal physical data for many industrial fluids, and correlations developed from a wide variety of experimental data. These models have been adapted and used to analyze heat exchanger test data for in-service units.

However, a large number of inputs are needed for geometry and boundary conditions. It is often not practical or cost effective to measure all of the parameters needed to confirm that an accurate model of the test unit has been developed, and therefore modeling assumptions are often applied in analyses of test data. Under circumstances where commercial interests are substantial, a detailed test plan and procedures are developed to specify required measurements, inspections, and assumptions needed to establish the thermal model that is acceptable to the test participants. These tests can become expensive in certain applications.

A simple heat transfer model is desired for the analysis of test data. However, simple models require assumptions that only approximate the test conditions, and therefore introduce errors into the analysis. A review of the traditional development of a heat exchanger thermal model is useful as a starting point to evaluate sources of error. The development presented here is considered typical for single-phase and idealized condensing applications based on the discussion in [5, 31, 32]. This traditional single-phase model provides the basis for the discussion of test analysis methods in this chapter.[1]
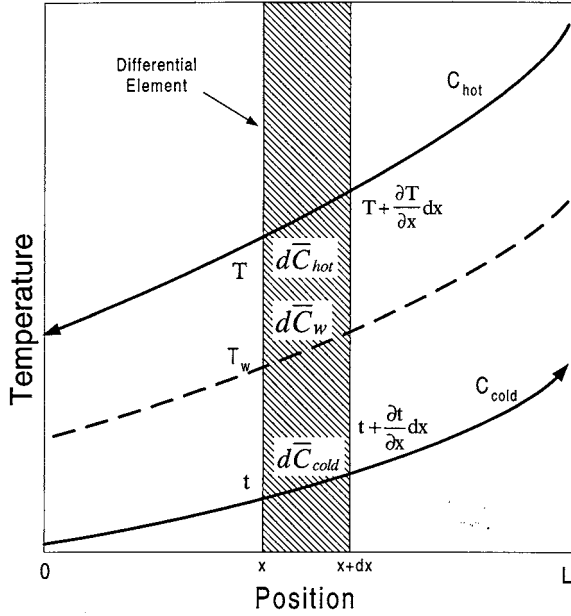
FIG. 1. Typical temperature profile for a counterflow heat exchanger arrangement.

Consider the temperature distribution for a small heat exchanger control volume element in a two-fluid, single-phase counterflow arrangement as shown in Fig. 1. Assume the following conditions:

- The hot stream, cold stream, and wall temperatures are a function of x and θ only.
- Heat transfer to the surroundings is negligible.
- Longitudinal conduction in the hot fluid, cold fluid and wall is negligible.
- The heat capacity rates of the hot and cold streams are constant or representative average values are used.

$$-C_{\text{cold}} \frac{\partial t}{\partial x} dx + \frac{dA_{\text{cold}}}{r_{\text{cold}}} (T_{\text{w}} - t) = d\bar{C}_{\text{cold}} \frac{\partial t}{\partial \theta} \qquad (1)$$

$$C_{\text{hot}} \frac{\partial T}{\partial x} dx - \frac{dA_{\text{hot}}}{r_{\text{hot}}} (T - T_{\text{w}}) = d\bar{C}_{\text{hot}} \frac{\partial T}{\partial \theta} \qquad (2)$$

[1]For most two-phase applications, the assumptions used in this model are not appropriate. The discussion of test issues is applicable for both single-phase and two-phase heat exchangers, but the calculations for test uncertainty are valid only for the model described. Different calculations are needed to assess test accuracy for most two-phase applications.

$$\frac{dA_{\text{hot}}}{r_{\text{hot}}}(T - T_{\text{w}}) - \frac{dA_{\text{cold}}}{r_{\text{cold}}}(T_{\text{w}} - t) = d\bar{C}_{\text{w}}\frac{\partial T_{\text{w}}}{\partial \theta} \tag{3}$$

Assuming that the heat transfer cross-section is uniform along the flow length and that the heat capacities of the cold fluid, hot fluid, and wall are constant within the heat exchanger (or representative average values are used), the following substitutions can be applied:

$$dA_{\text{hot}} = A_{\text{hot}}\frac{dx}{L}, \qquad dA_{\text{cold}} = A_{\text{cold}}\frac{dx}{L}$$

$$d\bar{C}_{\text{hot}} = \bar{C}_{\text{hot}}\frac{dx}{L}, \qquad d\bar{C}_{\text{cold}} = \bar{C}_{\text{cold}}\frac{dx}{L}, \qquad d\bar{C}_{\text{w}} = \bar{C}_{\text{w}}\frac{dx}{L}.$$

Equations (1), (2), and (3) can be rearranged as follows:

$$-C_{\text{cold}}\frac{\partial t}{\partial x} + \frac{A_{\text{cold}}}{r_{\text{cold}}L}(T_{\text{w}} - t) = \frac{\bar{C}_{\text{cold}}}{L}\frac{\partial t}{\partial \theta} \tag{4}$$

$$C_{\text{hot}}\frac{\partial T}{\partial x} - \frac{A_{\text{hot}}}{r_{\text{hot}}L}(T - T_{\text{w}}) = \frac{\bar{C}_{\text{hot}}}{L}\frac{\partial T}{\partial \theta} \tag{5}$$

$$\frac{A_{\text{hot}}}{r_{\text{hot}}}(T - T_{\text{w}}) - \frac{A_{\text{cold}}}{r_{\text{cold}}}(T_{\text{w}} - t) = \bar{C}_{\text{w}}\frac{\partial T_{\text{w}}}{\partial \theta}. \tag{6}$$

If r_{hot} and r_{cold} are assumed to be constant or if representative average values are used, Eqs. (4), (5), and (6) apply to any location x from 0 to L.

We introduce the overall heat transfer coefficient, U,

$$\frac{1}{UA} = \frac{r_{\text{hot}}}{A_{\text{hot}}} + \frac{r_{\text{hot}}}{A_{\text{cold}}}, \tag{7}$$

and integrate Eqs. (4), (5), and (6) based on steady-state conditions and a representative average (or constant) UA:

$$Q = C_{\text{cold}}(t_{\text{o}} - t_{\text{i}}) = C_{\text{hot}}(T_{\text{i}} - T_{\text{o}}) \tag{8}$$

$$Q = UA\Delta T_{\text{m}}. \tag{9}$$

The mean temperature difference, ΔT_{m}, is described traditionally as a function of the four terminal temperatures. For counterflow and parallel flow arrangements, the mean temperature difference is represented by the log mean temperature difference:

$$\Delta T_{\text{lm}} = \frac{\Delta T_1 - \Delta T_2}{\ln\left(\dfrac{\Delta T_1}{\Delta T_2}\right)} \tag{10}$$

where

$$\Delta T_1 = T_i - t_o \text{ and } \Delta T_2 = T_o - t_i \text{ for counterflow arrangement}$$

$$\Delta T_1 = T_i - t_i \text{ and } \Delta T_2 = T_o - t_o \text{ for parallel flow arrangement.}$$

For flow arrangements other than counterflow or parallel flow, it is typical to describe the mean temperature difference as the product of the log mean temperature difference for counterflow and a correction factor:

$$\Delta T_m = F(\Delta T_{lm})_{counterflow}. \tag{11}$$

F is usually described as a function of R and P:

$$F = \phi(P, R, \text{ flow arrangement})$$

$$P = \frac{t_o - t_i}{T_i - t_i}$$

$$R = \frac{T_i - T_o}{t_o - t_i}$$

Bowman, Mueller, and Nagle [33] summarize results of analysis of mean temperature difference for many common flow arrangements. Formulas for F are available for only a few arrangements and results are usually presented graphically.

In addition to the $F-\Delta T_{lm}$ method, alternate methods for exchanger heat transfer analysis are commonly used [31]. Each of these methods is derived based on the same assumptions used in this chapter but the integrated energy and rate equations are expressed differently. In this chapter, the $P-NTU$ method is used based on the following functional relationships:

$$Q = P_{cold} C_{cold}(T_i - t_i)$$

$$P_{cold} = \frac{t_o - t_i}{T_i - t_i} = \phi(NTU_{cold}, R, \text{ flow arrangement}) \tag{12}$$

$$NTU_{cold} = \frac{UA}{C_{cold}} = \frac{t_o - t_i}{\Delta T_m}.$$

It is common practice to expand the overall heat transfer coefficient into terms attributed to convection, fouling, and wall resistances. If we introduce the surface temperature effectiveness, η, the overall heat transfer resistance is expanded as shown in Fig. 2 into the following:

$$\frac{1}{UA} = \frac{1}{(\eta hA)_{cold}} + \frac{1}{(\eta hA)_{hot}} + \left(\frac{r_f}{\eta A}\right)_{cold} + \left(\frac{r_f}{\eta A}\right)_{hot} + R_w. \tag{13}$$

Since for most heat exchanger test applications where terminal temperatures

$$\frac{1}{UA} = \frac{1}{(\eta hA)_{hot}} + \left(\frac{r_f}{\eta A}\right)_{hot} + R_w + \left(\frac{r_f}{\eta A}\right)_{cold} + \frac{1}{(\eta hA)_{cold}}$$
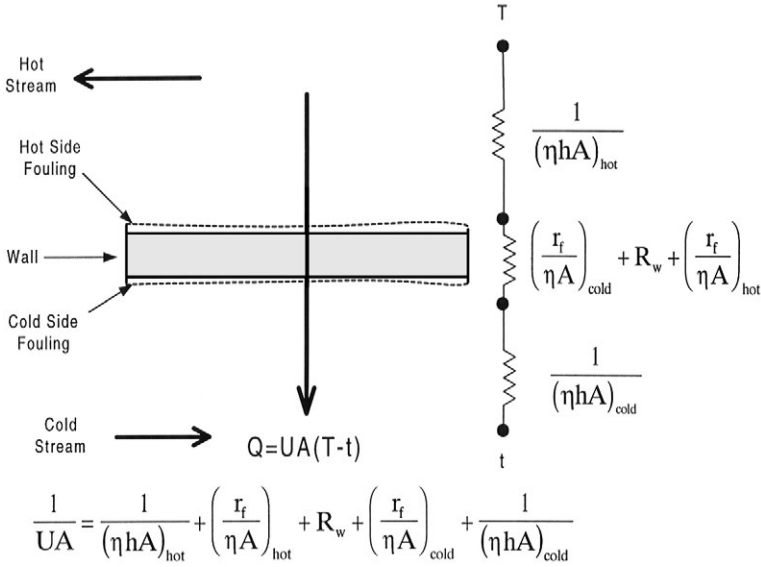
FIG. 2. Schematic representation of thermal resistances.

and flow rates are measured, it is not practical to distinguish between the hot and cold side fouling resistances, Eq. (13) is reduced to

$$\frac{1}{UA} = \frac{1}{(\eta hA)_{cold}} + \frac{1}{(\eta hA)_{hot}} + R_w + R_f \qquad (14)$$

where

$$R_f = \left(\frac{r_f}{\eta A}\right)_{cold} + \left(\frac{r_f}{\eta A}\right)_{hot} = \frac{(r_f)_{total}}{A}.$$

More comprehensive computer models are used for heat exchanger design, but additional information is needed to account for variations within the heat exchanger. In particular, variation of the heat transfer coefficient and temperature difference affect the accuracy of the model and analysis of test data. A generalized and complete theory for averaging the overall heat transfer coefficient and temperature difference for nonideal conditions does not exist.

Shah [34, 35] has reviewed the literature for nonuniform overall heat transfer coefficient. Expressions for area average overall heat transfer coefficient and temperature average overall heat transfer coefficient are described,

but calculation of combined position and temperature average heat transfer coefficient requires data between the terminal points for the exchanger (i.e., intermediate data). Since intermediate data are typically not measured for industrial heat exchanger tests, assumptions regarding the variation in heat transfer coefficient, fouling resistance, and fluid properties are usually required.

For determination of mean temperature difference, the impact of nonideal variations is a function of flow arrangement and operating conditions. As observed by Bowman, Mueller and Nagle [33], the curves for the log mean temperature difference correction all have a very steep gradient at lower values of the correction factor. As a result, a small change in temperature conditions will cause a large change in F, and a small deviation in assumed conditions will cause a large error in mean temperature difference. Intermediate temperature data are needed to reduce this sensitivity.

II. Test Methods

A. Industrial Process Measurements

An accurate assessment of industrial process measurements is needed for heat exchanger performance testing. Adverse trends in process stream temperatures may not indicate performance degradation unless it can be confirmed that instrument degradation or malfunction has not occurred. Experience has shown that distinguishing between instrument effects and process performance variations is difficult, and the uncertainty of measurements is often a substantial fraction of the overall margin of performance included in the heat exchanger. This section reviews the accuracy and sources of error for industrial process measurements. A general review of measurement practices used for heat exchanger testing is beyond the scope of this chapter. The Instrument Society of America (ISA) has assembled and organized a series of standards (from the ISA and other standards organizations) to address measurement practices [36].

1. Sources of Process Measurement Error

Industrial process measurements are typically not ideal, and it is often not practical to correct for these nonideal effects. In general, these sources of error are the same as with experimental measurements, except that it is more difficult to confirm and correct for biases. A thorough discussion of errors associated with practical industrial measurements is beyond the scope of this chapter, and the reader is referred to [37–43] for more complete discussion.

The error of measurements can be attributed to instrument calibration, spatial variation, installation, data acquisition, and random error.

Instrument Calibration   Instrument calibration is the process of comparing and quantifying the difference in the output of an instrument with an independent measurement standard. The estimated error attributed to instrument calibration is based on the instrument linearity, hysteresis, repeatability, calibration methods (and tolerances), and accuracy of calibration instruments. For many installations, the estimated error due to calibration is obtained from specifications from the instrument manufacturer. These specifications are frequently difficult to interpret since the methods used to develop their stated accuracies vary from manufacturer to manufacturer.

Spatial Variation   For flow and temperature measurements, spatial variation is attributed to flow profile and thermal streaming. The estimated error attributed to spatial variation is based on the measured or estimated nonuniform distribution of the parameter in the flow cross section.

Installation   The estimated error attributed to installation is based on nonideal installation practices (such as with temperature measurement on the outside surface of the pipe).

Data Acquisition   The estimated error due to data acquisition is attributed to misadjustments in the signal conditioning (e.g., filters, amplifiers, temperature compensation) and analog/digital conversion along with mistakes in the computer algorithms that process the digital data. For instances where the complete instrument and data acquisition system is calibrated, the estimated error attributed to data acquisition can be neglected since it is included in the calibration. As with instruments, it is often difficult to interpret data acquisition accuracy using manufacturing specifications.

Random Error   Estimated random error is attributed to random instrument loop effects (such as electrical noise) and process variations. For industrial instruments and practices, random instrument effects are usually small compared to the process variations.

2. Temperature Measurement

Permanent plant temperature instrumentation is typically installed at key locations in industrial process streams. Thermocouple and RTD sensors installed in thermowells that intrude into the flow stream are a common approach. These permanent instruments are used to control and monitor the process stream. The temperature sensors are often connected to an automated supervisory and monitoring system; however, local indication

(such as with a dial indicator) is still common. Periodic checks of the accuracy of the instrument loop are usually performed based on a field comparison of electrical output with a sensor simulator. Adjustment of the sensor output is only performed if the data are outside tolerance range in the procedure. Other diagnostic checks of the instrument operation are rarely performed.

Based on the experience of the authors, the tolerance range of permanent temperature instruments is generous and substantial degradation in measurement accuracy is expected after years of operation. Overall errors of ± 1 to $\pm 5°F$ (± 0.5 to $\pm 3°C$) are typical. The cost to improve the accuracy of the temperature instruments is difficult to justify. The cost associated with reducing the calibration tolerance range, diagnosing instrument drift, and implementing modern instrumentation with self-compensation and diagnostic capabilities is substantial compared to other needed plant upgrades.

Since permanent instrumentation is often of insufficient accuracy and rarely installed at enough locations for a successful test, temporary instruments are often used for heat exchanger testing. In general, surface mounted thermocouples or RTDs are used to avoid the need to modify the plant to support a test. Calibration uncertainties of $\pm 0.2°F$ ($\pm 0.1°C$) are typical. Spatial variation of the temperature of the outlet fluid stream is expected, and variations of 2 to $5°F$ (1 to $3°C$) are typical. Multiple instruments are often used to measure the temperature variation around the pipe circumference or across the flow cross section to calculate the mass weighted average temperature. However, the uncertainties associated with such calculations are not negligible and often dominate the overall test uncertainty. The uncertainty associated with the measurement and calculation of the weighted average temperature is approximately ± 0.2 to $\pm 1.0°F$ (± 0.1 to $\pm 0.5°C$) for well-designed tests.

3. Flow Measurement

Because of the initial and life-cycle cost, permanent flow instrumentation is reserved for critical applications in most industrial processes. Where permanent flow instruments are installed, periodic checks of the sensor electrical output are usually performed. A check of the instrument output against a flow standard (such as a weigh tank) is rarely performed after initial installation. As a result, drift in the flow instrument accuracy over the plant lifetime is expected. For differential pressure flow measuring instruments, ASME guidance [44, 45] establishes practices for design and installation. Without calibration in a flow loop, the error of the flow measurement using differential pressure instruments can be less than ± 1.5 to $\pm 2\%$ of flow reading when installed in accordance with industry

guidance. With a flow loop calibration, errors less than $\pm 1\%$ of flow reading are expected.

For most tests, installation of temporary flow instrumentation is required. Intrusive flow instruments are expensive to install and often not considered for industrial tests. In general, the accuracy of temporary flow instrumentation is variable because of the nonideal locations that are typical for industrial process streams. In particular, flow profile variations attributed to upstream disturbances and different flow regimes reduce the accuracy of flow measurements of temporary flow instruments. Errors of ± 3 to $\pm 10\%$ are considered typical when flow loop calibration based on installed pipe geometry and test conditions is not performed.

4. *Other Process Measurements*

Measurements other than temperature and flow rate are sometimes needed to establish thermal physical properties. For compressible fluids, pressure measurements are required. Fluid sampling and associated property measurements are performed for selected tests.

B. General Test Measurement Approach

Thermal performance testing of industrial heat exchangers consists of (1) measuring temperatures, flow rates, and pressures, (2) calculating test parameters, and (3) calculating performance parameters at reference conditions (projecting test results to reference conditions).

1. *Test Measurements*

Five of the following six process control parameters are needed to determine the thermal performance characteristics of a two-fluid heat exchanger under almost steady conditions:

- Cold stream inlet temperature, t_i
- Cold stream outlet temperature, t_o
- Cold stream heat capacity rate (mass flow rate and specific heat), C_{cold}
- Hot stream inlet temperature, T_i
- Hot stream outlet temperature, T_o
- Hot stream heat capacity rate (mass flow rate and specific heat), C_{hot}

Although only five of the above six parameters are needed, measuring all six parameters improves the confidence of the results and reduces the error (Fig. 3).
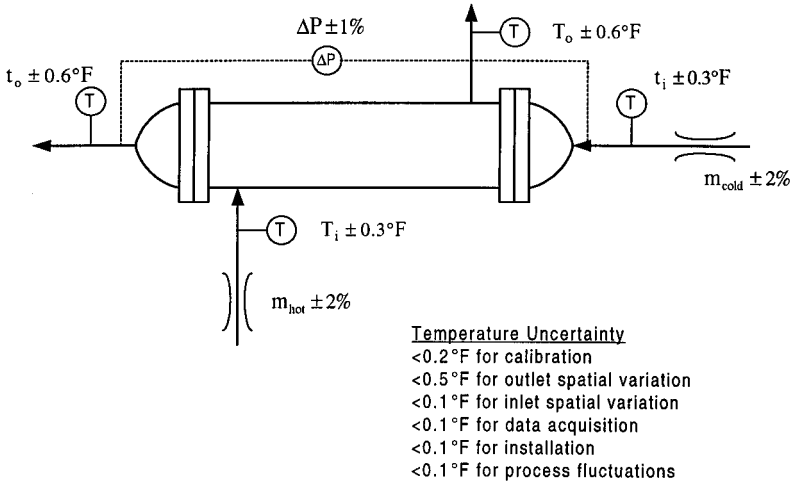
FIG. 3. Typical E-shell showing ASME PTC 12.5 [30] measurement stations and recommended accuracy limits.

2. *Test Performance Parameters*

Testing typically calculates a test parameter based on the measurements. A variety of test parameters are used, including heat transfer rate, overall heat transfer coefficient, overall heat transfer resistance, effectiveness, and fouling resistance. Depending on the test objectives and required accuracies, the complexity of the test parameter calculations vary with more complicated calculations requiring detailed heat exchanger geometry.

The function of process heat exchangers is to transfer heat, and therefore a direct measure of process performance is the determination of heat transfer rate for the test using Eq. (8). With specific heat data available for the fluid streams, the heat transfer rates for the hot stream and cold stream are determined based on the average specific heat[2]:

$$Q_{\text{cold}} = (mc_{\text{p}})_{\text{cold}}(t_{\text{o}} - t_{\text{i}}) \qquad (15)$$

$$Q_{\text{hot}} = (mc_{\text{p}})_{\text{hot}}(T_{\text{i}} - T_{\text{o}}). \qquad (16)$$

For instances where the heat transfer rate can be determined for both the hot and cold fluid streams, a comparison of the two heat transfer rates can

---

[2]For some fluids, the change in enthalpy is used to determine heat transfer rate. For these instances, a value for specific heat is not used explicitly; however, enthalpy is expressed as a function of temperature. Tabulations of enthalpy as a function of temperature may improve accuracy for applications where large changes in specific heat from the inlet to outlet are nonlinear.

be performed. The results of the comparison can be used to reduce the uncertainty using a weighted average or other optimization of the measurements.[3] Since process flow rates tend to vary on a day-to-day basis and since process inlet temperatures vary, evaluation of heat transfer rate alone does not provide enough information to assess the condition or degradation in unit performance.

For units where measurement of flow rate is not practical, temperature effectiveness, P, has been used. The effectiveness is a function of mass flow rate and as such, large day-to-day variations in effectiveness are expected for many process streams. Jeronimo *et al.* [20] discusses the need to adjust effectiveness data based on the mass flow rate.

The overall heat transfer resistance, $1/UA$, is a more general performance parameter that facilitates the use of corrections to account for process variations. By the $F-\Delta T_{\mathrm{lm}}$ or $P-NTU$ method,

$$\frac{1}{UA} = \frac{\Delta T_{\mathrm{m}}}{Q} = \frac{1}{NTU_{\mathrm{cold}} C_{\mathrm{cold}}}. \tag{17}$$

The overall heat transfer resistance varies with flow rate, temperature, fluid composition, and fouling conditions. Comparison of test data at different operating conditions is performed by correcting different sets of data to reference conditions. A generalized definition of reference conditions is not practical since it depends on the heat transfer model and process operating practices; however, it is typical to define reference conditions by specifying a set of process control variables (see Section II.B.1). Of the six process variables, any four variables can be constrained to define the operating state of the heat exchanger.[4] Using the heat transfer model and the four defined process control variables, the individual thermal resistances and the two remaining process control variables can be calculated. In

---

[3]A simple approach to determine a weighted average heat transfer rate is adopted by ASME Performance Test Code 12.5 [30] based on the assumption that errors contributing to cold stream heat transfer rate are random and independent of errors contributing to the hot stream heat transfer rate.

$$Q_{\mathrm{ave}} = \left(\frac{\delta Q_{\mathrm{hot}}^2}{\delta Q_{\mathrm{cold}}^2 + \delta Q_{\mathrm{hot}}^2} \right) Q_{\mathrm{cold}} + \left(\frac{\delta Q_{\mathrm{cold}}^2}{\delta Q_{\mathrm{cold}}^2 + \delta Q_{\mathrm{hot}}^2} \right) Q_{\mathrm{hot}}$$

where δQ_{cold} is the uncertainty of cold side heat transfer rate, and δQ_{hot} is the uncertainty of hot side heat transfer rate.

[4]For most industrial heat exchangers, reference conditions are defined by specifying the cold stream inlet temperature, cold stream flow rate, hot stream inlet temperature, and hot stream flow rate. Other definitions of reference conditions can be used. For heat exchangers with automatic control of the hot stream outlet temperature, reference conditions may be defined by specifying the cold stream inlet temperature, cold stream flow rate, hot stream inlet temperature, and hot stream outlet temperature.

general, determination of performance at reference conditions involves an iterative convergence calculation. To illustrate such a calculation, consider the overall heat transfer resistance at test conditions,

$$\left(\frac{1}{UA}\right)^{\mathrm{t}} = \frac{1}{(\eta hA)^{\mathrm{t}}_{\mathrm{cold}}} + \frac{1}{(\eta hA)^{\mathrm{t}}_{\mathrm{cold}}} + R^{\mathrm{t}}_{\mathrm{w}} + R^{\mathrm{t}}_{\mathrm{f}} \tag{18}$$

where $(UA)^{\mathrm{t}}$ is calculated from test data using Eq. (17). The overall heat transfer resistance at reference conditions is

$$\left(\frac{1}{UA}\right)^{\mathrm{r}} = \frac{1}{(\eta hA)^{\mathrm{r}}_{\mathrm{cold}}} + \frac{1}{(\eta hA)^{\mathrm{r}}_{\mathrm{hot}}} + R^{\mathrm{r}}_{\mathrm{w}} + R^{\mathrm{r}}_{\mathrm{f}}. \tag{19}$$

Subtracting (18) from (19),

$$\begin{aligned}
\left(\frac{1}{UA}\right)^{\mathrm{r}} = \left(\frac{1}{UA}\right)^{\mathrm{t}} &+ \left(\frac{1}{(\eta hA)^{\mathrm{r}}} - \frac{1}{(\eta hA)^{\mathrm{t}}}\right)_{\mathrm{cold}} \\
&+ \left(\frac{1}{(\eta hA)^{\mathrm{r}}} - \frac{1}{(\eta hA)^{\mathrm{t}}}\right)_{\mathrm{hot}} + (R^{\mathrm{r}}_{\mathrm{w}} - R^{\mathrm{t}}_{\mathrm{w}}) + (R^{\mathrm{r}}_{\mathrm{f}} - R^{\mathrm{t}}_{\mathrm{f}}).
\end{aligned} \tag{20}$$

Equation (20) is a generalized expression for the calculation of overall heat transfer resistance at reference conditions that are different from test conditions. Equation (20) is solved simultaneously with the following energy and rate equations at reference conditions:

$$Q^{\mathrm{r}} = C^{\mathrm{r}}_{\mathrm{cold}}(t^{\mathrm{r}}_{\mathrm{o}} - t^{\mathrm{r}}_{\mathrm{i}}) = C^{\mathrm{r}}_{\mathrm{hot}}(T^{\mathrm{r}}_{\mathrm{i}} - T^{\mathrm{r}}_{\mathrm{o}}) \tag{21}$$

$$Q^{\mathrm{r}} = (UA)^{\mathrm{r}}(\Delta T_{\mathrm{m}})^{\mathrm{r}} = P^{\mathrm{t}}_{\mathrm{cold}} C^{\mathrm{r}}_{\mathrm{cold}}(T^{\mathrm{r}}_{\mathrm{i}} - t^{\mathrm{r}}_{\mathrm{i}}). \tag{22}$$

By solving Eqs. (20), (21), and (22) simultaneously, Q^{r}, $(UA)^{\mathrm{r}}$, and the two unknown process variables can be calculated, provided that estimates of the corrections for individual heat transfer resistances are determined.

To reduce the effort needed to develop the heat transfer model and associated calculations used to assess performance at reference conditions, fouling resistance is often used as a parameter to monitor changes in performance:

$$R_{\mathrm{f}} = \left(\frac{\Delta T_{\mathrm{m}}}{Q}\right)^{\mathrm{t}}_{\mathrm{f}} - \left(\frac{\Delta T_{\mathrm{m}}}{Q}\right)^{\mathrm{t}}_{\mathrm{clean}} = \left(\frac{1}{UA}\right)^{\mathrm{t}}_{\mathrm{f}} - \left(\frac{1}{UA}\right)^{\mathrm{t}}_{\mathrm{clean}}. \tag{23}$$

If we multiply by the reference heat transfer area, A, the total fouling resistance for heat transfer per unit area is given by the following equation:

$$(r_{\mathrm{f}})_{\mathrm{total}} = R_{\mathrm{f}}A = \left(\frac{1}{U}\right)_{\mathrm{f}} - \left(\frac{1}{U}\right)_{\mathrm{clean}}. \tag{24}$$

Although fouling resistance is simple to calculate, interpretation of the results may be difficult because of the uncertainty of the measurements and variations in operating conditions. The uncertainty of fouling resistance is discussed in Section IV.B.2.

C. ASSESSMENT OF TEST QUALITY

In some form, quality is assessed for all tests. Test quality is assessed by evaluating whether the results can be used to determine performance with sufficient accuracy. Various techniques are used depending on the amount of data measured, unit margins,[5] and budget available to evaluate the results. For low-cost tests, quality is assessed solely using the judgment of the test engineer. For more thorough tests, more systematic and "rigorous" analysis methods are applied. A complete discussion of the methods that can be employed is beyond the scope of this discussion, but a few of the more common methods are introduced for completeness.

Model Comparison   Comparison of test data with results calculated from models of the overall or partial plant performance can be used to determine if results are reasonable. Mass and energy balances of portions of the process cycle are the most common and fundamental models used. If mass or energy balances are not maintained within acceptable thresholds, a gross error is detected. Gross errors may be attributed to measurement error (such as spatial variation of the temperature measurement) or modeling errors (due to nonsteady conditions or valve leak-by). For formal test and evaluation programs, hypothesis test methods or other statistical methods are sometimes used (when multiple sets of data are available) to confirm that gross errors are detected.

Gross Error Detection and Identification   Based on accurate models of the process and sources of error (including fundamental data that support the underlying assumptions), it is possible to identify the source of gross errors and correct for them. The study of data reconciliation focuses on gross error identification, and the reader is referred to [46–48] for further reading.

Uncertainty Analysis   Uncertainty analysis is a systematic evaluation to identify sources of error, determine estimates for such errors within certain confidence intervals, and propagate those errors into the overall results. An uncertainty analysis is a formal assessment of overall test accuracy and is discussed in Section IV.

[5]In this context, margin refers to the difference between the measured performance parameter and the minimum performance that defines unit acceptability.

The experience of the authors indicates that test quality is limited by the model for the sources of error. In general, statistical methods to minimize the error and optimize the results are only partially effective if some bias is unknown (and dominant), if multiple bias errors cannot be identified with confidence intervals, and if nonlinear (or nonideal) heat transfer characteristics are not accounted for. In general, the accuracy of industrial tests is limited by one or more of these sources of error.

III. Analysis of Results

As discussed previously, the conditions during industrial process operation change with time, and a thermal model of the heat exchanger is needed to adjust the results to a set of reference conditions. This section reviews the traditional heat transfer analysis methods for heat exchanger performance assessment, discusses the limitations, and identifies alternate methods to minimize the limitations.

A. Experimental Heat Exchange Methods

Experimental heat exchanger methods are test and analysis practices used in a laboratory or test facility. In general, the objective of experimental methods is to determine the heat transfer coefficients for a variety of test conditions with a specific heat exchanger geometry. Experimental practices are characterized by idealized process conditions that can be accurately controlled during a test, low fouling resistances, and accurate representation of heat exchanger geometry. In general, experimental thermal performance measurements are correlated based on methods described by Colburn [49]:

$$j = \frac{T_i - T_o}{\Delta T_m} \frac{S}{A} \left(\frac{c_p \mu}{k} \right)^{2/3} = \frac{\text{Nu}}{\text{RePr}^{1/3}} = \phi(\text{Re}). \tag{25}$$

To correlate Nusselt number as function of Reynolds number and Prandtl number, including the ratio of viscosities to account for variable fluid properties, the following form is often used:

$$\text{Nu} = B \, \text{Re}^n \text{Pr}^{1/3} \left(\frac{\mu_b}{\mu_w} \right)^{0.14}. \tag{26}$$

Here B and n are correlation constants.[6]

---

[6]The exponent 1/3 for the Prandtl number used by Colburn was selected because it is more or less an average value based on previous investigations. Other exponents are used such as 0.40 described by Shah and Zhou [50]. The term (μ_b/μ_w) is used to account for variable fluid properties as attributed to Sieder and Tate [51].

A review of experimental methods to test heat exchanger performance provides insight into the capabilities and limitations of testing industrial heat exchangers. Shah [50, 52] has provided discussions and comparisons of the most common experimental methods, and these summaries are the starting point of this review.

1. *Wilson Line Methods*

Wilson line methods are analysis methods of steady state tests to determine individual heat transfer characteristics (Nu or j) as a function of Reynolds number and Prandtl number for liquid–liquid or "ideal" phase-change applications. The original method is attributed to Wilson [53], who proposed the following expression to determine a correlation for tube-side resistance:

$$\frac{1}{UA} = \frac{1}{BV_r^a} + R_s. \tag{27}$$

Here, $1/UA$ is the overall heat transfer resistance based on experimental data, R_s is the sum of the shell-side and wall resistance, and V_r is the reduced velocity (or Reynolds number as it is known today). Equation (27) is plotted using the format $y = mx + b$, where $y = 1/UA$, $x = 1/V_r^a$, $m = 1/B$, and $b = R_s$. The exponent $a = 0.82$ was selected to best match the data. To meet this linear format, the shell-side resistance must be kept constant for different tube velocities. Wilson used condensing steam to approximate this condition, but accurate determination of tube-side coefficients is difficult with this original method. Even with the difficulties in controlling all of the test variables, the scatter of the best data correlated by Wilson is within $\pm 20\%$.

Modification of Briggs and Young Briggs and Young [54] relaxed the restriction for a constant shell-side heat transfer resistance. They proposed that shell-side heat transfer resistance be represented by the general expression

$$R_s = \frac{1}{B_s \left[\mathrm{Re}^d \mathrm{Pr}^{0.33} \left(\frac{\mu_b}{\mu_w}\right)^{0.14} Ak/D \right]_s}, \tag{28}$$

where B_s and d are constants for a particular shell-side geometry and range of fluid conditions tested. The following expression for heat transfer resistance is used:

$$\frac{1}{UA} - R_{\text{w}} = \frac{1}{B_{\text{t}} \left[\text{Re}^{0.8} \text{Pr}^{0.33} \left(\dfrac{\mu_{\text{b}}}{\mu_{\text{w}}} \right)^{0.14} Ak/D \right]_{\text{t}}} \tag{29}$$

$$+ R_{\text{s}} = \frac{1}{B_{\text{s}} \left[\text{Re}^{d} \text{Pr}^{0.33} \left(\dfrac{\mu_{\text{b}}}{\mu_{\text{w}}} \right)^{0.14} Ak/D \right]_{\text{s}}} .$$

The unknown constants are B_{t}, B_{s}, and the exponent d. Solution of Eq. (29) requires a nonlinear regression analysis. Briggs and Young used two successive linear regressions. First, the exponent d is assumed, and B_{t} and B_{s} are solved by linear regression. Second, B_{t} is assumed, and d and B_{s} are solved by linear regression. If convergence is not satisfied for B_{t}, B_{s}, and the exponent d, the procedure is repeated. The scatter of the data correlated is within $\pm 20\%$ for oil and glycerine on the shell side and within $\pm 10\%$ for water and condensing refrigerant on the shell side. Briggs and Young report that the correlation of data is substantially improved if variation in the Reynolds number exponent is considered for a wide range of Reynolds numbers.

Modification of Khartabil, Christensen, and Richards Khartabil, Christensen, and Richards [55] relaxed the restriction that the wall resistance and the tube-side Reynolds number exponent be known. The general expression for overall heat transfer resistance is given by

$$\frac{1}{UA} = \frac{1}{B_{\text{t}} \left[\text{Re}^{a} \text{Pr}^{0.33} \left(\dfrac{\mu_{\text{b}}}{\mu_{\text{w}}} \right)^{0.14} Ak/D \right]_{\text{t}}} \tag{30}$$

$$+ \frac{1}{B_{\text{s}} \left[\text{Re}^{d} \text{Pr}^{0.33} \left(\dfrac{\mu_{\text{b}}}{\mu_{\text{w}}} \right)^{0.14} Ak/D \right]_{\text{s}}} + R_{\text{w}} .$$

The unknowns are R_{w}, B_{t}, B_{s}, and the exponents d and a. General solution of Eq. (30) requires a nonlinear regression analysis. Khartabil *et al.* consider that a general nonlinear regression analysis provides less confidence in the validity of the results than linear regressions because linear regressions can identify transition regimes. Rather than solve the general nonlinear regression, Khartabil *et al.* perform a series of experiments and associated linear regressions of the data:

- *Series 1.* Data are measured with the shell-side heat transfer resistance dominant. The results are analyzed by assuming values for the wall resistance and tube-side resistance, and B_{s} and d are calculated.

- *Series 2.* Data are measured with the tube-side heat transfer resistance dominant. The results are analyzed by assuming values for the wall resistance and shell-side resistance, and B_t and a are calculated.
- *Series 3.* Data are measured with the wall resistance dominant. The results are analyzed by assuming values for tube-side resistance and shell-side resistance, and R_w is calculated.

The assumed values of a, d, R_w, B_t, and B_s are iterated to obtain convergence for the three series of data. For the case of a coiled tube-in-tube heat exchanger with a fluted inner tube, Khartabil *et al.* report the uncertainty of Nu_t, Nu_s, and R_w to be $\pm 9.6\%$, $\pm 14.1\%$, and $\pm 15.7\%$, respectively.

2. *Steady-State Test Methods for Gases*

Steady-state methods to test the heat transfer of compact heat exchanger surfaces for gases have been discussed by Kays and London [56] and Shah and Zhou [50]. On one side of the heat exchanger, fluids with high heat capacity rates such as steam or chilled water are used for the "known" heat transfer characteristic. On the other side, air is used for the unknown heat transfer characteristic. Based on the discussion in Kays and London, the estimated error in air flow measurement is $\pm 0.7\%$, the estimated error in point temperature measurement is $\pm 0.2°F$, and the error in bulk average temperature is estimated to be $\pm 0.5°F$ due to spatial variation. The accuracy of the results is a function of the effectiveness (and hence NTU), and the NTU range is generally restricted between 0.5 and 3. The overall uncertainty of the Colburn j factor is estimated to be $\pm 5\%$ for the most accurate tests.

3. *Transient Single Blow Methods*

Transient single blow methods to determine the heat transfer coefficient for gases consist of measuring the outlet gas temperature following a step change (or other nonperiodic change) in inlet temperature. Transient single blow methods were developed as a cost effective method to measure both the heat transfer characteristics (Colburn j-factor) and pressure drop characteristics (Fanning f-factor) for compact gas turbine recuperators. The principal advantages of the transient techniques are that only a single flowing fluid is needed, the wall temperature is not needed, and fin contact resistance and fin efficiency do not affect performance evaluation [57, 58]. In general, the test apparatus consists of a ducted air system with a flowmeter and air heater. The following initial and boundary conditions are applied (based on an arrangement where the test fluid is the hot fluid):

$$\varepsilon_f^*(x^*, 0) = \varepsilon_w^*(x^*, 0) = 0$$

$$\varepsilon_f^*(0, \theta^*) = \psi(\theta^*)$$

where

$$\varepsilon_f^* = \frac{T(x, \theta) - T_{initial}}{T_{max} - T_{initial}}, \ \varepsilon_w^* = \frac{T_w(x, \theta) - T_{initial}}{T_{max} - T_{initial}}, \ x^* = x/L, \ \theta^* = \frac{C_{hot}}{\bar{C}_w}\theta.$$

$T_{initial}$ is the initial temperature of test section, and T_{max} is the maximum fluid temperature. Traces of the dimensionless outlet air temperature as a function of dimensionless time are used to determine the average heat transfer coefficient, i.e., $\varepsilon_f^*(NTU_h, \theta^*)$, where $NTU_h = hA/C$.

Numerous methods to analyze the outlet temperature traces have been implemented as discussed by Heggs and Burns [59]. The first analysis is often attributed to Anzelius [60] and Schumann [61] using a simplified heat transfer model (consistent with the model in Section I.C) for an ideal step input. Early researchers determined NTU_h by matching the ideal response with the test data trace. Subsequent researchers used calculational methods based on characteristics of the trace to determine the best estimate of NTU_h. Locke [62] used the maximum slope of the temperature trace to determine NTU_h. Darabi [63] used the times of the 20% and 80% response to estimate NTU_h. Baclic *et al.* [64] developed a differential fluid enthalpy method which uses the time constant of the inlet forcing function, and the temperature difference between the inlet and outlet of the test section to determine the differential fluid enthalpy change. The enthalpy change is correlated with NTU_h. The most recent methods described by Mochizuki *et al.* [57, 58] use a curve matching method to ensure that experimental and theoretical temperatures agree within 3% at five points along the transient temperature response.

The impact of measurement error and modeling idealizations on the accuracy of the heat transfer results has been investigated. Uncertainty in transient temperature measurements of ± 0.2 to $\pm 0.5°F$ (± 0.1 to $\pm 0.3°C$) is considered typical. Differences in uncertainty are primarily attributed to differences in spatial variation [56, 65]. Uncertainties in fluid properties are estimated to be about ± 0.5 to $\pm 1.0\%$ [56, 65]. Uncertainties in geometric measurements are estimated to be less than 1 mm [56, 65]. Loehrke [66] has reported on the impact of modeling assumptions on the accuracy of a transient single blow heat exchanger test. Factors evaluated include inlet fluid temperature history, longitudinal conduction, variable heat transfer coefficient, and effective core mass. Loehrke describes the errors of several idealizations as a function of NTU_h and method of data reduction. The results indicate that the error in heat transfer coefficient ranges from 2% to

more than 50% with a mismatch in inlet temperature function, from 1% to more than 50% due to mismatch in longitudinal conduction, from 4% to more than 20% due to mismatch in spatial variation in heat transfer coefficient, and from 2% to more than 50% due to mismatch in effective core thermal mass. Modern experimental analysis methods can compensate effectively for these idealizations, but it is reasonable to expect that modeling assumptions contribute to the overall uncertainty of the results.

A wide range of overall heat transfer results have been reported. Kays and London [56] report that the uncertainty in the Colburn j factor is $\pm 14\%$ for the single blow method; Pucci *et al.* [67] report that the uncertainty in the j factor using the maximum slope method is on the order of ± 7.5 to $\pm 15\%$; Liang and Yang [65] report that the uncertainty in the j factor is $\pm 6\%$; and Mullisen and Loehrke [68] report that the uncertainty in the j factor is ± 2 to $\pm 8\%$.

4. *Periodic Test Methods*

Periodic test methods consist of imposing periodic fluctuations on a single fluid flowing into a test core and measuring the temperature response of the fluid flowing out of the core. The earliest methods are attributed to Hausen and his students Glaser, Langhans, and Yazicizade [69–72]. Stang and Bush [73] provide a general description of the method for test cores with $0.2 < NTU < 50$ based on the same idealizations used to develop equations (1), (2), and (3), except that the heat capacity of the hot and cold fluids is negligible compared to the heat capacity of the wall, and longitudinal conduction in the wall is considered. If a sinusoidal boundary condition is applied at the inlet,

$$\frac{T_{x=0} - T_{\text{ave}}}{\Delta T_0} = \sin\left(2\pi \frac{\theta}{\theta_0}\right)$$

where $T_{x=0}$ is the temperature at unit inlet, T_{ave} is the average temperature over a period of oscillation, ΔT_0 is the amplitude of oscillation, and θ_0 is the period of oscillation.

Assuming that longitudinal conduction is negligible, the following solution results [73]:

$$\left\{\begin{matrix} \text{amplitude} \\ \text{attenuation} \end{matrix}\right\}_{x=L} = \exp\left(\frac{-A_{\text{hot}}}{r_{\text{hot}} C_{\text{hot}}} \frac{\left(\frac{2\pi}{\theta_0}\right)^2}{\left(\frac{2\pi}{\theta_0}\right)^2 + \left(\frac{A_{\text{hot}}}{r_{\text{hot}} \bar{C}_{\text{w}}}\right)^2}\right) \qquad (31)$$

$$\left\{\begin{array}{c}\text{phase}\\\text{shift}\end{array}\right\}_{x=L} = \frac{A_{\text{cold}}}{r_{\text{hot}}C_{\text{hot}}} \frac{\dfrac{\theta_0 A_{\text{hot}}}{2\pi r_{\text{hot}}\bar{C}_{\text{w}}}}{1 + \left(\dfrac{\theta_0 A_{\text{hot}}}{2\pi r_{\text{hot}}\bar{C}_{\text{w}}}\right)^2} \qquad (32)$$

Stang and Bush have evaluated the uncertainty in heat transfer coefficient determined using the periodic method. Their evaluation indicates that the temperature measurements are the largest source of error, but with the appropriate selection of the oscillation period, the relative uncertainty in heat transfer coefficient is about three times the relative amplitude uncertainty in temperature measurement. They conclude that the results obtained using the periodic method are in good agreement with the results from transient single blow methods.

Roetzel *et al.* [74, 75] have modified this approach by removing the assumption that neglects longitudinal conduction in the fluid. With this modification, performance testing determines both the heat transfer coefficient and axial dispersion coefficient for the test unit. Roetzel *et al.* also conclude that uncertainty in temperature measurement is the largest source of error, and selection of optimal period of oscillation is needed to minimize error in heat transfer coefficient.

B. Sources of Analysis Error

To calculate performance parameters, data in addition to the terminal temperatures and process flow rates are needed. These additional data include fluid properties, heat exchanger geometry, and applicable heat transfer model data. For many industrial applications it is expensive and not practical to perform the measurements necessary to determine these data. As a result, typical published data for other similar applications are used, and substantial uncertainty may be introduced. This section examines these additional data and discusses the uncertainty.

1. *Heat Capacities of Fluid Streams*

Calculation of the heat transfer rate in accordance with Eqs. (15) and (16) requires that a representative value of specific heat be applied. For applications where the change in fluid temperature from inlet to outlet is small, the change in specific heat between the inlet and outlet is also small, and use of specific heat at the average fluid temperature[7] is adequate. If the change in

---

[7]The average fluid temperature is $(t_{\text{i}} + t_{\text{o}})/2$ for the cold fluid stream and $(T_{\text{i}} + T_{\text{o}})/2$ for the hot stream.

specific heat is large, the inlet and outlet enthalpy can be used to calculate heat transfer rate. For the most common engineering fluids (water, steam, and air), heat capacity data in the open literature [76, 77] are considered very accurate for performance test evaluations. For other fluids, heat capacity data in the open literature are considered to be less accurate [78–80].[8] For fluid streams where the composition or fluid properties are not well known, sampling of the fluid stream (and laboratory measurement of the properties) may be needed for an accurate test.

2. Idealizations in Mean Temperature Difference

The mean temperature difference is used to calculate overall heat transfer coefficient (or NTU) from the unit heat transfer rate. Without temperature data at intermediate points within the heat exchanger, a heat transfer model is applied to calculate the mean temperature difference using the terminal temperatures and mass flow rates. The differences between the true conditions and the idealizations applied in the calculation of mean temperature difference are sources of error for the performance assessment. The errors associated with many of these idealizations have been examined, and results for some nonideal conditions have been reported in the open literature.

Variation in Overall Heat Transfer Coefficient along Flow Length   For heat transfer models where the overall heat transfer coefficient is assumed to be constant or a representative average temperature is used, a bias in the mean temperature difference results if U varies along the flow length (due to variation in convective heat transfer coefficient and fouling resistance). Colburn [81] developed an analytical expression for the performance of counterflow heat exchangers where U is a linear function of temperature of either the hot or cold streams:

$$\frac{Q}{A} = \frac{U_1 \Delta T_2 - U_2 \Delta T_1}{\ln\left(\dfrac{U_1 \Delta T_2}{U_2 \Delta T_1}\right)} \tag{33}$$

---

[8]ASME PTC 12.5 [30] provides bounding estimates for uncertainty of specific heat based on open literature data:

$$\frac{\delta c_{\mathrm{p}}}{c_{\mathrm{p}}} = \pm 0.01 \text{ for water,} \qquad \frac{\delta c_{\mathrm{p}}}{c_{\mathrm{p}}} = \pm 0.05 \text{ for other liquids,}$$

$$\frac{\delta c_{\mathrm{p}}}{c_{\mathrm{p}}} = \pm 0.01 \text{ for stream and dry air,} \qquad \frac{\delta c_{\mathrm{p}}}{c_{\mathrm{p}}} = \pm 0.02 \text{ for other gases.}$$

where

$$\Delta T_1 = T_i - t_o$$

$$\Delta T_2 = T_o - t_i$$

$U_1 = U$ at hot stream inlet

$U_2 = U$ at hot stream outlet

For flow arrangements other than counterflow, a simple approach uses the traditional F correction factor combined with the preceding equation as originally suggested by Sieder and Tate [51] and reiterated by Gardner and Taborek [82]. The error in this approach was estimated to be about 10% by Gardner [83] for the case of a one shell pass-two tube pass configuration.

The bias in the mean temperature difference for counterflow arrangements, $(\delta\Delta T_m/\Delta T_m)_{\text{variable } U}$, can be estimated by comparing the result from Colburn, Eq. (33), with the results using the traditional approach based on an average U, $U_{\text{average}} = (U_1 + U_2)/2$. This method is similar to the one used by Gardner and Taborek to determine temperature correction:

$$\left(\frac{\delta\Delta T_m}{\Delta T_m}\right)_{\text{variable } U} = 1 - \frac{\left(\dfrac{Q}{A}\right)_{\text{variable } U}}{\left(\dfrac{Q}{A}\right)_{\text{average } U}}. \tag{34}$$

Using the same nomenclature as in Eq. (33),

$$\left(\frac{\delta\Delta T_m}{\Delta T_m}\right)_{\text{variable } U} = 1 - \frac{2(U_1/U_2 - \Delta T_1/\Delta T_2)\ln\left(\dfrac{\Delta T_1}{\Delta T_2}\right)}{(1 + U_1/U_2)(\Delta T_1/\Delta T_2 - 1)\ln\left(\dfrac{U_1/U_2}{\Delta T_1/\Delta T_2}\right)}. \tag{35}$$

Using Eq. (35), the bias in mean temperature difference due to variable U is shown in Fig. 4 for linear variation of U with temperature.

Shell-Side Bypass Flow   For traditional methods of evaluating mean temperature difference, the temperature is assumed to be uniform over a flow cross section. The effect of bypass flow on temperature profile for shell-and-tube heat exchangers has been investigated previously by Whistler [84] for the one shell pass/one tube pass counterflow configuration and by Fisher and Parker [85] for the one shell pass/two tube pass configuration based on the assumption that the main flow stream mixes thoroughly with the bypass stream after each baffle pass. The temperature profile and associated assumptions are shown schematically in Fig. 5 for the one shell pass/one
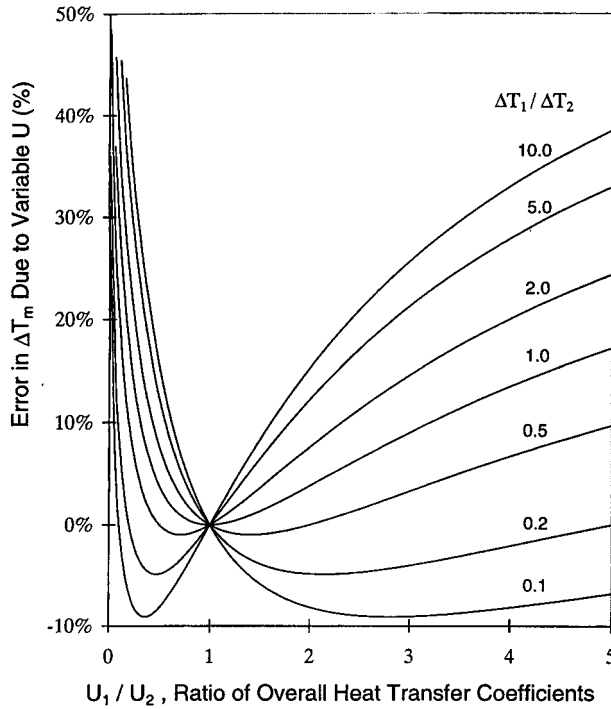
FIG. 4. Estimate of the error in mean temperature difference due to variation in overall heat transfer coefficient.

tube pass counterflow configuration. The bias in the mean temperature difference is a function of the bypass fraction, the number of baffle plates, and the ratio $(T_i - T_o)/\Delta T_{lm}$. Some investigation of the effect of bypass flow for conditions of partial mixing have been investigated, such as by Bell and Kegler [86]; however, a generalized method to estimate the effect of bypass flow on mean temperature difference has not been developed.

Flow Maldistribution For compact designs, the calculation of mean temperature difference may be impacted by maldistribution of flow. In particular, use of formulas based on idealizations regarding uniform temperature over a cross-section and uniform heat transfer coefficient may introduce a bias if flow is maldistributed. For compact heat exchanger tests where the $(T_i - T_o)/\Delta T_{lm}$ is large or flow maldistribution is significant, the bias due to this effect may be significant. The effects of flow maldistribution on heat
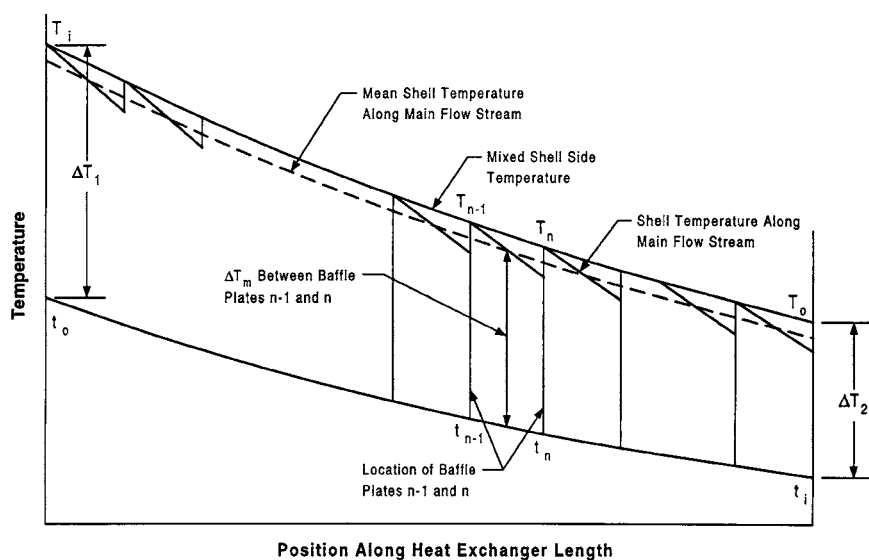
FIG. 5. Temperature profile for a one shell pass/one tube pass counterflow heat exchanger showing bypass flow effect.

exchanger performance have been evaluated in the open literature[9]; however, a generalized approach is not available to determine the true mean temperature difference from industrial test data when flow is maldistributed. One approach is to integrate $\int dQ/(T - t) = Q/\Delta T_m$ based on a model for flow distribution. Additional data are needed for this integration and errors are introduced if assumptions are inaccurate.

Limited Shell Side Baffles for Shell-and-Tube Heat Exchangers. For a baffled shell-side configuration, the flow and temperature distribution is complicated and the traditional assumption that the temperature distribution at a flow cross-section is uniform appears to be a poor approximation. The error attributed to this assumption has been investigated for shell-and-tube heat exchangers due to a limited number of baffles and bypass flow around baffle plates. If the number of baffles is large, the variation in

[9]Both passage-to-passage flow nonuniformity and gross flow maldistribution have been investigated for compact heat exchangers. Mueller and Chiou [87] provide a general review of the literature of the types of flow maldistribution. Mondt [88] and Shah and London [89] evaluate the performance attributed to passage-to-passage flow nonuniformity caused by manufacturing variations of compact plate-fin heat exchangers. Weimer and Hartzog [90], Sparrow and Ruiz [91], Chowdhury and Sarangi [92], and Thonon, Mercier, and Feidt [93] discuss gross maldistribution due to flow blockage and heat exchanger design.

temperature across the flow cross section is small compared to the overall temperature change for the fluid stream of the unit. If the number of baffles is small, the bias in mean temperature difference may be significant as investigated by Gardner and Taborek [82] and Shah and Pignotti [94]. The results of Gardner and Taborek indicate that more than 11 baffle crossings are needed to ensure that this effect is negligible for the one shell pass/one tube pass counterflow arrangement and that more than five baffle crossings are needed for the one shell pass/two tube pass arrangement. The results of Shah and Pignotti indicate that more than 10 baffles are needed to ensure that the effect is negligible for a 1-1 TEMA E counterflow heat exchanger and more than six baffles are needed for a 1-2 TEMA E exchanger.

3. *Convective Heat Transfer Resistance*

Calculations of the hot and cold stream heat transfer resistance are needed to adjust the results from test conditions to reference conditions as shown in Eq. (20). These calculations typically use correlations based on experimental data as described in Section III.A. In general, these experimental data were obtained under ideal conditions where the heat exchanger is clean, flow rates and inlet temperatures are steady, and geometry is known exactly (but test units often had few baffles and/or unknown bypass leakage effects). Application of correlations based on these experimental results to the analysis of an in-service industrial heat exchanger is uncertain. Measurement error in the experiments that form the basis of the model, flow distribution that is different than the distribution during the basis experiments, and differences in fluid properties result in sources of error for assessment of industrial heat exchanger performance.

For test analysis, the errors associated with the correlations of heat transfer coefficients result in an error in the calculation of the adjustment in convective heat transfer resistance, $1/(\eta Ah)^r - 1/(\eta Ah)^t$. The Technical Committee for the ASME PTC 12.5 [30] evaluated and applied practical assumptions regarding the error in the adjustment of convective heat transfer resistance. Most of the error in the adjustment in convective heat transfer resistance is assumed to be attributed to fixed sources of error or biases based on the specific heat exchanger geometry and fluid stream distribution. As a result, a heat transfer correlation that calculates the heat transfer coefficient 10% higher than the true value at test conditions would also calculate the coefficient about 10% higher at reference conditions. Based on this observation, the uncertainty in the adjustment in convective heat transfer resistance can be estimated using the following grouping of terms assuming that η and A are constant between test and

reference conditions:

$$\frac{1}{(\eta Ah)^{\mathrm{r}}} - \frac{1}{(\eta Ah)^{\mathrm{t}}} = \frac{1}{(\eta Ah)^{\mathrm{r}}}\left(1 - \frac{h^{\mathrm{r}}}{h^{\mathrm{t}}}\right).$$

If we introduce Eq. (26),

$$\frac{1}{(\eta Ah)^{\mathrm{r}}} - \frac{1}{(\eta Ah)^{\mathrm{t}}} = \frac{1}{(\eta Ah)^{\mathrm{r}}}\left(1 - \frac{\left(\mathrm{Re}^{n}\mathrm{Pr}^{1/3}\left(\frac{\mu_{\mathrm{b}}}{\mu_{\mathrm{w}}}\right)^{0.14} k/D\right)^{\mathrm{r}}}{\left(\mathrm{Re}^{n}\mathrm{Pr}^{1/3}\left(\frac{\mu_{\mathrm{b}}}{\mu_{\mathrm{w}}}\right)^{0.14} k/D\right)^{\mathrm{t}}}\right) = \frac{1}{(\eta Ah)^{\mathrm{r}}}(1 - X)$$

where

$$X = \frac{\left(\mathrm{Re}^{n}\mathrm{Pr}^{1/3}\left(\frac{\mu_{\mathrm{b}}}{\mu_{\mathrm{w}}}\right)^{0.14} k/D\right)^{\mathrm{r}}}{\left(\mathrm{Re}^{n}\mathrm{Pr}^{1/3}\left(\frac{\mu_{\mathrm{b}}}{\mu_{\mathrm{w}}}\right)^{0.14} k/D\right)^{\mathrm{t}}}$$

Neglecting any uncertainty in the correction factor X, the uncertainty in the adjustment in convective heat transfer resistance is represented by

$$\delta\left(\frac{1}{(\eta Ah)^{\mathrm{r}}} - \frac{1}{(\eta Ah)^{\mathrm{t}}}\right) = \frac{1 - X}{\eta A}\delta\left(\frac{1}{h^{\mathrm{r}}}\right) \tag{36}$$

Based on Eq. (36), the uncertainty of the term $1/(\eta Ah)^{\mathrm{r}} - 1/(\eta Ah)^{\mathrm{t}}$ is the product of the overall uncertainty of the average convective resistance and the percentage change between test and reference conditions. When test conditions are near reference conditions, $X \to 1$, the uncertainty attributed to the adjustment in convective heat transfer coefficient is small.

For tests where the convective thermal resistance dominates the overall thermal resistance and when test conditions are different from reference conditions (X is not near 1), the error due to the adjustment in convective heat transfer resistance may be significant.

Estimating the uncertainty in convective heat transfer resistance requires judgment since the accuracy of correlations is difficult to determine as applied to industrial exchangers. From the standpoint of an industrial test engineer, the accuracy of the underlying experimental data is not well understood and the error associated with the application of experimental data to industrial conditions is unclear. In rare instances, correlations of heat transfer coefficient can be developed based on *in situ* data; however, it

can be difficult and expensive to measure accurate data over a wide range of conditions. Instead, bounding estimates are used based on data in the open literature.[10]

Tube-Side Heat Transfer Coefficient Gnielinski [95] compares data from a large number of experiments and determines that 90% of the data are within $\pm 20\%$ of the predicted correlation. This data scatter is substantially greater than the uncertainty of the best experimental tests, and most of this variation is attributed to uncompensated experimental error for some of the results. Petukhov [96] estimates that the error in the tube-side correlation is about ± 5–6% based on comparisons with the best experimental data. For performance assessment of industrial heat exchangers, flow maldistribution in the tube bundle may increase the error in tube-side coefficient.[11]

Shell-Side Heat Transfer Coefficient Because of the complexity of the geometry and flow distribution for shell-side heat transfer, a large amount of detailed geometry data is needed and iterative computer programs are often used. Few data are published in the open literature that compare the results of generalized calculation methods (probably because of the commercial impact of a comparison of proprietary computer results). For baffled shell-side flow arrangements, the best published comparison of the predicted results with experimental data is presented by Palen and Taborek [99]. A sample of the data from the Heat Transfer Research Inc. (HTRI) files is plotted along with predicted results for the Tinker, Delaware and HTRI methods. The Tinker stream analysis [100] computes the heat transfer

---

[10]The Technical Committee for ASME PTC 12.5 evaluated the open literature data and identified bounding estimates for some typical geometries:

$$\frac{\delta(1/h)}{1/h} = \pm 0.1 \text{ for tube side of shell and tube heat exchangers}$$

$$\frac{\delta(1/h)}{1/h} = \pm 0.2\text{--}0.5 \text{ for shell side of shell and tube heat exchangers}$$

$$\frac{\delta(1/h)}{1/h} = \pm 0.1\text{--}0.2 \text{ for plate-frame heat exchangers}$$

$$\frac{\delta(1/h)}{1/h} = \pm 0.2 \text{ for plate-fin heat exchangers.}$$

[11]A number of other tube-side correlations are available in the open literature as discussed by Bhatti and Shah [97]. The work of Sieder and Tate [51] is of particular mention because of their application of the ratio of viscosities μ_b/μ_w to reduce data scatter. Dittus and Boelter [98] developed a pair of correlations (one for heating and one for cooling) that are still in wide use today in spite of their limitations at low Reynolds numbers and high Prandtl numbers.

coefficient as a function of 5 flow streams which subdivide the shell-side flow. The Delaware method [4] computes the heat transfer coefficient using correction factors applied to the heat transfer coefficient for the ideal case of crossflow across a tube bundle. The HTRI method [99] uses a modified Tinker analysis which has been correlated with an extensive body of heat exchanger data. For the Tinker and Delaware methods, the experimental data are within ±50% of the predictions with shell-side Reynolds numbers greater than 100. With the HTRI method, the data scatter is somewhat less. Most of this scatter is attributed to the inability to match the temperature and heat transfer coefficient variations with complicated flow geometries and fluid property variations. For air-side heat transfer with plain fin-and-tube heat exchangers, Kim, Youn, and Webb [101] have correlated 47 sets of data from various investigators. The heat transfer correlation (for three or more rows) predicts 94% of the data within ±20%.

Plate-Fin Heat Transfer Coefficient For plate-fin heat exchanger applications, a variety of fin designs are used, including plain fins, wavy fins, offset strip fins, perforated fins, pin fins, and louvered fins. Kays and London [5] probably provide the most comprehensive resource for plate-fin heat transfer data. Predictive correlations generally have limited application because empirical data are used to determine performance. For rectangular offset strip fin designs, Manglik and Bergles [102] summarize correlations developed by several investigations and develop formulas for predicting heat transfer for laminar and turbulent flow conditions. The results of the heat transfer formulas are correlated with 18 cores within ±20%.

4. Fouling Resistance

It is typically assumed that the average fouling resistance is the same at test conditions as at reference conditions. The investigation of the validity of this assumption has received little attention. Factors such as spatial variation of fouling resistance coupled with differences in temperature and flow conditions may affect the average fouling resistance. Using in-plant data, it is often difficult to distinguish changes in average fouling resistance from changes in flow distribution and other changes that affect the mean temperature difference. To understand trends in fouling or performance data, factors that change mean temperature difference and overall heat transfer coefficient need to be distinguished from other factors that affect the average fouling resistance. Assuming that fouling resistance is the same at test and reference conditions, performance test results are more accurate at clean conditions or near reference conditions.

5. Wall Resistance

For most heat exchangers, the thermal resistance of the wall is small compared to the other thermal resistances. Therefore, the adjustment in average wall resistance is small and any error has a negligible impact on the assessment of performance. However, for instances where the wall resistance is significant and varies greatly with temperature, the error in the wall resistance due to the variation in thermal conductivity (and its impact on mean temperature difference) may be significant.

6. Other Factors

Other factors may need to be considered in the evaluation of uncertainty. For compact plate-fin designs, longitudinal heat conduction in the wall may significantly affect performance for conditions where thermal gradients and effectiveness are high as discussed by Shah [103]. In these instances, longitudinal conduction should be considered in the heat transfer model. For very high or low temperature heat exchangers, heat transfer with ambient may affect the test results.

IV. Uncertainty Assessment

It is well accepted that test results differ from the true value. This difference is the error of the test. The estimate of this error is the test uncertainty. Uncertainty assessment provides a basis of comparison of results from different flow rates and temperatures, different instrumentation, and different heat exchangers. Modern methods of assessing and combining estimates of sources of error attribute their origins to Kline and McClintock [104]. A more complete statistical treatment of the methods of uncertainty analysis for test results is described in [105] and [106].

In general, error estimates of test variables are propagated into the overall uncertainty using a root sum-of-the-squares approach. For an arbitrary test performance parameter Y that is a function of n independent test variables, the overall uncertainty of the result is given by

$$\delta Y = \left[\left(\frac{\partial Y}{\partial x_1} \delta x_1 \right)^2 + \left(\frac{\partial Y}{\partial x_2} \delta x_2 \right)^2 + \cdots + \left(\frac{\partial Y}{\partial x_n} \delta x_n \right)^2 \right]^{1/2} \tag{37}$$

where $\partial Y / \partial x$ and δx are the sensitivity coefficient and uncertainty for variable x. Equation (37) is a rigorous description of the combination of independent random observations. Modern application of uncertainty analysis classifies sources of errors into two categories, fixed error (or bias)

and random error [107, 108]. Estimates of fixed errors are systematic uncertainties, and an estimate of random error is the standard deviation of the mean for a sample of observations. The overall uncertainty of a test result is given by

$$\delta Y = \hat{t}\sqrt{\left(\frac{\delta Y_{\text{fixed}}}{2}\right)^2 + \sigma_Y^2} \tag{38}$$

where δY_{fixed} is the root-sum-square of all systematic uncertainties for performance parameter Y, σ_Y is the standard deviation of the mean of a sample of individual measurements, and $\hat{t}$ is the Student t distribution for the random observations.[12] Application of root-sum-square combination of systematic uncertainties is based on the assumption of independent and random fixed errors. For fixed errors that are known, the observation should be corrected to account for the error. For fixed errors that are not independent (i.e., correlated), covariance terms should be added to the summation.

A. Evaluating Experimental Uncertainty

The objective of a well-designed experiment is to minimize (and eliminate if possible) fixed errors and bias. With such an experiment, the test results are dominated by random error and will be close to the true value if sufficient test runs are performed. To meet this objective, systematic diagnosis of all identified sources of error is attempted, and bounding estimates of the errors are determined or the results are corrected to eliminate the error. Moffat [109–111] describes a method for the analysis of uncertainty used for the design of an experiment. The method consists of establishing uncertainties for different replication levels. Each successive level of replication permits consideration of additional sources of error.

- *Zeroth Order*. Zeroth-order replication does not permit any changes in conditions except for the act of observation. The zeroth-order uncertainty is contribution to the overall uncertainty arising from the instrumentation and data acquisition system itself.
- *First Order*. First-order replication permits timewise variation in measurements. The first-order uncertainty is a measure of the repeatability of the experiment (using the same instruments) and steadiness of conditions.
- *Nth Order*. Nth-order replication permits variations in the instrumentation in addition to timewise variations. N-th order uncertainty

[12]For most practical industrial test applications, $\hat{t} = 2$. Earlier standards for uncertainty analysis applied the Student t to the random component of the uncertainty only.

includes effects due to instrument calibration, unsteadiness, and obser-
vation. The Nth-order uncertainty permits comparison of the results
from one experiment with the results from other similar experiments
or with "true" values.

This approach to estimating uncertainty allows a researcher to anticipate
scatter in the results, identify uncontrolled variables, and correct for fixed
errors. One method to diagnose uncertainty estimates is to compare the
standard deviation of the results with the uncertainty for successive orders
of replication. Moffat suggests that if the standard deviation of the results is
greater than $1/2\delta Y_i$, where Y is an arbitrary result and i is the order of
replication, the uncertainty estimate may be too low or an uncontrolled
variable may be influencing the results. To confidently determine and
correct fixed errors and uncontrolled variables, a comprehensive series of
diagnostic tests are necessary.

B. Evaluating Uncertainty of Industrial Tests

Based on the condition and operating limitations in an industrial process,
comprehensive diagnostic testing to identify uncertainty estimates is not
practical. Judgment is often needed to estimate the uncertainties for these
fixed errors. To assist the test engineer, guidelines have been developed to
standardize the methods of analysis of measurement uncertainty for indus-
trial tests [107, 108]. Based on the discussion by Abernathy et al. [112], the
work to standardize the uncertainty analysis method has been ongoing for
more than 20 years.

Since it is difficult to control all test conditions, the number of factors that
may contribute to the overall uncertainty of an industrial test is typically
greater than for a laboratory experiment. However, most of the potential
sources of error provide an insignificant contribution to the overall uncer-
tainty, and the uncertainty is dominated by two or three factors. Confidence
in the results of industrial testing is attained by identifying the key factors
and diagnosing the sources of errors for these factors. Before a test, analysis
of uncertainty is performed to identify instrument calibration and installa-
tion requirements and to determine operating conditions and constraints on
the process fluid streams. Judgment is used to estimate limits of error for
several factors such as spatial variation of the temperature measurements.
After a test, data are used to determine uncertainty for various factors. Since
it is not possible to perform Nth-order replications in an industrial process
stream, test data are often used only to confirm the uncertainties estimated
in the pretest analysis for some factors.

Application of uncertainty analysis methods for thermal performance tests of industrial heat exchangers is varied. Although general methods are consistent and based on industry standards, the sources of error included and methods to estimate their magnitude vary substantially [7, 9, 113–115]. To address these inconsistencies, ASME PTC 12.5 [30] provides detailed guidance regarding the types of error sources and methods to estimate their magnitude. Based on the evaluation of the PTC 12.5 Technical Committee, the overall uncertainty of thermal performance (with U or Q as the performance parameter) for controlled tests using calibrated instruments is in the range of ± 3 to $\pm 10\%$.

In this chapter, overall heat transfer resistance and fouling resistance have been selected for evaluation of test uncertainty. As discussed in Section II.B.2, overall heat transfer resistance is a general performance parameter that facilitates the use of corrections to account for differences between test and reference conditions. Fouling resistance is often used since it reduces the calculations performed for the heat transfer model. For both of these parameters, a generalized expression for test uncertainty is developed, and the sensitivity of the overall uncertainty to the most significant sources of error is assessed.

1. *Overall Heat Transfer Resistance*

At test conditions, the overall heat transfer resistance is given by

$$\frac{1}{(UA)^{\mathrm{t}}} = \frac{\Delta T_{\mathrm{m}}}{Q} = \frac{1}{C_{\mathrm{cold}} NTU_{\mathrm{cold}}}. \tag{39}$$

The uncertainty is a function of the uncertainty of the four terminal temperature measurements, the uncertainty of the hot and cold stream flow rate measurements, the uncertainty of the specific heat of the hot and cold fluids, and the uncertainty in the idealizations used in the calculation of mean temperature difference (or other assumptions used in the heat transfer model). Based on the root-sum-squares methodology for independent measurements:

$$
\begin{aligned}
\delta&\left(\frac{1}{UA}\right)^{\mathrm{t}} \\
&= \left[\left(\frac{\partial(1/UA)}{\partial t_{\mathrm{i}}}\delta t_{\mathrm{i}}\right)^2 + \left(\frac{\partial(1/UA)}{\partial t_{\mathrm{o}}}\delta t_{\mathrm{o}}\right)^2 + \left(\frac{\partial(1/UA)}{\partial T_{\mathrm{i}}}\delta T_{\mathrm{i}}\right)^2 + \left(\frac{\partial(1/UA)}{\partial T_{\mathrm{o}}}\delta T_{\mathrm{o}}\right)^2 \right. \\
&\quad \left. + \left(\frac{\partial(1/UA)}{\partial C_{\mathrm{cold}}}\delta C_{\mathrm{cold}}\right)^2 + \left(\frac{\partial(1/UA)}{\partial C_{\mathrm{hot}}}\delta C_{\mathrm{hot}}\right)^2 + \left(\frac{\partial(1/UA)}{\partial \Delta T_{\mathrm{m}}}\delta \Delta T_{\mathrm{m,ideal}}\right)^2 \right]^{1/2}
\end{aligned}
\tag{40}
$$

where $\delta\Delta T_{m,\text{ideal}}$ is the uncertainty attributed to the idealizations used in the calculation of mean temperature difference. The sensitivity coefficients $(\partial(1/UA)/\partial t_i, \partial(1/UA)/\partial t_o,$ etc.) are a function of the analytic model used and can be determined by differentiating an analytic expression or by performing a perturbation analysis using a computer program. Depending on the heat transfer model used and heat exchanger design, the sensitivity coefficients can vary substantially. For heat exchanger designs with one-two pass arrangement (one fluid has one pass across the heat transfer surface and the other fluid has two passes across the heat transfer surface), the sensitivity coefficients for the outlet temperatures are higher than for a single pass arrangement. In instances where one of the six process measurements has a high uncertainty (or is not measured), a heat transfer model can be applied that eliminates one of the six variables.[13] Furthermore, use of optimization methods can be used to reduce the impact of the error of any one variable on the overall thermal resistance. As such, a generalized expression for the sensitivity coefficients is not practical or desired for all applications.

Based on the uncertainty of heat transfer resistance at test conditions and the corrections to the overall thermal resistance given in Eq. (20), the uncertainty of the heat transfer resistance at reference conditions is given by

$$
\delta\left(\frac{1}{UA}\right)^{\text{r}} = \left\{ \begin{array}{l} \left[\delta\left(\frac{1}{UA}\right)^{\text{t}}\right]^2 + \left[\delta\left(\frac{1}{\eta A h^{\text{r}}} - \frac{1}{\eta A h^{\text{t}}}\right)_{\text{cold}}\right]^2 \\ + \left[\delta\left(\frac{1}{\eta A h^{\text{r}}} - \frac{1}{\eta A h^{\text{t}}}\right)_{\text{hot}}\right]^2 + [\delta(R_{\text{f}}^{\text{r}} - R_{\text{f}}^{\text{t}})]^2 + [\delta(R_{\text{w}}^{\text{r}} - R_{\text{w}}^{\text{t}})]^2 \end{array} \right\}.
$$

$$(41)$$

It is common industry practice to consider the uncertainty in thermal resistance at test conditions and neglect the terms associated with the corrections to the test resistance. This practice is acceptable for tests where $\delta(1/UA)^{\text{t}}$ is substantially greater than the uncertainty of the corrections. Judgment often is used to estimate the uncertainty associated with the

---

[13]The Technical Committee for ASME PTC 12.5 evaluated the impact of different heat transfer models on the results. Of particular interest are models that do not require one (or both) of the outlet temperatures for the calculation of mean temperature difference. For example, ΔT_{m} can be calculated using $R = C_{\text{cold}}/C_{\text{hot}}$ and P_{cold}, thereby eliminating T_{o} from the calculation. In addition, ΔT_{m} can be calculated using the heat capacity rates and inlet temperatures only. Other methods of calculation or optimization may reduce uncertainty for particular applications.

corrections to test resistance because specific data to calculate these corrections are rarely obtained for the test unit in industrial process streams. As a result, bounding estimates for the uncertainties of these corrections are often used to ensure that their effect is included in the overall test uncertainty. If the relative magnitude of the corrections is small, the uncertainties attributed to these uncertainties are usually negligible (even if large, bounding estimates are used). If the relative magnitude of these corrections is large (such as when test and reference conditions are in different flow regimes), diagnostic data at different operating conditions for the heat exchanger under test are needed to estimate the corrections and associated uncertainties.

Experience indicates that the uncertainty of the temperature measurements (and particularly the outlet temperature measurements) dominates the overall test uncertainty for well-designed tests. To investigate the impact of the uncertainty of temperature measurements on overall test uncertainty, the P-NTU method can be used to separate the uncertainty of the temperature measurements from the uncertainty of the flow measurements. The uncertainty of the overall heat transfer resistance is given by

$$\frac{\delta\left(\dfrac{1}{UA}\right)^{\text{t}}}{\left(\dfrac{1}{UA}\right)^{\text{t}}} = \left[\left(\frac{\delta NTU_{\text{cold}}}{NTU_{\text{cold}}}\right)^2 + \left(\frac{\delta C_{\text{cold}}}{C_{\text{cold}}}\right)^2\right]^{1/2}. \tag{42}$$

NTU_{cold} is a function of R and P_{cold} and therefore a function of $T_{\text{i}} - t_{\text{i}}$, $T_{\text{i}} - T_{\text{o}}$, and $t_{\text{o}} - t_{\text{i}}$. The uncertainty of NTU is reduced by ensuring that errors of the temperature measurements are small compared to the corresponding temperature differences. Since the uncertainty of the outlet temperature measurement is larger than the uncertainty of inlet temperatures, it appears that the uncertainty of NTU can be minimized by reducing the uncertainty in the hot stream and cold stream temperature change, $T_{\text{i}} - T_{\text{o}}$ and $t_{\text{o}} - t_{\text{i}}$. However, R and P are "tightly coupled" for several typical industrial applications such that small variations result in large changes in NTU. One example is a high-efficiency compact heat exchanger where the changes in hot and cold stream temperatures are large ($T_{\text{i}} - T_{\text{o}}$ and $t_{\text{o}} - t_{\text{i}}$), and the differences between the hot and cold stream temperatures are small ($T_{\text{i}} - t_{\text{o}}$ and $T_{\text{o}} - t_{\text{i}}$). Small errors in the assessment of mean temperature difference can result in large errors in NTU. Another example is a liquid–liquid heat exchanger with a TEMA E shell and two tube passes. For this design, the log mean temperature correction factor F may be low (less than 0.75) for low fouling conditions, especially if the heat exchanger is designed

with a substantial fouling margin. With a low F, the uncertainty in NTU is high even for very accurate temperature measurements.

A bounding estimate of the uncertainty in NTU[14] can be calculated by considering NTU_{cold} as function of three correlated differential temperatures:

$$NTU_{\text{cold}} = \phi(R, P_{\text{cold}}) = \psi(\Delta T_{\text{a}}, \Delta T_{\text{b}}, \Delta T_{\text{c}}) \tag{43}$$

where $\Delta T_{\text{a}} = t_{\text{o}} - t_{\text{i}}$, $\Delta T_{\text{b}} = T_{\text{i}} - t_{\text{i}}$, and $\Delta T_{\text{c}} = T_{\text{i}} - T_{\text{o}}$. The uncertainty in NTU_{cold} is represented by

δNTU_{cold}

$$= \left[\begin{array}{l} \left(\dfrac{\partial NTU_{\text{cold}}}{\partial \Delta T_{\text{a}}} \delta \Delta T_{\text{a}} \right)^2 + \left(\dfrac{\partial NTU_{\text{cold}}}{\partial \Delta T_{\text{b}}} \delta \Delta T_{\text{b}} \right)^2 + \left(\dfrac{\partial NTU_{\text{cold}}}{\partial \Delta T_{\text{c}}} \delta \Delta T_{\text{c}} \right)^2 \\[12pt] + 2 \left(\dfrac{\partial NTU_{\text{cold}}}{\partial \Delta T_{\text{a}}} \right) \left(\dfrac{\partial NTU_{\text{cold}}}{\partial \Delta T_{\text{b}}} \right) \delta(\Delta T_{\text{a}} \Delta T_{\text{b}}) \\[12pt] + 2 \left(\dfrac{\partial NTU_{\text{cold}}}{\partial \Delta T_{\text{b}}} \right) \left(\dfrac{\partial NTU_{\text{cold}}}{\partial \Delta T_{\text{c}}} \right) \delta(\Delta T_{\text{b}} \Delta T_{\text{c}}) \end{array} \right]^{1/2}$$

$$\tag{44}$$

where $\delta(\Delta T_{\text{a}} \Delta T_{\text{b}})$ and $\delta(\Delta T_{\text{b}} \Delta T_{\text{c}})$ are the applicable covariance terms.[15] For the counterflow arrangement, the uncertainty in NTU_{cold} is shown in Fig. 6. For the one hot stream pass and two cold stream pass arrangement (as with a TEMA E-shell and two tube passes), the uncertainty in NTU_{cold} is shown in Fig. 7.

The uncertainty of NTU_{cold} in Figs. 6 and 7 is a function of P_{cold}, R, and the cold stream temperature change, $\Delta T_{\text{a}} = t_{\text{o}} - t_{\text{i}}$, for accurate temperature measurements. Several general observations can be made regarding the effect of temperature uncertainty on overall test uncertainty. First, tempera-

---

[14]The method of calculating the uncertainty in NTU as a function of R and P presented in this section is useful for test planning because instrument requirements can be established. The method overestimates uncertainty for tests where four temperatures and two flow rates are measured because optimization methods can be applied to reduce the uncertainty. Equations (40) and (41) are the generalized uncertainty expressions and should be used where a heat balance is confirmed and optimization methods are applied.

[15]Most elementary statistics texts provide a formal definition of covariance. For this application, the covariance is the portions of the uncertainties of ΔT_{a}, ΔT_{b}, and ΔT_{c} that are correlated. Assuming that uncertainties of the four terminal temperature measurements are independent, the covariance is the square of the uncertainty of the common terminal temperature such that $\delta(\Delta T_{\text{a}} \Delta T_{\text{b}}) = (\delta t_{\text{i}})^2$ and $\delta(\Delta T_{\text{b}} \Delta T_{\text{c}}) = (\delta T_{\text{i}})^2$.

$$\delta t_i = \delta T_i = 0.1°C$$
$$\delta t_o = \delta T_o = 0.2°C$$
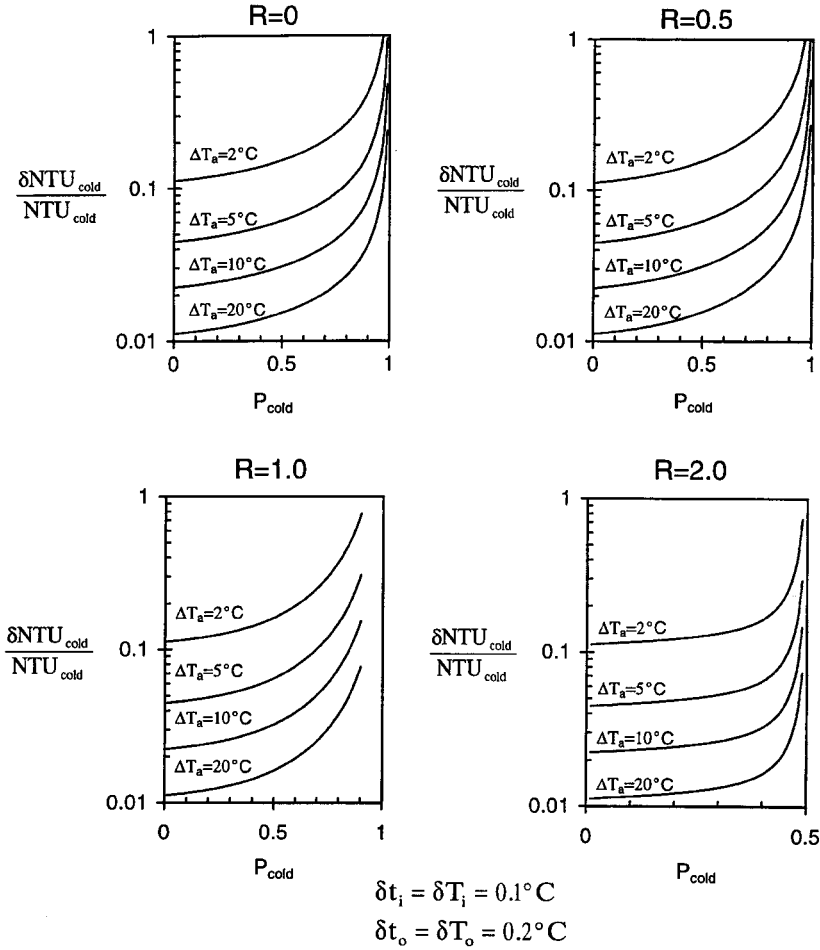
FIG. 6. Uncertainty of NTU_{cold} attributed to uncertainty in temperature measurements for counterflow arrangement.

ture changes greater than 2°C (4°F) are desirable if an accurate performance assessment is needed. This implies that a sufficient heat load should be available for the heat exchanger under test. In addition, the uncertainty in NTU_{cold} becomes excessive as P_{cold} approaches its theoretical limit. Under test conditions where P_{cold} is high (within 10% of its theoretical limit), small variations in test conditions have a large impact on test accuracy. Conversely, small changes in the condition of the heat exchanger have a large impact on the heat exchanger performance when P_{cold} is high.
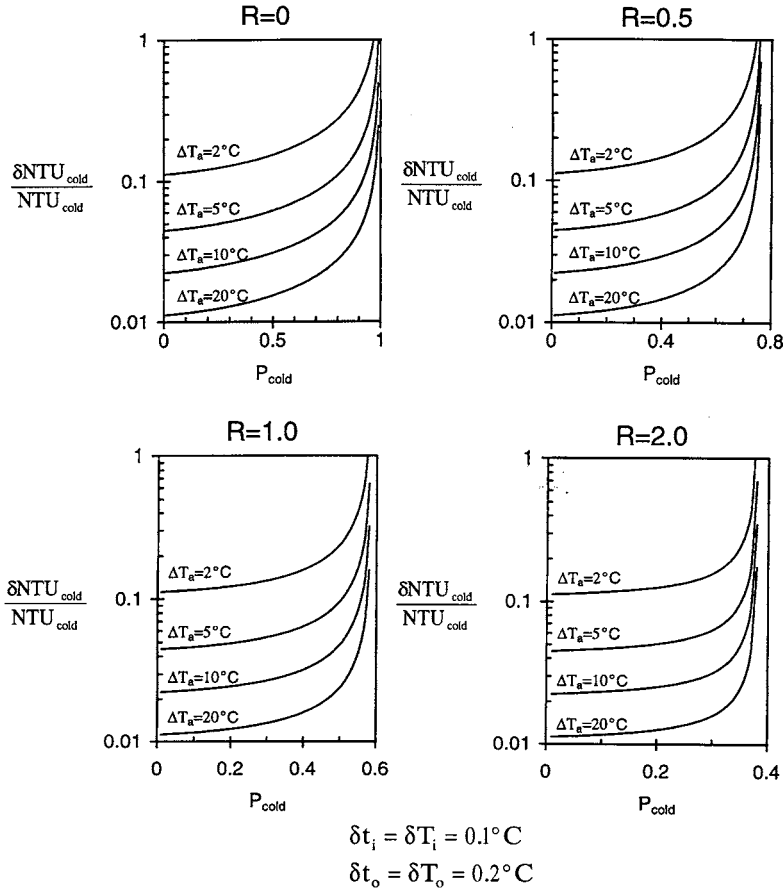
FIG. 7. Uncertainty of NTU_{cold} attributed to uncertainty in temperature measurements for one hot stream pass, two cold stream pass arrangement.

2. Fouling Resistance

Based on Eq. (23), the fouling resistance is defined as follows:

$$R_f = \left(\frac{1}{UA}\right)_f - \left(\frac{1}{UA}\right)_{clean} = \left(\frac{1}{NTU_{cold}C_{cold}}\right)_f - \left(\frac{1}{NTU_{cold}C_{cold}}\right)_{clean}.$$

$$(45)$$

Considering that the uncertainties of $(NTU_{cold})_f$, $(C_{cold})_f$, $(NTU_{cold})_{clean}$, and $(C_{cold})_{clean}$ are independent, the following expression for the uncertainty

in fouling resistance is developed:

$$(\delta R_f)^2 = \frac{1}{(UA)_f^2}\left[\left(\frac{\delta NTU_{cold}}{NTU_{cold}}\right)_f^2 + \left(\frac{\delta C_{cold}}{C_{cold}}\right)_f^2\right]$$
$$+ \frac{1}{(UA)_{clean}^2}\left[\left(\frac{\delta NTU_{cold}}{NTU_{cold}}\right)_{clean}^2 + \left(\frac{\delta C_{cold}}{C_{cold}}\right)_{clean}^2\right]. \qquad (46)$$

As with overall heat transfer resistance, the uncertainty of the temperature measurements is a dominant contributor to the overall uncertainty. As such, the discussion of the uncertainty of NTU in Section IV.B.1 is applicable to fouling resistance. In addition to the uncertainty of the temperature measurements, the overall uncertainty is a function of the relative fouling resistance. The fouling Biot number is a measure of the relative magnitude of fouling on a heat exchanger surface as described by Fryer and Slater [116] and Somerscales et al. [117]:

$$Bi_f = (r_f)_{total}U_{clean} \qquad (47)$$

When the fouling Biot number is large, the overall heat transfer resistance is dominated by fouling. When the fouling Biot number is small, the overall heat transfer resistance is dominated by factors other than fouling. Based on data from Chenoweth [118], the fouling Biot number is calculated for several typical industrial applications in Table 1[16].

The investigations by Somerscales et al. [117] have shown that the uncertainty of the fouling resistance is inversely proportional to the fouling Biot number. In this chapter, the uncertainty of fouling resistance is assessed

---

[16]Excess area is defined by Chenoweth [118] as $A_f/A_{clean} - 1$ where A_f is the area required under fouled conditions and A_{clean} is the area required under clean conditions. Under Chenoweth's conditions, $Q/\Delta T_m = U_{clean}A_{clean} = U_fA_f$. Excess area is the equivalent value as the fouling Biot number based on the following:

$$\frac{A_f}{A_{clean}} - 1 = \frac{U_{clean}}{U_f} - 1 = U_{clean}\left(\frac{1}{U_f} - \frac{1}{U_{clean}}\right) = U_{clean}(r_f)_{total} = Bi_f.$$

It is observed that the fouling Biot number is a function of the geometry of heat transfer enhancements such as finned surfaces. For heat transfer surfaces where $A_{hot} > A_{cold}$, a small fouling resistance on the cold side has a large contribution to total fouling resistance and fouling Biot number. This effect can be shown using the relationship between cold side, hot side, and total fouling resistance from Eqs. (13) and (14) and where $A = (\eta A)_{hot}$:

$$(r_f)_{total} = R_f A = \frac{(\eta A)_{hot}}{(\eta A)_{cold}}(r_f)_{cold} + (r_f)_{hot}.$$

For low-finned tubes, $(\eta A)_{hot}/(\eta A)_{cold}$ is approximately 3–5. For tube-in-plate-fin surfaces, $(\eta A)_{hot}/(\eta A)_{cold}$ is approximately 7–30. Since enhancements are typical for many applications where U_{clean} is low, low fouling Biot numbers (less than 0.1) are encountered only in the most lightly fouled conditions.

TABLE I
TYPICAL FOULING BIOT NUMBER FOR INDUSTRIAL HEAT EXCHANGERS

Fluid streams	U_f (Btu/hr-ft^2-°F)	U_{clean} (Btu/hr-ft^2-°F)	Bi_f
Water–water	250–300	400–546	0.60–0.82
Steam–water	300–400	429–667	0.43–0.67
Light organic liquid–light organic liquid	100–130	125–175	0.25–0.35
Light organic liquid–water	125–175	154–238	0.23–0.36
Medium organic liquid–medium organic liquid	50–80	59–105	0.18–0.32
Medium organic liquid–water	75–125	89–167	0.18–0.33
Heavy organic liquid–heavy organic liquid	5–30	5–35	0.03–0.18
Heavy organic liquid–water	5–75	5–64	0.02–0.19
Gas–water	15–100	15–111	0.02–0.11
Gas–steam	15–110	15–116	0.01–0.06

based on a method adapted from the development in [117]. Consider the simplifying assumption that the relative uncertainty of the cold stream heat capacity rate and NTU_{cold} are the same for the fouled and clean conditions[17]:

$$\left(\frac{\delta NTU_{cold}}{NTU_{cold}}\right)_f = \left(\frac{\delta NTU_{cold}}{NTU_{cold}}\right)_{clean}$$

$$\left(\frac{\delta C_{cold}}{C_{cold}}\right)_f = \left(\frac{\delta C_{cold}}{C_{cold}}\right)_{clean}.$$

Equation (46) becomes

$$(\delta R_f)^2 = \left(\frac{1}{(UA)_f^2} + \frac{1}{(UA)_{clean}^2}\right)\left[\left(\frac{\delta NTU_{cold}}{NTU_{cold}}\right)^2 + \left(\frac{\delta C_{cold}}{C_{cold}}\right)^2\right]. \quad (48)$$

If we apply the fouling Biot number,

$$Bi_f = (r_f)_{total}U_{clean} = R_f(UA)_{clean} = \frac{(UA)_{clean}}{(UA)_f} - 1. \quad (49)$$

---

[17]When test data are available for both clean and fouled conditions, simplifying assumptions are not needed and the uncertainty in fouling resistance is calculated using Eq. (46). With most industrial test applications, $(\delta NTU_{cold}/NTU_{cold})_f < (\delta NTU_{cold}/NTU_{cold})_{clean}$. For planning purposes, it is reasonable to consider that the uncertainty of NTU_{cold} under fouled conditions is bounded by the uncertainty under clean conditions.
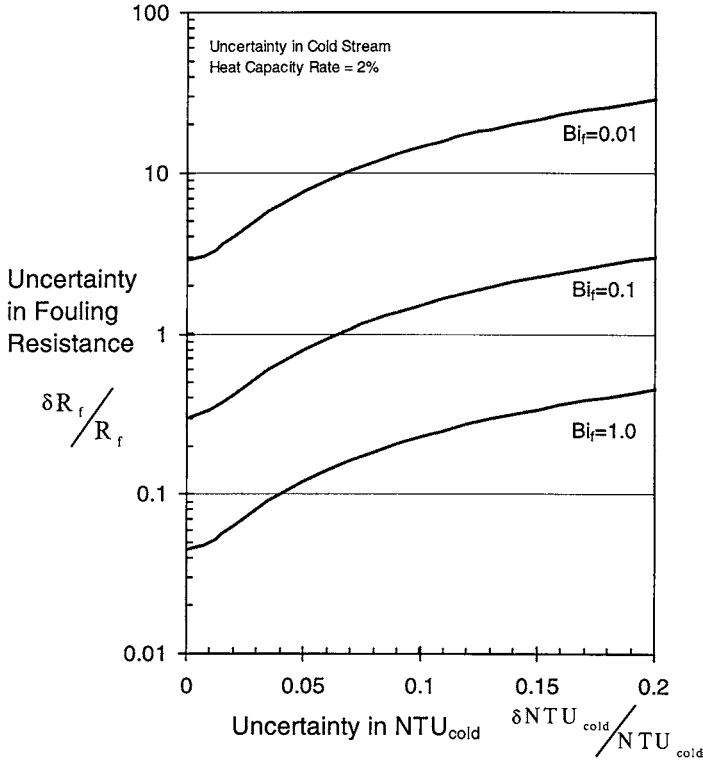
FIG. 8. Uncertainty of fouling resistance.

If we substitute for the fouling Biot number in Eq. (48),

$$\frac{\delta R_f}{R_f} = \sqrt{\frac{(\mathrm{Bi_f} + 1)^2 + 1}{\mathrm{Bi_f^2}} \left[\left(\frac{\delta NTU_{\mathrm{cold}}}{NTU_{\mathrm{cold}}}\right)^2 + \left(\frac{\delta C_{\mathrm{cold}}}{C_{\mathrm{cold}}}\right)^2 \right]}. \qquad (50)$$

The results of Eq. (50) are shown in Fig. 8 for typical fouling Biot numbers. Based on these results, measurement of fouling resistance is impractical for heat exchangers with $\mathrm{Bi_f} \leqslant 0.1$.

V. Conclusions and Future Work

Performance testing of heat transfer surfaces is a mature technology. Methods of measurement and analysis have been developed, revised, and

implemented for numerous heat exchangers in research and industrial applications. The incentive to carefully assess performance is strong since the cost of operating an industrial process stream under excessive fouling conditions is substantial. However, the use of comprehensive thermal performance test methods for industrial heat exchangers is infrequent even for the most critical applications. This lack of use can be attributed to a number of factors:

- *Sensitivity to Temperature Measurement Error.* For most testing applications, the required accuracy of temperature measurements is greater than the capability of installed instrumentation. As a result, calibration and careful installation of temporary instrumentation are needed for a performance test.
- *High Cost of Temperature and Flow Instruments.* The life-cycle cost (installation plus maintenance and calibration) of permanent temperature and flow instruments is a sizable fraction of the life-cycle cost of a process heat exchanger. The total cost of a well-designed thermal performance test with temporary instrumentation can exceed the cost of a heat exchanger. As a result, a process designer is tempted to increase the size of process heat exchangers. (This practice of implementing excessive heat transfer area is known to often accelerate fouling buildup.)
- *Uncertainty of the Assumptions Applied in the Heat Transfer Model.* A heat transfer model is needed to analyze performance data. Idealizations of some attributes of the model can result in substantial error in the results. The most significant idealizations are the assumptions applied to calculate the mean temperature difference using the four terminal temperatures, the assumption that the fouling resistance is the same at test conditions as at reference conditions, and the application of correlations of convective heat transfer coefficient based on ideal experimental data.

In a competitive, cost-driven industrial marketplace, high-quality test practices are needed as a foundation. Such practices (if inexpensively applied) provide a basis and justification for reducing fouling factors (and heat transfer area) in replacement heat exchangers and provide confirmation of guaranteed performance. However, additional work is needed to improve the accuracy and broaden the application of thermal performance test methods in industrial applications. The following areas of research and development are needed:

Implement Reliable, Cost-Effective Smart Sensors. Development of inexpensive smart sensors that compensate for typical bias errors (such as calibration and spatial variation) will have a significant impact on

application of thermal performance test practices. Although much of the basic technology is available for such sensors, implementation is either expensive or impractical at this time. Sensor arrays (based on simple measurement methods) embedded in the heat exchanger may be the most practical method to meet this need.

Facilitate Online Heat Transfer Analysis Methods Suitable for Industry Applications. Most existing computer software used to analyze test results is based on design methods that require a large amount of unit geometry and fluid property data. Analysis of small changes or trends in performance using simplified heat transfer models may provide accurate assessments of fouling trends. Features of these heat transfer models should include a fouling model that addresses spatial variation of fouling resistance and uncertainty of the measurements and analysis methods. Use of embedded sensors along with these simplified analysis methods could be a cost-effective alternative to fouling monitors currently used in selected applications.

Improve Heat Exchanger Performance Test Standards for Industry and Experimental Platforms. Because of the sensitivity of test results to small variations in test and analysis methods, industry personnel often consider open literature data of heat exchanger performance as a site-specific result. Standards provide the basis to plan tests and correlate the results from several installations. Current standards developments address a large number of factors needed to improve the confidence of test results and interpret the results from numerous installations. Use and continual improvement of these standards is needed to improve accuracy (reduce overall uncertainty). In addition, development of experimental test standards may improve the confidence (and reduce the uncertainty) of data used as input for industrial test analysis.

Nomenclature

A	reference heat transfer surface area corresponding to U, m^2, ft^2	C	heat capacity rate of fluid stream, W/K, Btu/(hr-°F)
A_{cold}	cold fluid side heat transfer surface area, m^2, ft^2	C_{cold}	heat capacity rate of cold stream = $(mc_{\text{p}})_{\text{cold}}$, W/K, Btu/(hr-°F)
A_{hot}	hot fluid side heat transfer area, m^2, ft^2	C_{hot}	heat capacity rate of hot stream = $(mc_{\text{p}})_{\text{hot}}$, W/K, Btu/(hr-°F)
B	correlation constant, dimensionless		
Bi_{f}	fouling Biot number = $U_{\text{clean}}(r_{\text{f}})_{\text{total}}$, dimensionless	$\bar{C}_{\text{cold}}$	heat capacity of cold fluid in heat exchanger, J/K, Btu/°F

$\bar{C}_{\text{hot}}$ — heat capacity of hot fluid in heat exchanger, J/K, Btu/°F

$\bar{C}_{\text{w}}$ — heat capacity of wall that separates hot and cold fluids, J/K, Btu/°F

c_{p} — specific heat of fluid at constant pressure, J/(kg-K), Btu/(lbm-°F)

D — hydraulic diameter of flow passage, m, ft

F — log mean temperature difference correction factor, dimensionless

h — convective heat transfer coefficient on one side of the exchanger, W/(m²-K), Btu/(hr-ft²-°F)

$1/h$ — convective thermal resistance on one side of the exchanger, (m²-K)/W, (hr-ft²-°F)/Btu

j — Colburn j factor $= \text{Nu}/(\text{Re}\,\text{Pr}^{1/3})$, dimensionless

k — thermal conductivity, W/(m-K), Btu/(hr-ft-°F)

L — length of heat exchanger, m, ft

m — mass flow rate of fluid stream, kg/s, lbm/hr

m_{cold} — mass flow rate of cold fluid stream, kg/s, lbm/hr

m_{hot} — mass flow rate of hot fluid stream, kg/s, lbm/hr

Nu — Nusselt number $= hD/k$, dimensionless

NTU — number of transfer units $= UA/C$, dimensionless

NTU_{cold} — number of transfer units based on cold side conditions $= UA/C_{\text{cold}}$, dimensionless

NTU_{h} — number of transfer units for one fluid of an experimental unit $= hA/C$, dimensionless

P — temperature effectiveness $(t_{\text{o}} - t_{\text{i}})/(T_{\text{i}} - t_{\text{i}})$, dimensionless

P_{cold} — temperature effectiveness based on cold side $= (t_{\text{o}} - t_{\text{i}})/(T_{\text{i}} - t_{\text{i}})$, dimensionless

Pr — Prandtl number $= \mu c_{\text{p}}/k$, dimensionless

Q — heat transfer rate, W, Btu/hr

Q_{ave} — weighted average heat transfer rate based on measurements for the hot and cold fluid streams, W, Btu/hr

Q_{cold} — heat transfer rate based on cold stream temperatures and heat capacity rate, W, Btu/hr

Q_{hot} — heat transfer rate based on hot stream temperatures and heat capacity rate, W, Btu/hr

R — $(T_{\text{i}} - T_{\text{o}})/(t_{\text{o}} - t_{\text{i}})$

Re — Reynolds number $= \rho V D/\mu$, dimensionless

R_{f} — resistance to heat transfer due to total fouling of the hot and cold heat transfer surfaces, K/W, (hr-°F)/Btu

R_{s} — resistance to heat transfer due to shell side and wall for Wilson line methods, K/W, (hr-°F)/Btu

R_{w} — resistance to heat transfer due to the wall separating the hot and cold heat fluid streams, K/W, (hr-°F)/Btu

r_{cold} — average total cold side resistance to heat transfer per unit cold side area including contributions attributed to convection, fouling, and a portion of the wall, (m²-K)/W, (hr-fr²-°F)/Btu

$(r_{\text{f}})_{\text{cold}}$ — average fouling resistance to heat transfer per unit cold side area, (m²-K)/W, (hr-ft²-°F)/Btu

$(r_{\text{f}})_{\text{hot}}$ — average fouling resistance to heat transfer per unit hot side area, (m²-K)/W, (hr-ft²-°F)/Btu

$(r_{\text{f}})_{\text{total}}$ — average total fouling resistance to heat transfer per unit reference area including contributions attributed to hot side and cold side fouling, (m²-K)/W, (hr-ft²-°F)/Btu

r_{hot} — average total hot side resistance to heat transfer per unit hot side area including contributions attributed to convection, fouling, and a portion of the wall, (m²-K)/W, (hr-ft²-°F)/Btu

S — flow area, m², ft²

t — cold stream temperature, K, °F

$\hat{t}$ — Student t, dimensionless

T — hot stream temperature, K, °F

T_{w} — wall temperature, K, °F

ΔT_{lm}	log mean temperature difference, K, °F
ΔT_m	true mean temperature difference, K, °F
U	overall heat transfer coefficient, W/(m²-K), Btu/(hr-ft²-°F)
$1/(UA)$	overall heat transfer resistance, K/W, (hr-°F)/Btu
V	flow velocity, m/s, ft/hr
x	position along heat exchanger length, m, ft

GREEK SYMBOLS

δY	uncertainty of parameter Y, units of Y
ε	nondimensional temperature, dimensionless
η	overall surface temperature effectiveness, dimensionless
θ	time, s, hr
μ	absolute viscosity, kg/(m-s), lbm/(ft-hr)
ρ	fluid density, kg/m³, lbm/ft³
σ_Y	standard deviation of Y, units of Y

SUBSCRIPTS

b	bulk fluid conditions
clean	clean conditions without fouling
cold	cold fluid stream
f	fouled
hot	hot fluid stream
i	inlet
initial	initial test conditions
o	outlet
s	shell side
t	tube side
w	wall
1	one end of heat exchanger flow length
2	other end of heat exchanger flow length

SUPERSCRIPTS

r	reference conditions
t	test conditions
*	nondimensional parameter

References

1. Bergelin, O. P., Colburn, A. P., and Hull, H. L. (1950). Heat transfer and pressure drop during viscous flow across unbaffled tube banks. *University of Delaware Engineering Experiment Station, Bulletin No. 2*, Newark, DE.

2. Bergelin, O. P., Leighton, M. D., Lafferty, W. L. Jr., and Pigford, R. L. (1958). Heat transfer and pressure drop during viscous and turbulent flow across baffled and unbaffled tube banks. *University of Delaware Engineering Experiment Station, Bulletin No. 4*, Newark, DE.

3. Bell, K. J. (1963). Final report of the cooperative research program on shell and tube heat exchangers. *University of Delaware Engineering Experiment Station, Bulletin No. 5*, Newark, DE.

4. Bell, K. J. (1960). Exchanger design, based on the Delaware research program. *Petro./Chem. Engineer* **32**, C26–C40c.

5. Kays, W. M., and London, A. L. (1984). *Compact Heat Exchangers*, 3rd ed. McGraw Hill, New York.

6. NRC Generic Letter 89-13 (1989). Service water system problems affecting safety-related equipment. U. S. Nuclear Regulatory Commission, Rockville, MD.

7. Hannah, B. W., and Scott, B. H. (1994). On-line testing of heat exchangers. In *Proceedings of the 1994 ASME Joint International Power Generation Conference*. American Society of Mechanical Engineers, New York.

8. Bowman, C. F., and Craig, E. F. (1995). Plate heat exchanger performance in a nuclear safety–related service water application. In *Proceedings of the 1995 ASME Joint International Power Generation Conference*. American Society of Mechanical Engineers, New York.

9. Pesce, M. (1994). Applying the temperature effectiveness method to heat exchangers. In *Proceedings of the 1994 ASME Joint International Power Generation Conference*, pp. 41–53. American Society of Mechanical Engineers, New York.

10. Closser, W. H., and Glueck, J. (1998). Evaluating the performance of shutdown cooling heat exchangers at Waterford 3 Steam Electric Station utilizing off design conditions. Presented at the 1998 American Power Conference, Chicago, Illinois, Institute of Technology.

11. Bowman, C. F. (1998). Influence of water-side fouling on air–water heat exchanger performance. In *Proceedings of the American Power Conference*, Vol. 60, Chicago, Illinois Institute of Technology.

12. Missimer, J. R., and Sedlack, T. E. (1995). Methodology for assessment of safety-related heat exchanger performance in response to NRC generic letter 89-13. In *Proceedings of the 1995 American Power Conference*, Chicago, Illinois Institute of Technology, pp. 915–921.

13. Burns, J. M., Almquist, C. W., Bell, R. J., Hernandez, E., Siewert, R. N., and Tsou, J. L. (1991). Improved test methods, modern instrumentation and rational heat transfer analysis proposed in revised ASME Surface Condenser Test Code 12.2. In *Proceedings of the 1991 ASME Joint International Power Generation Conference*. American Society of Mechanical Engineers, New York.

14. Yost, J. G., Burns, J. M., and Roma, F. P. (1986). Condenser tube heat transfer testing—an alternative approach to ASME PTC 12.2. In *Proceedings of the 1986 ASME Joint International Power Generation Conference*. American Society of Mechanical Engineers, New York.

15. Arnold, G. (1983). Changes to ASME PTC 12.2 and TVA condenser test experience. In *Symposium on State-of-the-Art Condenser Technology, 1983*. Electric Power Research Institute, Palo Alto, CA.

16. Milligan, M. W., Wheeler, D. E., and Missimer, J. R. (1983). How to evaluate a condenser's performance while it's on line. *Power* **127**(10), 99–101.

17. Diaz-Tous, I. A., Khan, A. H., Wong, Murphy, S., Bartz, J. A., Pace, S., Clark, J., Hoffman, R., and Schaub, E. (1992). First header-type feedwater heater performance test. In *Proceedings of the 1992 ASME Joint International Power Generation Conference*. American Society of Mechanical Engineers, New York.

18. Stellern, J. L., Hoobler, J. V., Milton, J. W., Welch, T., Kona, C., Thompson, H. H., and Tsou, J. L. (1992). Testing, instrumentation and analysis proposed for revision of ASME PTC 12.1—Closed Feedwater Heaters. In *Proceedings of the 1992 ASME Joint International Power Generation Conference*. American Society of Mechanical Engineers, New York.

19. Thompson, N. (1990). Development and implementation of a feedwater heater testing program. In *Proceedings of the 1990 ASME Joint International Power Generation Conference*. American Society of Mechanical Engineers, New York.

20. Jeronimo, M. A. S., Melo, L. F., Braga, A. S., Ferreira, P. J. B. F., and Martins, C. (1997). Monitoring the thermal efficiency of fouled heat exchangers: A simplified method. *Exp. Therm. Fluid Sci.* **14**(4), 455–463.

21. Madron, F., Horáková, J., and Hoštálek, M. (1986). Measurement of heat transfer coefficient of industrial shell-and-tube exchangers (in Czech). *Chemickŷprûmysi* **36**, 508–511.

22. Guo, P., Ciepliski, D. L., and Besant, R. W. (1998). A testing and HVAC design methodology for air-to-air heat pipe heat exchanger. *Int. J. Heating, Ventilating, Air Conditioning and Refrigerating Res.* **4**(1), 3–26.

23. Knudsen, J. G. (1981). Apparatus and techniques for measuring of fouling of heat transfer surfaces. In *Fouling of Heat Transfer Equipment* (E. F. C. Somerscales and J. G. Knudsen, eds.), pp. 57–81. Hemisphere, Washington D. C.

24. Chenoweth, J. M. (1988). Liquid fouling monitoring equipment. In *Fouling Science and Technology* (L. F. Melo, T. R. Bott, and C. A. Bernardo, eds.), pp. 49–65. Kluwer Academic Publishers, Netherlands.

25. Marner, W. J., and Henslee, S. P. (1985). A survey of gas-side fouling measuring data. In *Industrial Heat Exchangers* (A. J. Hayes *et al.*, eds.). American Society of Metals, Materials Park, Ohio.

26. American Institute of Chemical Engineers (1968). *AIChE Equipment Testing Procedure— Heat Exchangers*. American Institute of Chemical Engineers, New York.

27. Society of Automotive Engineers (1995). *Laboratory Testing of Vehicle and Industrial Heat Exchangers for Heat Transfer Performance*. SAE J1994, Society of Automotive Engineers, Warrendale, PA.

28. Stambaugh, N., Closser, W., and Mollerus, F. J. (1991). *Heat Exchanger Performance Monitoring Guidelines*. EPRI NP-7552, Electric Power Research Institute, Palo Alto, CA.

29. American Society of Mechanical Engineers (1995). *In-Service Performance Testing of Heat Exchangers in LWR Plants*, ANSI/ASME OM Part 21. American Society of Mechanical Engineers, New York.

30. American Society of Mechanical Engineers (2001). *Single Phase Heat Exchangers*, ASME Performance Test Code 12.5. American Society of Mechanical Engineers, New York.

31. Shah, R. K., and Sekulic, D. P. (1998). Heat exchangers. Chapter 17 of *Handbook of Heat Transfer Applications*, 3rd ed. (W. M. Rohsenow, J. P. Hartnett, and Y. I. Cho, eds.). McGraw Hill, New York.

32. Spalding, D. B. (1998). Heat exchanger theory. Part 1 of *Heat Exchanger Design Handbook* (G. F. Hewitt, ed.). Begell House, New York.

33. Bowman, R. A., Mueller, A. C., and Nagle, W. M. (1940). Mean temperature difference in design. *ASME Trans.* **62**(5), 283–294.

34. Shah, R. K. (1993). Nonuniform heat transfer coefficients for heat exchanger thermal design. In *Aerospace Heat Exchanger Technology* (R. K. Shah, and A. Hasemi, eds.), pp. 417–445. Elsevier, New York.

35. Shah, R. K., and Sekulic, D. P. (1998). Nonuniform overall heat transfer coefficients in conventional heat exchanger design theory. *ASME J. Heat Transf.* **120**, 520–525.

36. Instrument Society of America (1988). *ISA Standards and Practices for Instrumentation*, 9th ed. Instrument Society of America, Research Triangle Park, NC.

37. Benedict, R. (1984). *Fundamentals of Temperature, Pressure, and Flow Measurements*, 3rd ed. John Wiley & Sons, New York.

38. Miller, R. W. (1996). *Fluid Measurement Engineering Handbook*, 3rd ed. McGraw Hill, New York.

39. Nicholas, J., and White, D. (1994). *Traceable Temperatures*. John Wiley & Sons, New York.

40. American Society for Testing and Materials (1993). *Manual on the Use of Thermocouples in Temperature Measurement*, ASTM STP 470B, 4th ed. American Society for Testing and Materials, Philadelphia.

41. Hennecke, D. K., and Sparrow, E. M. (1970). Local heat sink on a convectively cooled surface—application to temperature measurement error. *Int. J. Mass Heat Transf.* **13**(2), 287–303.

42. Sparrow, E. M. (1976). Error estimates in temperature measurement. In *Measurements in Heat Transfer*, 2nd ed. (E. R. Eckert and R. J. Goldstein, eds.), pp. 1–22. McGraw Hill, New York.

43. Kerlin, T. W., and Shepard, R. L. (1982). *Industrial Temperature Measurement.* Instrument Society of America, Research Triangle Park, NC.

44. American Society of Mechanical Engineers (1971). *Fluid Meters, 6th ed.* American Society of Mechanical Engineers, New York.

45. American Society of Mechanical Engineers (1989). *Measurement of Fluid Flow in Pipes Using Orifice, Nozzle, and Venturi*, ASME MFC-3M-1989. American Society of Mechanical Engineers, New York.

46. Madron, F. (1992). *Process Plant Performance, Measurement and Data Processing for Optimization and Retrofits.* Ellis Norwood, London.

47. Mah, R. S. H. (1990). *Chemical Process Structures and Information Flows.* Butterworths, Boston.

48. Bard, Y. (1974). *Nonlinear Parameter Estimation.* Academic Press, New York.

49. Colburn, A. P. (1933). A method of correlating forced convection heat transfer data and a comparison with fluid friction. *Trans. AIChE* **29**, 174–210.

50. Shah, R. K., and Zhou, S. Q. (1997). Experimental techniques for obtaining design data of compact heat exchanger surfaces. In *Proceedings of the Conference for Compact Heat Exchangers for the Process Industries*, pp. 365–379. Begell House, New York.

51. Sieder, E. N., and Tate, G. E. (1936). Heat transfer and pressure drop of liquids in tubes. *Industrial Eng. Chem.* **28**(12), 1429–1435.

52. Shah, R. K. (1990). Assessment of modified Wilson plot techniques for obtaining heat exchanger design data. In *Proceedings of the 9th International Heat Transfer Conference*, pp. 51–56. Hemisphere Publishing, New York.

53. Wilson, E. E. (1915). A basis for rational design of heat transfer apparatus. *ASME Trans.* **37**(6), 47–82.

54. Briggs, D. E., and Young, E. H. (1969). Modified Wilson plot techniques for obtaining heat transfer correlations for shell-and-tube heat exchangers. *Chem. Eng. Prog. Symp. Ser.* **65**(92), 35–45.

55. Khartabil, H. F., Christensen, R. N., and Richards, D. E. (1988). A modified Wilson plot technique for determining heat transfer correlations. In *Proceedings of the Second U.K. National Conference on Heat Transfer*, IChE, pp. 1331–1357.

56. Kays, W. M., and London, A. L. (1950). Heat transfer and flow friction characteristics of some compact heat exchanger surfaces, Part 1 — test system and procedure. *ASME Trans.* **72**, 1075–1085.

57. Mochizuki, S., Yagi, Y., and Yang, W. (1989). Advances in single-blow method for performance evaluation of heat transfer surfaces. In *Proceedings of the 2nd International Symposium on Heat Transfer*, pp. 623–630. Hemisphere Publishing, New York.

58. Mochizuki, S., and Yagi, Y. (1990). Performance evaluation of pin-fin heat exchangers by automated transient testing method. In *Proceedings of the 9th International Heat Transfer Conference*, pp. 217–222. Hemisphere Publishing, New York.

59. Heggs, P. J., and Burns, D. (1988). Single-blow experimental prediction of heat transfer coefficients: A comparison of four commonly used techniques. *Exp. Therm. Fluid Sci.* **1**(3), 243–251.

60. Anzelius, A. (1926). Über Erwarmung Vermittels durch stromender Medien. *Z. Angew. Math. Mech.* **6**, 291-294.

61. Schumann, T. E. W. (1929). Heat transfer: A liquid flowing through a porous prism. *J. Franklin Trust Inst.* **208**, 405–416.

62. Locke, G. L. (1950). Heat transfer and flow friction characteristics of Porous Solids. TR No. 10 Department of Mechanical Engineering, Stanford University, Stanford, CA.

63. Darabi, F. (1982). Heat and momentum transfer in packed beds. Ph.D. thesis, University of Leeds.

64. Baclic, B. S., Heggs, P. J., and Ziyan, H. A. (1986). The differential fluid enthalpy method. In *Proceedings of the 8th International Heat Transfer Conference* **5**, 2616–2622.

65. Liang, C. Y., and Yang, W. (1975). Modified single-blow technique for performance evaluation on heat transfer surfaces. *Trans. ASME* **97**(1), 16–21.

66. Loehrke, R. I. (1990). Evaluating the results of the single-blow transient heat exchanger test. *Exp. Therm. Fluid Sci.* **3**(6), 574–580.

67. Pucci, P. F., Howard, C. P., and Piersall, C. H. (1967). The single-blow transient testing technique for compact heat exchanger surfaces. *ASME J. Eng. Power* **89**, 29–40.

68. Mullisen, R. S., and Loehrke, R. I. (1986). A transient heat exchanger evaluation test for arbitrary fluid inlet temperature variation and longitudinal core conduction. *ASME J. Heat Trans.* **108**, 370–376.

69. Hausen, H. (1976). *Wärmeübertragung im Gegenstrom, Gleichstrom und Kreuzstrom*, 2nd ed. Springer-Verlag, Berlin.

70. Glaser, H. (1938). Der Wärmeübertragung in Regeneratoren. *Z. VDI. Beih. Verfahrenstech* **4**, 112–125.

71. Langhans, W. U. (1962). Wärmeübertragung und Druckverlust in Regeneratoren mit rostgitterartiger Speichermasse. *Arch. Eisenhüttenw.* **33**, 347–353, 441–451.

72. Yazicizade, A. Y. (1966). Untersuchung der Wärmeübertragung und des Druckabfalls in Regeneratoren mit körniger oder schachtartig aufgebauter Speichermasse. *Glastech. Ber.* **39**, 201–217.

73. Stang, J. H., and Bush, J. E. (1974). The periodic method for testing compact heat exchanger surfaces. *Trans. ASME* **96**, 87–94.

74. Roetzel, W., Luo, X., and Xuan, Y. (1993). Measurement of heat transfer coefficient and axial dispersion coefficient using temperature oscillations. *Exp. Therm. Fluid Sci.* **7**, 345–353.

75. Roetzel, W., Sarit, K. Das, and Luo, X. (1994). Measurement of heat transfer coefficient in plate heat exchangers using a temperature oscillation technique. *Int. J. Heat Mass Transf.* **37**, 325–331.

76. American Society of Mechanical Engineers (1998). *ASME Steam Tables*, 7th ed. American Society of Mechanical Engineers, New York.

77. American Society of Heating, Refrigerating, and Air Conditioning Engineers (1985). *ASHRAE Handbook of Fundamentals*. American Society of Heating, Refrigerating, and Air Conditioning Engineers, Atlanta.

78. Tubular Exchanger Manufacturer's Association (1998). *Standards of the Tubular Exchanger Manufacturer's Association,* 8th ed. TEMA, Tarrytown, NY.

79. Schunck, M., Maddox, R. N., and Shulman, Z. P. (1998). Physical properties. Part 5 of *Heat Exchanger Design Handbook* (G. F. Hewitt, ed.). Begell House, New York.

80. Reid, R. C., Prausnitz, J. M., and Poling, B. E. (1987). *The Properties of Liquids and Gases*, 4th ed. McGraw Hill Book Company, New York.

81. Colburn, A. (1933). Mean temperature difference and heat transfer coefficient in liquid heat exchangers. *Industrial Eng. Chem.* **25**(8), 873–877.

82. Gardner, K., and Taborek, J. (1977). Mean temperature difference: A reappraisal. *AIChE J.* **23**(6), 777–786.

83. Gardner, K. (1945). Variable heat transfer rate correction in multipass exchangers, shell-side film controlling. *ASME Trans.* **67**, 31–38.

84. Whistler, A. (1947). Effect of leakage around cross-baffles in a heat exchanger. *Petroleum Refiner* **26**(10), 114–118.

85. Fisher, J., and Parker, R. (1969). New ideas on heat exchanger design. *Hydrocarbon Proc.* 147–154.

86. Bell K., and Kegler, W. (1978). Analysis of bypass flow effects in tube banks and heat exchangers. *AIChE Symp. Ser.* **74**(174), 47–52.

87. Mueller, A. C., and Chiou, J. P. (1988). Review of various types of flow maldistribution in heat exchangers. *Heat Transf. Eng.* **9**(2), 36–50.

88. Mondt, J. R. (1977). Effects of nonuniform passages on deepfold heat exchanger performance. *ASME J. Eng. Power* **99**(4), 657–663.

89. Shah, R. K., and London, A. L. (1980). Effects of nonuniform passages on compact heat exchanger performance. *ASME J. Eng. Power* **102**, 653–659.

90. Weimer, R. F., and Hartzog, D. G. (1973). Effects of maldistribution on the performance of multistream, multipassage heat exchangers. *Adv. Cryogenic Eng.* **18**, 52–64.

91. Sparrow, E. M., and Ruiz, R. (1982). Effect of blockage-induced flow maldistribution on the heat transfer and pressure drop in a tube bank. *ASME J. Heat Transf.* **104**, 691–699.

92. Chowdhury, K., and Sarangi, S. (1985). Effect of flow maldistribution on multipassage heat exchanger performance. *Heat Transf. Eng.* **6**(4), 45–54.

93. Thonon, B., Mercier, P., and Feidt, M. (1991). Flow distribution in plate heat exchangers and consequences on thermal and hydraulic performances. In *Proceedings of the Eurotherm Seminar No. 18*, pp. 245–254. Springer-Verlag, New York.

94. Shah, R. K., and Pignotti, A. (1997). The influence of a finite number of baffles on the shell-and-tube heat exchanger performance. *Heat Transf. Eng.* **18**(1), 82–94.

95. Gnielinski, V. (1976). New equations for heat and mass transfer in turbulent pipe and channel flow. *Int. Chem. Eng.* **16**(2), 359–368.

96. Petukhov, B. (1970). Heat transfer and friction in turbulent pipe flow with variable physical properties. *Adv. Heat Transf.* **6**, 503–564.

97. Bhatti, M. S., and Shah, R. K. (1987). Turbulent and transition flow convective heat transfer in ducts. Chapter 4 of *Handbook of Single Phase Convective Heat Transfer* (Kakac, S., Shah, R. K., and Aung, W., eds.). John Wiley & Sons, New York.

98. Dittus, F. W., and Boelter, L. M. K. (1930). Heat transfer in automobile radiators of the tubular type. *Univ. Calif. Publ. Eng.* **2**(13), 443–461.

99. Palen, J., and Taborek, J. (1969). Solution of shell side flow, pressure drop and heat transfer by stream analysis method. *Chem. Eng. Prog. — Symp. Ser.* **65**(92), 53–63.

100. Tinker, T. (1958). Shell-side characteristics of shell-and-tube heat exchangers, a simplified rating system for commercial heat exchangers. *ASME Trans.* **80**, 36–52.

101. Kim, N. H., Youn, B., and Webb, R. L. (1999). Air-side heat transfer and friction correlations for plain fin-and-tube heat exchangers with staggered tube arrangements. *ASME J. Heat Transf.* **121**, 662–667.

102. Manglik, R. M., and Bergles, A. E. (1995). Heat transfer and pressure drop correlations for rectangular offset strip fin compact heat exchanger. *Exp. Therm. Fluid Sci.* **10**, 171–180.

103. Shah, R. K. (1994). A review of longitudinal wall heat conduction in recuperators. *J. Energy Heat Mass Transf.* **16**, 15–25.

104. Kline, S. J., and McClintock, F. A. (1953). Describing uncertainties in single-sample experiments. *Mech. Eng.* **75**(1), 3–7.

105. Dietrich, C. F. (1991). *Uncertainty, Calibration, and Probability: The Statistics of Scientific and Industrial Measurement*, 2nd ed. Adam Hilger, Ltd., Philadelphia.

106. Coleman, H. W., and Steele, W. G. Jr. (1989). *Experimentation and Uncertainty Analysis for Engineers*. John Wiley & Sons, New York.

107. American Society of Mechanical Engineers (1998). *Test Uncertainty*, ASME PTC 19. 1-1998. American Society of Mechanical Engineers, New York.

108. International Organization for Standardization (1993). *Guide to the Expression of Uncertainty in Measurement*. International Organization for Standardization, Geneva.

109. Moffat, R. J. (1982). Contributions to the theory of single sample uncertainty analysis. *Trans. ASME* **104**, 250–260.

110. Moffat, R. J. (1985). Using uncertainty analysis in the planning of an experiment. *Trans. ASME* **107**, 173–182.

111. Moffat, R. J. (1988). Describing the uncertainties in experimental results. *Exp. Therm. Fluid Sci.* **1**, 3–17.

112. Abernathy, R. B., Benedict, R. P., and Dowdell, R. B. (1985). ASME measurement uncertainty. *Trans. ASME* **107**, 161–164.

113. Lestina, T., and Scott, B. (1997). Assessing uncertainty of thermal performance measurements of industrial heat exchangers. In *Compact Heat Exchangers for the Process Industries* (R. K. Shah *et al.*, eds.), pp. 401–416. Begell House, New York.

114. Evans, D. M. (1980). The role of probable uncertainty in the design and testing of compact heat exchangers. *ASME Heat Transf. Div.* **10**, 135–143.

115. James, C. A., Taylor, R. P., and Hodge, B. K. (1995). The application of uncertainty to cross-flow heat exchanger performance predictions. *Heat Transf. Eng.* **16**(4), 50–62.

116. Fryer, P. J., and Slater, N. K. H. (1985). A direct simulation procedure for chemical reaction fouling in heat exchangers. *Chem. Eng. J.* **31**, 97–107.

117. Somerscales, E. C., Sanatagar, H., and Khartabil, H. F. (1993). The uncertainty of fouling thermal resistance measurements. *AIChE Symp. Ser.* **89**, 341–346.

118. Chenoweth, J. M. (1988). General design of heat exchangers for fouling conditions. In *Fouling Science and Technology* (L. F. Melo, T. R. Bott, and C. A. Bernardo, eds.), pp. 477–494. Kluwer Academic Publishers, Netherlands.

This Page Intentionally Left Blank

Boiling Heat Transfer and Bubble Dynamics in Microgravity

JOHANNES STRAUB

Technische Universität München,
Institute für Thermodynamiks, D-85748 Garching, Germany

Abstract

This article presents results for pool boiling heat transfer under microgravity conditions that the author and his team have gained in a succession of experiments during the past two decades. The objective of the research work was to provide answers to the following questions: Is boiling an appropriate mechanism of heat transfer for space application? How do heat transfer and bubble dynamics behave without the influence of buoyancy, or more general, without the influence of external forces? Is microgravity a useful environment for investigating the complex mechanisms of boiling with the aim of gaining a better physical understanding? Various carrier systems that allow simulation of a microgravity environment could be used, such as drop towers, parabolic trajectories with NASA's aircraft KC-135, ballistic rockets such as TEXUS, and, more recently, three Space Shuttle missions. As far as the possibilities of the respective missions allowed, a systematic research program was followed that was continuously adjusted to actual new parameters. After a general survey concerning the importance of boiling for technical applications, an introduction is given especially for those individuals not closely familiar with the fields of microgravity and boiling. Surprising results have been obtained: not only that saturated pool boiling can be maintained in a microgravity environment, but also that at small heater surfaces and lower values of heat fluxes, even higher heat transfer coefficients have been attained than under terrestrial conditions. The bubble departure can be attributed to surface tension effects, to "bubble ripening" and coalescence processes. Under subcooled conditions only,

thermocapillary flow was observed that transports the heat from the bubble interface into the bulk liquid, but does not enhance the heat transfer compared with boiling at saturated conditions. Direct electrical heated plane surfaces lead to a slow extension of dry spots to dry areas below bubbles, the increasing surface temperature suggesting transition to film boiling. The critical heat flux in microgravity is lower than under earth conditions, but considerably higher than the hitherto accepted correlations predict when extrapolated to microgravity. The nearly identical heat transfer coefficients received for nucleate boiling under microgravity as well as terrestrial conditions, and for both saturated and subcooled fluid states, also suggest identical heat transfer mechanisms. These results lead to the conclusion that the primary heat transfer mechanism must be strongly related to the development of the microlayer during bubble growth. Secondary mechanisms are responsible for the transport of enthalpy in form of latent energy of the bubbles and hot liquid carried with them. Under terrestrial conditions, that mechanism is caused by external forces such as buoyancy; under microgravity conditions, the self dynamics of the bubbles and/or thermocapillary flow under subcooled conditions are responsible. The results demonstrate clearly that boiling can be applied as a heat transfer mechanism in a microgravity environment and that microgravity is a useful means to study the physics of boiling.

I. Introduction

A. Importance of Fluid Studies under Microgravity

The elimination of gravity-driven flow and its utilization in fluid science is one of the major attractions of microgravity (see, for instance, [80]). Under terrestrial conditions, buoyancy-driven flow is induced by density differences caused mainly by temperature and/or concentration gradients. Therefore, heat and mass transfer under microgravity conditions is a major subject of consideration and plays an important role with respect to industrial application. As an example, material processing with melting and solidification has been of major interest in the past, but it is still an important matter with respect to present technological developments. During material processing, heat and mass transfer, and the flow induced by these, determine the crystallization and solidification dynamics, the growth rate of the solidification front, and the quality of the product. Flow instabilities may lead to unwanted, and with respect to their origin, unknown secondary effects, resulting in structural imperfections in crystals, metals, and alloys. These negative effects could be avoided with the

elimination of gravity-induced flow as long as the material is in the liquid state, thus preventing flow structures from being frozen within the solid. If thermocapillary flow can be excluded under microgravity conditions, one expects an ideal, quiescent growth regime in which heat and mass transport is decoupled from convection and becomes diffusion-controlled. Such situations are ideally suited for studying the fundamentals of growth front development, of crystallization and solidification dynamics, or of segregation phenomena under controlled conditions.

A more complex problem in the field of heat and mass transfer is boiling and two-phase flow. Both phases are in a fluid state, having no fixed structure, are therefore three-dimensional, and influence each other directly. In two-phase systems with heat transfer, the interaction and interrelation of the various involved parameters is so complex that the real physics of the process is to a great extent not well understood as yet. Under terrestrial conditions, the buoyancy effects caused by the large density differences of the phases are so dominant that weaker forces also contributing to heat transfer are masked and cannot be studied separately. Often this leads to an incorrect physical view of the process itself, and to an inadequate mathematical description, as well. Experiments in microgravity offer the unique chance to exclude, or at least to minimize, the buoyancy effect and with it convection, and to study boiling phenomena and their self-induced dynamics without the influence of external forces. Furthermore, it reinforces our physical knowledge, and thus the results may be used to improve correlations used hitherto.

This article presents the experience and results of more than two decades of research in microgravity, especially in boiling phenomena, and the attempt is made to interpret the sometimes strange and unexpected results. Most of them have been published only in excerpt, aside from their documentation in the doctoral theses of the author's co-workers. For readers not so familiar with microgravity and boiling, a short introduction is given to both. In spite of the long period in which the author and his team had the chance to conduct experiments in a microgravity environment, many open questions are still to be answered. Considering the seven decades of boiling research, and the great number of researchers who have been and still are involved, it is hoped that the results will bring us a step forward, and that they will encourage researchers to use microgravity as a valuable experimental platform. As far as the limited opportunities to perform microgravity experiments allowed, we tried to conduct a systematic research program. Recently some singular results on microgravity boiling have been published that could not easily be included under this common view. Their authors will pardon their not being cited here, but some of their research is recognized in a recent review article of Di Marco and Grassi [37].

B. Short Historical Review

Nearly all experiments on boiling heat transfer in the past have been conducted under earth gravity conditions. Despite the fact that the gravity term exists in most theoretical analyses and empirical correlation as a parameter, for a long time no attempts had been made to verify experimentally whether the influence of gravity is modeled correctly. During the 1950s and 1960s an interest in boiling performance in gravity fields, different from those on earth, arose in the United States with regard to the design of heat transfer devices for space vehicle applications. As a result NASA initiated various studies to examine both reduced and enhanced gravity effects on fluid dynamics, including boiling. One of the main goals of this research was to study heat transfer and two-phase behavior of fluids with concern for the proper design of fuel tanks and other liquid vessels for space vehicles. Most of the experiments have been carried out in small drop-tower facilities with a short period of 0.3 to 1.4 sec of reduced gravity. A review of approximately 25 NASA reports and papers was presented by Siegel [59], covering experiments performed with various liquids by himself and his co-workers. Another summary concerning experiments with cryogenic liquids was presented by Merte and Clark [40] and Clark [9]. Often the results were contradictory, so that no clear conclusion could be drawn. These experiments suffered mainly from the short period of reduced gravity during which the convection flow induced by gravity before the drop had not come to rest. For this reason the really interesting results did not receive full recognition in the heat transfer society. With the change of NASA's space program at the beginning of the 1970s, the interest in basic research of boiling and other fluid science fields came to an end, but was reinitiated at the end of the 1980s.

In the course of American–German cooperation concerning the development of the Spacelab, a scientific program for microgravity studies was initiated by the German government in the mid-1970s as a precursor program. Among others, experiments were selected to study boiling behavior under microgravity conditions over a longer period than had previously been possible. The first experiments could be performed within the German TEXUS (Technologische Experimente unter Schwerelosigkeit) program, which consisted of ballistic rocket flights providing a period of 6 min microgravity of high quality, and within the parabolic trajectory flights of NASA's aircraft KC-135. The results of this precursor program could be supported in the 1990s with those of three Space Shuttle missions, during which a very good quality of microgravity was sustainable over a long period. These missions were provided in co-operation with NASA by ESA and DLR. The various carriers offered the possibility to investigate the influence of gravity on many important parameters systematically.

C. APPLICATION

Liquid–vapor phase-change processes play a vital role in the cyclic processes of our environment, in evaporation, condensation, and precipitation. They are essential for the existence of life on earth. Phase-change processes associated with boiling and condensation play also a vital and very dominant role in many technical processes and their applications. The almost isothermal processes of boiling and condensation associated with high heat transfer coefficients make their application in power and refrigeration cycles indispensable if an economically acceptable efficiency is the goal. These phase-change processes are also applied in chemical and petroleum processing, in liquefaction and separation of gases at normal and cryogenic temperatures. In the past decades very intensive studies of boiling processes have been performed to aid the design of nuclear power plants, both for normal operating conditions and for the control of critical accident scenarios. In addition, because of the high heat transfer coefficients associated with boiling and condensation, these processes are employed in heat exchangers of high loads, and for thermal control of devices with high heat dissipation rates, such as the cooling of electronic components in computers and of aircraft and spacecraft equipment.

Heat transfer processes associated with boiling belong to the most complex transport phenomena encountered in engineering applications [8]. These processes may show all the complexities of single-phase convective transport, such as nonlinearity, instabilities, transition to turbulence, three-dimensionality, and time-varying behavior; additionally, the processes exhibit all two-phase phenomena resulting from nucleation, such as growth and motion of the bubble interface along the surface of the heater, non-equilibrium effects, and complex dynamic and kinetic interactions between the two fluid phases and between the fluid phases and the solid wall of the heater surface. The highly complex nature of boiling on one hand and the demand for heat transfer correlations on the other hand often proved to be a formidable challenge. Nevertheless, research efforts during the past several decades have provided fairly well-founded empirical or semiempirical correlations for the proper technical design of constructions on earth. However, these equations based on terrestrial experiments and optical observations are mostly confined to the specific fluid, the liquid state, the heater configuration, and the heat flux range for which they were developed. This becomes even more evident from the fact that the usefulness of most correlations diminishes very rapidly when they are used outside the physical range for which they were developed [14]. These facts call into question our basic physical understanding of the boiling phenomena.

Up to now, it has been more or less generally assumed that heat transfer in boiling is strongly related to the vapor transport, and is therefore

influenced by external forces. In pool boiling, or free convection boiling, it is the impact of buoyancy, caused by the gravitational field and the great difference between vapor and liquid density, mostly expressed by the Laplace or Bond number. In flow boiling, it is the shear forces acting on the bubbles, which are considered by the Reynolds number. Thus, in pool boiling gravity is considered as an important parameter in most physically or empirically based correlations describing heat transfer. Experiments performed under microgravity provide a means to study the actual influence of gravity and to separate gravity-related from gravity-independent mechanisms. In the case of pool boiling no external forces are acting on the bubbles; thus, exclusively the bubble dynamics itself, its interaction with the surrounding liquid, and the heater surface are of influence and determine the transport process. Under terrestrial conditions these effects are masked by strong buoyancy-induced convection. Therefore, in this article our consideration is focused on and confined to microgravity pool boiling.

At the beginning of boiling studies under a microgravity environment, the most important question was, whether nucleate pool boiling can be maintained at all without buoyancy, and therefore whether boiling could be used as a heat transfer process for space application [59]. After the first positive results, attention focused on the mechanisms of boiling, which are able to provide the observed high heat flux rates comparable to those under terrestrial conditions with buoyancy, with shear force, or other external forces. Where is the limit of nucleate boiling and its application? The answer to these questions is not restricted only to space application; rather it is important for future development of terrestrial technologies as the optimization of energy conversion, the transportation and exchange of thermal energy, and for cooling processes. Additionally, it may be emphasized that with better fundamental knowledge, better physically based mathematical correlations may be developed, for the benefit of both terrestrial and space applications.

II. Compensation of Earth Gravity

A. Principle of Compensation

The principle of free fall is the only possibility to compensate earth gravity and simulate "weightlessness"; it is used in all facilities that provide a microgravity environment for experiments. The vertically falling box method is realized, for example, in drop tubes, drop towers or drop shafts, with a duration of the microgravity period from less than 1 sec to up to 10 sec. However, this principle for compensating the earth gravity is not

restricted to vertical free fall. Low gravity can be achieved in any freefall trajectories with an approximately parabolic shape, such as in aircraft or sounding rocket, with a typical duration from 25 sec to 6 min, respectively. A freely drifting spacecraft, satellite, or space station offers the unique opportunity of an unlimited trajectory, with gravity is continuously compensated by centrifugal force.

All those facilities cannot provide perfectly weightless conditions. Therefore, the term microgravity or reduced gravity is commonly used; in this article the abbreviations μg for microgravity, and 1g for earth gravity are applied. Nearly all facilities are affected by air drag in low earth orbits, providing the most of the residual acceleration in all systems. In the following, the various facilities are discussed concisely.

B. Drop Towers and Drop Shafts

Drop towers and drop shafts use the principle of vertical free fall, where all gravity-induced effects disappear because of the absence of a reaction force to the earth's gravitational force. The acceleration is the second derivative of the free falling height s versus time, and after integration the velocity w and the time t for free fall of height H in vacuum is achieved as

$$\frac{d^2 s}{dt^2} = g$$

$$w = g \cdot t \tag{1}$$

$$t = \sqrt{\frac{2H}{g}}.$$

However, even if the drop takes place in an evacuated tube at the tower, the remaining gas molecules produce a drag force, which can be calculated as

$$F_d = \tfrac{1}{2} c_w \cdot \rho_g A \cdot w^2 \tag{2}$$

where c_w is the aerodynamic drag coefficient of the falling object depending on its shape, ρ the density of the gas in the tube, A the cross-section, and w the velocity of the falling object. With Eq. (2) the residual acceleration ratio can be calculated via a force balance as

$$\frac{a}{g} = \frac{F_d}{mg}. \tag{3}$$

Under normal atmospheric pressure the residual acceleration on an experimental capsule 0.8 m in diameter, as used in the Bremen drop tower,

will be less than 10^{-3} g for only 1.5 sec and will reach 10^{-2} g within 5 sec. From Eq. (3) it is obvious that only at the beginning of a drop at small velocities can a low level of residual gravity be achieved, which can be improved with reduction of the gas density ρ_g to vacuum conditions.

The simple concept of performing drop experiments in open air provides an acceptable quality of microgravity only for a short period of time. To minimize the influence generated by the aerodynamic drag, the experimental package is often dropped floating freely in a large falling capsule acting as a drag shield. For larger fall heights with longer duration of the microgravity period, the capsule is equipped with auxiliary gas thrusters to compensate for the increasing air friction during the fall. In this way various research laboratories operate their own small facilities using drag shields or small vacuum tubes.

Some of the larger facilities existing in Japan, the United States, and Germany are briefly described in the following.

The largest drop facility with a duration of 10 sec at a gravity level of $10^{-4}g$ is JAMIC, located on Hokkaido Island in Japan. The drop shaft is installed in a 710 m deep coal mine that is no longer used. An evacuated capsule 7.85 m in length and 1.8 m in diameter includes a 3.2 m long experimental module on which the experiments are mounted. This module is released independently and is free falling within the outer capsule, which is rail guided, propelled and controlled by 50 air nozzles to compensate the air friction over the free-fall height of 490 m. To stop the capsule it plunges into a braking tank 200 m in height, which decelerates the capsule smoothly at $8g$ by means of an air-damping mechanism, utilizing the compressibility of air. Once the capsule is significantly slowed down, mechanical brakes are used to stop it completely. The maximum experimental payload is 500 kg and the size in volume is $0.87 \times 0.87 \times 0.92$ m^3, which provides space for several experiments to be dropped simultaneously. Two to three drop experiments can be performed per day.

Another drop shaft in Japan is a reused mine located in Gifu prefecture that is operated by MGLAB. The drop shaft of 6 m diameter and 150 m length is equipped with a 1.5 m diameter steel tube, which can be evacuated. It consists of a 100 m free drop zone and a 50 m braking zone. The duration of microgravity of $10^{-5}g$ quality is 4.5 sec, and the payload mass is 400 kg. Friction dampers and bellows are used for a smooth deceleration of about $10g$.

In the United States NASA operates a 100 m drop tower at Marshall Space Flight Center, Huntsville, AL. Experimental packages of up to 180 kg are accommodated in a drag shield riding on two guide rails. Gas thrusters are used to overcome the friction of both the air and the rails, so that the residual acceleration can range between $10^{-2}g$ and $10^{-5}g$ during the 4.3 sec of free fall.

Another facility is located at NASA Glenn Research Center, the former Lewis Research Center, Cleveland, OH. A 145 m height shaft with a 6.1 m diameter vacuum tube enables tests with an autonomous experiment package weighing up to 450 kg for 5 sec at $10^{-5}g$. The deceleration occurs in a tank filled with polystyrene pellets.

The drop tower "Bremen" is installed at the Center for Applied Space Technology and Microgravity, ZARM, at Bremen, Germany. The experiments are accommodated in a pressurized capsule, which is dropped in an evacuated tube of 110 m height and 3.5 m diameter. The steel tube is free standing inside a concrete tower of 145 m height. A free fall duration of 4.7 sec with a residual acceleration lower than $10^{-5}g$ is achieved. In the drop capsule of 0.81 m diameter, the experimental setup is mounted on a standard platform specially designed for a quick damping of the vibrations originating from the release. The deceleration occurs with polystyrene pellets and reaches peak values up to $30-50g$. The maximum payload mass is 170 kg.

The microgravity centers operating larger drop facilities offer special support services to users. The experimentalists can choose their own experiment control system or use the on-board computer. It can be programmed to run the experimental sequence during the free fall and to store experiment specific and housekeeping data. Experiment data and video images are transmitted to a control room and tele-commands can be sent to the capsule. For short-term experiments the drop facilities offer great advantages: laboratory hardware can be used, experiments can be repeated, a high quality of microgravity is achieved without g-jitter effects, experimental parameters can be easily changed, and the experimental setup can be improved between drops.

C. Parabolic Trajectories

1. Aircraft KC-135

For a number of years at the Johnson Space Center in Houston, Texas, NASA has used parabolic trajectories flown by the famous KC-135 aircraft for training astronauts. NASA has also provided the opportunity for microgravity research, and since 1985 in cooperation with ESA and DLR has done so for European researchers as well. A typical parabolic trajectory is seen in Fig. 1. The low gravity period lasts about 20–25 sec, with a period of high gravity level of $1.8g$ before and after each parabola. Within a 3-hour flight about 30–40 parabolas can be flown; thus, a sequence of experiments can be performed. A great advantage of this facility is that even voluminous and heavy laboratory equipment can be flown directly. The researcher can operate his experiment by himself and gain experience with microgravity

JOHANNES STRAUB
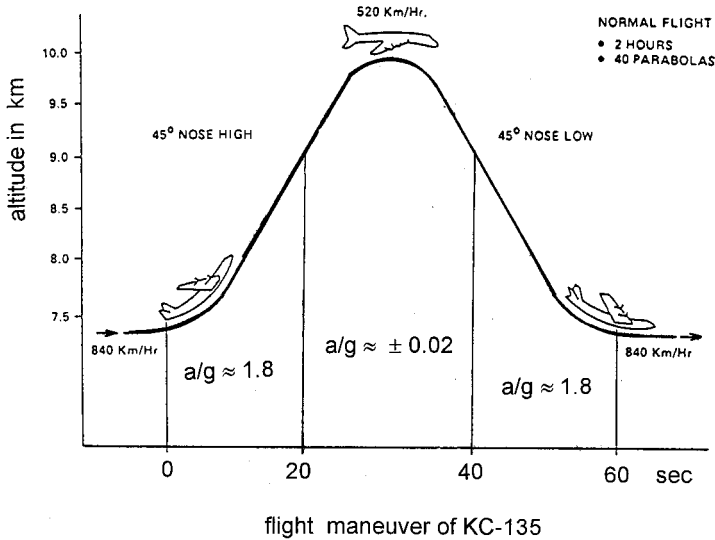
FIG. 1. Parabolic trajectory maneuver of the KC-135 aircraft.

environment. The safety restrictions are much less than in manned, orbital flights, and for some types of experiments sequences from high to low gravity can be of additional benefit. A disadvantage is that the gravity level is fluctuating around $\pm 2 \times 10^{-2}g$, caused by air turbulence and maneuvers of the pilot, which is why very g-sensitive experiments in fluid science can hardly be performed (see also Fig. 16).

Small and relatively light experimental setups can be left free floating in the aircraft cabin for about 5 sec. Large and massive structures with power supply, measuring devices and optical systems are usually fixed to the floor structure of the aircraft, and therefore all disturbances are directly transmitted to the experiment. As the main gravity perturbations are in the z-axis of the airplane, Zell [87] designed a vertically free floating experimental platform moving along a guide rail. Peak disturbances can be damped, as seen in Fig. 2, as long as the provided height in the airplane of about 1.8 m is sufficient for compensation. On that platform even larger and more sensitive experimental setups can be mounted, for instance, interferometers to perform measurements on the growth of single bubbles [79]. However, the friction of the rail and the wire connections to the power supply and to the data acquisition system are in any case responsible for an alternating residual gravity.
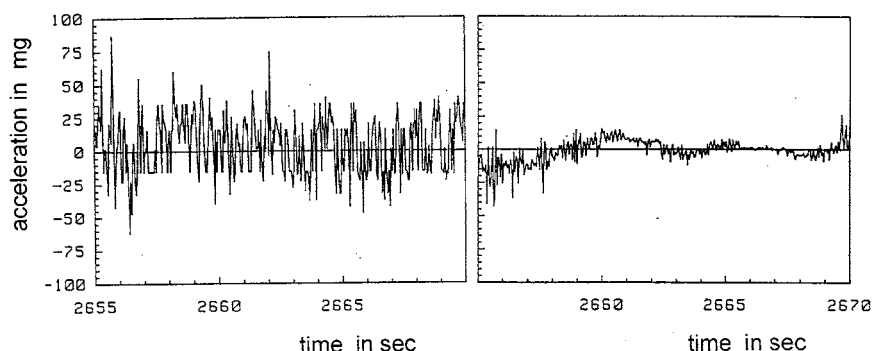
FIG. 2 *g*-jitter disturbances in the aircraft KC-135. *Left side*: experiment fixed mount; *right side*: damped by the free-floating platform [87].

At NASA Glenn Research Center, a DC-9 and a Lear Jet are used for parabolic flights. The French Space Agency CNES operates an Airbus for parabolic flights, which replaced a Caravelle used some years before. The Airbus is offered to all European researchers by the European Space Agency, ESA. Japanese researchers may use a Mitsubishi MU-300, operated by Diamond Air Service, which provides space for one experiment and one researcher.

2. Ballistic Rockets

In preparation for microgravity experiments to be performed in the Spacelab, carried in the cargo bay of the Space Shuttle, the German Ministry for Research and Development in 1976 initiated the TEXUS sounding rocket program (Technologische Experimente unter Schwerelosigkeit). It was managed first by DLR, and later by ESA and by the space company ERNO, Bremen. Every year one or two campaigns are scheduled with about 6 to 7 autonomous experiments. With a gross payload mass of typically 360 kg an apogee of 260 km is reached, and a microgravity condition of $a/g \leqslant 10^{-4}$ is achieved over 370 sec. The payload is recovered by parachute. A similar program managed by the Swedish Space Corporation, SSC, is called "MASER" (Material Science Experiment Rocket) and is comparable to the TEXUS rocket. The launch place for these European programs is near Kiruna in the northern part of Sweden.

The Japanese Space Agency NASDA offers the TR-1A rocket program with a launch site at the island of Tanegashima and recovery of the payload by parachute in the Pacific.

3. Orbital Flights

These days the best-known facility employed for experimental microgravity research is the Space Shuttle with the Spacelab in its cargo bay. In case of an orbital trajectory the gravity is compensated by centrifugal force in which g_H is the actual gravity in the orbital radius R:

$$F_c = \frac{m \cdot w^2}{R} = m \cdot g_H. \tag{4}$$

From this follows the velocity necessary to keep the shuttle in a circular orbit:

$$w = \sqrt{g_H \cdot R}. \tag{5}$$

For the altitude of 300 km the velocity of the orbiter results in 27,626 km/h. The relative residual acceleration caused by atmospheric drag at the altitude of 300 km is about 10^{-6} and can be reduced by one order of magnitude at 400 km height, which is the orbit of the Russian MIR station and the International Space Station (ISS).

Another residual effect is the gravity gradient effect, the magnitude of which is proportional to the distance from the center of mass and equals $0.3\,\mu g$ per meter. All experimental facilities of Spacelab are contained within a 3.5-m radius from the center of mass. Thus, the upper limit that influences the experiments by the gradient effect is close to 1 μ-g and hence of the same order of magnitude as the atmospheric drag acceleration. Sometimes rotation of the spacecraft is required for altitude changes. Rotation rates of the space shuttle are usually low, i.e., two revolutions per hour. The related centrifugal acceleration at a distance of 3.5 m from the center of mass is less than 5 μ-g. Thus, the average residual acceleration will be below $10^{-5}g$ and in the low-frequency range. Further disturbances on fluid science experiments can be caused by internal activities needed to operate the spacecraft and its payload. They are completely different and depend strongly on the structural parameters such as natural frequencies and the structural damping and contribute to the high frequency acceleration. Such disturbances may include the following:

- Thruster firing by the orbiter for maneuvers and altitude maintenance
- Running machines and operating experiments
- Crew exercise and push-off by crew members

To diminish the impact of such disturbances on sensitive experiments and to optimize the scientific results of the experiments, NASA offers many possibilities in a very cooperative way, such as mission profile optimization,

payload location, mission timeline, facility design, and crew behavior. An example of the last is that very sensitive experiments are performed during the rest period of the crew members.

Very important for the performance and success of fluid experiments is that the experimentalist — the principal investigator and his crew — are in nearly permanent telecommunication contact with the experiment. The investigators can observe the reaction of fluid behavior due to changes of parameters and receive the electronic data nearly online down on earth. Thus, an immediate first evaluation can be made and adjustments concerning further parameters are possible. In other words, the experiment is to a large extent controlled by the scientists. A similarly comfortable system will be provided at the International Space Station when it is ready for operation in the near future.

III. Boiling Curve at 1-g and μ-g

A. NEWTON'S LAW OF HEAT TRANSFER

As already mentioned, boiling is a very complex process, because of the interaction and interrelation of numerous mechanisms and effects. It begins with heterogeneous bubble nucleation, and later with consecutive bubble activation in the superheated liquid boundary layer at the heater surface. Bubble growth and motion follow, which induce microconvection, the interaction between the heater surface with liquid and vapor with the development of the three-phase line, the interfacial mass transfer with evaporation at the liquid–vapor interface, and finally, the detachment of the bubble. With that, the transportation process of latent heat by the vapor in the bubbles and by the heated liquid around them is initiated. This complex behavior entails that the physics of the boiling process itself is not properly understood yet, and is poorly represented in most correlations, despite almost seven decades of boiling research. Even if the physics were completely understood and all boundary and coupling conditions were known, it would be impossible at present to solve boiling heat transfer problems for practical application by numerical integration of the conservation laws for mass, momentum, and energy. Therefore, as for almost all practical problems of convective heat transfer, Newton's law will be applied:

$$\dot{Q} = \alpha \cdot A \cdot (T_{\mathrm{w}} - T_{\mathrm{ref}}), \qquad (6)$$

where $\dot{Q}$ is the heat flux. α is the heat transfer coefficient, depending in the case of boiling on the temperature difference itself, and it incorporates all the complex interactions. In the case of nucleate boiling, α is many times

larger than the coefficients in single phase heat transfer under natural convection. A is the heater area. $(T_w - T_{ref})$ is the driving temperature difference, with T_w the heater surface, respectively the wall temperature, and T_{ref} is a convenient reference temperature of the liquid. In the case of boiling this is mostly the saturation temperature T_{sat} of the fluid, which depends on the system pressure. The difference is usually written as ΔT_{sat}. In order to transfer a certain amount of heat for practical application, the area A and the temperature difference should be kept as small as possible, the first to minimize the size and weight of the heat exchangers, and with that investment costs, the second to minimize the entropy production and thus increase the efficiency of the thermal process.

B. BOILING REGIMES

In this section the various boiling regimes are qualitatively described, and the general behavior at 1-g and μ-g is compared. For additional information we recommend textbooks: van Stralen and Cole [69], Carey [8] and others.

1. Nucleate Boiling

Boiling occurs in the supersaturated or superheated boundary layer of a liquid at the surface of a heating element. This boundary layer is in the metastable liquid state either while the bulk liquid still remains at saturation temperature, referred to as saturated boiling, or while the bulk liquid has a temperature lower than the saturation temperature, referred to as sub-cooled boiling. The saturation temperature is related to pressure by the vapor-pressure curve, which is a property of the specific fluid. The various regimes of pool boiling, and the qualitative differences between terrestrial, 1-g, and microgravity, μ-g, can be understood in terms of the so-called boiling or Nukiyama curve, demonstrated in the qualitative sketch of Fig. 3. Nukiyama [47] was one of the first to investigate the boiling regimes of wetting liquids. The heat flux density $\dot{q} = \dot{Q}/A$ is plotted versus the temperature difference ΔT_{sat}, referred to as wall superheat. A quantitative diagram of the boiling curve depends on the thermophysical properties of the fluid itself, on the liquid state, as pressure and temperature, and on the heater configuration.

At low heat flux the wall superheat increases slowly with the heat flux (line A−B$_{1g}$ in Fig. 3). No nucleation site on the heater surface may be active and heat is transferred to the ambient liquid under terrestrial conditions by natural convection, under microgravity conditions by heat conduction (line A−B$_{\mu g}$). The heat transfer coefficient associated with natural convection is relatively low, but it is still higher than in the case of heat conduction at μ-g.
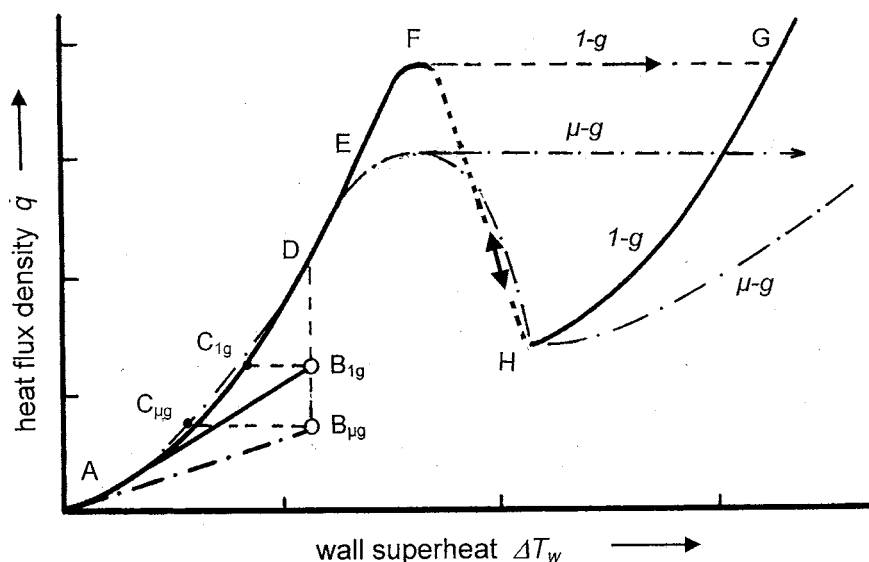
FIG. 3. Qualitative comparison of boiling curve at 1-g and μ-g. The quantitative scale depends on the fluid, liquid state, and heater configuration.

Eventually the superheat becomes large enough to initiate nucleation at some cavity on the surface. According to the nucleation theory the nucleation process or the bubble activation itself should be independent of gravity. However, it depends on the temperature at the heater surface and the temperature distribution in the liquid thermal boundary layer, which is obviously temporarily and locally influenced by convection. If we disregard that, we can assume that the onset of nucleate boiling occurs more or less at the same superheat temperature at 1-g, point B_{1g}, and μ-g, point $B_{\mu g}$, but the latter one at a lower heat flux. In the absence of buoyancy convection, the mean heater temperature is more evenly distributed; therefore, in the μ-g case boiling sets in at a lower heat flux. If the heat flux is controlled, a sudden decrease of the surface temperature occurs to C_{1g}, respectively $C_{\mu g}$, whereby the heat transfer coefficient is larger at μ-g. If the temperature of the surface is precisely controlled, the phase change at nucleation does not change the surface temperature, but rather increases the heat flux suddenly to point D. In both cases the heat transfer intensity is enhanced.

Once nucleate boiling is initiated, any further increase in heat flux or in wall temperature activates more nucleation sites and the operating point of the system moves upward from C or D to E and F. This range is the nucleate boiling regime and is the most important for technical application,

because in this region a small rise of the surface temperature results in a large nonlinear increase of the heat flux as

$$\dot{q} \propto (\Delta T_{sat})^m \qquad \text{with } 3 \leqslant m \leqslant 5 \tag{7}$$

On the line up to E the active sites are few and widely separated; this is is referred to as the isolated bubble regime. With increasing surface superheat, more and more sites become active, and the bubble frequency at each site generally increases. Eventually the active sites are spaced so closely that bubbles from adjacent sites merge together during the stage of growth; at 1-g they are released mainly by buoyancy and at μ-g mainly by coalescence. Vapor is being produced so rapidly that bubbles merge together and form columns of vapor slugs that rise upward in the liquid pool toward its free surface under terrestrial conditions. This segment E–F of the nucleate boiling regime is referred to as the regime of slugs and columns at 1-g. Depending on the heater configuration the vapor volume covers the heater surface in the absence of gravity at lower heat flux and prevents liquid–vapor exchange, with the consequence of increasing mean surface temperatures. The decrease of the slope of the curve indicates that below large bubbles or vapor volumes dry spots are developing.

2. Critical Heat Flux

With increasing heat flux the vapor production becomes so intense that the vapor mass moving away prevents the liquid from moving toward the heater surface, so that liquid is unable to reach the surface and keep it wetted everywhere. Dry spots on the surface either below a single bubble or below an accumulated vapor volume grow, and if the cooling of these spots becomes insufficient and the surface temperature cannot be reduced, the dry spots spread to a dry area very fast. In case of heating with constant heat flux or at direct electrical resistance heating, the local temperature increases very rapidly from F to point G, where the film boiling regime is reached. The temperature at this point may increase to the melting point of the heater material and consequently destroy the heater. Therefore, this peak value of heat flux at F is called the critical heat flux (CHF) or referred to as the burnout point. This event happens at μ-g at a lower heat flux than at 1-g, but at a higher value as the present CHF correlations predict. In μ-g the extension of the dry area is in some cases slower than at 1-g; it is a moderate transition to film boiling.

3. Transition Boiling

If the average heater surface temperature is controlled, the peak heat flux attains a maximum, because with increasing temperature the mean overall

heat flux is decreasing. Now dry portions of the heater are covered with a vapor film and transfer locally lower heat fluxes than wetted portions, where nucleate boiling is still maintained. Thus, the surface temperature will not be uniform, but rather will vary locally and temporarily with alternating wetted and nonwetted surface portions. Further rise of temperature lowers the heat flux; the dry portions increase until the minimum heat flux is reached at point H, often referred to as the Leidenfrost point. The section F–H is referred to as transition boiling regime. This transition boiling is observed in microgravity on wires as well, where the position of wetting and nonwetting fluctuates at the heater.

4. Film Boiling

At point H a stable vapor film on the entire heater surface is formed, thus marking the transition to the film boiling regime. With further increase of the temperature the heat flux monotonically increases with the superheat (section H–G and beyond G). This trend is a consequence of the increasing conduction and radiation transport at μ-g, and of additional convection at 1-g across the vapor film due to the increasing driving temperature difference $T_w - T_{sat}$. At μ-g surface tension forces and in subcooled liquids thermocapillary flow maintain film boiling for a while, especially on wires.

5. Reverse Process

If a surface is heated up to the film boiling regime, and if the surface temperature is slowly diminished, the boiling system will pass through each of the regimes described above in reverse order; the line G–F is excluded. Further differences between the increasing and decreasing superheat curves may arise in the transition regime H–F, due to the change in the wetting and rewetting conditions. At the transition from nucleate boiling to natural convection or conduction, line C–A, differences are caused by different mechanisms in the activation and deactivation of nucleation sites. At 1-g the curves merge together with the line of free convection, whereas at μ-g the curves merge together with the line of conduction close to the saturation temperature, as was observed.

C. Influence of Gravity on Boiling Correlations

To meet the demands of industrial applications, numerous heat transfer correlations for boiling have been developed in the past, being theoretically, semiempirically, or empirically based. They are restricted to special fluids and limited to the range of the liquid state, and they have been proven for the design and development of technical equipment. With the development

of space technology it was, and still remains, important to know which of the existing correlations can also be applied to space applications. But more generally, for the fundamental knowledge of boiling it is important to know which correlation correctly represents gravity as a real parameter, because one may assume that such a correlation is based on a reliable physical concept.

As an example, the well-known and often-used semitheoretical correlation proposed by Rohsenow [56], based on assumptions for forced convection heat transfer, may be considered. Rohsenow regarded the velocity of a vapor bubble at the instant of departure from the surface as being the most meaningful velocity in the heat transfer mechanism. Since this velocity depends on the buoyancy force exerted on the bubble, the heat transfer intensity would be expected to be a function of gravity. The correlation expressed explicitly for the heat flux is written as

$$\dot{q} = \mu_1 \cdot \Delta h \left[\frac{g(\rho_1 - \rho_g)}{\sigma} \right]^{1/2} \cdot \left[\frac{c_{pl} \cdot (T_w - T_{sat})}{C_{sf} \cdot \Delta h} \right]^{3.0} \cdot Pr_1^{-5.15}, \qquad (8)$$

where the heat flux density depends on gravity to the power 1/2. Consequently, at a given temperature difference $T_w - T_{sat}$, the heat flux and heat transfer coefficient would be reduced by a factor of 10^{-2} to 10^{-3} if the gravity were reduced to the level of the Space Shuttle between 10^{-4} to $10^{-6}g$, but this could not be confirmed in microgravity experiments.

From the same initial situation, Forster and Zuber [15] proposed that the radial growth velocity of the bubbles, while still close to the surface, is the significant velocity governing the turbulent motion induced by bubble action. As a result, this heat transfer correlation appears to be independent of the gravity field, but the difficulty remains to determine this velocity. Both correlations are derived by bubble behavior characteristics obtained during boiling observations at earth gravity.

Even if in some correlations gravity is not explicitly expressed, it is often implicitly contained in the dimensionless numbers of heat transfer, as in the Nu, Re, or Ra number. These dimensionless numbers should be independent of the applied scale. Therefore, the departure diameter D_d of the bubbles is used most frequently as a characteristic length scale written in terms of the Laplace coefficient L:

$$D = C \times L = C \times \left(\frac{\sigma}{g(\rho_1 - \rho_g)} \right)^{1/2} \qquad (9)$$

The departure diameter was first introduced by Fritz [17] with $C = 0.0208 \times \beta$, where β is assumed to be a contact angle in degrees. It considers

the static force balance between buoyancy and surface tension force. Based on experimental data a number of investigators have proposed correlations that can be used to predict the departure diameter of bubbles during nucleate boiling (see, for instance, Table 6.1 in Carey [8]). All of them are in inverse proportion to gravity, which means that the departure diameter is increasing with decreasing gravity. In almost all cases the gravity dependence of the departure diameter can be expressed with the ratio of gravity as

$$D_{d,\mu g}/D_{d,1g} = (a/g)^{-m}. \tag{10}$$

In the Fritz relation and most others, m is $1/2$. With the departure diameter the gravity dependency is implicitly included in a number of correlations. An extrapolation of these to lower gravity levels and the comparison with experimental microgravity data will provide an indication whether the significant physical mechanisms were included and the dominating effects considered. The influence of gravity may be expressed by the heat transfer efficiency, represented as the ratio of the heat transfer coefficients or heat fluxes determined under microgravity to those under earth conditions observing identical experimental conditons. The relation between efficiency and the fraction of gravity is then given by a power law:

$$\varepsilon_{\mu g} = \frac{\alpha_{\mu g}}{\alpha_{1g}} = \left(\frac{a}{g}\right)^n \tag{11}$$

for

$$\dot{q} = \text{const} \quad \frac{\alpha_{\mu g}}{\alpha_{1g}} = \frac{\Delta T_{\text{sat},1g}}{\Delta T_{\text{sat},\mu g}}$$

and for

$$\Delta T_{\text{sat}} = \text{const} \quad \frac{\alpha_{\mu g}}{\alpha_{1g}} = \frac{\dot{q}_{\mu g}}{\dot{q}_{1g}}.$$

The analysis of the gravity dependence of various correlations by Straub et al. [75] regarding the same fluid and heating conditions results in values for the exponent n in the range $0.5 > n > -0.35$. Therefore, no common trend concerning the gravity dependence could be deduced from the existing correlations; see Fig. 4.

For this reason until quite recently it was assumed to be questionable if boiling may be used as a heat transfer mechanism for space application at all. Most often it was expected that in absence of the buoyancy force, the bubbles would not depart from the heater surface, and thus would coalesce there and merge to a vapor layer covering the heater surface. That vapor
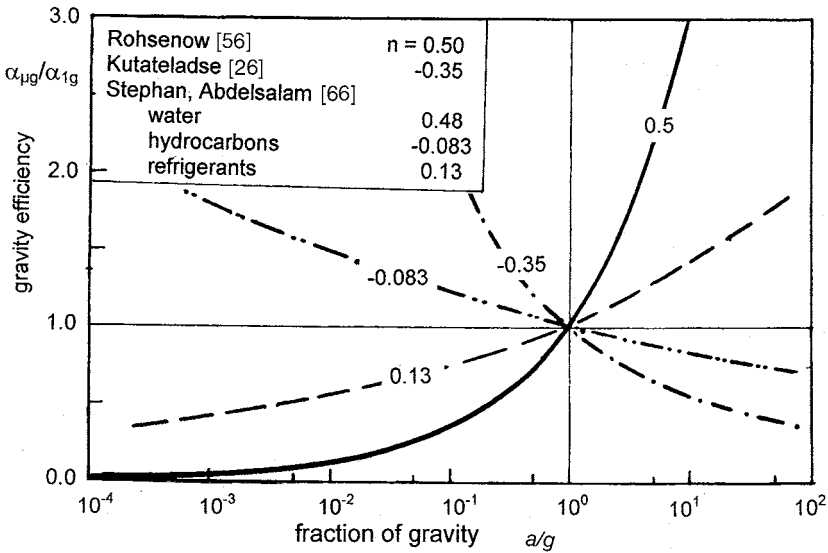
FIG. 4. Gravity dependence of various correlations, expressed by Eq. (11).

IV. Realization of Experiments

A. LIMITATIONS

For the study of boiling phenomena under microgravity, the various carriers able to compensate earth gravity, as described in Section II, can be used. At present, all microgravity experiments are subject to a number of limitations such as size, volume, and mass (weight) of the experimental hardware, as well as limitations for safety reasons concerning the permitted materials, which must be nonflammable and nontoxic. There are limitations with respect to the electrical power supply, both in average and peak values, and to systems for data recording and transmission to ground. The available experimental time is restricted, and limitations of frame rates and length of optical recording must be observed. There may further be restrictions on the supervision and control of the experimental runs, and last but not least on the possibility of repeating experiments after parameter adjustment follow-

layer would isolate the heater from heat and mass exchange with the ambient liquid, resulting in a strong increase of the heater temperature as with film boiling. But fortunately these apprehensions were unrealistic, as experiments performed under microgravity confirmed.

ing the evaluation of previous runs. The design of experimental equipment is, therefore, a compromise between the requirements for achieving the scientific objectives and the possibilities that can be realized with the selected carrier system.

B. Multiuser Facility

Depending on the carrier, the outfit of the experimental equipment is adjusted and the available period in microgravity lasts from seconds in drop-tower experiments to weeks in Space Shuttle missions. In the latter case the experiments are either directly installed inside the Spacelab and partially operated by the astronauts, or mounted in an autonomously operating container in the cargo bay of the Shuttle, called a Get Away Special (GAS). In principle the experimental equipment for boiling experiments has been similar for various missions and has been oriented toward specific tasks. Differences in the structural and design features adjusted the experiment to the potentialities of the carrier.

In contrast to similar setups for terrestrial use, the apparatus had to be scaled down in order to save space, weight, and power, leading to a design of extreme compactness. As an example, the scheme of the experimental arrangement used in two Space Shuttle missions, ILM-2 (1994) and LMS (1996), is shown in Fig. 5, while Fig. 6 provides a photo view into the open
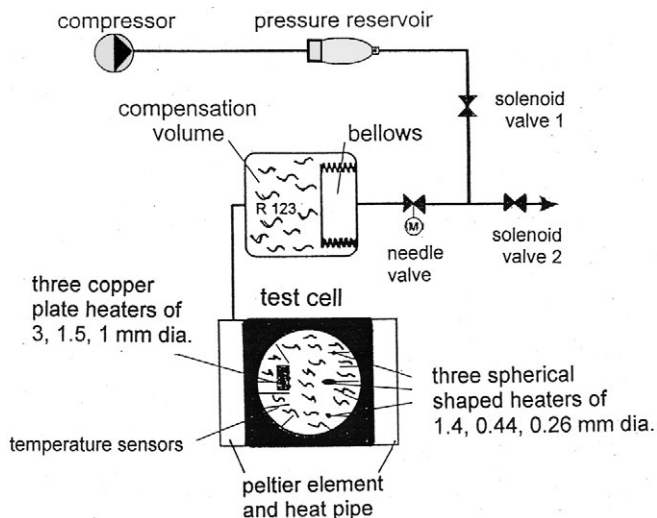
Fig. 5. Experimental arrangement, used in the BDPU multiuser facility ILM-2 (1994) and LMS missions (1996); the principal equipment for other missions was similar.
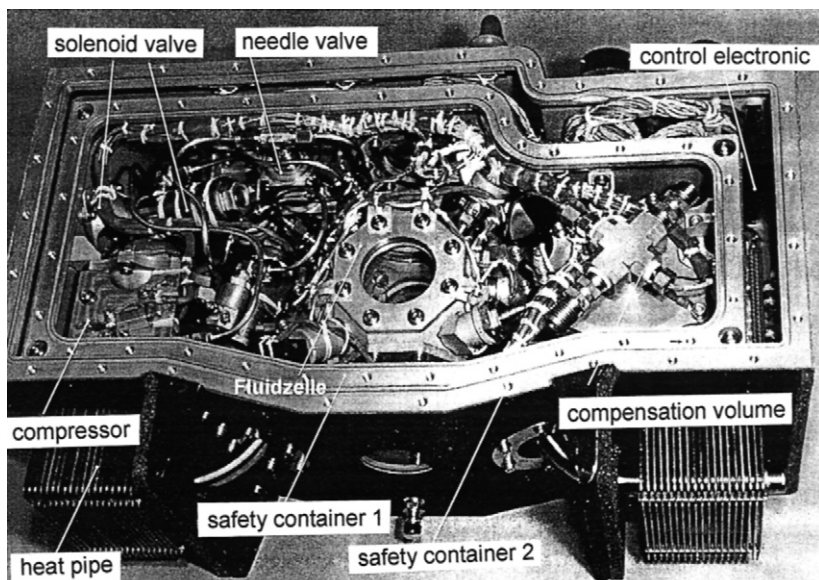
Fig. 6 View into the open experimental container, developed by Astrium-Space, Dornier, Friedrichshafen, Germany, and Ferrary Engineering, Modena, Italy.

experimental container. The latter container, with dimensions $45 \times 15 \times 30$ cm, was exchangeably inserted in the ESA multiuser facility BDPU (Bubble, Drop, Particle Unit; [36]), which was developed and provided by ESA and designed and manufactured by ALENIA, Italy. ESA develops multiuser facilities with the philosophy that during the course of one mission more experiments of different researchers can be performed, and that by the common use of diagnostics and power supplies the costs for any single experiment can be reduced. Thus, the BDPU was equipped with all electronic and optical diagnostics, with the basic power supply, with video recording and electronic data, and with a teleconnection from space to ground. Also, optical observations in two perpendicular directions were made possible. One light path was for direct observation with diffuse background illumination, the other alternatively for a Wollaston differential interferometer, Schlieren optics, or particle image velocimetry (PIV). Therefore, the experimental container, developed by DASA, Dornier, Friedrichshafen (today Astrium-Space GmbH), and Ferrary Engineering, Modena, had four windows of sapphire with 40 mm optical diameter for two axes of observation. During the Space Shuttle missions the investigators could make use of telescience, and could observe the experimental runs in a nearly

real-time video at NASA's Marshall Space Flight Center in Huntsville as long as a space-to-ground connection was available. Simultaneously, they received the most important data of power input, heat flux and temperatures in graphs on computer screens. On the basis of these observations and first evaluations, essential parameters were adjusted and new experimental runs could be begun by telecommanding.

C. Experimental Equipment

The fluid cell is mounted in the center of the experiment container (see Fig. 5). It must be mechanically rigid against high pressures and high accelerations during launch and landing, and chemically resistant. In order to compensate for the expansion of the fluid volume during boiling and to keep the pressure constant at the same time, a pressure control and volume compensation system was developed for the first TEXUS experiments by Weinzierl and Straub [84] and Weinzierl [83] and was improved in the subsequent missions. It consists of bellows and valves controlling the counterpressure of the bellows to provide a constant pressure in the fluid cell. This pressure system is supplied with pressurized nitrogen from a pressure vessel. In the case of BDPU it was filled up during experimental breaks with a small gas compressor installed in the test container. A combined electronic and mechanical system controls the gas pressure and achieves the adjustment of pressure over a wide range of saturated and subcooled liquid states; see Fig. 7. The fluid temperature is controlled by Peltier elements used for heating and cooling in connection with heat pipes. A stirrer installed in the liquid enables fast temperature homogenization during experimental breaks. After the stirrer was switched off, the liquid's motion calmed down completely within 3 minutes.

The mission with a completely autonomous experimental setup in a Get Away Special (GAS) was not as comfortable as the experiments and their control in the Space Shuttle Spacelab missions. The total equipment, including the experimental cell, measurement and optical diagnostics, and the power supply by batteries, had to be accommodated in a container of 50 cm diameter and 71 cm in length, and was further restricted by the total allowable mass of 90 kg. The full course of all the experimental steps had to be programmed in advance, as during flight the experimentalist was not in contact with his experiment. The useable experimental time depended on the power resources, and thus the mass of batteries, and in our case, on the resources of pressurized nitrogen, and thus the volume and weight of the pressure bottle. The experimental facility, designed and manufactured by ERNO, Bremen, was similar to those described before. The experimental cell had two optical windows of sapphire with 62 mm diameter. It was equipped
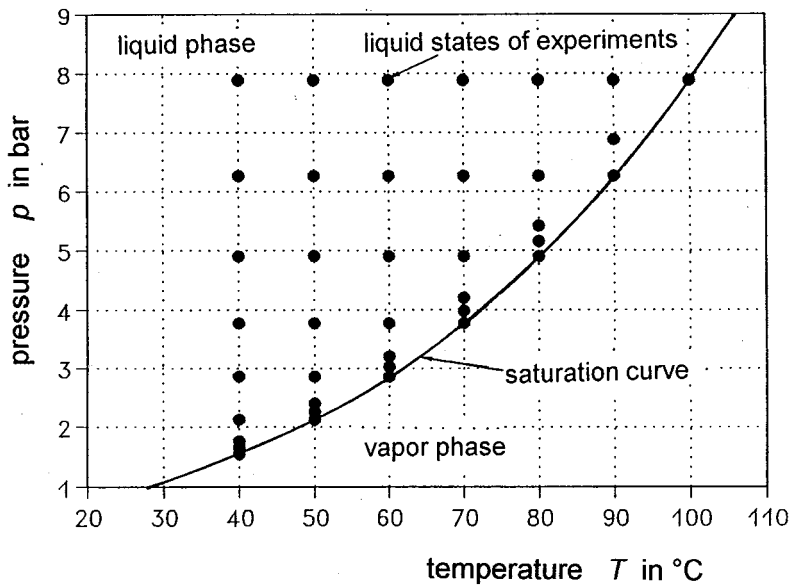
FIG. 7. Investigated saturated and subcooled liquid states in the pressure–temperature phase diagram of R123. With the volume compensation and pressure system, the fluid states could be controlled.

with means for direct observation with diffuse background illumination and a video camera, which allowed a frame resolution of 50 Hz. The optics was further equipped with a zoom focusing, which was activated during each boiling sequence for 6 sec and provided a $10 \times$ enlargement of the boiling process. All experimental runs were controlled by a preprogrammed computer that also received and stored the data. Lee *et al.* [33, 34] could use GAS missions four times to study nucleation, bubble growth, and heat transfer in pool boiling.

An interesting experience for investigators are parabolic trajectory flights with aircraft. The experimenter can use modified laboratory hardware and operate and control his experiment himself during the flights. Thus, he can directly observe the behavior of the boiling fluid under the influence of variable gravity and receive the sensation of gravity in his own body at the same time.

D. HEATER ELEMENTS

Test heaters of different size and geometry have been applied, such as platinum wires, microheaters based on semiconductor material (thermi-

stors), plates, and tubes consisting of a quartz substrate coated with a thin gold layer. These types of heaters respond quickly to changes of power and heat transfer mechanisms. Except for thermistors, all types have been used in KC-135 flights and in TEXUS missions, wires (0.2 and 0.05 mm diameter) and plates (20×40 mm^2), and wires of 0.2 and 0.05 mm diameter in the GAS mission. In the Shuttle missions, spherical miniature heaters were investigated using thermistors of various diameters from 0.26 mm to 1.4 mm, and small circular plane heaters of 1 mm to 3 mm diameter. Ohta [48], Ohta *et al.* [49], and Lee and Merte [32] used plane heaters with transparent coating to observe the bubble dynamics at the heated surface from below. The 25×40 mm^2 heater of Merte was used in drop towers and the GAS mission experiments. Ohta developed a circular heater of 50 mm diameter coated for heating on the back side of a sapphire glass plate of 3 mm thickness. On the heat transfer surface thin temperature sensors of 0.2 μm thickness were directly coated to the sapphire substrate. With that arrangement he could measure the surface temperature and the thickness of the remaining liquid layer below a large bubble during a NASDA TR-1A rocket flight mission.

All the these heaters are fast in response and can be used both as electrical resistance heaters and simultaneously as resistance thermometers to determine the mean temperature on the heater surface. Local temperatures could be measured solely with the heater arrangement of Ohta. The heat flux was determined by recording voltage and current. A temperature control system protected the heater from overheating in case the average heater temperature had reached a certain critical value. Various liquids, mostly refrigerants (R113, R12, R11, R134a, R123), and ethanol (Ohta), were investigated at saturated and subcooled conditions. The convenient thermophysical properties of these fluids allow study of boiling and the influence of the fluid properties over a wide range of saturation states, sometimes up to near critical states. With pressure and temperature records the liquid state could be exactly determined.

V. Heat Transfer at Saturated Nucleate Boiling

A. Wires as Heating Elements

Wires are often used as heating elements to study basic boiling phenomena. Their advantage is that they may be used both as heaters and as resistance thermometers. Wires made of platinum are especially preferable because of their well-defined electrical resistance to temperature characteristics and their stability against chemically aggressive fluids. They can also be used up to rather high temperatures. In addition, a wire heater can be

regarded as a line heat source, which facilitates the optical observation and evaluation of the bubbles in a nearly two-dimensional frame. For experiments in microgravity it is especially important that, with the use of wires, the power necessary to achieve high heat flux densities is relatively low. For these reasons, wires were used in the first μ-g boiling experiments performed by Siegel [59] and by Weinzierl [83] and Weinzierl and Straub [84].

1. Onset of Boiling

The results received during the TEXUS 3b mission, in 1981, were the first in which pool boiling under microgravity conditions ($a/g < 10^{-4}$) could be maintained over a period of 360 sec. The experiments were performed using a wire of 0.2 mm diameter in subcooled Freon-113, investigating three heat flux steps of 17, 39, and 77 kW/m². Each heat flux step lasted for 120 sec, which was much longer than in the earlier drop tower experiments performed by Merte and Clark [40] and Siegel [59] with 1.4-sec and 0.3-sec durations, respectively. The development of the temperature course during onset of boiling at μ-g is compared with the reference experiment at 1-g in Fig. 8. Nucleation occurred at μ-g during the first heat flux step after a rapid increase of temperature up to an overheating of about $\Delta T_{sat} = 34$ K due to mere heat conduction, whereas in the reference run at 1-g the onset of boiling appeared only during the switch to the third power step to 77 kW/m². Cooling by natural convection at 1-g was apparently so efficient that the temperature for heterogeneous nucleation could not be achieved within the first and the second power step. Immediately after onset of boiling at μ-g the heater temperature dropped from $\Delta T_{sat} = 34$ K to 18 K. Steady-state conditions were achieved very rapidly with a constant heater surface temperature over the full period of constant heat flux, even though the vapor production and vapor volume was increasing in the fluid cell (the fluctuation in the temperature course is due to the poor electronic resolution usual 20 years ago). It is interesting to note that at the first power step the temperature of the wire with boiling at μ-g is higher than with free convection at 1-g, and consequently, at this state cooling by free convection is more efficient than by boiling: $\alpha_{1g} > \alpha_{\mu g}$. However, the reverse happens at the second power step, as there is still convection at 1-g, but the heater temperature is now higher than at μ-g. This means that the heat transfer coefficient with boiling at μ-g is now higher than with convection: $\alpha_{\mu g} > \alpha_{1g}$. At the third power step with boiling as the heat transfer mechanism in both situations there is still $\alpha_{\mu g} > \alpha_{1g}$.

The first experiments over a longer period of microgravity boiling demonstrated clearly that 20 sec is sufficient to achieve a constant mean heater temperature. Therefore, this interval may be regarded as long enough
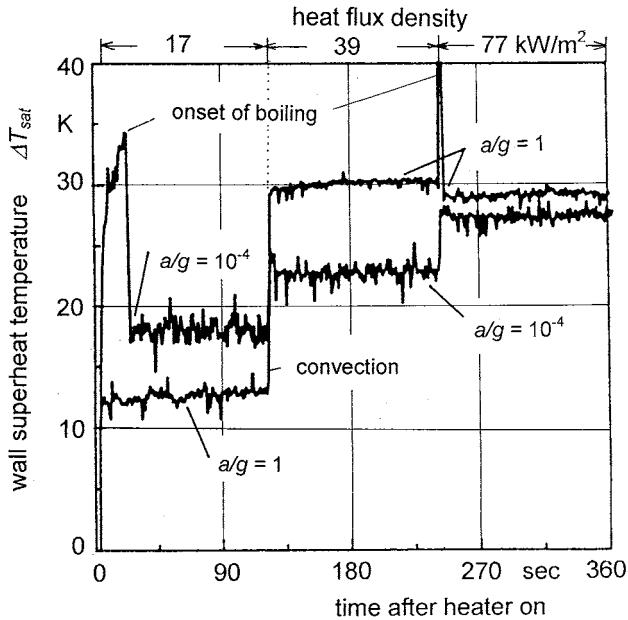
FIG. 8. Temperature development during onset of boiling at μ-g and 1-g, from TEXUS 3b (1981) [83, 84].

to define steady-state boiling conditions (exception was the boiling on a direct electrically heated flat plate). In order to make best use of the valuable time under microgravity and to receive more boiling results during one mission, a period of 20 to 30 sec of constant heat flux was provided in all further experiments. After that period the heat flux was usually increased stepwise up to the critical heat flux where the power supply was automatically switched off by a temperature control device that prevented overheating. Thus, at higher system pressures even film boiling could be achieved without the risk of damaging the heater. In most cases the fluid cell was not actively cooled, however; because the heat capacity of the fluid and the vessel was large compared with the power input of the heater, the temperature of the liquid did not change measurably during an experimental run.

The onset of boiling was also studied during a GAS flight in 1996 with STS 77 on platinum wires of 0.2 and 0.05 mm diameter and 75 mm in length [41]. About 1 liter of R134a was used as test liquid in a cell designed for pressures up to 70 bar. With the pressure and temperature control system various liquid states could be adjusted. In Fig. 9 the temperature course versus time is demonstrated, after the power of the heater was switched on
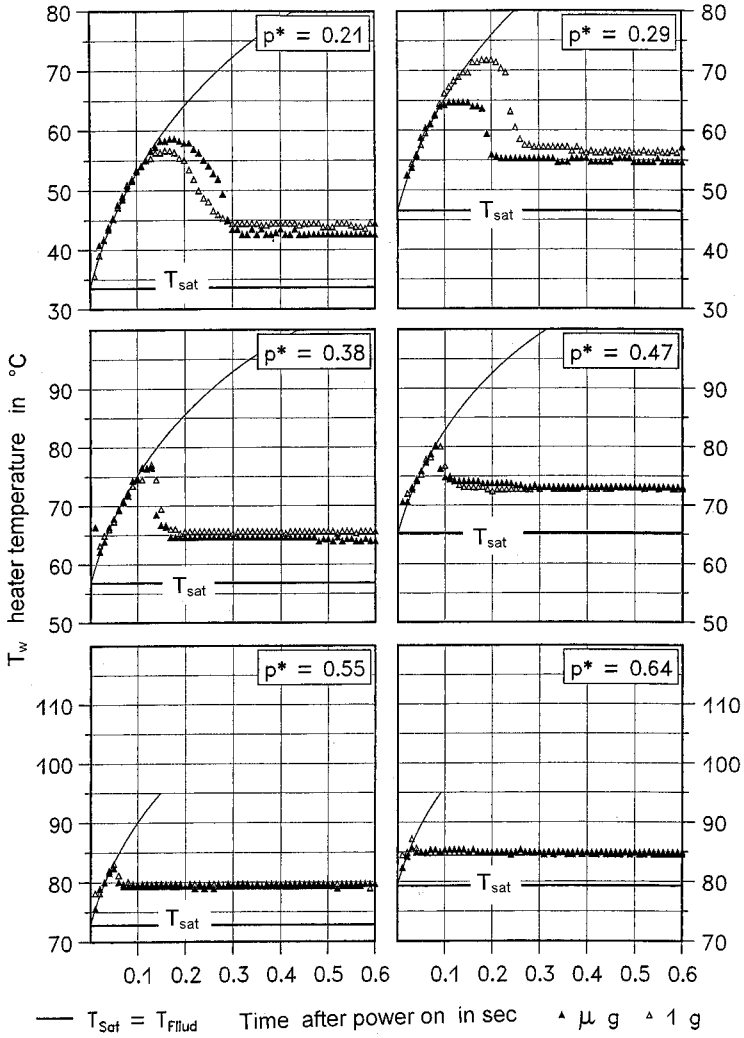
FIG. 9. Temperature development at onset of boiling for μ-g and 1-g, at saturation pressures in the range $0.21 \leqslant p^* \leqslant 0.64$, fluid R134a, wire 0.2 mm, GAS mission 1996 [41].

at six different saturation states expressed by the reduced pressure $p^* = p/p_c$. The solid line demonstrates the transient increase of the heater temperature as calculated numerically under the assumption of pure heat conduction in the liquid. The measured data for both μ-g and 1-g agree well with the

calculated values, which reveals that close to the onset of boiling the transient temperature increase is determined predominantly by conduction even at 1-g. The exact temperature at onset of boiling is difficult to determine. The maximum temperature recorded is not at all the correct one, as boiling starts at a certain local point, decreasing the temperature only locally, while on the average it may still increase. Therefore a better definition would be the temperature at which the slope dT/dt deviates from the transient temperature rise.

The sequence of pictures in Fig. 10 (for magnitude estimation, the circular window of the cell had a diameter of 62 mm) corresponds to the temperature course at the pressure $p^* = 0.21$. First tiny bubbles may be observed at the wire 0.14 sec after power switch-on, which coincides with the change in the temperature slope. In the following sequence of pictures the rapid covering
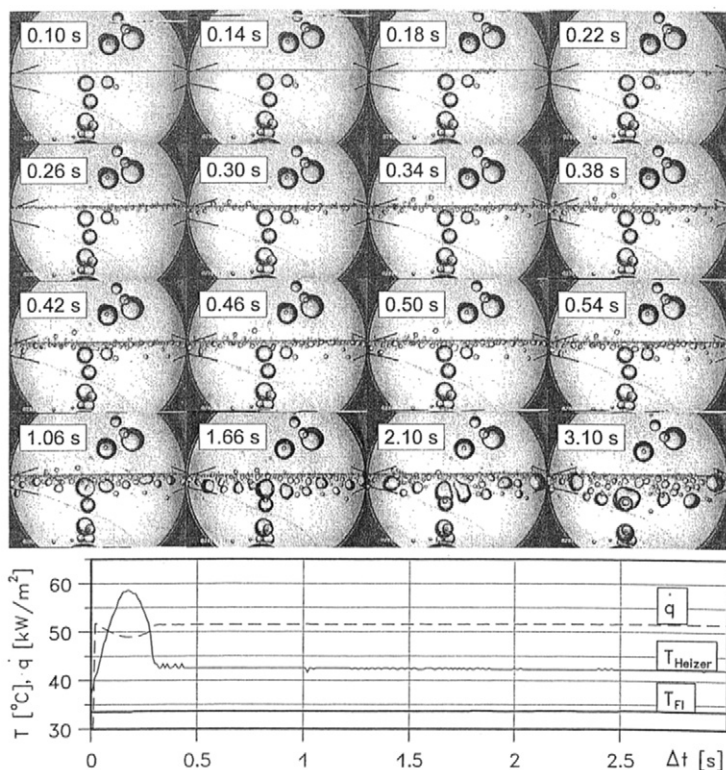
FIG. 10. Photo sequence of bubble development and growth after onset of boiling, and vapor transport by coalescence at a wire of 0.2 mm dia., fluid R134 at saturation state, $p^* = 0.21$ corresponding to Fig. 9, glass window diameter 62 mm.
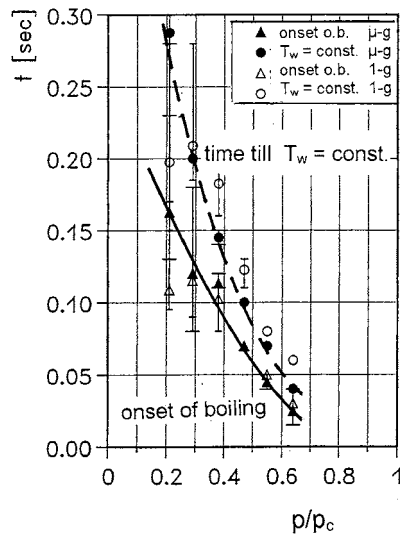
FIG. 11. Delay times for onset of boiling after poweron and lapse times until establishment of steady-state boiling at 50 kW/m^2, corresponding to Figs. 9 and 10.

of the wire with bubbles is shown. At 0.30 sec after power switched on, the whole wire is already covered with bubbles corresponding in the temperature–time plot of Fig. 9 with steady-state boiling, indicated by the constant heater temperature. The time delays for onset of boiling and for obtaining a constant wall temperature with fully developed boiling are plotted as functions of saturation pressures in Fig. 11, both of them decreasing rapidly with increasing saturation pressure.

The growth and development of the bubbles can also be observed in this sequence. The bubbles to be seen in the first picture, labeled "0.10 sec," were remaining from the previous experimental run. In order to condense the produced vapor after each experimental run, the system pressure was increased by means of the pressure control system and the liquid stirred for 2 min and let calm down for 3 min. This procedure was tested on earth and had proved to be sufficient for re-condensing all the vapor, but it was not always sufficient under microgravity conditions. However, these bubbles indicate on one hand that the liquid state was saturated, and on the other that there was no motion in the liquid at all, because these bubbles remained in their positions all the time. It is interesting to speculate why most of the visible bubbles are generated on one side of the wire and why they preferentially move in one direction. The only unproved explanation for that behavior could be that there remain some depositions on the wire from the
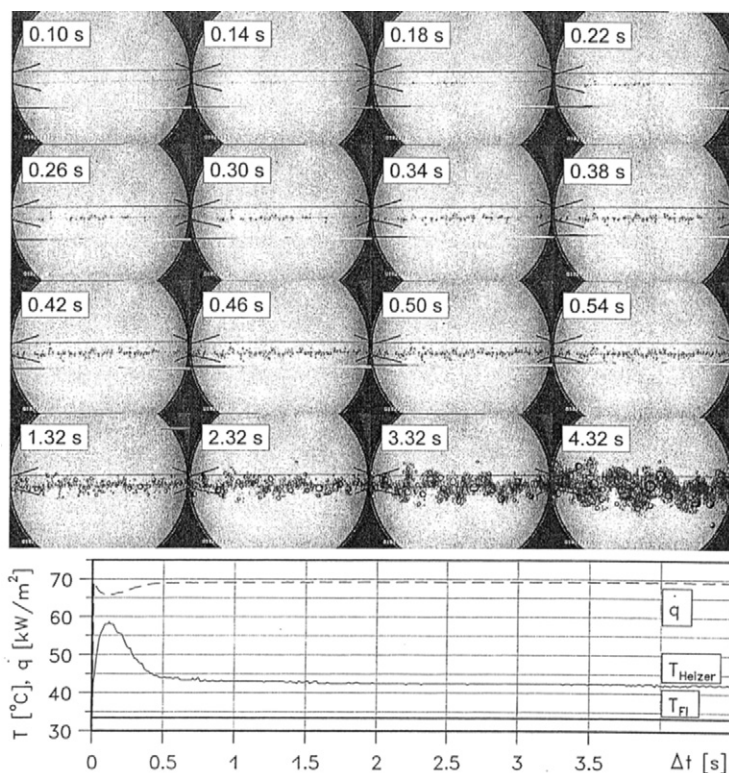
FIG. 12. Development of spiral-like bubble formation on the 0.05 mm wire. The liquid conditions are the same as in Fig. 10; heat flux was 69 kW/m².

reference tests on ground before the mission where the boiling bubbles moved in the opposite direction. In subsequent experimental runs the bubbles develop and move with cylindrical-symmetry around the wire, as shown in Fig. 12 on the 0.05 mm wire. It must, however, be emphasized that no difference could be observed in the heat transfer values between the "cylindrically symmetrical" and the "two-dimensional plane" boiling. The last one offers the advantage that the bubble dynamics can be observed clearly as in Fig. 10, whereas in Fig. 12 after 3 sec the wire is concealed by the bubbles around it. In both figures it may be seen that the bubbles depart, move, and grow by continuous coalescence processes.

The "cylindrically symmetrical" bubble boiling development in Fig. 12 happened under the same saturated liquid conditions as the sequence of Fig. 10, but at the platinum wire of 0.05 mm diameter, and a heat flux density
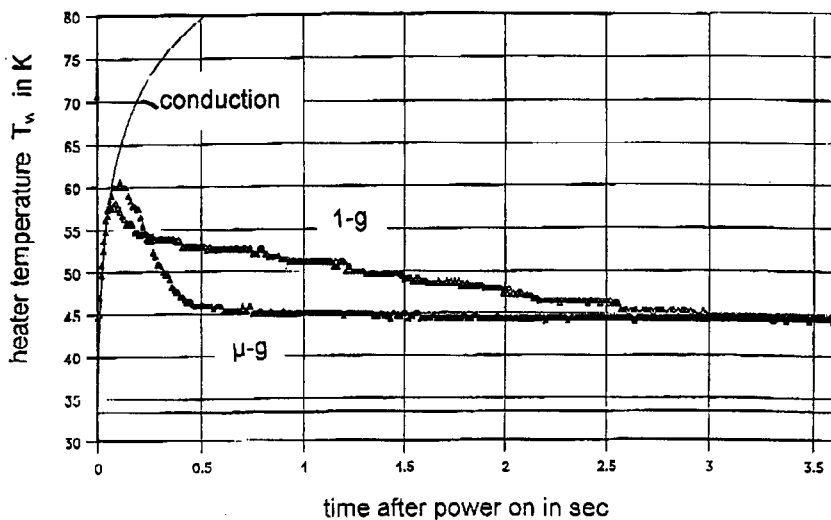
F<small>IG</small>. 13. Temperature development at onset of boiling appropriate to Fig. 12 at μ-g compared with 1-g.

of about 69 kW/m². The bubble formation developed like a spiral around the wire, the departure and bubble motion being caused by coalescence processes. The corresponding temperature course is shown in Fig. 13. The onset of boiling occurs 0.08 sec after power on. Steady-state boiling is obtained after about 0.5 sec in μ-g and after 3 sec at 1-g. The last fact demonstrates, that simultaneously to boiling incipience free convection sets in and impairs the rapid extension of boiling over the whole wire, and thus delays the attainment of steady-state boiling.

The temperature development at onset of boiling in subcooled liquids is compared with saturated boiling in Fig. 14 at a constant heat flux of 50 kW and under the same conditions as before. At constant liquid temperature, different subcooling states could be achieved by increasing the pressure, but the saturation temperature also changes with it. At high subcooling states cooling by free convection at 1-g is so efficient that with a given heat flux, the nucleation temperature cannot be attained, even if the heater temperature exceeds the saturation temperature. The left column in Fig. 14 shows the temperature course at 1-g, the right one at μ-g. At the beginning the temperature rise is due to conduction. At a fluid temperature of $T_{li} = 33.4°C$, boiling occurs under μ-g at saturation and for the two subcooling states $\Delta T_{sub} = 12.9$ and 23.2 K. At 1-g and for a subcooling of $\Delta T_{sub} = 12.9$ K, the nucleation temperature is just reached and the heater temperature slowly
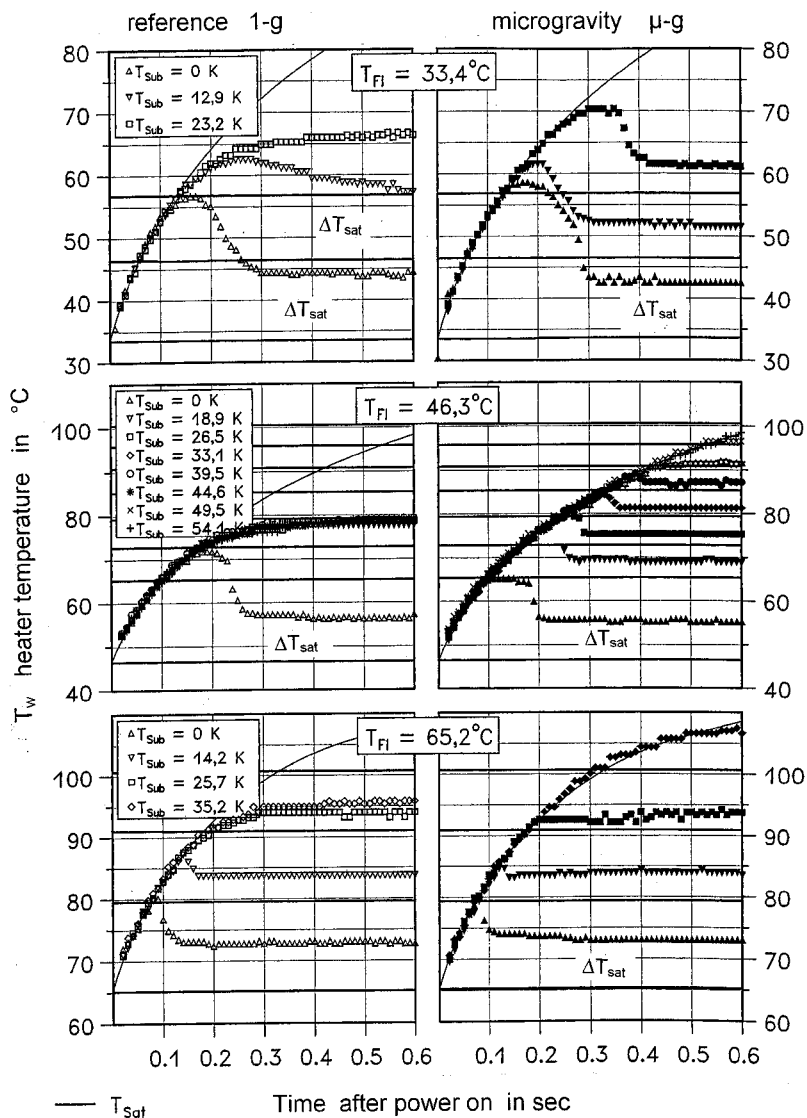
FIG. 14. Development of the temperature at the onset of boiling for various liquid saturation and subcooling temperatures, under 1-g and μ-g.
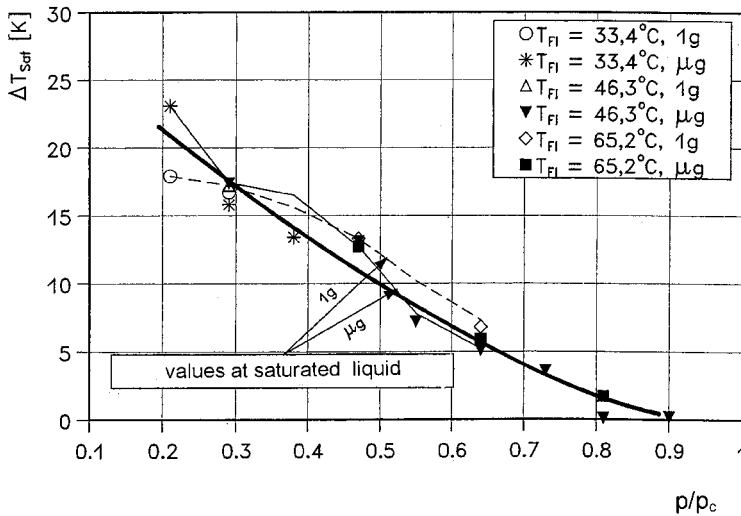
FIG. 15. Supersaturating temperatures at boiling onset, at saturated, and subcooled conditions, and under μ-g and 1-g conditions.

decreases, indicating that more and more nucleation sites are activated over the heater surface. At $\Delta T_{sub} = 23.2$ K the nucleation temperature is not reached and the wire is cooled by free convection. At the liquid temperature $T_{li} = 46.3°C$, boiling is only observed at the saturation state at 1-g and all subcooled curves merge in one curve, which indicates convection. At $T_{li} = 65.2°C$ and for 35.2 K subcooling the heater exceeds both the saturation temperature and the critical temperature the heat transfer being comparable with that of conduction. But at 1-g free convection confines the temperature increase and keeps it below saturation.

The study of boiling onset demonstrates, as is generally expected, that the nucleation temperature is more or less independent of gravity and of subcooling if overheating due to the saturation state is regarded (see Fig. 15). Free convection cooling at 1-g can be so efficient that at high subcooling the nucleation temperature will not be attained. The supersaturating temperature for nucleation depends on the saturation state and decreases with increasing saturation pressure according to nucleation theory.

2. Heat Transfer from KC-135 Missions

The heat transfer results of the first long duration microgravity experiments by Weinzierl [83], using TEXUS as carrier, demonstrated that the nucleate pool boiling heat transfer coefficients are nearly independent of

gravity and of free convection induced by buoyancy. A wide range of parameters such as fluid states, heat fluxes, and heater configurations were studied by Zell [87] during parabolic trajectories with aircraft KC-135 using R12 as test liquid. The results were only partially published [70, 75, 76, 88, 89].

One parabolic trajectory provided a sequence of normal–high–low–high, and normal gravity level (Fig. 1). The low gravity period lasted about 20 to 25 sec, but with a randomly alternating variation of $\Delta a/g \approx \pm 0.02$ (Fig. 2). The high-gravity phase went up to a peak value of about $a/g \approx 1.8$. From these experiments boiling can be studied in one trajectory during various gravity levels at nearly steady state conditions, which were reached within less than 0.5 sec as mentioned before. The simultaneous recording of the gravity level a/g, the mean heater temperature superheat ΔT_{sat}, and the stepwise increase of the heat flux $\dot{q}$ during one trajectory period is demonstrated in Fig. 16. The heater was switched on after the low-gravity phase had been reached in order to avoid free convection effects before boiling was initiated. After the first power step of about 130 kW/m^2 the temperature rose immediately to $\Delta T_{sat} = 9.5$ K and remained there nearly constant for about 10 sec. After that the power was increased to about 200 kW/m^2, resulting in a temperature rise to about 10.4 K. The following power steps to 270 and 330 kW/m^2 were accompanied by nearly constant temperature rises to 11.3 K and 11.8 K. But when after the trajectory period the gravity level increased by more than two decades, the heater temperature and power remained constant until the power supply was switched off. Although no noticeable change concerning heat transfer could be registered, bubble size and bubble behavior changed remarkably.

During several KC-135 missions between 1985 and 1988, boiling was investigated on platinum wires of 0.05 and 0.2 mm diameter, on a gold-coated cylinder of 8 mm diameter, and on a gold-coated plane plate of 20×40 mm^2 with R12 as test fluid. The gold coating was used simultaneously for direct electrical heating and as a resistance thermometer to determine the mean surface temperature of the heating elements. For example, a boiling curve with the heat flux versus the wall superheat temperature $\Delta T_{sat} = T_w - T_{sat}$ on the 0.2 mm wire is shown in Fig. 17 at various saturated states indicated by the reduced pressure p^*. The symbols represent the measurements at reduced gravity and the lines the reference measurements taken immediately after the trajectory had returned to normal gravity, whereas no difference in the heat transfer between the high 1.8g and normal gravity could be detected. It can be seen that there is generally not a big difference in the heat transfer intensity, although the gravity level had changed at least by two orders of magnitude. The influence of gravity can be revealed more clearly with the ratio of the heat transfer coefficients taken at the same heat flux and under identical liquid conditions,

JOHANNES STRAUB
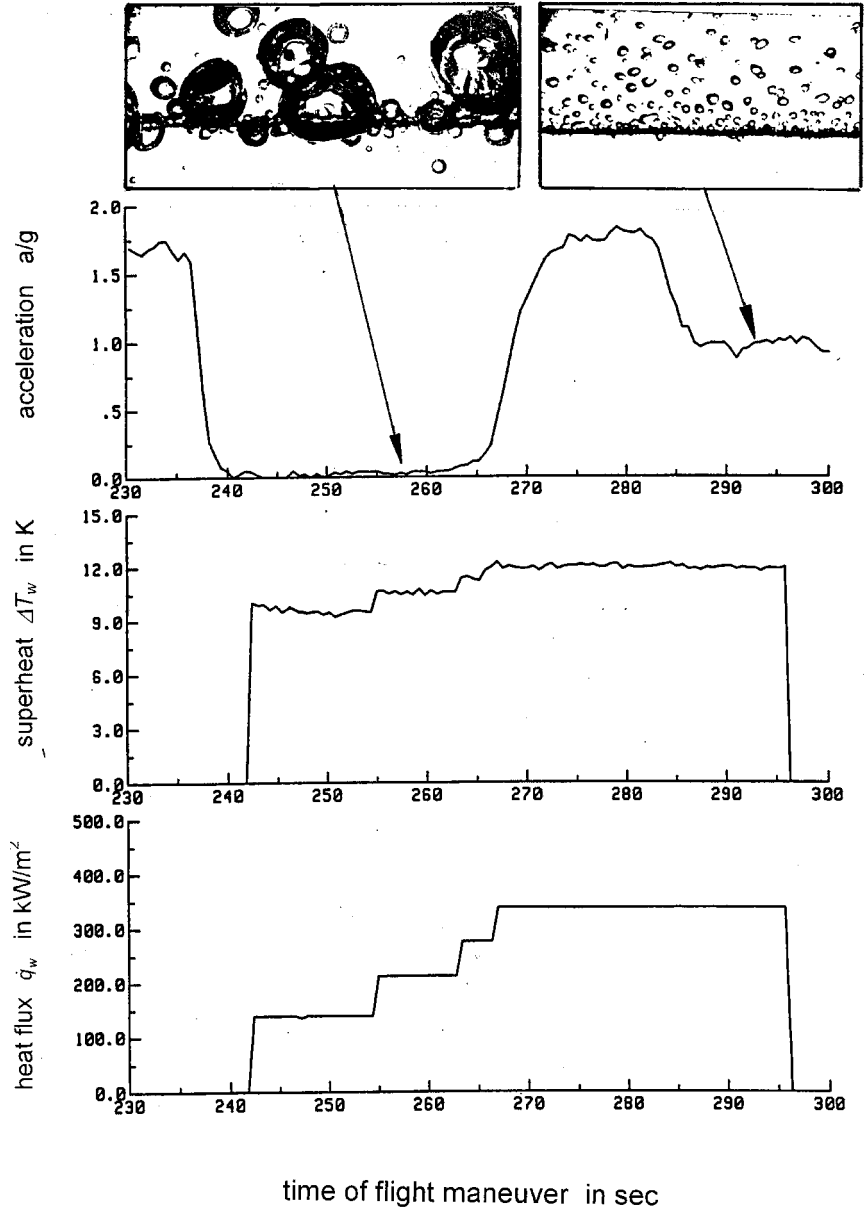
FIG. 16. Course of acceleration, superheat temperature, and heat flux recorded during a trajectory with KC-135.
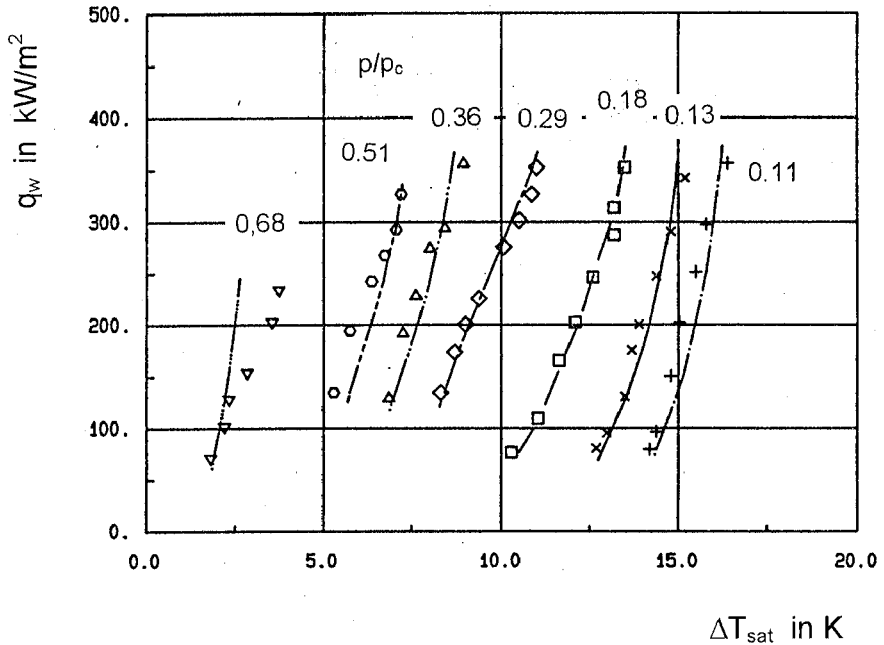
FIG. 17. Boiling curves at various saturation states $p*$ with R12 on wire of 0.2 mm diameter from KC-135 [87]. Symbols at μ-g, lines at 1-g.

which may be defined as the heat transfer efficiency [Eq. (11): $\alpha_{\mu g}/\alpha_{1g}$] and is demonstrated in Figs. 18 and 19. It is interesting to note that for both wires (0.2 and 0.05) at lower heat fluxes up to about 200 kW/m² the heat transfer at microgravity is higher than at 1-g and is slowly decreasing with increasing heat flux. However, with high system pressure $p* = 0.68$ the efficiency strongly decreases above 100 kW/m².

Heat transfer under microgravity depends on the heat flux and the liquid state; it decreases moderately with higher heat fluxes, but it is by no means as drastically diminished as has been generally expected and predicted by most correlations extrapolated to the residual gravity value of the aircraft, which is $a/g \approx 10^{-2}$. On the contrary, at lower heat fluxes the heat transfer intensity was enhanced and was only reduced with increasing heat flux [70, 75, 76]. This tendency could be confirmed in the following experiments performed on Shuttle missions: ILM-2 in 1994, a GAS mission in 1996, and LMS mission in 1996 with long duration of the experimental runs and at a high quality of the gravity level $a/g < 10^{-4}$ [41, 64, 72–74]. Some detailed results from the Space Shuttle mission are presented in the following.
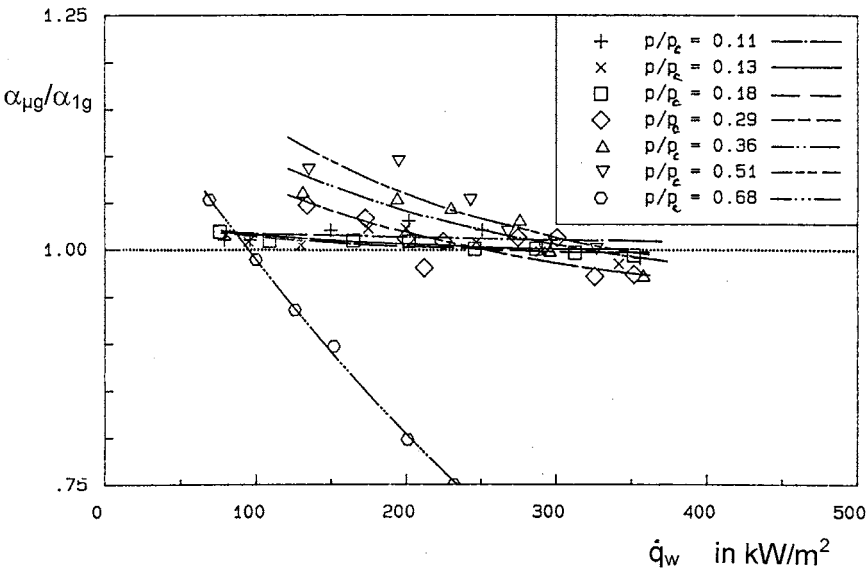
FIG. 18. Microgravity efficiency on heat transfer at saturation boiling appropriate to Fig. 17.
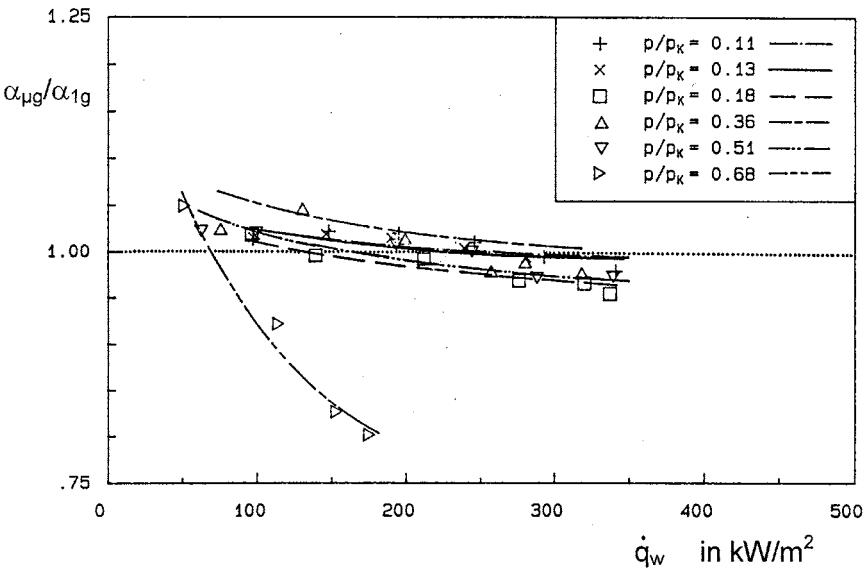
FIG. 19. As in Fig. 18, but with 0.05 mm wire.

3. *GAS Mission in STS -77*

In an autonomous experiment during a GAS mission, boiling was studied with the refrigerant R134a in a liquid container of about 1 liter under saturation and subcooled conditions using two platinum wires of 0.2 and 0.05 mm diameter with a length of 75 mm [41, 73]. Temperatures and pressures were registered and the boiling process was observed with a video camera, which allowed a 50-Hz time resolution. Under μ-g conditions the heat transfer efficiency of saturated boiling, represented in Fig. 20, up to a heat flux of 300 kW/m² and in the investigated pressure range of $0.21 < p^* < 0.64$ is on an average about 8% higher than at 1-g, but, with the wire of 0.05 mm diameter, 10% lower than at 1-g. Reference measurements were conducted before and after the mission with identical equipment. Agreement exists in principle with the KC-135 experiments, but it is conspicuous that at the 0.2 mm wire only a slight reduction with heat flux could be detected, in contrast with the 0.05 mm wire, which showed a constant decrease of 10% at all heat fluxes. During the switch from power step 200 to 250 kW/m², a real burnout occurred that broke the wire and was only discovered after the mission. The event itself could not be registered at the video, because the break of the wire happened outside the view field of the camera and was additionally hidden by vapor. No further results have been recorded from the experimental program with the 0.05 mm wire.
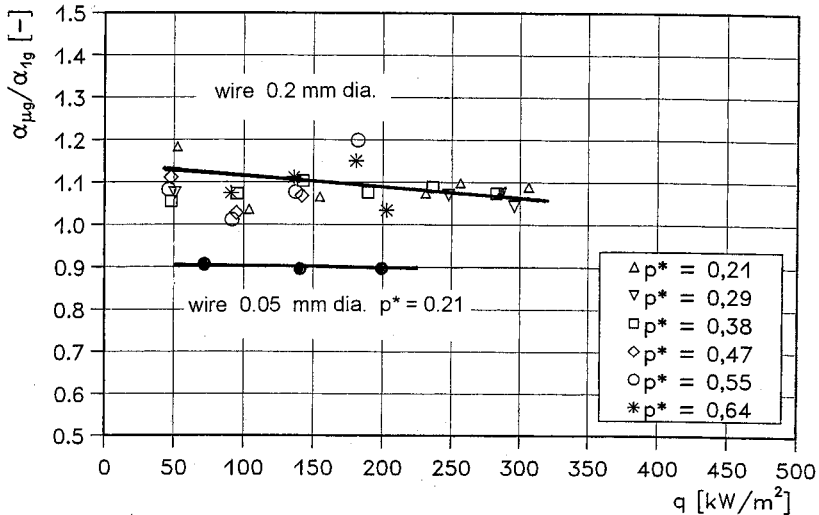
FIG. 20. Microgravity efficiency on heat transfer at 0.2 and 0.05 mm wire in R134a, from GAS mission [41].

B. SMALL SURFACES

Small heater surfaces contribute to simulate the cooling effectiveness of electronic devices [72] and to test these cooling systems for space application. They need only low power at high heat fluxes and a relatively small amount of liquid. Therefore, these experiments were just suitable for the BDPU facility (Section IV.B). During the LMS missions in 1994 and 1996 saturated and subcooled boiling was studied using the refrigerants R11 and R123, respectively, and various small heaters such as circular plane surfaces of 1, 1.5, and 3 mm diameter, or glass coated thermistors as spherical and hemispherical heaters [64, 65, 72, 74]. The basic heating elements of the circular plane heaters were also thermistors, inserted into a cylindrical copper cup; see Fig. 21. The thermistors were also used simultaneously as heaters and as resistance thermometers. In order to determine the real surface temperature, the thermal resistance to the heater surface, especially the glass coating, has to be considered. The heat flux was limited by the total available power for the experimental container in the BDPU, and the maximum permissible temperature of the thermistor bead.

From the many data, which will be published elsewhere, some nucleate boiling curves measured at μ-g are discussed and compared with 1-g data received at otherwise identical conditions. For instance, concerning the circular 3 mm plane heater, boiling curves for various saturated liquid pressure conditions are shown in Fig. 22. The differences in the wall superheat temperature are small, which means that the differences in the heat transfer coefficients are small as well. They can be revealed more distinctly with the gravity efficiency, shown in Fig. 23 for the 3 mm circular plane heater and for the spherical heater in Fig. 24. An enhancement of the heat transfer efficiency up to about 20% was achieved at lower heat fluxes
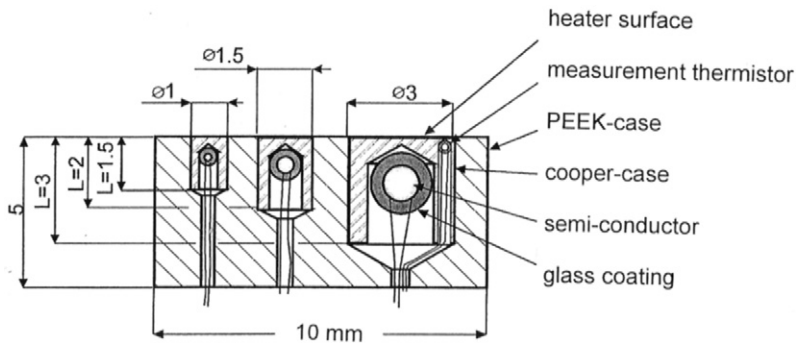
FIG. 21. Design for three small circular plane heaters.
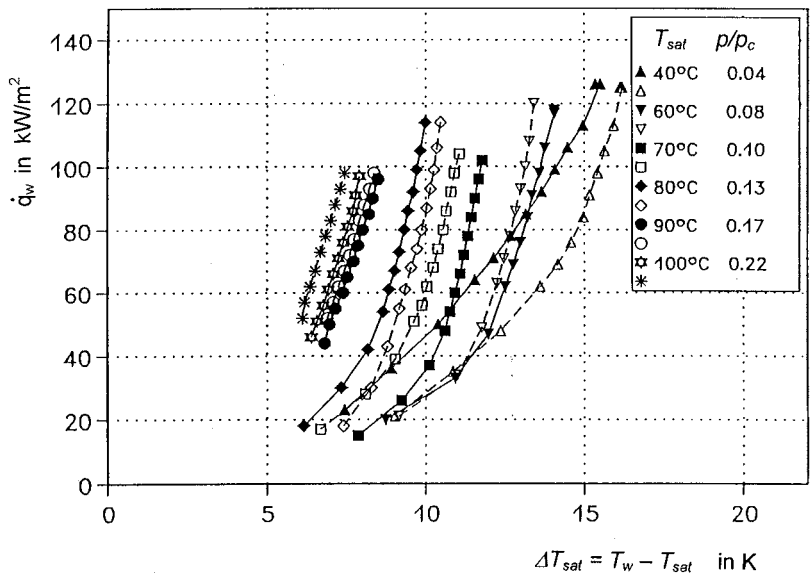
FIG. 22. Nucleate boiling curves at various saturation pressures p/p_c, fluid R123, at a circular plane heater of 3 mm diameter. LMS mission (1996); solid symbols μ-g, open symbols 1-g [64].
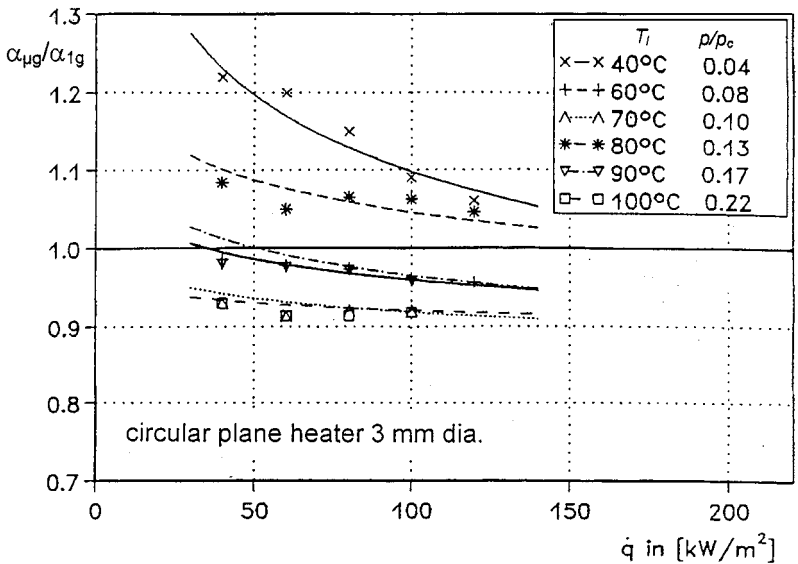
FIG. 23. Efficiency of gravity on heat transfer at saturated pool boiling evaluation of data from Fig. 22.
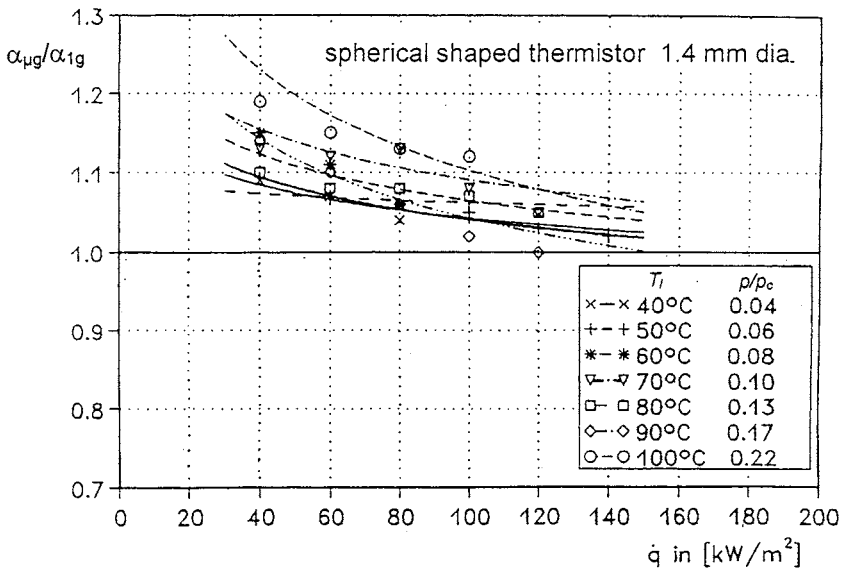
FIG. 24. Efficiency of gravity on heat transfer at spherical heater of 1.4 mm diameter.

that decreased with increasing heat flux. But also at the plane heater a reduction was found at several pressures. The microgravity efficiency depends on the heat flux itself, and on the liquid state represented by the pressure ratio p/p_c as parameter, but the influence of the latter has not been clarified at present. Similar results were generally observed during all studies using various fluids and heaters. The results of Abe et al. [1], Ohta et al. [49], and Lee et al. [33] not covering a larger variation of parameters, are in agreement with these results.

Saturated boiling was studied using R11 as test liquid at low pressures in the range $0.03 < p^* < 0.09$ during the ILM-2 mission in 1994 [74]. As heating element, a very small hemispherical thermistor of 0.26 mm outer diameter with a glass coating of 0.05 mm thickness was used. The primary task of that experiment was the investigation of the growth and the condensation of bubbles in an uniformly superheated fluid. In order to determine the evaporation coefficients the experimental procedure was different from those of common boiling studies [50, 51]. At a constant liquid temperature and a constant controlled temperature T_i of the thermistor bead, the pressure was decreased stepwise. Because of the thermal resistance of the glass coating R_λ (determined by the size and thermal conductivity of the glass), and the variable mode of heat transfer, the heater surface

temperature T_w and the heat transfer coefficient $\alpha(T_w)$ were coupled mutually by the expressions

$$T_w = T_i - \dot{Q}R_\lambda \quad \text{and} \quad \alpha = \frac{\dot{Q}}{A(T_w - T_{li})}. \quad (12)$$

In Fig. 25 an example is shown that demonstrates the experimental procedure in a pressure–temperature and a pressure–heat flux plot, also exhibiting the evaluated surface temperature and the corresponding heat flux density. In this plot the saturation condition and the subcooling are also marked. The experimental run starts at a liquid temperature of $T_{li} = 30°C$ and a pressure of 6.5 bar with a high subcooling of nearly 60 K. The bead temperature of the thermistor T_i is the parameter. At first it was at 200°C, and according to Eq. (12) T_w and α result from the measured heat flux. There is a high heat flux density of about 880 kW/m² and a wall temperature of about $T_w = 108°C$, and a wall superheat $\Delta T_{sat} = 20$ K. With decreasing pressure combined with decreasing subcooling, the heat flux is moderately increasing with a moderate increase of wall superheat of ΔT_{sat}. At 20 K subcooling the heat flux is strongly decreasing with simultaneous increase of the heater surface temperature or wall superheat. The next experimental runs were performed with bead temperatures of 180, 160, and 150°C. At saturation state film boiling and transition boiling occurred. It is interesting
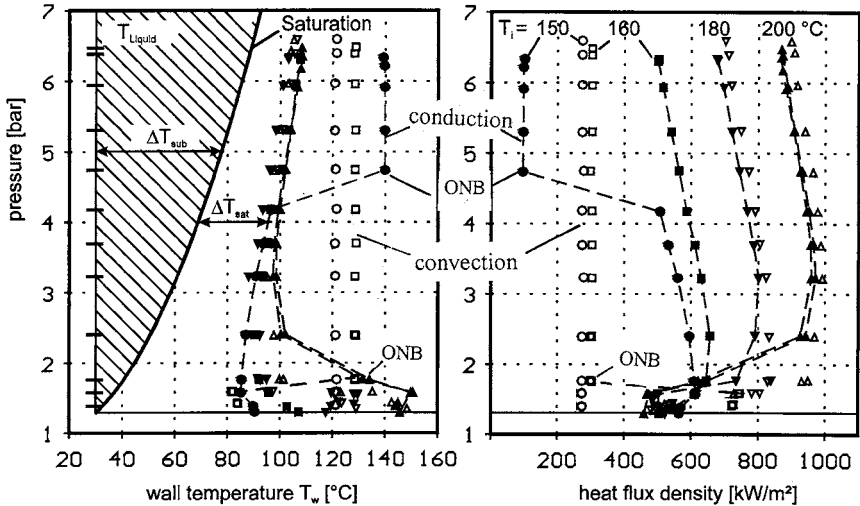
FIG. 25. Boiling sequence at a constant liquid temperature of 30°C; wall temperature and heat flux as function of liquid state and temperatures of the thermistor bead.

to note that at a bead temperature of 160°C boiling occurred under microgravity at the beginning of the experimental run even at high subcooling, whereas at 1-g the onset of boiling started at a pressure of 1.8 bar and a subcooling of $\Delta T_{sub} = 10$ K. Up to that, free convection kept the heater below the nucleation temperature. At a bead temperature of 150°C, onset of boiling happened at a subcooling of about 45 K during the pressure step from 4.7 to 4.2 bar (Fig. 25) with an increase in the heat flux from 100 to 500 kW/m² and a decrease of the surface temperature from 140°C to 95°C. Under identical but terrestrial conditions no boiling occurred at all; the surface temperature remained constant at 125°C and the heat flux at 231 kW/m². Of additional interest is that as long as the subcooled nucleate boiling mode determines the heat transfer intensity, the wall superheat is nearly independent from heat flux and gravity level. From these studies we can evaluate saturated and subcooled boiling curves, and with the optical observation facilities we get an imagination of the boiling dynamics, which will be discussed in a later section.

In Fig. 26 boiling curves for the saturation state in R11 at the hemispherical 0.26 mm diameter thermistor are presented. For reduced saturation pressures $p^* = 0.03$ and 0.04 the heat flux increases with decreasing overheating temperatures, indicating transition or film boiling. The heat flux fluctuated by about ± 100 kW/m² around the average values indicated by
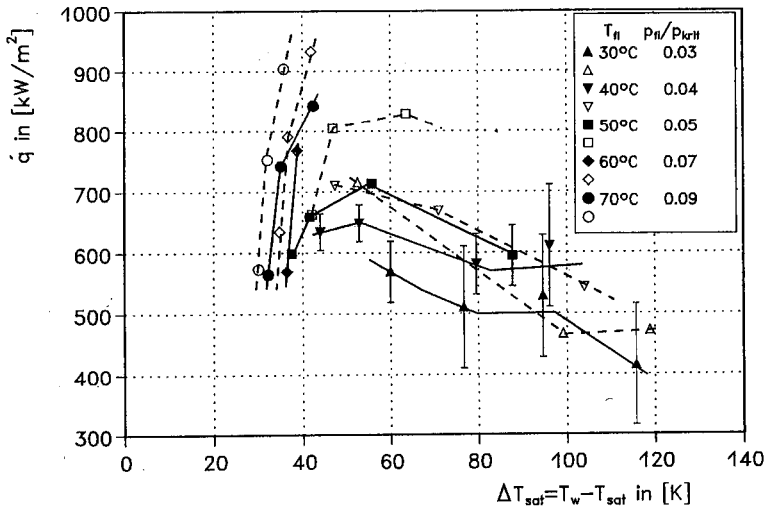
FIG. 26. Transition and maximum heat flux at a small hemispherical heater at saturation state. Solid symbols are μ-g, open symbols 1-g.

the line, and the temperature fluctuated by about 10 K. It was observed that bubbles of a size 2–4 times larger than the heater departed from the heater surface. This suggests that around the heater a vapor film is formed that at a certain thickness becomes unstable and forms a bubble that departs. This unstable film may be caused by the fact that the heater is not exactly spherical or hemispherical and the thickness of the coating is not constant. Under μ-g and 1-g conditions and at a pressure of $p^* = 0.05$, a maximum heat flux was obtained with the ratio $(\dot{q}_{\mu g}/\dot{q}_{1g})_{max} \approx 0.87$. At reduced pressures $p^* = 0.06$ and 0.07 nucleate boiling is the mode of heat transfer with a heat transfer efficiency of $\alpha_{\mu g}/\alpha_{1 g} \approx 0.93$. The highest heat flux data points tend in their slope to a maximum heat flux, but higher heat fluxes could not be investigated without the risk of destroying the heater.

C. Plane Plate Surface

1. *KC-135 Results*

Experiments performed by Zell [87] during KC-135 flights on a direct electrically heated surface using a gold-coated flat plate of 20×40 mm^2 with refrigerant R12 in the pressure range $0.18 \leqslant p/p_c \leqslant 0.68$ resulted generally in lower heat transfer efficiency as discussed above for wires and small heater geometry, presented in Figs. 27 and 28. The efficiency decreases with the heat flux to 0.90. Similar results were attained with a gold-coated cylinder of 8 mm diameter (see Fig. 29); however, the heat transfer efficiency is on the average higher than for the plate. This may be caused by the curvature of the heater, as with that the bubbles have more space for their expansion during growth and the liquid transport to the heater is easier than on the flat surface. But, as on the wires (Figs. 18 and 19), at the high pressure of $p^* = 0.68$ a strong reduction of the heat transfer efficiency is observed, which may be caused by the reduction of the surface tension at that high pressure.

2. *TEXUS Results*

Different observations were made by Zell [87] during saturation boiling on a flat plate with R113 at a low reduced pressure of $p^* = 0.01$ during a TEXUS mission in 1984 [70, 75, 76]. After onset of boiling at a heat flux of 29 kW/m^2, the first bubble grew within 0.5 sec nearly spherically to a size of > 20 mm diameter; see Fig. 30. Beside this large bubble smaller bubbles were generated in the liquid triangle between the heater and the vapor–liquid interface, but coalesced immediately with the large ones. After onset of boiling the mean surface temperature dropped a bit and increased
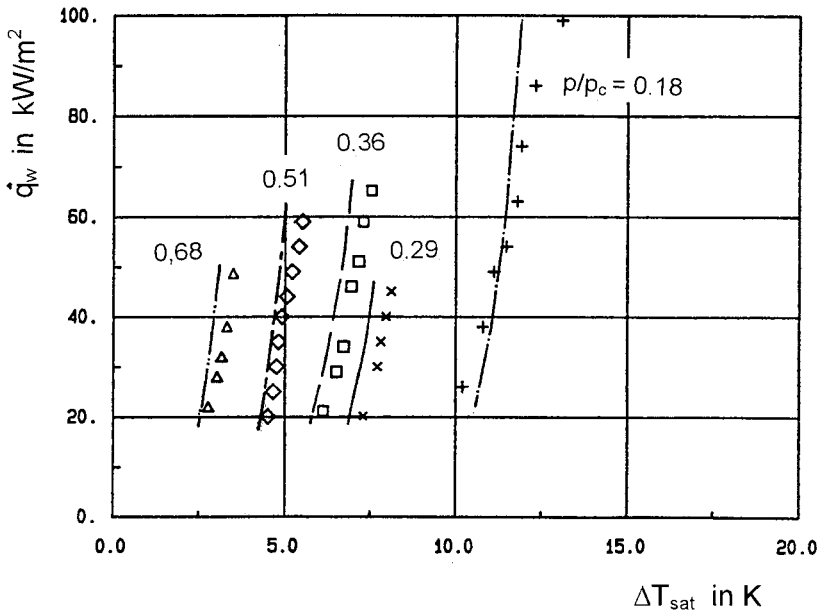
FIG. 27. Heat transfer on a plane plate during saturated boiling at R12 performed during KC-135 mission.
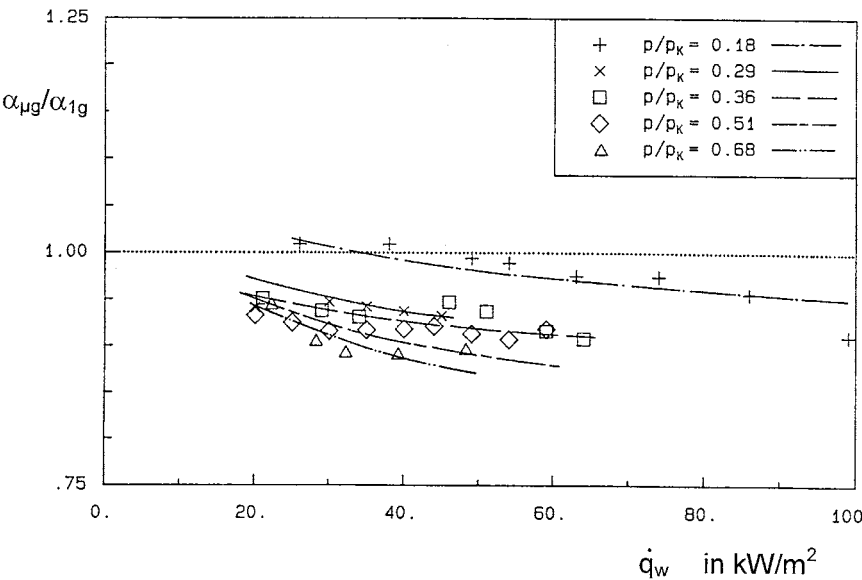
FIG. 28. Gravity efficiency of heat transfer at the plate appropriate to Fig. 27.
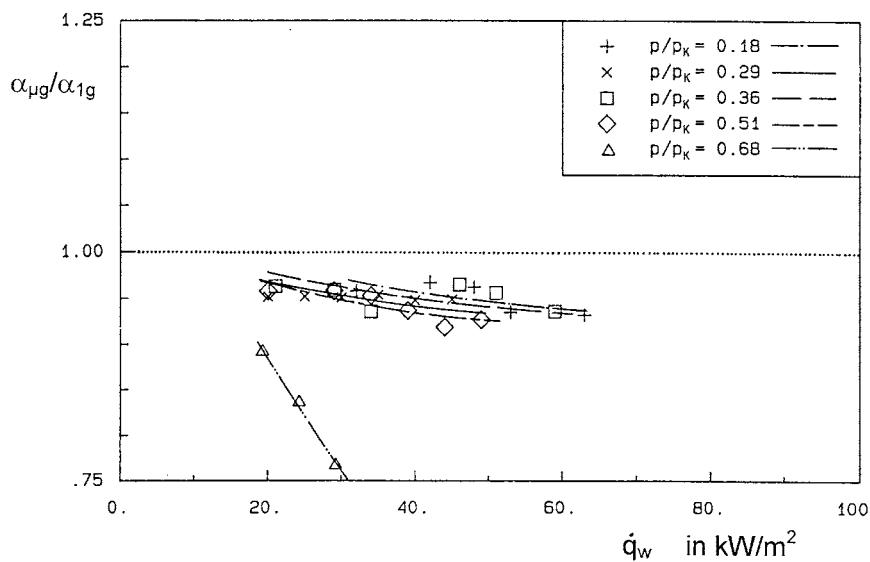
FIG. 29. Gravity efficiency of heat transfer at a gold-coated cylinder of 8 mm diameter, at the same experimental conditions as in Fig. 27.
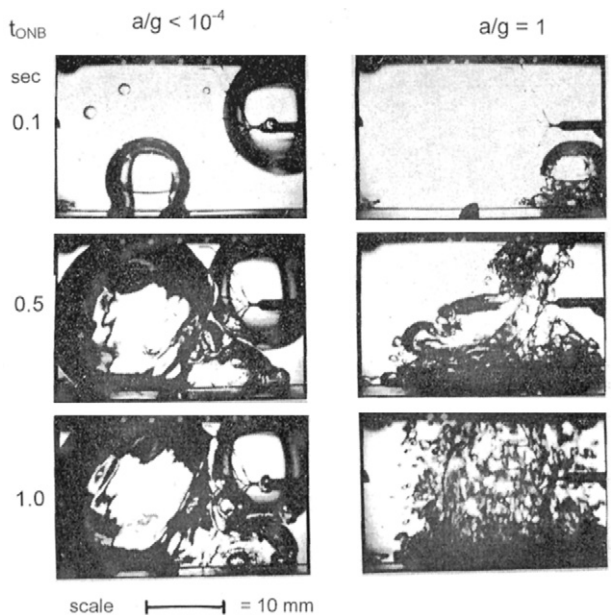
FIG. 30. Onset of boiling and bubble growth under saturated conditions in R113 at $p^* = 0.01$, at 1-g (*right*) and μ-g (*left*), from TEXUS. The bubble in the right corner remained from a previous experimental run.

immediately after. The heat flux at onset of boiling was about three times higher than the calculated critical heat flux for 10^{-4}g. The temperature development with increasing heat flux is demonstrated in Fig. 31. This temperature increase under microgravity conditions was caused by the development of a relatively large dry area formed below this large bubble. The reference measurements at 1-g of heater power and mean temperature were taken at a horizontal plate position and at a vertical position with the length side of the plate. The temperature course indicates a strong attenuation of the heat transfer intensity at μ-g in contrary to the results from KC-135 (Figs. 27 and 28). Because of the direct electrical heating of the surface the liquid was in direct contact with the heat source and thus without any heat-absorbing damping layer in between. The thermal isolation effect enhanced the local surface temperature of this area and prevented rewetting with liquid. Therefore, the heat transfer efficiency decreased with heat flux and time, whereas in the KC-135 experiments this reduction was not observed. For this discrepancy two reasons may be relevant: as already mentioned, the pressure of R12 used in the KC-135 experiments was at saturation state with $p^* \geqslant 0.18$, substantially higher than the $p^* = 0.01$ in the TEXUS experiment with R113. Consequently, the generated vapor volume was much higher in the TEXUS experiment than in the KC-135 experiment, with the result that the liquid and vapor exchange on the heater surface was hindered. Additionally, on the KC-135 flight rapidly alternating g-jitter effects, on the order of $\Delta a/g \approx \pm 2 \times 10^{-2}$, caused momentum fluctuations that supported bubble departure; therefore, the bubbles could not grow to a comparably large size.

The heat flux in the TEXUS experiment was increased every 20 sec in steps of 10 kW/m^2; see Fig. 31a. This power increase can be noticed at μ-g in the steeper temperature rise, but it shows a declining tendency of the slope to an asymptotic value. Thus it cannot be excluded that at larger heater surfaces and longer heat flux periods steady-state conditions could have been achieved with a final transition to film boiling. The slope of the temperature rise (dT/dt) is decreasing after each power step ($d^2T/dt^2 < 0$); however, at 76 sec, about 11 sec after the switch from 50 to 60 kW/m^2, the slope changed its tendency from decrease to increase indicating the instability of a burnout situation ($d^2T/dt^2 > 0$). An automatic overheating system switched the power off, but the experimental control system initiated power on every 5 sec during the time interval 76 to 112 sec, followed immediately by power off due to overheating. As soon as the power was reduced to 50 kW/m^2 the average heater temperature decreased. It was thus indicated that a constant surface temperature might be reversibly achieved at about the same level as during the heating up procedure, but in the timeline of the experimental run a prolongation of the time was not planned. The system
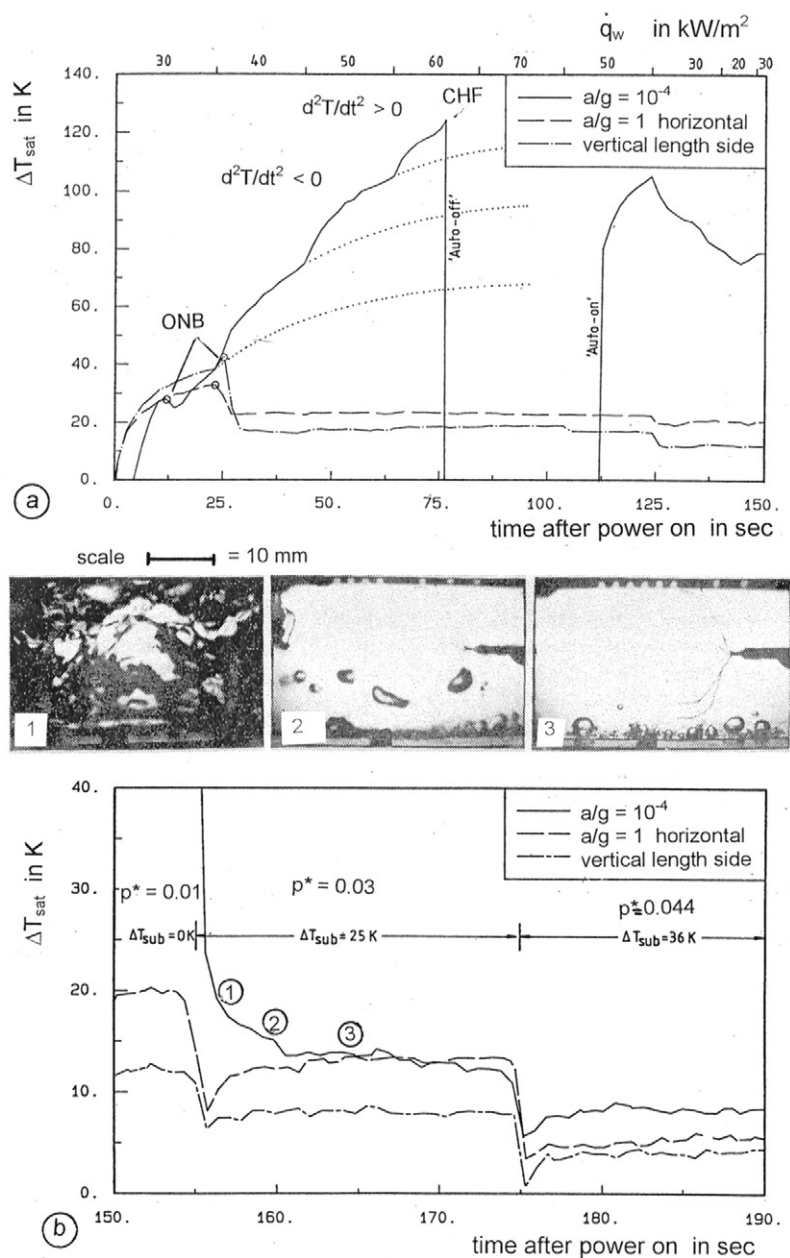
FIG. 31. (a) Development of the mean heater temperature ΔT_{sat} with time at saturation, $p^* = 0.01$ in R113, when the heat flux was increased by 10 kW/m² every 20 sec; see the scale above. (b) Development of the mean heater temperature after increase of pressure in two steps: from $p^* = 0.01$ to 0.03 and to 0.04, corresponding to a subcooling temperature $\Delta T_{sub} = 0.0$, 25.0, 36.0 K.

reacted at further decrease of the power with reduction of the mean temperature, indicating that larger parts of the surface were rewetted. The temperature records at 1-g at both heater orientations indicated normal nucleate boiling with only a small increase of the surface temperature with heat flux, whereas the situation at μ-g under identical conditions revealed a transition from nucleate to film boiling, first with slowly increasing mean temperature and finally at 75 sec with a sudden, unstable, and fast increase to a burnout situation.

Figure 31b demonstrates a transition from saturated to subcooled boiling after a pressure increase and the immediate thermal stabilization of the μ-g system described previously. The heater was nearly completely covered with vapor; at 155 sec the pressure in the fluid was suddenly increased from saturation state at $p^* = 0.01$ to 0.03 (from 0.34 bar to 1 bar), resulting in subcooling of $\Delta T_{sub} = 25$ K, whereas the heat flux was kept constant at 30 kW/m^2. The vapor condensed and the situation turned to steady state subcooled nucleate boiling within 4 sec, whereas the surface temperature of the heater returned almost to the terrestrial reference value with the plate in horizontal position. A further pressure increase at 175 sec to $p^* = 0.044$ (1.5 bar) increased the subcooling temperature to $\Delta T_{sub} = 36$ K and lowered the wall overheat temperature again. But the heater surface temperature was now higher than the temperature at the horizontal position, which is in agreement with the results at subcooling conditions.

Up to now there has been uncertainty about the boiling behavior between direct electrically heated and indirectly heated flat plates under microgravity conditions, because there is a lack of nucleate boiling experiments, performed at saturated conditions and various pressures. The other experiments described hitherto using an indirect heater surface with a heat capacity between the heat source and the boiling surface confirm that even steady-state nucleate boiling is possible under saturated state and microgravity conditions. The effect of this heat capacity — even the relatively thin glass coating is sufficient — where the temperature may oscillate with the bubble departure frequency is discussed in Section XI.B.

VI. Heat Transfer at Subcooled Nucleate Boiling

A. General Observations

Subcooled boiling is characterized by the fact that the ambient liquid temperature is lower than the saturation temperature corresponding to the saturation pressure: $T_{li} < T_{sat}$. To achieve boiling in subcooled liquids, the boundary layer must be heated up above saturation to nucleation tempera-

ture. The subcooled state itself is defined at isobaric condition as the difference between saturation and bulk liquid temperature: $\Delta T_{sub} = T_{sat} - T_{li}$. At subcooled boiling the wall overheating temperature, the heat transfer coefficients related to ΔT_{sat}, and the influence of gravity are similar to those under saturation conditions. However, the bubble dynamics and the mechanisms of heat transport from the heater surface into the bulk liquid are entirely different. Very remarkable is the strong thermocapillary or Marangoni convection, which develops around the bubbles at subcooled boiling, but could never be observed at saturated boiling (see Section XI.C).

B. Subcooled Heat Transfer on Wires

During microgravity experiments the operational program was optimized in order to save time and power. The following operation was proved to be successful: The bulk liquid temperature was kept constant while the pressure was changed. Thus, at the same liquid bulk temperature one saturation and different subcooling states are controlled by pressure as indicated in Fig. 7. From the numerous results only a few can be discussed within the frame of this review. Figure 32 shows results of the heat transfer efficiency on the wire from GAS mission, gained with R134a at a constant liquid temperature of 33.4°C for saturation and various subcooling conditions. Generally, at μ-g
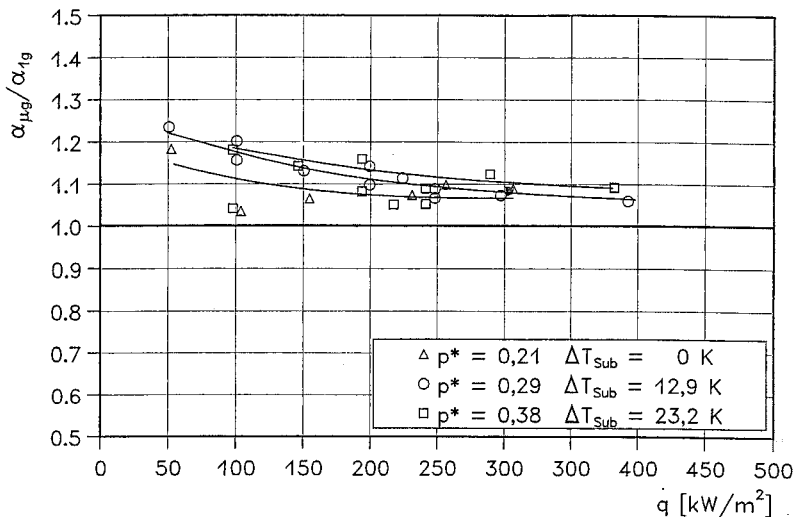
FIG. 32. Efficiency of heat transfer at subcooled boiling on the 0.2 mm wire versus heat flux at constant liquid bulk temperature of 33.4°C (GAS, 1996) [41].
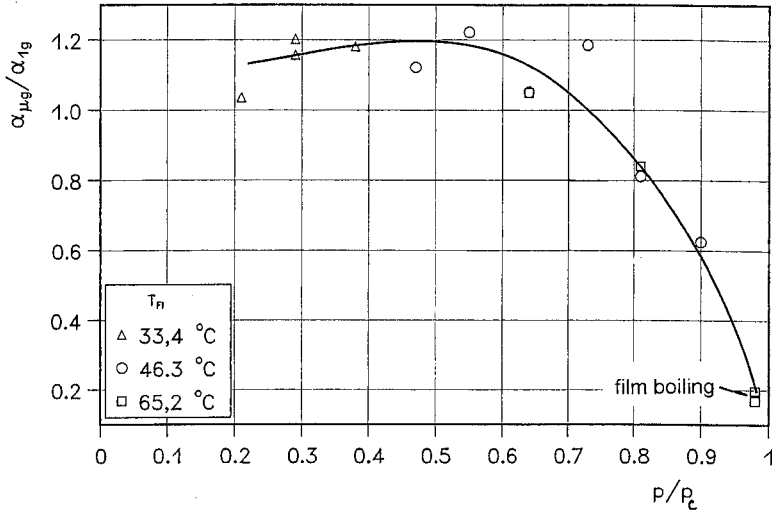
FIG. 33. Efficiency at a constant heat flux of 100 kW/m^2 at various subcooling states versus reduced pressure p/p_c. The data at $p/p_c \approx 0.98$ are under film boiling conditions (GAS, 1996) [41].

an enhancement of the heat transfer coefficient by about 10 to 20% could be observed that diminished with increasing heat flux.

The dependence of heat transfer efficiency on reduced pressure at a constant heat flux of 100 kW/m^2 and different subcooling conditions is shown in Fig. 33. Up to a pressure of $p^* \approx 0.5$ there is an increasing tendency with a maximum of about 20%, followed by a decrease with the approach to $p/p_c = 1$. At reduced pressures of $p^* = 0.8$ and 0.9 with subcooling of 44.6 and 49.5 K, there is still nucleate boiling, but with a small wall superheat of less than 2 K. At the highest pressure close to critical, it is with $p^* \approx 0.98$; the boiling mode is film boiling with a reduction of the efficiency value down to 0.2. The ratio of the heat transfer coefficients $\alpha_{sub}/\alpha_{sat}$, each one related to the wall superheat ΔT_{sat} at a constant heat flux of 100 kW/m^2, in Fig. 34 shows an increase with subcooling and indicates only a small dependency on gravity.

C. SUBCOOLED HEAT TRANSFER ON SMALL SURFACES

In Fig. 35 subcooled boiling curves are shown for a spherical heater of 1.4 mm diameter in the fluid R123 from the LMS mission of 1996 [64]. As ordinate, the difference $\Delta T_w = T_w - T_{li} = \Delta T_{sat} + \Delta T_{sub}$ has been selected so
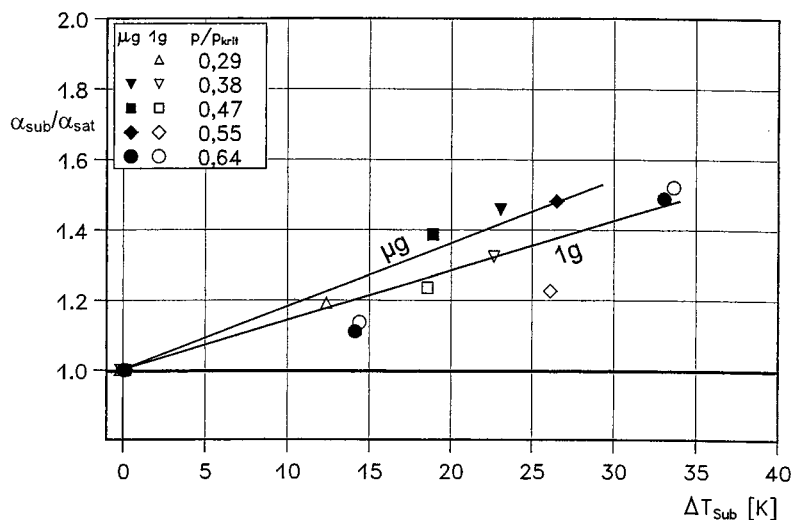
FIG. 34. Ratio of heat transfer coefficients subcooled to saturation versus subcooling evaluated for 1-g and μ-g (GAS, 1996) [41].
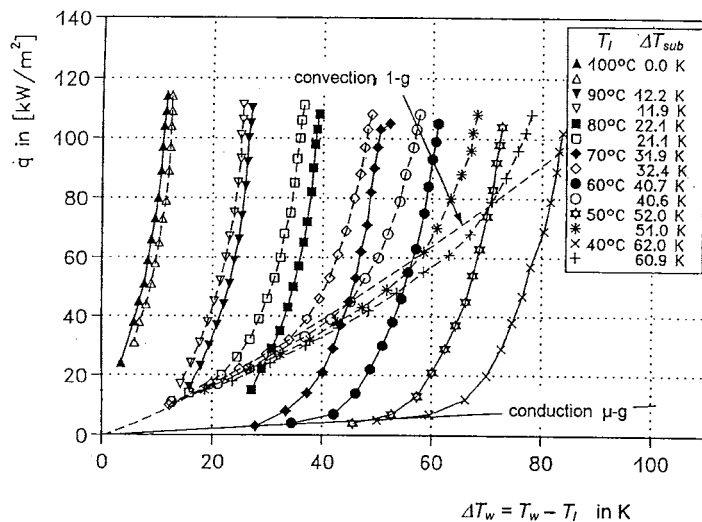
FIG. 35. Subcooled boiling at a spherical heater of 1.4 mm diameter, fluid R123, at a constant liquid pressure $p^* = 0.22$. [64].

that the different subcooling curves will not merge into each other, because the values of ΔT_{sat} are rather close together. These boiling curves are obtained during a stepwise decrease of the heat flux. It may be seen that the boiling curves merge into the curve for natural convection at 1-g [Eq. (13)] and for conduction at μ-g [Eq. (14)], respectively. Because of convection, the deactivation of the nucleation sites at 1-g begins at higher heat fluxes than at μ-g and ends for both approximately at the saturation temperature, where $\Delta T_w = \Delta T_{sub}$. The heat transfer coefficients for natural convection and for conduction concerning small spheres are calculated with the Nusselt relation:

$$Nu = Nu_o + 0.668 \cdot (2/\pi)^{1/4} \cdot [1 + (2 \cdot Pr)^{-9/16}]^{-4/9} \cdot Ra^{1/4}. \qquad (13)$$

At microgravity with $Ra \approx 0$, heat transfer is dominated by heat conduction, which for small spheres has the value $Nu_o = 2$, and means that the heat flux depends linearly on the temperature difference ΔT_w,

$$\dot{q} = \frac{2 \cdot \lambda}{D_H} \cdot (T_w - T_f), \qquad (14)$$

where D_H is the diameter of the heater. With increasing heat flux onset of boiling would occur on the line according to Eqs. (13) and (14), but at a superheat far above saturation; below that, all nucleation sites are deactivated. Figure 36 demonstrates the heat transfer efficiency versus subcooling
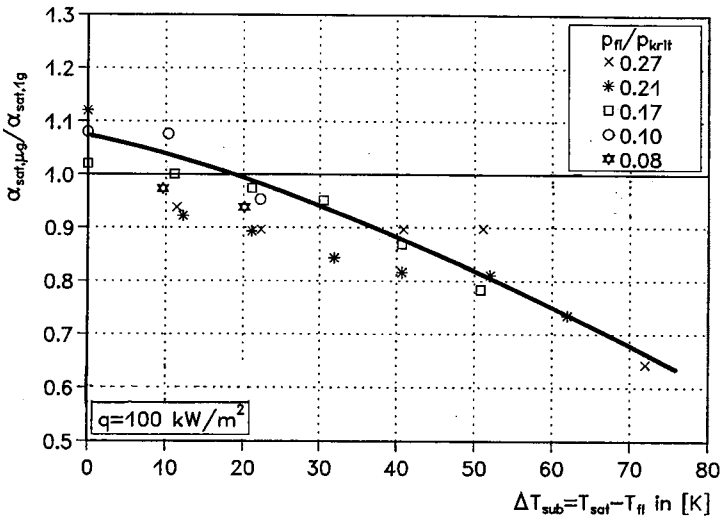
FIG. 36. Heat transfer efficiency versus subcooling at 100 kW/m^2 and various pressures.
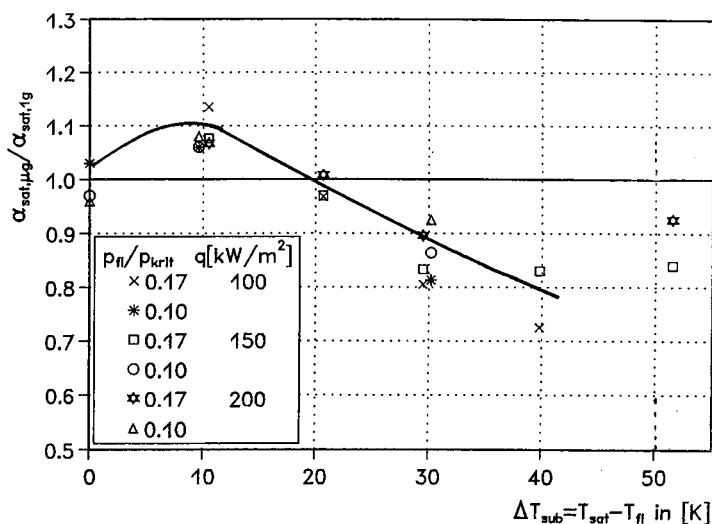
FIG. 37. Heat transfer efficiency versus subcooling at various heat fluxes.

for a spherical heater element of 1.4 mm diameter and a constant heat flux of 100 kW/m^2, and Fig. 37 for various heat fluxes and a circular plate of 1 mm diameter. At low subcooling the efficiency is above 1 and decreases with increasing subcooling. The heat transfer coefficients α_{sat} are referred to ΔT_{sat}.

D. Direct Electrical Heated Flat Plate

Zell [87] performed TEXUS experiments on subcooled boiling with R113 in the mid-1980s. He used the same facility and heater mentioned in Section V.C. The subcooled state was established by increasing the pressure, but keeping the liquid bulk temperature constant. A typical series of pictures with onset of boiling at $\Delta T_{sub} = 17$ K is shown in Fig. 38. The photos were obtained with a 16-mm cine film camera at a frame rate of 100 Hz. After onset of boiling a hemispherical shaped bubble developed, which covered the heater in less than 0.1 sec. The rapid growth of the bubble pushed the superheated boundary layer aside, thus accumulating superheated liquid at their edge. In this accumulated superheated liquid, preferred new small bubbles were easily generated. The thermocapillary flow induced at the interface of the large bubble carried these small bubbles along to the top where they coalesced with the large one.

Lee and Merte [31, 33] observed similar bubble roughness in drop tower experiments at NASA Glenn with slightly subcooled R113 at a heater superheat of 70 K. The photos reveal that the liquid–vapor interface of the
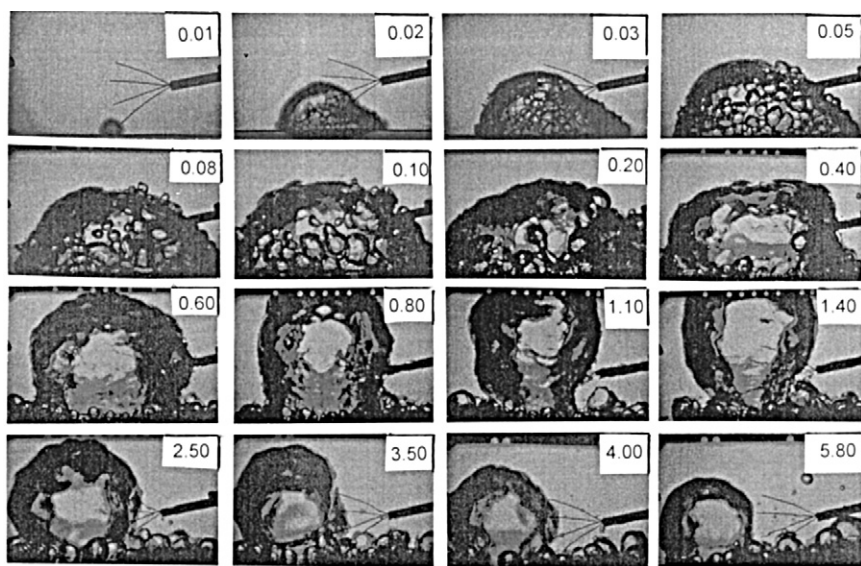
FIG. 38. Photo sequence of onset of boiling at subcooled condition, fluid R113, $\Delta T_{sub} = 17$ K, TEXUS 11, plane plate.

rapidly growing bubble becomes wrinkled and corrugated, which the authors explain as a mechanism of Rayleigh–Taylor instability.

The temperature development during the boiling sequence shown in Fig. 39 reveals that after onset of boiling (ONB) the temperature dropped within 1.4 sec while the large bubble was still attached to the heater surface. Four thermocouples were mounted at distances of about 1.5, 4, 8, and 15 mm above the heater. They were all inside the large bubble and indicated saturation temperature for few seconds. After that the thermocouple close to the surface, T_1 oscillated somewhat below saturation, whereas that with the largest distance, T_4, returned to the temperature of the liquid. In Fig. 40a–d the further temperature development with experimental time and heat flux is demonstrated. The photos show the development of relevant bubbles. At heat fluxes of 30 kW/m² the mean temperature of the heater surface remained at a constant level close to that at the 1-g reference situation. At 140 sec experimental time the heater was switched to 40 kW/m²; its temperature slowly increased by about 0.1 K/sec. At 50 kW/m² the increase was about 0.5 K/sec, but with a declining gradient. At each new power step initiated after every 20 sec a temperature increase with decreasing slope was registered. From the photos it can be observed that at each power step two larger bubbles were always formed. The top of the bubbles
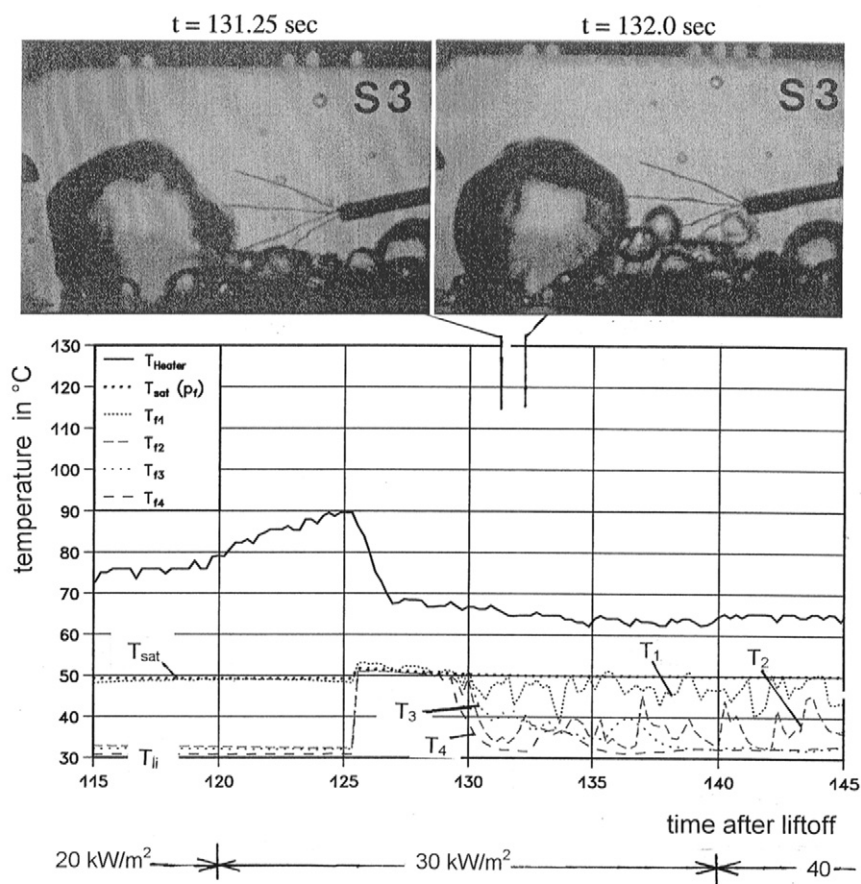
FIG. 39. Temperature recorded at onset of boiling corresponding to Fig. 38; the thermocouples in the liquid are $T_1 = 1.5$ mm, analogs 4, 8, and 15 mm distant from the heater surface.

reached up into the subcooled temperature domain where the vapor condenses, and the heat was removed from the bubble interface by self-induced thermocapillary convection and transported into the bulk liquid. The large bubbles were fed with vapor by evaporation on the base and by coalescence with the smaller bubbles around, which moved to the large bubbles. The size of these large bubbles adjusted itself according to the succession of the heat transfer mechanisms. If the large bubbles had grown to a size where they touched each other and coalesced, then the remaining large bubble would have extended further into the subcooled region where
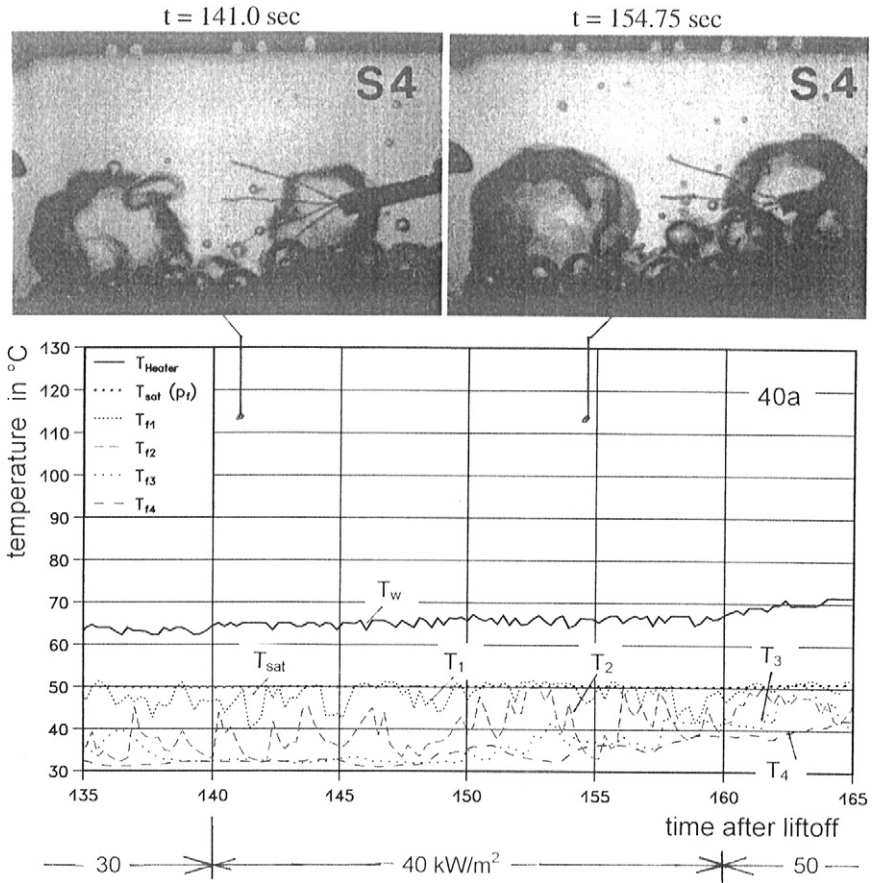
FIG. 40a. Continuation of the temperature development from Fig. 39 with increasing power, and appropriate development of bubbles: (a) at 40 kW/m² heat flux.

the vapor recondensed and caused the bubble to shrink. This process can be maintained as long as subcooled liquid is available. The rising mean surface temperature indicates a slow enlargement of dry areas below the large bubbles. If two large bubbles coalesce the mean temperature drops, which happened at 190 sec (Fig. 40c); all thermocouples were inside the large bubble and registered saturation temperature. The short drop of the mean heater temperature was recovered after less than 5 sec to the former level. The thermocouple in 15 mm distance returned below saturation. At 200 sec the power was switched to 70 kW/m² and 5 sec later two large
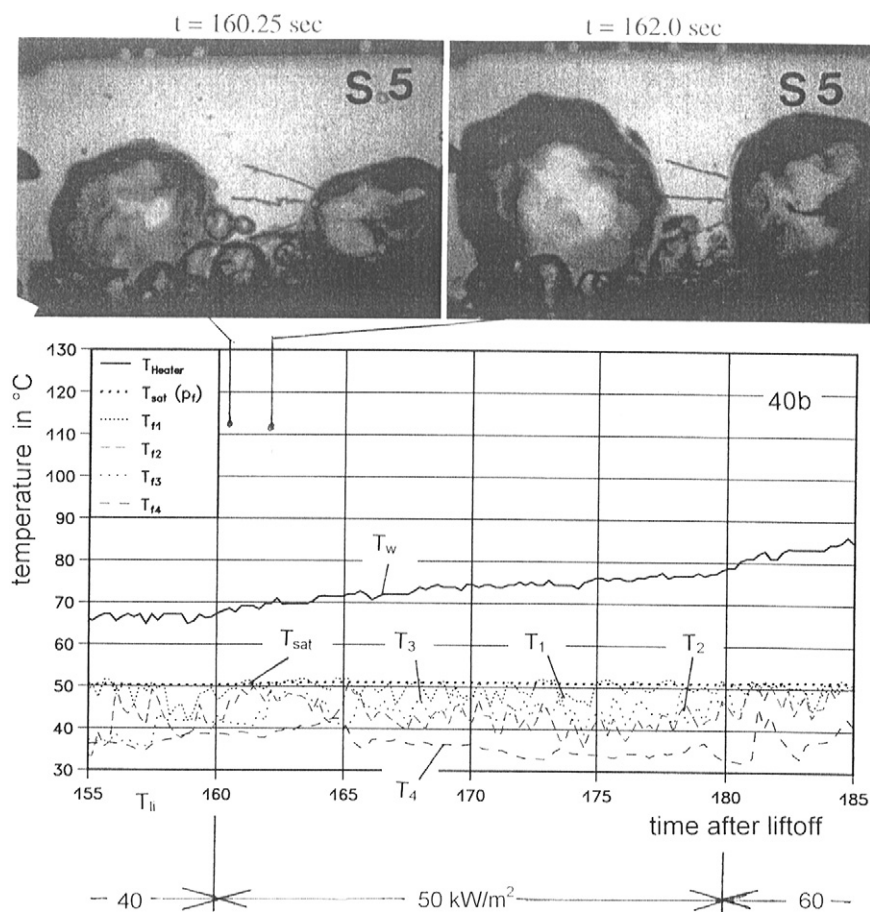
FIG. 40b. Continuation of the temperature development from Fig. 39 with increasing power, and appropriate development of bubbles: (b) at 50 kW/m².

bubbles coalesced again; see Fig. 40d. Immediately afterwards all thermocouples were located inside the large bubble, and their temperatures rose above saturation temperature. It is interesting that the temperatures of the thermocouples with the largest distances from the heater surface, i.e., 15 and 10 mm, increased by 20 K above the saturation temperature. The latter, being controlled via pressure, increased only by about 2 K during the experimental run because of the increasing vapor mass. This temperature record indicates that with higher heat fluxes, the bubble base area becomes truly dry, and further that the vapor inside the bubble circulates because of
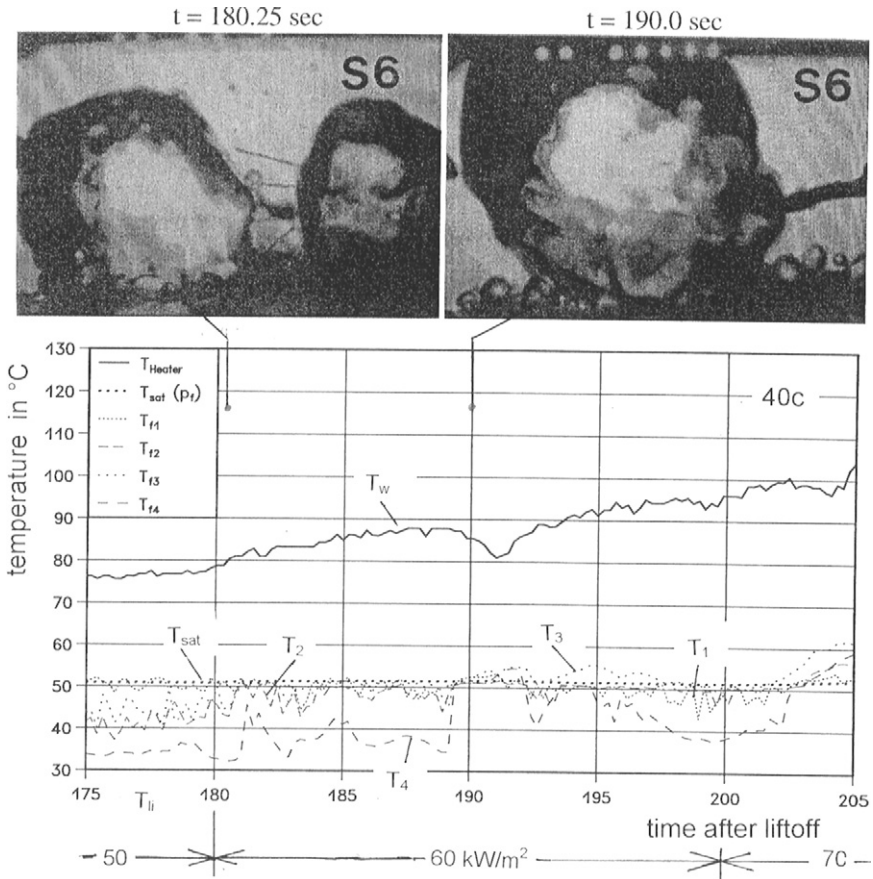
FIG. 40c. Continuation of the temperature development from Fig. 39 with increasing power, and appropriate development of bubbles: (c) at 60 kW/m².

shear forces caused by the thermocapillary convection at the interface liquid-gas and superheats at the dry area. Even after the switch to the next power step of 80 KW/m², the mean heater temperature increased only with a reasonable slow slope and did not show any tendency for a rapid burnout.

In Fig. 41 the heat transfer versus superheat temperature is shown under conditions of saturation and subcooling of 17 and 48 K for 1-g and μ-g experiments. It must be considered that the liquid bulk temperature is constant, but the saturation temperature changes with pressure and with it the amount of subcooling. Therefore, a direct comparison would only be possible for identical saturation pressures. The decrease in the slope of the
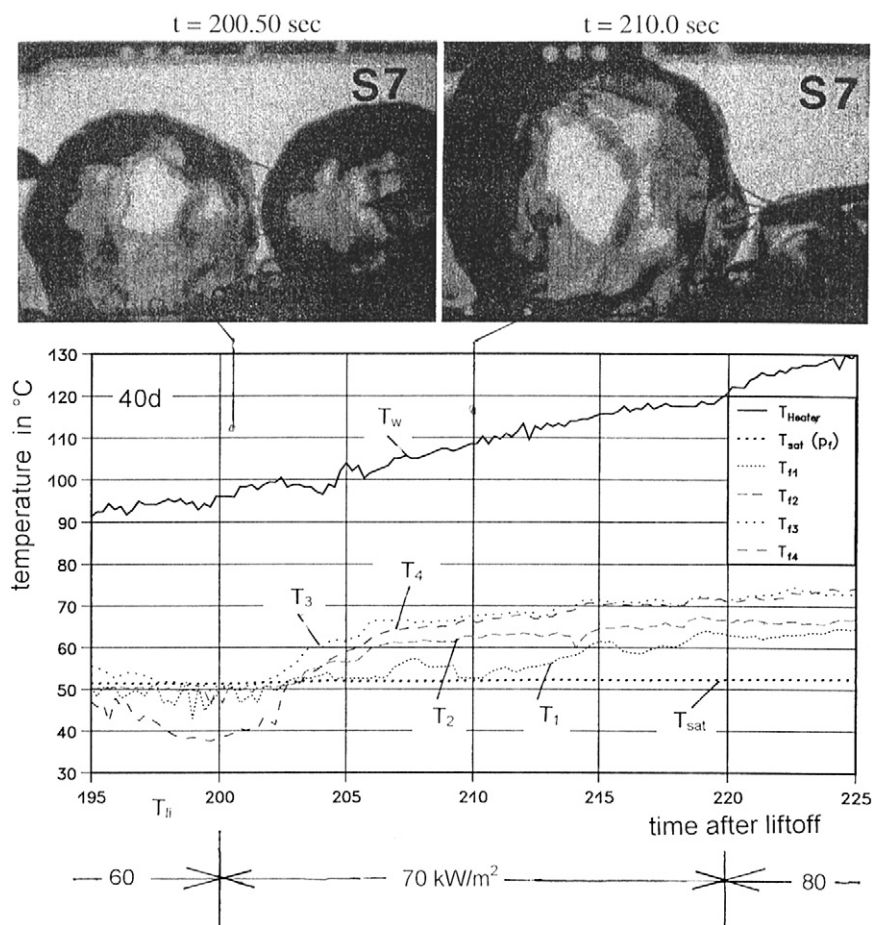
FIG. 40d. Continuation of the temperature development from Fig. 39 with increasing power, and appropriate development of bubbles: (d) at 70 kW/m² the temperatures inside the bubble rose up 20 K above saturation.

boiling curve with increasing heat flux may be due to the increasing extent of the dry area inside the large bubble. In this figure microgravity data from Lee and Merte [32, 34] from GAS experiments are recorded additionally at various subcooling amounts of 22.2, 11.1, 2.7, and 0.3 K, but only for 22.2 and 11.1 K subcooling were three data points available; they do not agree so well with the data of Zell [87]. The discrepancies may be caused by the fact that Zell increased the heat flux step by step, whereas Lee and Merte started the experiment with a high power level of 80 kW/m². Thus, it can be assumed that by the rapid bubble growth the inertia lifted the vapor mass
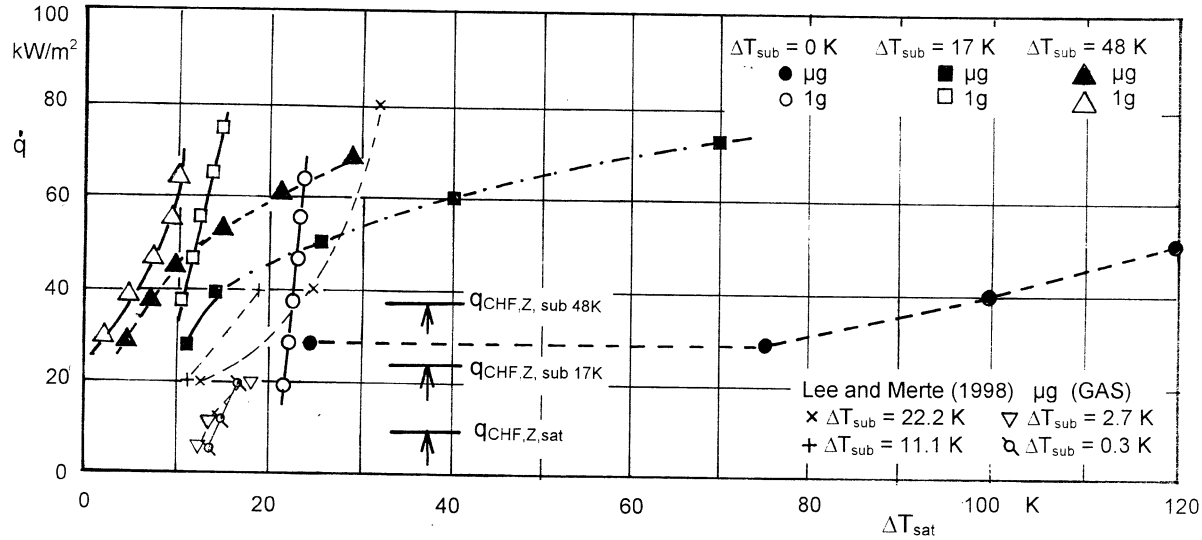
FIG. 41. Heat flux versus wall superheat on the plane plate at various subcooling at 1-g and μ-g, and CHF according to Zuber extrapolated to $10^{-4}g$.

and formed a large bubble under the influence of the surface tension, which hovered at a distance of about 1 mm above the heater surface. Liquid can flow into the gap between the lifted bubble and the heater, where it starts boiling and the small bubbles created are soaked up by the large one. This fact prevented the formation of large dry areas and maintained heat transfer as long as a large bubble was hovering in close distance above the heater surface, collecting the vapor of all the smaller bubbles.

Ohta *et al.* [49] performed boiling experiments on a flat sapphire disk of 50 mm diameter with ethanol as test liquid in a Japanese sounding rocket TR-1A mission. During the experimental run the liquid had an almost constant temperature of 25 to 30°C and liquid subcooling was adjusted from 3 to 95 K. Ohta *et al.* measured local temperatures with small 1 mm^2 resistance sensors directly attached at the boiling surface, and additionally with electrical resistance the thickness of the liquid micro-layer, which was varying between 100 and 10 μm. Unlike our experiment, the coated heating surface was on the opposite side of the boiling surface, and therefore the liquid was indirectly heated, with heat capacity being confined between the heat source and the boiling liquid. This arrangement enables local temperature fluctuations at the heater surface correlated with the growth and departure cycle of the boiling bubbles. These local fluctuating temperature enforces the bubble departure, as described later. Ohta *et al.* observed the immediate formation of a large bubble, which was trapped in the cylinder of 70 mm diameter above the heater and was about 1 mm above the heating surface, soaking up the smaller bubbles continuously generated, and thus sustaining heat transfer.

VII. Critical Heat Flux

The study of critical heat flux (CHF) in microgravity is a difficult task, because of the risk of heater destruction, and thus of failure of the whole mission. Suzuki *et al.* [78] have reported systematically performed CHF measurements carried out on metallic ribbons in 10 to 40 K subcooled water during parabolic flights with an aircraft. In that case they were forced to heat up the ribbon very fast and measure the heat flux at burnout, which was indicated by the breaking of the ribbon. They found the ratio of the experimental maximum heat flux values at μ-g and at 1-g to be between two and four times higher than the CHF values predicted by the theory of Zuber [91] and Kutateladse [26] for a gravity level a/g between 0.01 and 0.04. In laboratory experiments they found additionally that the CHF values are reduced by a factor of 0.6 if the time of heating is extended to at least 100 sec. But these results could not be tested in microgravity, because of the

short period of only 25 sec of reduced gravity available. The experiments further indicated that the CHF values do not depend only on the parameters considered in the relation of Zuber and Kutateladse, but also on the dynamics of the heat transfer process itself.

During normal boiling experiments in microgravity, CHF values are obtained more accidentally than systematically, and with less risk of heater destruction at higher system pressures. Such results were reported by Zell [87], Straub *et al.* [75], Steinbichler [64], and Micko [41]. The general discovery was that the obtained μ-g CHF values are certainly lower than the values at 1-g, but are higher than those predicted by the correlations of Zuber [91] and Kutateladse [26], if these were extrapolated to microgravity conditions. We restrict the comparison with the experimental values to Zuber's relation mostly, because the gravity dependencies of correlations from other authors (for instance, Borishanskij [5], Moissis and Berenson [42], Noyes [46], Katto and Yokoya [24], Haramura and Katto [21], Sun and Lienhard [77], and Yagov and Zudin [86] are nearly identical and result in similar exponents as in Eq. (16) derived from Zuber:

$$\dot{q}_{\text{CHF,Zuber}} = K \cdot \Delta h \cdot \rho_{\text{g}} \cdot [\sigma \cdot g(\rho_1 - \rho_{\text{g}})]^{1/4}. \tag{15}$$

Zuber's relation is based on the hydrodynamic theory of film instability and on experimental results, where K is a factor, sometimes referred to as the Kutateladse number, that depends on the heater geometry and on liquid properties. For an infinite extended flat plate K attains a constant value of 0.16 according to Kutateladse, and of $\pi/24 = 0.130$ after Zuber. Under identical conditions the gravity dependence is derived as:

$$\frac{\dot{q}_{\text{CHF,Z},\mu\text{g}}}{\dot{q}_{\text{CHF,Z,1g}}} = \left(\frac{a}{g}\right)^{1/4}. \tag{16}$$

This gravity influence predicts a reduction of CHF of about 0.1–0.03 if the gravity level is reduced to 10^{-4}–$10^{-6}g$. The calculated CHF values for the TEXUS experiments on the flat plate are marked in Fig. 41, where for subcooled conditions the subcooling extension of Zuber *et al.* [92] was considered. These calculated values are lower than the heat flux values at which onset of boiling occurred. Even steady-state nucleate boiling values are more than two to three times higher than the predicted CHF values. The transient increase of the temperature in Figs. 39 and 40a–d, caused by a slow increase of the dry area on the bubble base, may suggest an asymptotic rise to a steady-state value and a moderate transition to film boiling. The TEXUS results are in reasonable agreement with those of Suzuki *et al.*, revealing that the influence of gravity in Eq. (16) should be considered by an exponent of about 0.1–0.15.

For finite heaters the CHF value depends on the geometry of the heater. Many papers were devoted to these geometry dependences (see Carey [8], p. 252). A typical dimension that influences hydrodynamic instability is provided by the Laplace coefficient L of Eq. (9). For small tubes and wires with radius R, Lienhard and Dhir [35] proposed the use of a dimensionless radius, corresponding to the square root of the Bond number Bo:

$$R' = \frac{R}{L} = R \cdot \left(\frac{g \cdot (\rho_1 - \rho_g)}{\sigma}\right)^{1/2} = \sqrt{\text{Bo}}. \tag{17}$$

With Eq. (17) the Zuber correlation is extended to

$$\dot{q}_{\text{CHF,wire}} = \dot{q}_{\text{CHF,Zuber}} \cdot 0.94 \cdot (R')^{-1/4}, \tag{18}$$

valid in the range

$$0.15 \leqslant R' \leqslant 1.2.$$

Some recent data on wires from the GAS experiment by Micko [41] are compared in Fig. 42 with the relations of some authors at 1-g and extrapolated to 10^{-4}g. The 1-g data can be best represented by the correlation of Haramura and Kato [21], while the μ-g data are anywhere in the middle between the calculated 1-g and $10^{-4}g$ values. These data, together with former data provided Weinzierl [83] and Zell [87] in KC-135 experi-
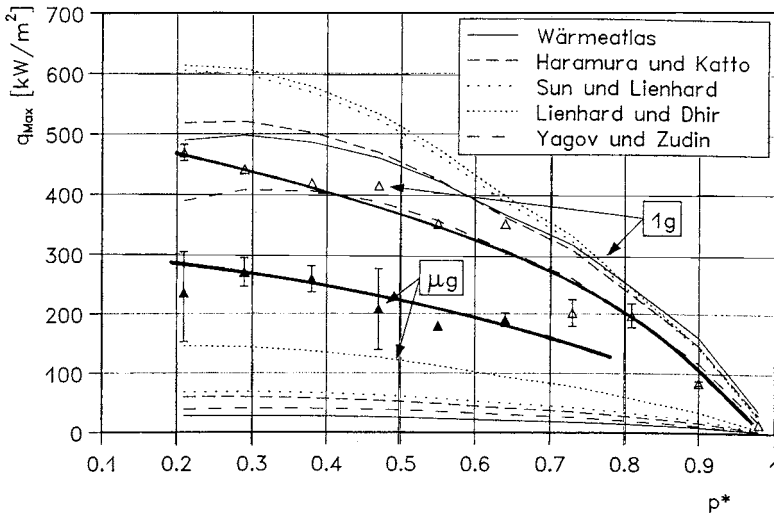
FIG. 42. Critical heat flux values obtained on wires in GAS mission compared with various relations [41], at saturation state.
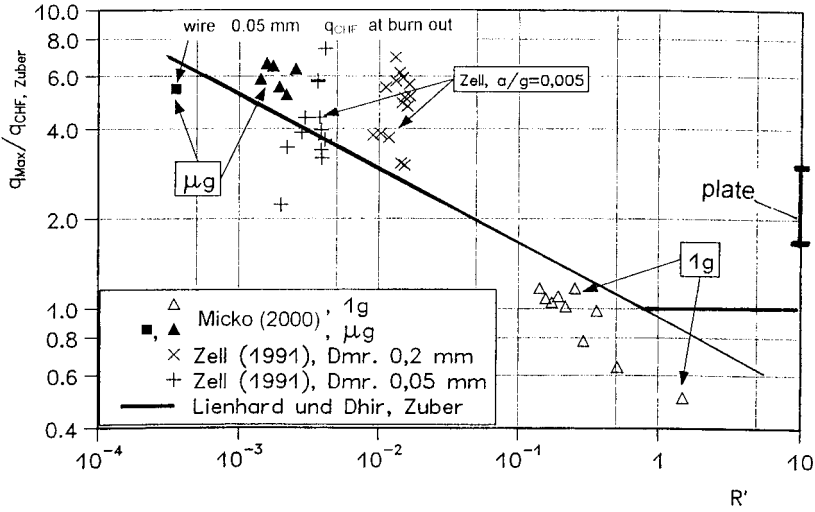
FIG. 43. Critical heat flux data obtained on wires compared with Eq. (18), at saturation state.

ments are plotted in Fig. 43. The range of the dimensionless radius is extended by three decades above the originally set limit. It may be seen that a range limitation is not necessary and that the experimental data are even higher than those predicted. However, it must be considered that R' has been calculated with $a/g = 10^{-4}$, whereas in reality this ratio may be range from 10^{-4} to 10^{-6} in the Shuttle, shifting the data by a factor of 0.1 to smaller values of R'.

The influence of subcooling states on CHF at wires is demonstrated in Fig. 44 as a function of reduced pressure and is further compared with the data at saturation from Fig. 42. At subcooled boiling both the data at 1-g and at μ-g are higher than at saturation, and the difference between the subcooled 1-g and μ-g data is lower than at saturation. This behavior may be explained by the mechanism of thermocapillary flow, which acts very effectively at subcooled boiling conditions.

In Fig. 26 boiling curves of a small hemispherical thermistor are presented. Some of these curves show a maximum value for the heat flux which is the CHF value for this configuration. Concerning small spherical heaters, Ded and Lienhard [12] proposed for the critical heat flux the correlation

$$\frac{\dot{q}_{max,sphere}}{\dot{q}_{max,Z}} = 1.734 R'^{-1/2}, \qquad \text{valid for } 0.15 \leqslant R' \leqslant 4.26. \qquad (19)$$

Together with Eq. (15), the gravity dependence is eliminated. This
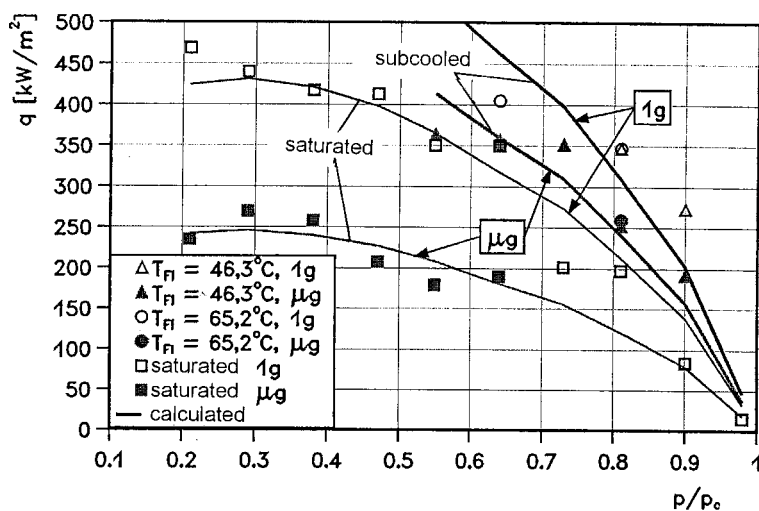
FIG. 44. CHF values compared at saturated and subcooled states and at 1-g and μ-g conditions. GAS mission (1996) [41], on wire 0.2 mm diameter.

adaptation to small spheres disagrees with the experimental results for a sphere of 0.26 mm dia. The terrestrial data with $R' \approx 0.13$ are at the limit of the validity range, but the values calculated with Eq. (19) are higher by a factor 1.4 to 1.7 compared to the experimental data at 1-g. A comparison with the microgravity data at identical conditions showed a small deviation of only $(\dot{q}_{\mu g}/\dot{q}_{1g})_{max} \approx 0.85$; thus, a small gravity dependence still prevails (see also Section XI.D).

In Fig. 45 a quasi-steady situation of transition boiling is shown on the 0.2-mm wire during the GAS experiment with film boiling on the left and nucleate boiling on the right side. The overall situation is quasi steady; however, the location of the transition where the two boiling regimes lie against one another fluctuates and moves forward and backward on the wire collecting the small vapor bubbles into the large ones.

VIII. Film Boiling

Film boiling happens when the temperature of the heater surface exceeds the CHF value. The heater surface becomes covered with a vapor film, which isolates it largely from the cooling liquid. Heat and mass transport from the heater surface to the liquid interface is governed by heat conduction, and convection and at higher temperatures is progressively supported
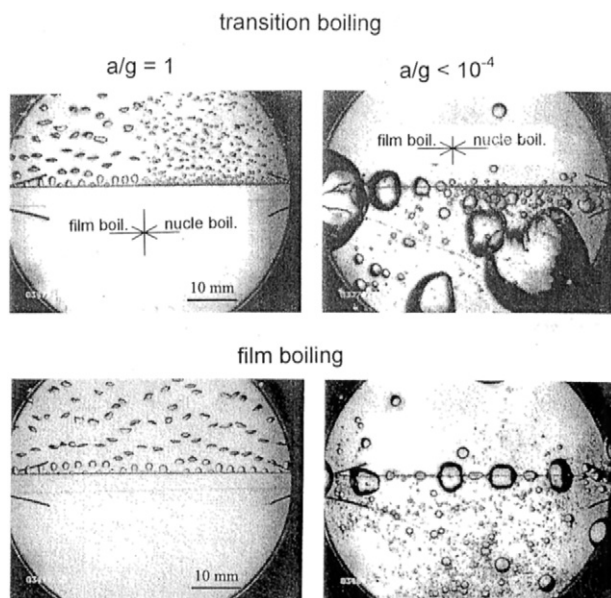
FIG. 45. Photos of transition and film boiling compared between 1-g and $10^{-4}g$ under saturated condition of R134a at $T_{sat} = 33.4°C$ and $p = 8.5$ bar, on a wire 0.2 mm dia.

by radiation. In a microgravity situation the convection transport in the vapor between heater and liquid interface is prevented to a large extent, as the convection of vapor through the surrounding liquid by buoyancy has broken down completely. Therefore, we may raise the question: Is film boiling possible at all?

Transient film boiling data measured in short-term drop towers are reported by Siegel [59], Steinle and Schwartz [63] on wires, and by Merte and Clark [40] on spheres and more recently in experiments with a longer period of microgravity by Weinzierl [83], Zell [87], Straub et al. [75], and Micko [41]. As shown in Fig. 46, they indicate that some existing correlations may obviously be extrapolated to lower gravity values at least down to $a/g \approx 10^{-2}$. Up to this limit the gravity dependence can be expressed by the heat transfer ratio with the exponent n in Eq. (11), taking the value $n = 0.25$ from the correlation of Bromley [7], $n = 0.33$ from that of Frederking and Clark [16], and attaining best fit with $n = 0.16$ from the correlation of Pitschmann and Grigull [52]. Although these correlations are not fitted on microgravity data, they are based on the concept of Nusselt's film theory, which is why they describe the physical mechanisms and, with that, the influence of gravity much better than the correlations for nucleate
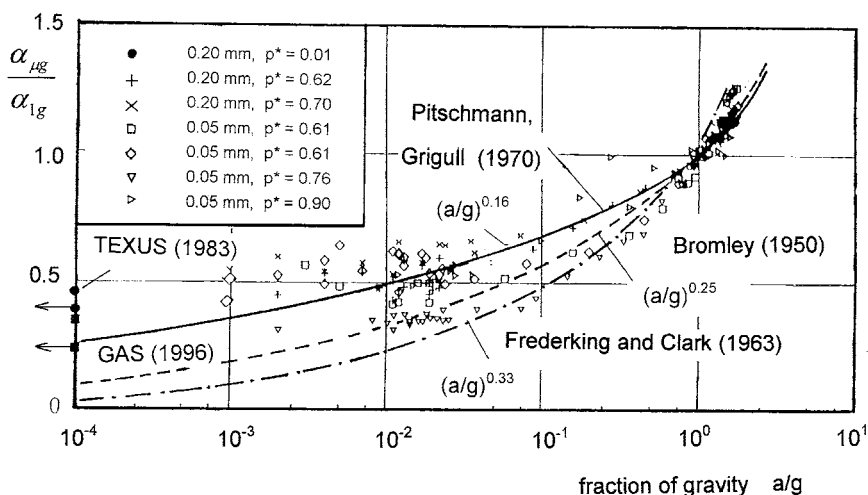
FIG. 46. Gravity dependence of film boiling on wires, experimental data compared with correlations.

boiling. As shown in Fig. 46, these relations can be extrapolated, fitting the data quantitatively well down to $a/g \approx 10^{-2}$, where the heat transfer ratio attains a value of about 0.5. For gravity values $a/g \leqslant 10^{-4}$ data are available from TEXUS experiments [83] and from GAS [41]. These data provide heat transfer ratios between 0.46 and 0.25, and they may be placed between gravity values of 10^{-4} to $10^{-6}g$.

For cylinders and wires at 1-g, buoyancy caused the film surrounding the wire to develop unsymmetrically, whereas at μ-g, because of Kelvin–Helmholtz instability (Fig. 47) and surface tension, the film formed a chain of alternating larger and smaller bubbles connected to each other by a small vapor hose (Figs. 45 and 47). As film boiling heat transfer is proportional to the reciprocal thickness of the vapor layer, these hoses and small bubbles contribute most to it. Because of the difference in the capillary pressure $\Delta \rho = 2\sigma/R$, the vapor flows from the hoses and the small bubbles to the larger ones. Consequently most vapor is collected in large bubbles connected by hoses with a chain of smaller bubbles, which decrease in size the farther they are from the large one. In Fig. 48 a sequence of film boiling dynamics is shown, where the large bubbles oscillate along the wire collecting the smaller bubbles and enhance the heat transfer by that means. Sometimes the wire inside the large bubble was even glowing red, while the mean heater temperature was much lower. It is obvious that microgravity film boiling in a pool in which saturated liquid conditions prevail cannot be
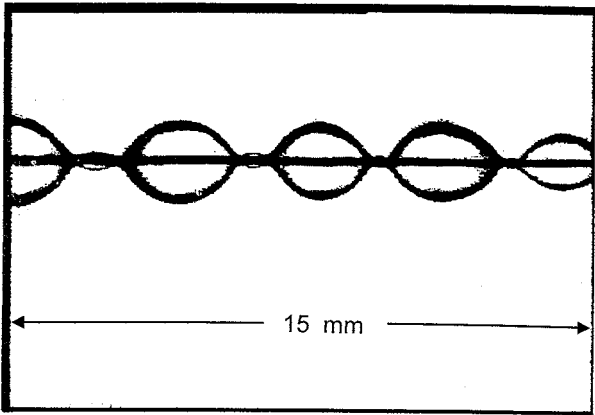
Fɪɢ. 47. Kelvin−Helmholtz instability in film boiling on a wire, developed immediately after imposition of a high heat flux.
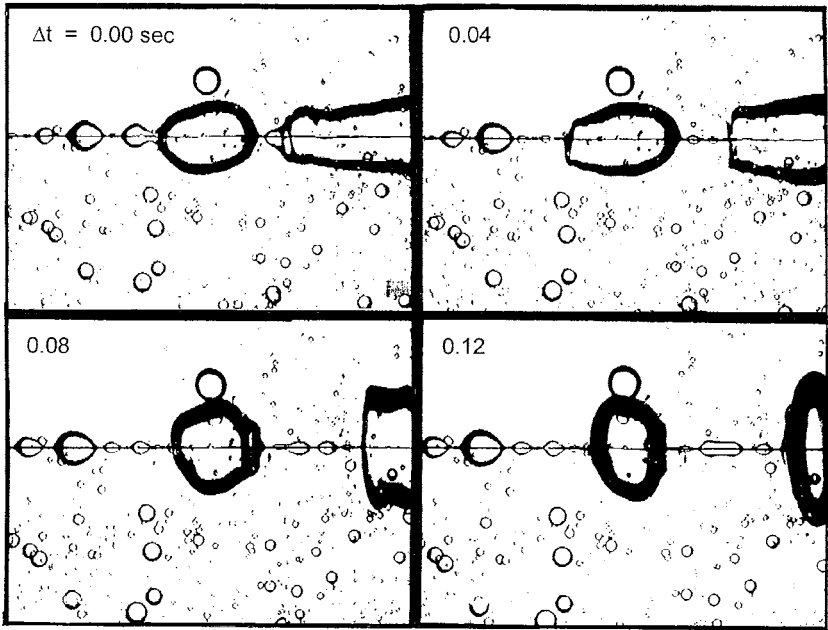
Fɪɢ. 48. Sequence of film boiling after various time intervals on a wire.

maintained over a longer period, because the vapor mass near the heater is continuously increasing, and to date no mechanism is known for vapor transport from the heater.

In contrast, film boiling can well be maintained in a subcooled liquid, because the vapor condenses predominantly inside the larger bubbles. Their size adjusts itself according to the heat and mass balance between evaporation at the liquid–vapor interfaces of the vapor hoses and small bubbles and condensation on top of the large bubbles. Thermocapillary convection develops there and transports the condensed warm liquid into the ambient liquid, and simultaneously carries cold liquid to the interface. Zell [87] fitted the heat transfer ratio of subcooled film boiling from KC-135 data with the relation $\alpha_{\mu g}/\alpha_{1g} = (a/g)^{0.25}$. Because of the thermocapillary flow at the liquid–vapor interface, the assumption seems to be justified that subcooled film boiling can be maintained over a longer period even in microgravity.

IX. Conclusions Drawn from Microgravity Boiling

In contrast to the existing concepts and correlations for nucleate pool boiling, the insight from microgravity experiments is that the influence of gravity on nucleate boiling heat transfer is much less than was hitherto generally expected, although the observed bubble dynamics at microgravity differ widely from that revealed by terrestrial experiments. The critical heat flux is lower than at 1-g, but considerably higher than would be predicted from the extrapolation of well-acknowledged correlations. Saturated film boiling can be maintained for a limited period only, whereas in subcooled film boiling a transport mechanism is established by condensation at the vapor side and thermocapillary flow at the liquid side of the interface. In nucleate pool boiling under a high quality of microgravity, the bubble dynamics is not at all supported by buoyancy, but the heat transfer intensity is to a large extent identical to the terrestrial case, if high heat flux values, close to CHF, are excluded from this consideration. We may therefore conclude that the predominant heat transfer mechanisms in nucleate boiling region are identical, and the following classification of the nucleate boiling process seems to be justified:

Primary mechanisms determine the nucleate boiling heat transfer. These mechanisms are so powerful that they are to a large extent independent of gravity, and probably more or less independent of other external forces as well. The heat transfer for both cases — saturated and subcooled boiling—is to a large extent determined by the latent heat of evaporation at the bubble's interface. The evaporation is induced by the superheated liquid boundary layer around the bubble, but results mainly from the heat transferred

through the thin wedge-shaped liquid microlayer at the bubble base, which is formed between the heater surface and the bubble interface by bubble growth.

Secondary mechanisms provide the mass transport, transferring the latent energy by means of the vapor or by hot liquid carried with the bubbles. Under terrestrial conditions this transport is caused mainly by buoyancy or other external forces of influence. In microgravity the transport of vapor and warm liquid is initiated by the bubble dynamics itself, resulting from bubble growth, bubble coalescence, and momentum-induced transfer by them into the liquid. Additionally, in subcooled boiling, energy is transported as enthalpy from the bubble interface to the bulk liquid by thermocapillary convection. Inside the bubbles a heat pipe effect develops with evaporation at the bubble base, vapor transport through the bubble, and condensation at the top. Outside the liquid interface a thermocapillary flow is initiated, which transports the warm liquid into the bulk and cold liquid to the interface. Additionally, at high subcooling a pumping effect is observed, which consists of rapid bubble growth followed by immediate condensation of the vapor with bubble collapse.

Most correlations for nucleate boiling heat transfer and critical heat flux are based on secondary mechanisms and are therefore limited to terrestrial application only.

X. Bubble Growth Model

A. DEVELOPMENT OF A MICROWEDGE

Following the preceding statement, a model for the nucleate boiling regime claiming general validity should be based on the primary mechanisms. It is often stated that from the entire heat transfer, a relatively large portion should be attributed to buoyancy convection. But in microgravity this contribution is minimized to an almost negligible quantity, and only microconvection caused by bubble growth and its dynamics are of influence. Therefore, the significant mechanisms for the heat transfer may be identified as the generation of bubbles and their rapid growth in the superheated boundary layer by evaporation.

The importance of the evaporation at a thin microlayer underneath a growing vapor bubble was early described by Cooper and Lloyd [11], Cooper [10], and at the same time by Jawurek [23], based on the experimental observation that the surface temperature of the heater beneath the bubbles was oscillating with the frequency of their departure. Taking into account the viscous effect at the wall, the authors deduced the thickness

of this microlayer as depending on the growth time of the bubble via a simplified momentum equation:

$$\delta = 0.8(v_1 \cdot t)^{1/2}. \tag{20}$$

Plesset and Sadhal [53] postulated that this liquid microlayer is probably not of constant thickness as assumed, but wedge-shaped. They derived the thickness of the liquid layer δ_0 as a function of the lifetime of the bubble t_0 and the radius R_0 at departure as

$$\delta_0 \cong 2 \cdot (3 \cdot v_1 \cdot t_0)^{1/2} \cdot \left(\frac{r}{R_0}\right)^{3/2}. \tag{21}$$

It is obvious that these analytical solutions cannot take into account the complete complexity of the bubble growth; therefore, a short outline of the present concept is presented in the following.

After nucleation has set in, bubble growth is controlled by the evaporation process at the liquid–vapor interface, for which the energy is drawn from the superheated boundary layer by transient heat conduction. Only for the first bubble does the temperature distribution in the boundary layer show a profile of heat conduction, which is already disturbed and undefined for the following. The local heat flux $\dot{q}$ around the growing bubble depends on the temperature gradient in the liquid around its interface,

$$\dot{q}(R, \phi) = -\lambda_{\mathrm{li}} \left(\frac{\partial T}{\partial r}\right)_{r=R,\phi}, \tag{22}$$

where R and the temperature gradient depend on the growth time t and on the temperature field in the thin thermal boundary layer. With the assumption of a spherical bubble, the growth rate follows as

$$\frac{dR}{dt} = \dot{R} = -\frac{\lambda_{\mathrm{li}}}{\rho_{\mathrm{g}} \Delta h} \left(\frac{\partial T}{\partial r}\right)_{r=R,\phi}. \tag{23}$$

During the rapid bubble growth the expanding interface pushes the liquid away (see the sketch in Fig. 49) because the generated vapor volume may be up to three orders of magnitude larger than the liquid volume that was evaporated. The momentum of the extending vapor bubble presses the bubble on to the heater surface; flattens the bubble base, forming an apparent contact angle; and generate a thin wedge-shaped liquid microlayer by viscous effects between its moving interface and the solid heater. All external forces $\Sigma F_{ex,i}$ (such as buoyancy force, shear force, or force due to electrical field), together with the dynamic forces from bubble growth $\Sigma F_{dy,i}$ (such as surface tension force, inertia force, drag force, static and dynamic pressure force, reaction force due to evaporation and condensation kinetics
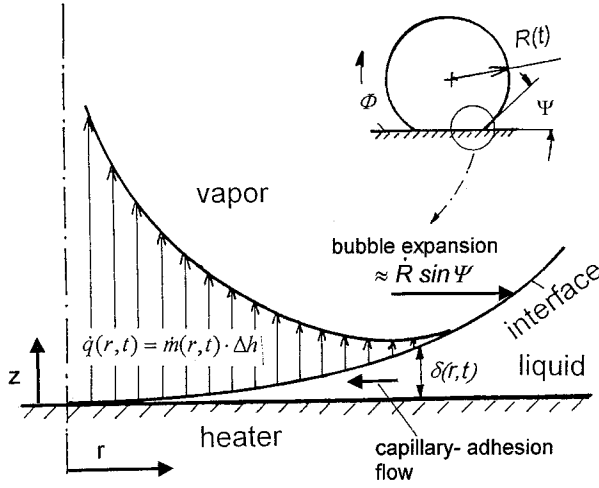
FIG. 49. Sketch of microwedge model underneath a growing bubble.

at the bubble interface [recoil force], or Marangoni force, partly described by Keshock and Siegel [25], Beer *et al.* [2], and Marek [38], influence the growth rate and determine the shape and thickness of this microwedge layer $\delta(r, t)$. The dynamic forces are functions of bubble size $R(t)$, of the growth velocity $\dot{R}(t)$, and the acceleration of the interface $\ddot{R}(t)$, with the consequence that $\delta(r, t)$ must show the following dependence:

$$\delta(r, t) = f\left(R, \dot{R}, \ddot{R}, \sum F_{ex,i}\right). \tag{24}$$

A short time after nucleation has set in, the bubble grows beyond the thin thermal boundary layer of the heater surface, pushing a small part of the boundary layer with it and consuming the superheat in the liquid around. Therefore, it may be assumed that the main heat transport to the bubble takes place across the thin liquid layer $\delta(r, t)$ directly from the heater surface to the liquid–vapor interface, where the liquid evaporates. If for simplification only conduction is assumed in this thin layer, then the local heat flux at the bubble base can be written as

$$\dot{q}(r, t) = \frac{\lambda_{li}}{\delta(r, t)} \times [T_w(r, t) - T_i(r, t)], \tag{25}$$

where λ_{li} is the thermal conductivity of the liquid, and T_i is the temperature at the liquid–vapor interface, which will be a little higher than the satura-

tion temperature to overcome the resistance of the evaporation kinetics. Beneath the center of the bubble the liquid layer becomes very thin; therefore, high heat fluxes may be expected there, which will influence the local wall temperature $T_w(r, t)$, as well as the interface temperature $T_i(r, t)$. The evaporating mass flow rate $\dot{m}_{ev}$ depends on the difference between the interfacial temperature on the liquid side $T_i(r, t)$ and the temperature T_g on the vapor (gas) side of the bubble, and can be determined by the kinetic theory of Hertz–Knudsen,

$$\dot{m}_{ev} = \beta \cdot \rho_g \cdot \sqrt{\frac{k}{2 \cdot \pi \cdot m^*}} \cdot (\sqrt{T_i} - \sqrt{T_g}), \tag{26}$$

where k is the Boltzmann constant, m^* the mass per molecule, and ρ_g the density of the vapor. β is the so-called evaporation coefficient, which considers the dynamic interaction of real gas molecules at the interface in relation to the kinetic theory with idealized assumptions and is of the order 10^{-2} to 10^{-3}, as Winter [85], Picker [50], and Picker and Straub [51] have determined from experiments in microgravity. For small bubbles with large curvature K the vapor temperature inside the bubble depends not only on the bulk liquid pressure, but also on the capillary pressure, which can be determined with the Clausius–Clapeyron equation if a homogenous temperature distribution T_{sat} around the interface and in the vapor T_g is assumed:

$$T_g = T_{sat} \cdot \left(1 + \frac{\sigma \cdot K}{\Delta h \cdot \rho_g}\right). \tag{27}$$

With Eq. (26) the interfacial heat transfer is determined as

$$\dot{q}(r, t) = m_{ev} \cdot \Delta h = \alpha_i \cdot (T_i - T_g), \tag{28}$$

where Δh is the latent heat of evaporation. If we consider the fact that the temperature difference $T_i - T_g$ is small compared to the value of T_g itself, the interfacial heat transfer coefficient α_i can be derived from Eqs. (26) and (28):

$$\alpha_i = \Delta h \cdot \beta \cdot \rho_g \cdot \sqrt{\frac{k}{8 \cdot \pi \cdot m^* \cdot T_g}}. \tag{29}$$

Taking into consideration the thermal resistance in the liquid wedge, Eq. (25), and the interfacial resistance expressed with the heat transfer coefficient, Eq. (29), the heat flux from the wall to the vapor inside is determined

via a thermal balance as

$$\dot{q}(r, t) = \frac{T_{\mathrm{w}}(r, t) - T_{\mathrm{g}}}{\dfrac{\delta(r, t)}{\lambda} + \dfrac{1}{\alpha_{\mathrm{i}}}} = -\lambda_{\mathrm{solid}}\left(\frac{\partial T_{\mathrm{w}}}{\partial z}\right)(r, t)_{z=0}, \qquad (30)$$

where T_{g} may be considered with Eq. (27). The right side of Eq. (30) represents the energetic coupling with the solid heater wall. By numerical integration of $\dot{q}(R, \phi)$, Eq. (22), and considering $\dot{q}(r, t)$ of Eq. (30) over the appropriate areas and time, the energy for evaporation $Q(R, t)$ feeding the bubble growth and $R(t)$ can be determined. During the integration the dynamic forces and the external forces also have to be considered; these influence the thickness of the microwedge layer, and with that the heat transfer and the bubble growth itself. Analytical solutions of bubble growth models must be regarded as only rough approximations.

B. Capillary-Adhesion Flow

In observations made during saturated and subcooled boiling experiments (see Sections V.C.2 and VI.D), using TEXUS as carrier in 1986, Zell [87] and Straub *et al.* [75, 76] showed that bubbles at microgravity remain attached to the heater surface for a longer time and grow to a larger size than under terrestrial conditions. That indicates that liquid is probably supplied beneath the bubble into the microwedge toward the center of the bubble; otherwise the center would dry out faster, and consequently the mean wall temperature would increase more rapidly. Additionally, another observation was made, namely, that small bubbles are moving along the heater surface toward the large one, where they merge. This motion must be caused by a liquid flow along the heater surface toward the large bubble, which supplies the mass for the strong evaporation. This may just happen when the liquid velocity caused by the bubble growth and its expansion has slowed down. An explanation for that flow could be provided by capillary-adhesion forces. Straub [70, 71] reported the model by Wayner [81, 82] and Stephan [67], which attributes the evaporation at the contact line in heat pipes to the three-phase line of boiling bubbles being attached to the surface longer at microgravity. Numerical solutions of heat and mass transport in this microwedge model, based on Wayner's model, have been presented by Lay and Dhir [29, 30], Stephan and Hammer [68], Hammer [20], Son and Dhir [61], Fujita and Bai [18], Son *et al.* [62], and Qiang and Fujita [55].

Because of the high heat flux beneath the center of the bubble, the liquid film becomes thinner and thinner; finally, only a layer of few molecules will be adsorbed at the solid surface and a dry, "adiabatic" spot in the center

ought to be assumed. Now the adhesion forces between solid and liquid molecules come into play. They originate from the van der Waals long-range intermolecular forces and are considered with the adhesion or disjoining pressure according to Derjaguin [13] as

$$p_A = -A\delta^{-3}, \tag{31}$$

where A is the dispersion or Hamaker constant, which may have a positive or negative value depending on the combination of the liquid–solid material and whether or not the liquid wets the surface. In the case of complete wetting, A is about 10^{-20} J.

The strong evaporation causes a momentum change at the interface due to the density change between liquid and vapor, entailed by the related velocity change. A reaction force or recoil pressure is thus exerted on the bubble interface, which presses the bubble to the heater surface. At the interface the gas and liquid mass flow rates must be equal:

$$\rho_g \cdot w_g(r, t) = \rho_1 \cdot w_1(r, t) = \dot{m}_{ev}(r, t) = \frac{\dot{q}(r, t)}{\Delta h}. \tag{32}$$

Thus, the recoil pressure effect on the interface is

$$p_R(r, t) = \rho_g \cdot w_g^2 - \rho_1 \cdot w_1^2 = \rho_g \cdot w_g^2 \cdot \left[1 - \frac{\rho_g}{\rho_1}\right] = \frac{1}{\rho_g} \cdot \left(\frac{\dot{q}(r, t)}{\Delta h}\right)^2 \cdot \left(1 - \frac{\rho_g}{\rho_1}\right). \tag{33}$$

If for a first approach the hydrostatic pressure and other dynamic pressures are neglected, the pressure difference at the interface between liquid and vapor is related as

$$p_1(r, t) - p_g = -\sigma \cdot K(r, t) - \frac{A}{\delta(r, t)^3} + \frac{1}{\rho_g} \cdot \left(\frac{\dot{q}(r, t)}{\Delta h}\right)^2 \cdot \left(1 - \frac{\rho_g}{\rho_1}\right). \tag{34}$$

This pressure difference together with external forces and the other dynamic forces due to bubble growth leads to a deformation of the bubble base and to a flow into the microwedge. The liquid will be superheated along the heater surface and thus support evaporation. The curvature $K(r, t)$ of the bubble interface is related to the thickness of the microwedge layer δ according to the rules of differential geometry [68] as

$$K = \frac{\delta''}{(1 + \delta'^2)^{3/2}} + \frac{\delta'}{r(1 + \delta'^2)^{1/2}}, \tag{35}$$

where r is the distance to the axis through the bubble center. δ' and δ'' are the first and second derivatives of the liquid film thickness δ with respect to r.

The liquid flow into the microwedge can be calculated by the Navier-Stokes equations. A simplified solution was proposed by Wayner et al. [81] in the form of a steady-state one-dimensional approximation, neglecting the inertia terms as is usually done in "film theories." With that, the momentum equation is written for the radial direction with the liquid velocity u and the kinematic viscosity v_1 of the liquid:

$$v_1 \cdot \rho_1 \cdot \frac{d^2 u}{dr^2} = \frac{dp_1}{dr}. \tag{36}$$

According to Wayner the boundary conditions are

$$
\begin{array}{lll}
\text{At the wall} & z = 0 & u(r, z) = 0 \\
\text{At the interface} & z = \delta & \left(\dfrac{\partial u}{\partial r}\right)_{z=\delta} = 0
\end{array}
\tag{37}
$$

The boundary condition at the interface $z = \delta$ is only acceptable if the bubble is no longer growing, or if the remaining motion can be neglected, and further if no thermocapillary flow at the interface of the microwedge has to be considered. The integration over a cross-section with the boundary conditions just stated results in the average local velocity

$$\bar{u}(r) = \frac{\delta^2}{3 \cdot v_1 \cdot \rho_1} \cdot \frac{dp_1}{dr} \tag{38}$$

and the averaged mass flow rate at r

$$\dot{m}(r) = \rho_1 \cdot \bar{u}(r). \tag{39}$$

From the mass balance the evaporating mass flow rate in the z-direction can be derived:

$$\frac{d\dot{m}(r)}{dr} = \dot{m}_{\mathrm{ev}}(r) = \frac{\dot{q}(r)}{\Delta h} = -\frac{d}{dr} \cdot (\rho_1 \cdot \bar{u}(r) \cdot \delta(r)) = -\frac{1}{3 \cdot v_1} \cdot \frac{d}{dr}\left(\frac{dp_1}{dr}\delta^3\right). \tag{40}$$

By employing the mass, energy, and momentum equation, a fourth-order nonlinear ordinary differential equation for the liquid film thickness is obtained. Integration of the heat flux equation Eqs. (22), (27), and (30) over the bubble area and the growth time results in the latent energy Q_B accommodated in one bubble before detachment. To achieve the overall heat transfer over the heater area A, it must be multiplied by the number of bubbles N at the area A or the activated nucleation size and the departure or bubble cycle frequency f:

$$\dot{Q} = Q_B \cdot N \cdot f. \tag{41}$$

In order to obtain a numerical solution for the heat and mass transport

around a single bubble, the previously mentioned authors divided the single bubble system into micro and macro regions. The micro region, with a very fine mesh, contains the thin film that is formed underneath the bubble, whereas the macro region consists of the rest of the bubble and the liquid surrounding it. For a rigorous theory the forces caused by the bubble's growth should be evaluated until departure. If the sum of them tends to zero, the bubble is ready to depart. The number N of activation sites depends on the material of the heater and on the quality and temperature of the surface, and it must be evaluated from experiments.

The boundary conditions at the interface of the microwedge may be different from the assumption of Eq. (37), and this is discussed by means of Fig. 50. They can even be time dependent and change with growth time of the bubble itself. According to the numerical analysis of [20, 68] the local heat flux densities in the belt surrounding the adiabatic bubble center are very high, i.e., on the order of 10^8 W/m^2. Also, very high temperature gradients of 10^4 K/m along the interface are predicted from these calcula-
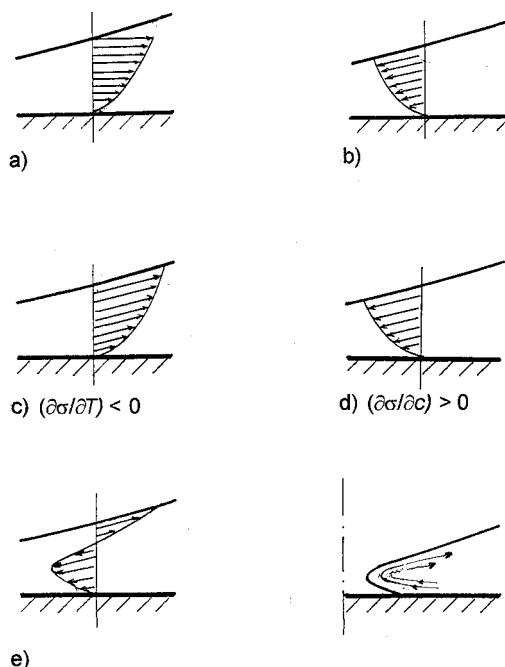
FIG. 50. Possible flow conditions in a cross-section of the microwedge. (a) Bubble growth, (b) capillary-adhesion flow, (c) thermocapillary flow of a pure liquid, (d) thermocapillary flow of mixtures, (e) combination of a and b, or a and d, or b and c, resulting in a recirculating flow.

tions and consequently a strong thermocapillary flow should be initiated along the interface at the microwedge, sketched in Fig. 50c, which is in opposite direction to the capillary-adhesion flow if pure fluids are regarded (Fig. 50b). This thermocapillary flow can block the flow toward the center or can even induce a re-circulating flow as suggested in Fig. 50e. This would transport the supersaturated liquid from the heater surface directly to the liquid–vapor interface and would support the evaporation there. Consequently, in Eq. (25) the heat transfer mode must be changed from a conduction to a convection one. In case of mixtures, the Marangoni flow may be caused by predominant concentration gradients and can be directed toward the bubble center, supporting the flow to it (Fig. 50d), as Abe *et al.* [1] has proposed. If Marangoni flow is considered, the boundary condition at the interface [Eq. (37)] must be changed to the thermocapillary flow condition, with the consequence that the one-dimensional momentum equation, on which the preceding derivation was based, cannot be applied further.

Under terrestrial conditions the lifetime of bubbles attached to the heater surface is very short as compared to microgravity situation. Therefore, it is doubtful whether an adhesion flow can be developed during the rapid growth and against the liquid motion generated by the bubble's growth. However, in microgravity bubbles at saturation grow to a diameter 3 to 4 times larger than at 1-g before they depart. Consequently a bubble carries 3^3 to 4^3 times more energy than a bubble on earth. Its attachment to the surface is extended by the square of the departure diameter, and the bubbles will remain about 10 times longer at the heater surface than at 1-g.

As flow and heat transfer in this microwedge are of paramount significance for the understanding of boiling phenomena under μ-g as well as 1-g situations, careful numerical and experimental studies on single and multiple bubbles will be an important task for future microgravity research.

XI. Bubble and Boiling Dynamics

A. Analytical Bubble Growth Models in Homogeneous Liquid

Analytical bubble growth models in the first very short period are inertia-controlled, followed by the thermal-controlled period, based on transient heat conduction, according to Eq. (22), which can be solved analytically if the boundary conditions around the bubble are known and simple. Generally an infinitely extending fluid of constant supersaturating temperature is assumed. But in reality this simplified condition is not applicable for boiling. As discussed before, the bubble growth problem is

much more complex, calling for a more realistic numerical treatment [60]. The analytical solutions for transient heat conduction are generally of the form

$$R_B = C \cdot (a \cdot t)^{1/2}, \tag{42}$$

where a is the thermal diffusivity of the liquid, and C is a function of the thermophysical properties and the wall superheat, being mostly expressed with the Jakob-number and an empirical or analytical factor:

$$Ja = \frac{\Delta T \cdot c_f \cdot \rho_f}{\Delta h \cdot \rho_g}. \tag{43}$$

For instance, Scriven [57] proposed for small superheating $C = (2 \cdot Ja)^{1/2}$ and for large superheating $C = (12/\pi)^{1/2} \cdot Ja$, which corresponds to the asymptotic solution of Plesset and Zwick [54]. Picker [50] and Picker and Straub [51] investigated the bubble growth experimentally and numerically under microgravity in drop towers and Space Shuttle experiments, where a bubble was initiated by a heat pulse and grew in an overall supersaturated liquid that was generated by a pressure drop. In the experiment a bubble growth period was followed by a shrinking period with re-condensation of the vapor, caused by a sudden increase of the pressure. Figure 51 shows the numerical solution of growth and shrinking to be in good agreement with the experimental results. From the numerical evaluation of 58 experimental growth sequences, Picker achieved the best fitting with a mean value of $C = 2.03$ Ja and for the exponent 0.43, confirming that the analytical model of Plesset and Zwick [54] and Scriven [57] is the best to describe bubble growth in a supersaturated liquid of homogeneous temperature. But it must be emphasized that this analytical model can only be valid under the idealized assumptions of the boundary conditions, which were realizable only in microgravity. It should not be applied to boiling bubbles, because these bubbles grow in a thermal boundary layer in which strong temperature gradients exist, and the bubbles, attached to the wall, are not spherical. Even if they push a part of the thermal layer with them during growth, their tops soon enter the region of saturated liquid, where no further energy supply for evaporation is available. In case of subcooled boiling the bubbles enter a region where vapor condensation is possible.

The growth of a single bubble in microgravity that grew immediately after nucleation at a flat gold-coated heater to a size of about 15 mm radius was observed during the TEXUS 11 mission by Zell [87] in saturated Freon R113 at a pressure of $p^* = 0.01$ (see section V.C.2, Fig. 30). A careful regression analysis of this single growing bubble (Fig. 52) performed by
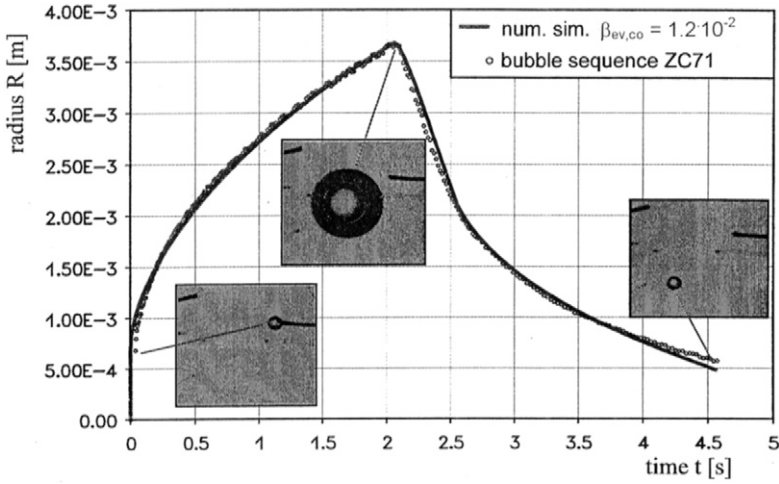
FIG. 51. Numerical solution of the growth and shrinking process of a bubble in super-saturated liquid at homogeneous temperature, compared with experiments performed at the drop tower in Bremen. The best fit was achieved with the same kinetic coefficient for evaporation and condensation: $\beta_{ev,co} = 1.2 \times 10^{-2}$. Fluid was R11, $T_{li} = 35.16°C$, Ja number for evaporation 5.3, Ja number for condensation 6.0 [50].

Vogel [79] resulted in the relation

$$R_B = 0.42 \cdot \text{Ja} \cdot (a \cdot t)^{0.555}. \tag{44}$$

This bubble grew considerably farther than the extension of the thermal boundary layer reached, and therefore the growth rate became slower than the factor C of the analytical solution predict for growth in a homogeneous superheated liquid. In this case the larger part of the bubble surface no longer contributed to the growth, and most of the evaporating mass certainly came from the microwedge layer.

Also Vogel [79] analyzed several single bubbles under subcooled conditions from TEXUS 10, 11, and 26 and received a mean exponent of 1/3. But he also noticed that at an analysis of the growing curve in sections the exponent depends on the bubble size and decreases with the growing bubble from 0.527 for small bubbles with $R < 1.5$ mm, up to 0.286 for $R \leqslant 3.5$ mm, where R is the equivalent radius of a spherical bubble calculated from the measured volume V_B. In subcooled boiling the bubble growth rate reaches a maximum value and may change its sign, if the condensation mass flow at the top $\dot{Q}_{con}$ exceeds the evaporating one at the base $\dot{Q}_{ev}$, where-
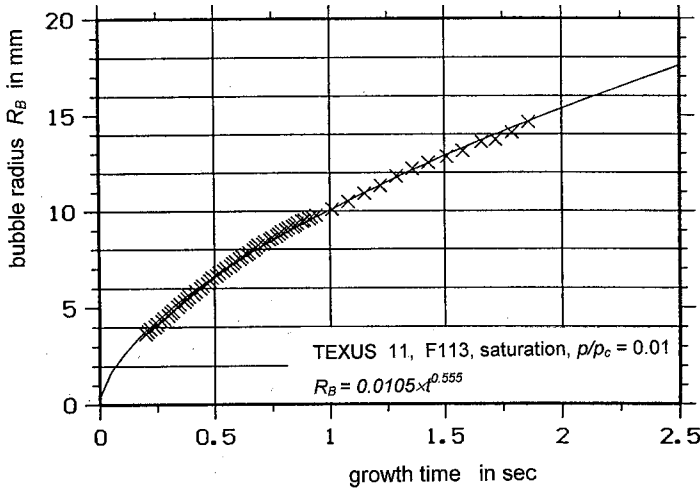
FIG. 52. Growth curve of a first bubble; evaluation of the sequence from Fig. 30 [79].

upon the bubble begins to shrink. Generally the volume growth rate can be formulated as

$$\frac{dV_B}{dt} = \frac{1}{\rho_g \Delta h}(\dot{Q}_{ev} - \dot{Q}_{con}).$$
(45)

The condensation in the upper part of larger bubbles is not evenly distributed over the interface. It fluctuates dynamically with the strength of the thermocapillary flow, which again depends on temperature gradients developing at the interface. Asymmetrical condensation induces momentum forces at the interface by the liquid flow, which fills up the condensed vapor volume and keeps the bubble surface in a permanently fluctuating motion.

B. Bubble Detachment in Saturated Liquids

1. Departure by Residual Gravity Forces

The detachment of bubbles and the vapor transportation is a key problem for the understanding of boiling in microgravity. Under terrestrial conditions the bubbles detach mainly under the influence of buoyancy, whereas the inertia forces induced by displaced liquid during bubble growth are effective in microgravity as well. Zell [87] evaluated departure diameters
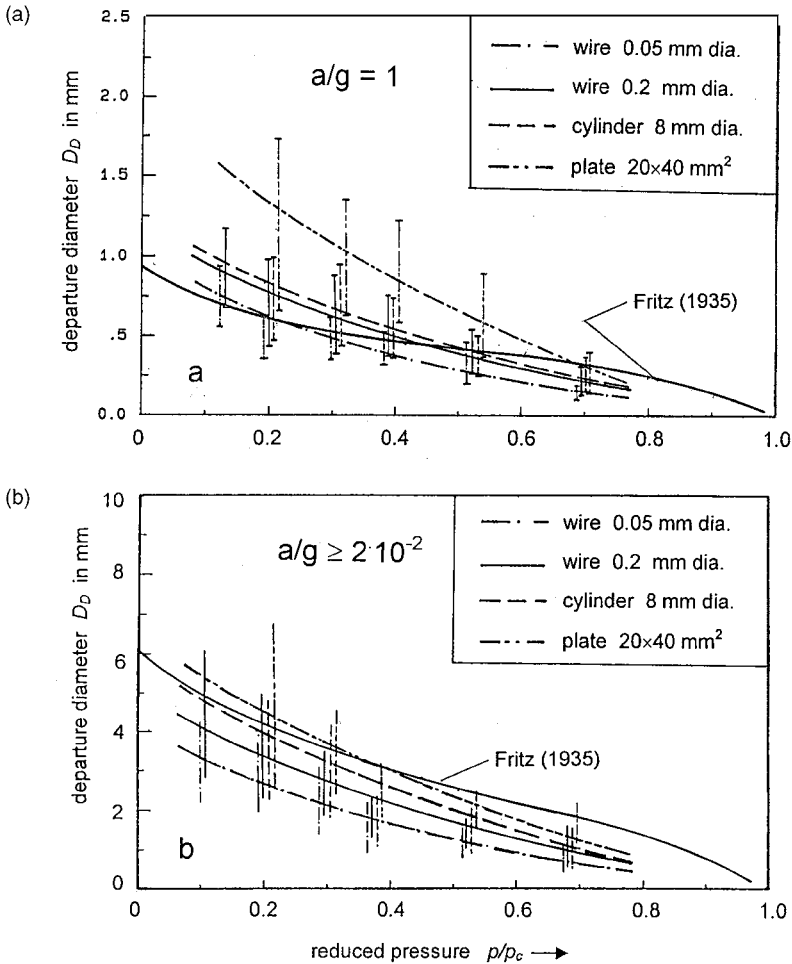
FIG. 53. Bubble departure diameter versus reduced pressure, for various heater geometry, in the fluid R12 (a) at 1-g, and (b) at $a/g \geqslant 2 \times 10^{-2}$; KC-135 [87].

from experiments performed during KC-135 flights. Comparing several relations for the departure diameter D_d, he found that at 1-g only the relation proposed by Fritz [17], Eq. (9), can be extended over a larger range of saturation pressures from $0.1 < p/p_c < 0.8$; see Figs. 53a and 53b. For $a/g \approx 2 \times 10^{-2}$ this relation yields ratio $D_{d,\mu g}/D_{d,1g} \approx 7$, whereas an evaluation over the entire pressure range of KC-135 experiments yielded a value of about 4 for wires and cylinder, and a value of 3 for the plate. The

experimental μ-g data can be fitted by means of an extension to the relation of Fritz using the ratio

$$\frac{D_{d,\mu g}}{D_{d,1g}} = \left(\frac{a}{g}\right)^{-m}. \tag{46}$$

Zell evaluated m for wires and cylinders within the range $0.30 < m < 0.39$, and for the flat plate of 20×40 mm^2 area in the range $0.24 < m < 0.31$. It must be emphasized that these values were not evaluated on single bubbles but during normal boiling at the entire surface. The size of the departing bubbles was by no means evenly distributed, but rather scattered widely, which is indicated by the bars in Figs. 53a and 53b. Additionally, it must be considered that during the KC-135 flights the gravity jitter alternated randomly between positive and negative values of about $\Delta a/g \approx \pm 2 \times 10^{-2}$. Because of the momentum and inertia induced by these g-jitters, sometimes all bubbles departed simultaneously from the heater. Zell excluded these g-jitter events from his evaluation and rather selected calm periods, which lasted up to several seconds. If the relation of Fritz, extended by Zell, were extrapolated down to $a/g = 10^{-4}$, departure diameters would result between 10 to 30 times larger than those observed under the high quality of microgravity during Space Shuttle experiments.

2. Departure Diameter from Space Shuttle Experiments

In the GAS Space Shuttle experiment with R134a on a 0.2-mm platinum wire, in the pressure range $0.21 < p^* < 0.64$ at saturation conditions, Micko [41] found departure diameters on the order of the wire size, namely between 0.18 and 0.12 mm for 1-g, and for microgravity $D_{d,\mu g}/D_{d,1g} \approx 1.5$ to 1.2. As usual for such experiments, the scatter was as high as about $\pm 50\%$. Figure 54 shows the results from 1-g and μ-g experiments compared with the relations of Fritz [17], Kutateladse and Gogonin [28], and Zeng et al. [90] calculated for 1-g. In the correlation of Borishanskij et al. [6], the departure diameter does not depend on gravity, but on the pressure ratio p/p_c:

$$D_d = 5 \times 10^5 \cdot \left(\frac{k \cdot T_c}{M \cdot p_c}\right)^{1/3} \cdot \left(\frac{p}{p_c}\right)^{-0.46}. \tag{47}$$

This relation goes relatively well with the μ-g results, whereas the 1-g data are best expressed by the correlation of Kutateladse and Gogonin. However, this must be regarded as purely accidental, because the last correlation extrapolated to μ-g would result in values two orders of magnitude higher than those resulting from the Fritz equation. Stimulated by the Borishanskij
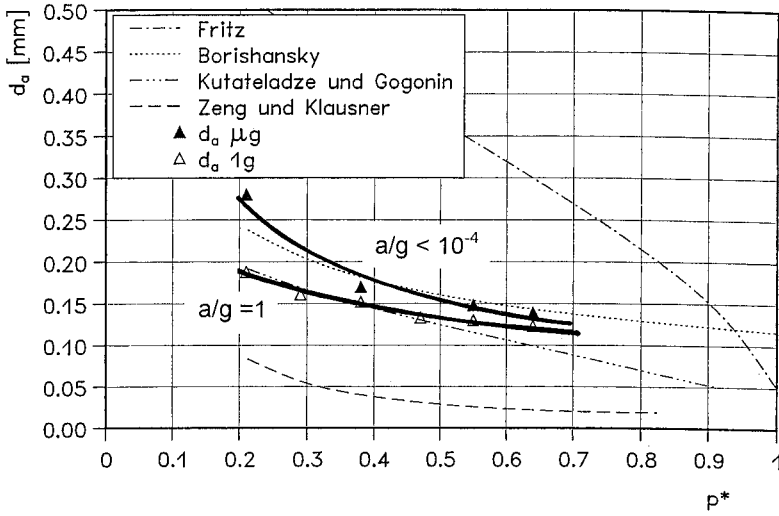
FIG. 54. Bubble departure from GAS and reference experiment at saturation compared with various correlations evaluated for 1-g.

equation, Micko fitted his data with the empirical correlation of Nishikawa and Urakawa [45],

$$D_{\mathrm{d}} = C \cdot \left(\frac{p}{p_{\mathrm{c}}}\right)^{-n}, \tag{48}$$

where the parameters for the fit are, for 1-g, $C = 0.1029$ and $n = 0.3785$, and for μ-g, $C = 0.1009$ and $n = 0.6287$.

Steinbichler [64] also observed in the pressure range $0.04 < p^* < 0.22$ in R123 at saturation a ratio of the departure diameters in the range $D_{\mathrm{d},\mu\mathrm{g}}/D_{\mathrm{d},1\mathrm{g}} \approx 2$ to 2.6, much smaller than the predicted ones. The heater was a spherical thermistor with 1.4 mm diameter, and the absolute departure diameters at μ-g ranged from 2.2 to 1.6 mm.

It must be concluded that at a high quality of microgravity, buoyancy is no longer the driving force for the bubble detachment, but rather other mechanisms come to have influence and must be carefully investigated and considered in future experiments. From his meticulous analysis, Micko [41] observed that bubbles depart after two and more coalescence processes, and even at the low heat flux of 50 kW/m² the nucleation site density is so high that the bubbles touch each other and merge together before they depart. Therefore, it is questionable whether the departure diameter or the Laplace

coefficient, Eq. (9), will be the appropriate length scale for heat transfer correlations extrapolated to microgravity.

3. Bubble Growth until Ripeness, Influence of Growth Cycle Oscillation

As discussed in Section X, the growth of a bubble is a transient event and is determined by the local heat and mass transfer around the bubble, coupled with the transient heat conduction in the wall. Assuming a microgravity environment and no other external forces, only the growth and the strong evaporation (recoil pressure) at the bubble base generates dynamic forces ΣF_{dy}, which press the bubble to the heater surface. The bubble is thus deformed; assuming a wetting liquid, an apparent contact angle ψ is formed and the bubble base is flattened. The apparent angle is due to the forces acting on a bubble and should not be confused with the wetting angle, which is a physical property determined by the adhesion forces between molecules of the liquid and of the solid material. The acting forces are balanced by surface tension, and the bubble is under tension like a spring,

$$\sum F_{dy} = \frac{2\sigma}{R_B} \pi R_{rest}^2 = 2 \cdot \pi \cdot R_B \cdot \sigma \cdot \sin^2 \Psi \tag{49}$$

where the bubble rests on a flat surface with a radius R_{rest} (see Fig. 55):

$$R_{rest} = R_B \times \sin \Psi. \tag{50}$$

After a short growth period the greater part of the supersaturating energy of the liquid that surrounds the bubble will be consumed, and because of the high heat flux at the base of the bubble, the wall temperature will also drop, in accordance with Cooper and Lloyd [11], and computations and experiments by Golobic et al. [19]. The wall temperature oscillates with the frequency of bubble growth and departure. Thus, the heat supply across the
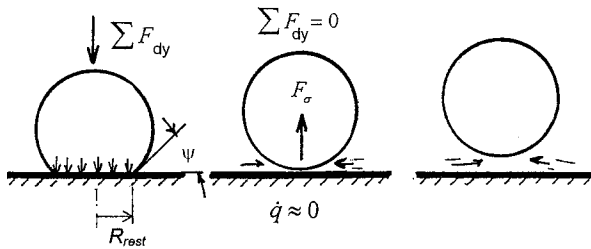
FIG. 55. Bubble detachment by ripeness; bubble released by the holding forces reforms to spherical shape because of surface tension force.

microlayer is slowed down periodically, and with it the bubble growth and all dynamic forces that hold the bubble. Assuming wetting of the liquid with the solid wall, surface tension reforms the bubble's shape to a sphere. As a result the bubble is lifted like a released spring; the static rise is as $\Delta z = R_B \times \cos \Psi$ by only geometrical considerations. Now liquid flows underneath the bubble and detaches it from the heater by its momentum, as sketched in Fig. 55. One may say, "The bubble ripens until detachment"; if the heat supply is interrupted, the bubble is ripe and detaches (like a ripe apple if the sap supply is interrupted). The momentum with which a bubble detaches depends on the rate at which the holding forces tend to zero. This bubble detachment mechanism was confirmed by the observation that at μ-g bubbles immediately detach from a surface if the power of the heater is switched off. Normally under terrestrial conditions the bubbles cannot "ripen until departure," because gravity lifts them off before.

4. Lateral and Vertical Bubble Coalescence

Bubble detachment can also be caused by coalescence processes occurring tangential to the heater surface. When bubbles grow at the surface and touch each other, they coalesce and merge. By the dynamics of this process, the coalesced bubble is lifted up from the surface. Already static consideration shows that the center of gravity of two coalesced spherical bubbles with the same radius R is lifted from the heater surface by the distance

$$\Delta z = R(2^{1/3} - 1) = 0.26R, \tag{51}$$

as sketched in Fig. 56. But this static lifting effect is strongly supported by the dynamics of the coalescence process itself. A coalesced bubble oscillates tangentially and perpendicularly to the surface of the wall because of the released surface energy which dissipates by oscillatory motion:

$$\Delta E = 4 \cdot \pi \cdot \sigma \cdot R^2 (2 - 2^{2/3}). \tag{52}$$

During oscillation in the perpendicular direction, the bubble moves toward the solid wall, which limits its amplitude and pushes it off the wall; subsequently, it is the momentum induced into the liquid by volume regrouping, coalescence, and oscillation that detaches the bubble and pushes it farther from the solid surface into the liquid.

For vertical coalescence of two bubbles of the same size, it can be assumed that the center of gravity of the two coalescing bubbles remains at its position (Fig. 56). The combined bubble is geometrically lifted up by

$$\Delta z = (1 - 1.26/2) \times D. \tag{53}$$
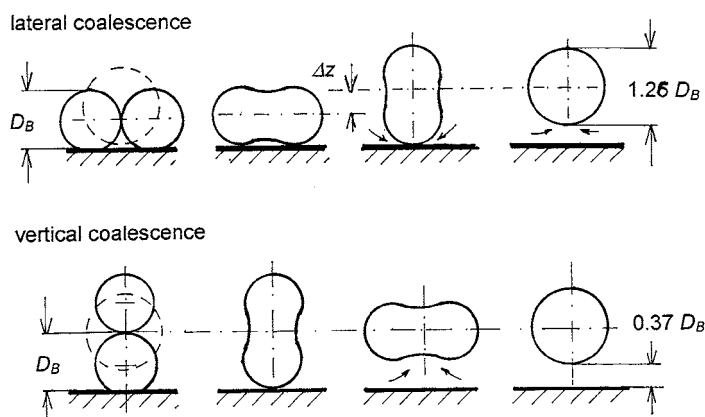
FIG. 56. Detachment by lateral and vertical bubble coalescence processes.

5. Vapor Transport by Perpendicular Bubble Coalescence

In microgravity the detached bubbles are hovering a short distance above the surface. At the wall further growth and coalescence of bubbles in the lateral and perpendicular direction takes place. If a hovering bubble touches a newly grown bubble at the surface, the interface breaks up, and the vapor from the smaller bubble flows, because of the pressure difference, into the larger hovering bubble. The interface of the smaller bubble collapses and the momentum induced by the following liquid bulk pushes the bubbles stepwise away from the heater. This is a typical process of vapor transport at saturated boiling. Similar observations have been described by Siegel [59]. By continuous coalescence processes the bubbles are getting larger and larger with increasing distance from the wall, as may be observed in Fig. 10. In this picture the stepwise bubble motion and growth by coalescence after onset of boiling on a wire of 0.2 mm diameter is clearly shown.

The dynamics of coalescence processes may be observed in a sequence of pictures (Fig. 57), during the same experimental run as Fig. 10, but at steady-state boiling about 15 sec after power on. The pictures were taken with a frequency of 50 Hz and zoomed to the picture length of 6.4 mm. Let us observe the two bubbles marked by arrows. Their centers of gravity in the first frame are about 1.2 and 3.4 mm from the wire. The coalescence starts between the third and fourth frame. Clearly one may follow the oscillations in both directions; after the 15th picture, equivalent to 0.3 sec, the oscillation is nearly completely calmed, and the center of the coalesced bubble moved to a distance of 4.8 mm from wire. This may demonstrate
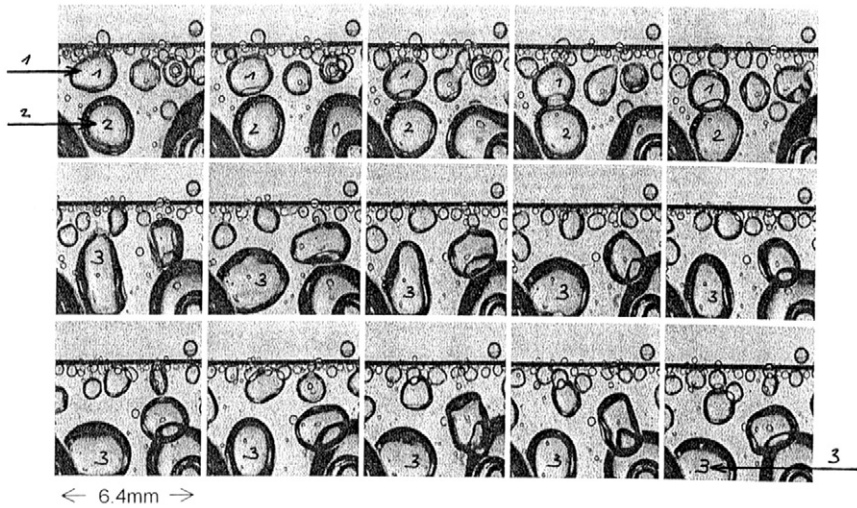
FIG. 57. Bubble coalescence during steady-state saturation boiling, liquid: R134a, $T_{li} =$ 33.4°C; wire 0.2 mm diameter; heat flux $\dot{q} = 50$ kW/m². Frame frequency 50 Hz, zoom observation picture length 6.4 mm.

how efficient coalescence processes are for the departure and movement of bubbles at saturated boiling. Also, it can be observed that the primary bubbles at the heater are about of the size of the wire and they already start coalescing at the heater surface. At the same liquid state, but at a heat flux of 300 kW/m², bubbles reached a size of about 10 mm after more than 100,000 coalescence processes of primary bubbles with a size of 0.2 mm; see Fig. 58.

Different observations were made during saturation boiling at the small circular plane heater of 3 mm diameter during the LMS mission; see Fig. 59. A large bubble of about 22 mm diameter, free-floating and not constrained, formed by about 10,000 coalitions with small bubbles, hovers at a distance of about 1 to 2 mm in front of the heater. This large bubble absorbs all bubbles that are generated at the heater surface when they have grown to a size of 1 mm, probably by coalescence as well [65]. Similar observations have been made by Ohta *et al.* [49]. These authors observed a large bubble in ethanol during a TR1-1A rocket flight above a heater area of 50 mm diameter constrained in a cylindrical cell of 120 mm diameter. Between this bubble and the heater a liquid layer of about 1–2 mm was established and all newly generated bubbles were absorbed by the large one. By this coalescence mechanism, saturated boiling can be maintained in microgravity
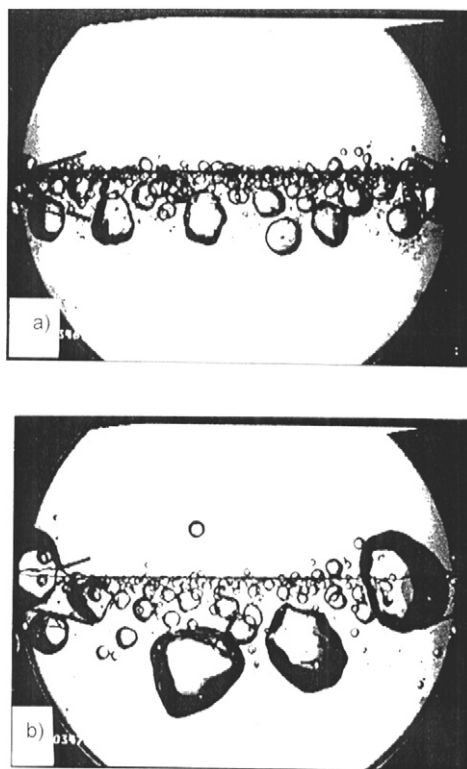
FιG. 58. Bubble development at a heat flux of 300 kW/m²; fluid state as in Fig. 57. Picture (b) is taken 10 sec after (a); window diameter is 62 mm.

as long as a larger vapor bubble is hovering in front of the surface adsorbing the small bubbles from the heater surface.

C. DYNAMICS IN SUBCOOLED BOILING

1. *Observations*

In subcooled boiling a strong thermocapillary flow, also called Marangoni convection, around the bubbles was always observed, in contrast to saturated boiling where a thermocapillary flow could never be detected. This is demonstrated in the interferometer sequence of Fig. 60 [87]. The experiment is performed in the laboratory with R113 of 20°C bulk temperature. A plane heater with the heating surface facing downward was prepared with a
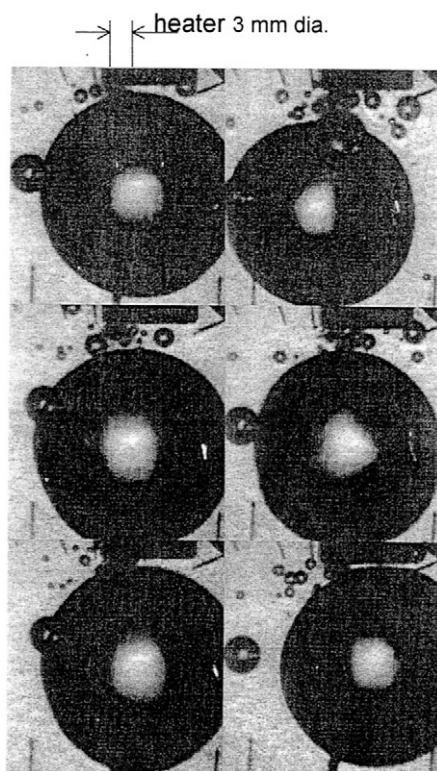
FIG. 59. Boiling and vapor transport by coalescence at a small circular plane surface of 3 mm dia, at saturation state, R123, $T_{sat} = 39.5°C$.

nucleate site in order to receive a single bubble. At left in Fig. 60 is the fluid under saturation condition. At right is the same fluid and bulk temperature, but because of the higher pressure, the liquid is under a subcooled condition of 28 K. Immediately after nucleation the bubble grew and pushed the hot liquid boundary layer away. At saturation the liquid soon came to rest and the temperature patterns dissolved (Figs. 60b and 60c), each after 0.25 sec, although at subcooled conditions immediately after nucleation a thermo-capillary flow was developed, maintained, and pushed the hot liquid from the bubble interface into the bulk liquid even against the buoyancy.

Nevertheless, it was observed that the overall heat transfer at moderate subcooling is similar to saturated boiling and also nearly unaffected by gravity. This means that thermocapillary flow does not directly influence the heat transfer from the heater surface to the fluid itself. It must be regarded

saturation $\Delta T_{sub} = 28$ K
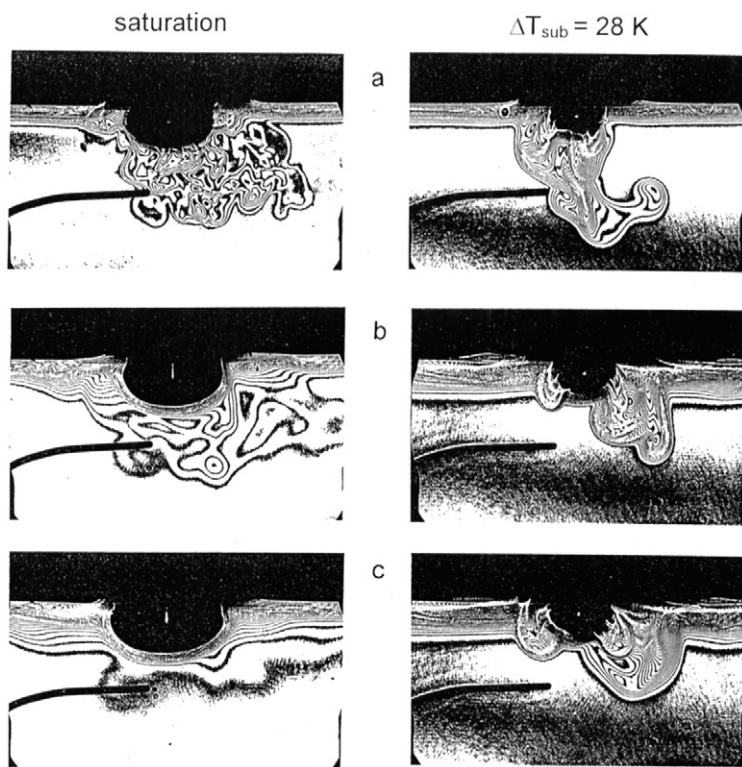
FIG. 60. Development of thermocapillary flow in subcooled liquid compared with the identical situation in saturated liquid [87].

as a secondary transport mechanism, which transfers the heat into the bulk liquid and contributes to the maintenance of subcooled pool boiling. The reaction force of the thermocapillary flow pushes the bubbles to the wall, for which reason they remain attached longer there. The bubbles may grow to a quasi steady size, at which the vapor mass flow inside is balanced by evaporation at the base and condensation at the top [Eq. (45)] if $\dot{Q}_{ev} = \dot{Q}_{con}$. If the vapor production by evaporation at the base is predominant, the bubble will grow; if condensation at the top is predominant, it will shrink. Thus, the bubbles control and adjust their size according to the heat and mass balance at evaporation and the heat and mass balance at condensation, which depends on the subcooled liquid condition. After a while most bubbles collapse at the surface; a few also depart, stand still at a certain distance from the heater, and condense. At higher subcooling very small bubbles are generated; they grow, condense, and collapse directly at the wall.

Depending on the conditions of subcooling, the bubble dynamics is different and will be discussed later. A first question may be asked: What is the origin of this thermocapillary convection? One might assume that the kinetics of evaporation and condensation is so effective that the interfacial temperature around the bubble should be evenly distributed and should be at saturation temperature. That is already the case at saturation boiling, where a thermocapillary convection could never be detected.

2. Origin of Thermocapillary Convection

If a bubble grows beyond the supersaturated boundary layer and enters into the subcooled region with its top, the vapor inside the bubble begins to condense. A vapor flow inside the bubble is induced with evaporation at the base and condensation at the top (Fig. 61), the bubble acting as a small heat pipe. Even if there exists only a small amount of dissolved inert gas in the liquid (on the order of parts per million), these gas molecules evaporate together with the liquid molecules at the base of the bubble and are transported with the vapor to the interface at the top. But here only a small part of the gas molecules will condense with the vapor and be dissolved into the liquid again. Another small part will diffuse as Stefan flow against the streaming vapor, but the greater part of the inert gas will be left at the interface and accumulate there. Different concentration profiles may be developed according to the local balance of heat and mass transfer caused
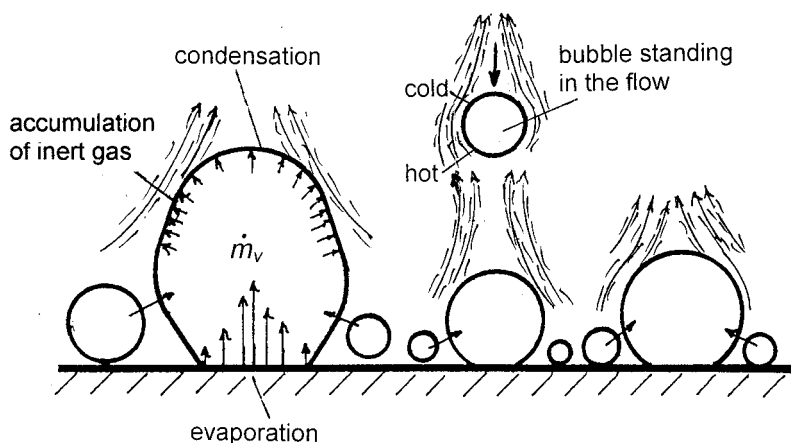
FIG. 61. Origin of thermocapillary flow around a bubble in subcooled liquid and the induced dynamics, evaporation and bubble coalescence feeding the large bubbles, and a bubble standing still in the main stream because of thermocapillary convection around it.

by the self-induced thermocapillary flow at the liquid side of the interface. The accumulation of inert gas causes differences in the partial vapor pressure and, with that, also differences in the saturation temperature along the interface, which results in temperature gradients along the interface toward the bubble base. These temperature gradients generate thermocapillary convection in direction to the bubble's top, which carries the warm condensed liquid away from the interface and transports cold liquid from the bulk to it. By that the condensation at the top and the vapor flow through the bubble may be maintained.

Based on this concept, Straub (in preparation) developed an equation for the growth rate of the thickness x of the inert gas layer dx/dt perpendicular to the interface, under the assumption that the solubility of the gas in the liquid at the interface and the Stefan diffusion flow can be ignored:

$$\frac{dx}{dt} = \frac{1}{p_g(\phi)} \frac{A_{ev}}{A_{con}} \frac{(RT)_g \cdot \dot{q}}{(\Delta h + c_p \Delta T_{sub})} \frac{\xi_g}{1 - \xi_g}. \tag{54}$$

ξ_g is the mass concentration of the dissolved gas in the boiling liquid; $p_g(\phi)$ is the partial inert gas pressure, which can be expressed due to Clausius–Clapeyron as $T(\phi)$ along the interface; and A_{ev}/A_{con} is the ratio of the evaporation to condensation area in the bubble. If this ratio is assumed to be constant, an integration is possible for a first estimation. In accordance with Marek [38] and Marek and Straub [39], small amounts of impurities of dissolved gas, on the order of parts per million, accumulate rapidly and are sufficient to generate thermocapillary convection. Even if very pure liquids were ordered from the supplier, these will always contain tiny amounts of dissolved gases. Even additional refinement will not result in an absolute "pure liquid," meaning that Marangoni convection will not be initiated. This holds especially for refrigerants with their great ability to dissolve gases.

Thermocapillary flow is caused by surface tension forces, based on the well-known physical effect that the surface or interfacial tension σ is a function of temperature, concentration c, and electrical potential ζ. Local differences of surface tension along an interface s may be induced by gradients of temperature, concentration, and/or electrical potential:

$$\sigma = \sigma(T, c, \zeta); \quad \rightarrow \quad \frac{d\sigma}{ds} = \frac{\partial \sigma}{\partial T} \frac{\partial T}{\partial s} + \frac{\partial \sigma}{\partial c} \frac{\partial c}{\partial s} + \frac{\partial \sigma}{\partial \zeta} \frac{\partial \zeta}{\partial s}. \tag{55}$$

The flow is determined by a balance of the forces in the shear layers on the liquid $(\tau_{r\varphi})_{li}$ and on the gas side $(\tau_{r\varphi})_g$. With R the bubble radius and

the circumference angle φ given by $ds = R \cdot d\varphi$, the following equation is obtained:

$$\frac{d\sigma}{d\varphi} = R((\tau_{r\varphi})_{li} + (\tau_{r\varphi})_g) \approx R(\tau_{r\varphi})_{li}. \tag{56}$$

The dynamic viscosity of most gases (vapors) is much smaller than the liquid viscosity; therefore, the shear force on the gas side can often be neglected. For most liquids the surface tension decreases with increasing temperature, which results in a strength gradient from warm to cold and induces a flow in the same direction, in the case of boiling from the heater side into the ambient liquid.

The intensity of the thermocapillary flow is often expressed with the dimensionless Marangoni number as

$$\text{Ma} = -\frac{\partial \sigma}{\partial T} \frac{B}{a\eta} [T_{s=0} - T_{s=B}]. \tag{57}$$

In boiling it would be difficult to express the strength of the thermocapillary flow by means of the Marangoni number. One could assume that B is the radius or the diameter of the bubble, and for the temperature difference $T_{s=0} - T_{s=B}$ the superheat $T_w - T_{sat}$ would be the appropriate difference. However, as mentioned before, at saturated boiling a thermocapillary flow from the bubble to the ambient liquid could never be observed; therefore, this temperature difference cannot be the driving force. The kinetics of evaporation and condensation at the interface is so efficient that total temperature equalization is effected. As already mentioned in Section X, numerical calculations indicate that near the center of the microwedge, strong temperature gradients may occur because of the strong evaporation and may induce thermocapillary convection there. However, this convection would only appear in the micro region of the microwedge and could never affect a convection outside of it as observed.

In subcooled boiling one may assume that for the temperature difference $T_{s=0} - T_{s=B}$ the appropriate one may be the subcooling $T_{sat} - T_{li}$ or $T_w - T_{li}$, but this is in contradiction to the fact that with higher subcooling the thermocapillary velocities decrease (see next section). All these considerations led to the hypothesis that the thermocapillary convection is induced by the accumulation of dissolved gases, which was discussed earlier, and this seems difficult to express in a dimensionless number.

3. Measurements of Thermocapillary Flow

The thermocapillary flow forms jet streams at the top of the bubbles, which can be seen in the interferometer pictures of Fig. 62, taken from the
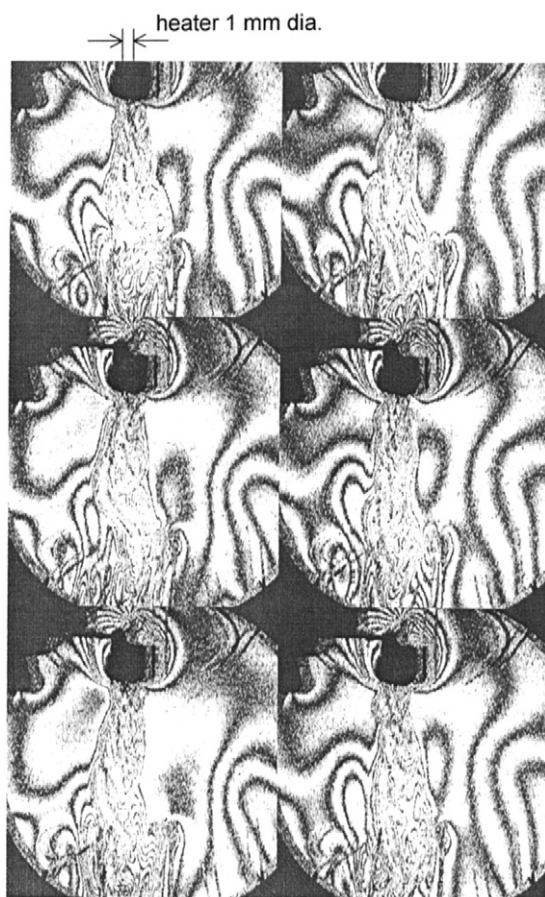
FIG. 62. Thermocapillary jet flow from bubbles at subcooled boiling, at a small circular heater of 1 mm dia., taken with differential interferometer during LMS mission (1996), R123, $T_l = 39.5°C$, $\Delta T_{sub} = 9.9$ K.

small circular heater in the LMS mission, 1996 [64]. As already mentioned, the reaction force pushes the bubbles to the wall with the consequence that the detachment is slowed down or completely held up. Of course, these thermocapillary flows appear under terrestrial conditions as well; however, they are mostly hidden by buoyancy or forced convection flow modes.

With the optical diagnostics of BDPU the radial velocity distribution $w(r)$ could be measured with particle image velocimetry (PIV) on a small circular heater of 1.5 mm diameter. For example, at a subcooling of $\Delta T_{sub} = 4.8$ K
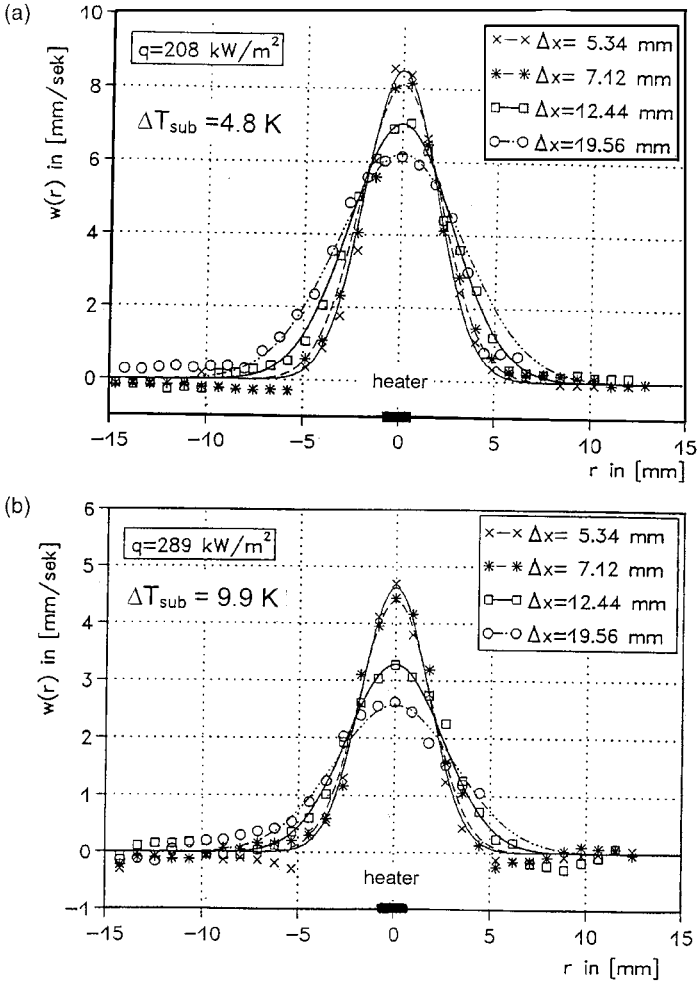
FIG. 63. Gaussian velocity distribution in the thermocapillary jet stream, fluid R123, $T_1 = 34.0°C$. (a) $\Delta T_{sub} = 4.8$ K, $\dot{q} = 208$ kW/m²; (b) $\Delta T_{sub} = 9.9$ K, $\dot{q} = 289$ kW/ m².

and 9.9 K, the Gaussian radial velocity distributions are shown in Figs. 63a and 63b, where the parameter Δx indicates the distance from the heater surface. $w(r)$ can be expressed as

$$w(r) = w_{r=0} \cdot \exp\left(C \cdot \left(\frac{r}{r_\infty}\right)^2 \right) \qquad \text{with } C = \ln(0.001). \qquad (58)$$

With this value of C the velocity at a radial distance r_∞ from the center is $w_{r=\infty}/w_{r=0} = 0.001$. The maximum velocity in the core of the center $w_{max} = w_{r=0}$ is increasing with the heat flux and decreasing with the distance from the heater. It is also a function of the amount of subcooling. It should be zero at zero subcooling, increasing with increasing subcooling up to a maximum value, and decreasing with further increase of subcooling (Fig. 63). It must tend toward zero at higher subcooling if the process of vapor condensation is faster than the development of the thermocapillary convection; this happens at the described experiments at about $\Delta T_{sub} > 30$ K. At a constant subcooling the averaged mass flow density increases linearly with heat flux (see Fig. 64), and the enthalpy flow integrated over the cross-section is in good agreement with the heat flux input at the heater (Fig. 65) [64]. On the one hand, this confirms that the thermocapillary flow is able to transport the heat because of the enlarged surface by the bubbles into the bulk liquid; certainly this flow is not generated by only one bubble (in Fig. 63, compare the heater diameter to the flow extension). On the other hand, it confirms that all bubbles departed and carried with the flow have already been recondensed within a distance of 5.34 mm from the heater, where the first velocity profile was measured. Therefore, thermocapillary convection is an important mechanism for the removal of heat in subcooled boiling.

If all departing bubbles are recondensed and no longer carried with the thermocapillary flow, confirmed by Fig. 65, an energy balance can be
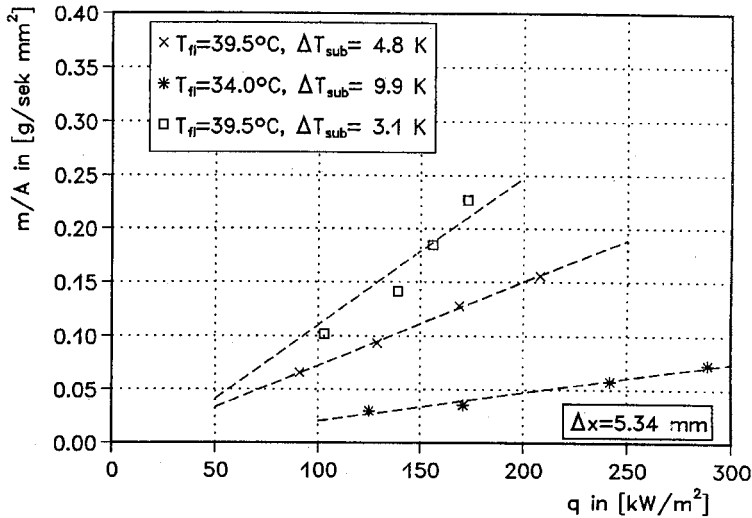
FIG. 64. Mass flow density versus heat flux, with subcooling as parameter.
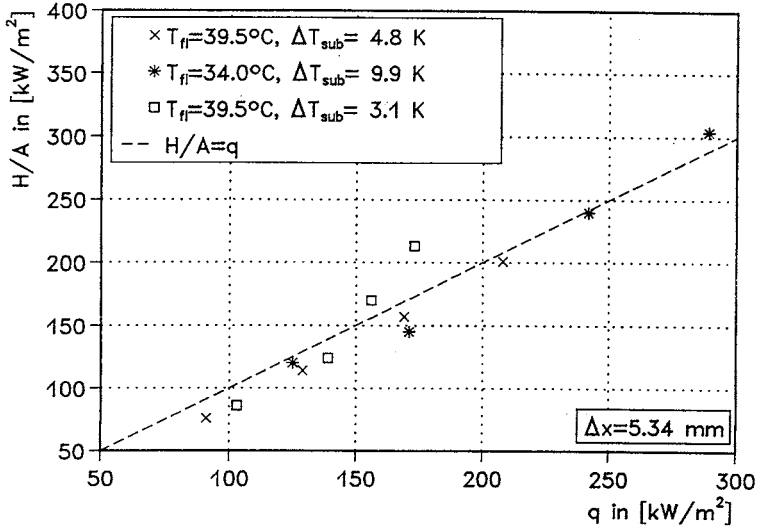
FIG. 65. Integrated enthalpy flow versus heat flux, demonstrating their equality.

written

$$\dot{q} = \dot{m} \cdot c_{\mathrm{p}} \cdot \Delta T_{\mathrm{sub}} \tag{59}$$

where $\dot{m}$ is the average mass flow per heater area. This mass flow directed perpendicular to the heater surface induces a momentum on the bubbles, which as reaction force pushes the bubbles to the surface with an averaged pressure as

$$p_{\mathrm{rea}} = \frac{1}{\rho_{\mathrm{li}}} \left(\frac{\dot{q}}{c_{\mathrm{p}} \Delta T_{\mathrm{sub}}} \right)^2. \tag{60}$$

The resulting Marangoni force in

$$F_{\mathrm{M}} = p_{\mathrm{rea}} \cdot A, \tag{61}$$

where A is the heater surface area.

This force can even contribute to the heat transfer as long as the microwedge thickness $\delta(r, t)$ below the bubble is influenced as predicted by Eq. (24). But relations (59) and (60) can be applied in this simple form only in the subcooled region where no bubbles depart from the surface. They may not be applied at saturation where $\Delta T_{\mathrm{sub}} = 0$, and where other mechanisms are dominant, and they cannot be applied at high subcooling, where the vapor is immediately condensing before thermocapillary flow can be developed.

It must be repeated that the thermocapillary flow does not enhance heat transfer at the wall itself, but contributes substantially to the secondary mechanisms of enthalpy transport and to the maintenance of subcooled boiling in microgravity. This was confirmed by experimental and numerical investigations by Betz [3] and Betz and Straub [4] on gas bubbles in various liquids to attest to the enhancement of heat transfer by thermocapillary flow. This was achieved by keeping a gas bubble attached to the upper heated wall of the test cell by buoyancy in a stable temperature gradient field at 1-g. Consequently, the thermocapillary flow had to act against buoyancy, and even in this case the heat transfer was enhanced, although less than in boiling heat transfer.

4. *Various Modes of Subcooled Boiling*

In the preceding sections, various modes of subcooled boiling have been mentioned that will now be briefly discussed, following the degree of subcooling. The numerical values given should be regarded only as examples; they certainly depend on the fluid itself, the liquid state, the heat flux, and the heater configuration.

a. Low Subcooling   At low subcooling up to $\Delta T_{sub} < 10$ K, most bubbles are attached to the heater and develop a strong thermocapillary flow, as described previously. Nevertheless, some bubbles collapse directly at the surface; others depart, move with the liquid flow, and convey the impression of sparkling. Their departure is caused by coalescence processes and by "ripening," as just explained. Owing to the decreasing evaporation into the bubble, the thermocapillary flow is also slowed, and with it its attaching effect. Now the bubbles may detach, and the flow inertia and the drag of the induced bulk thermocapillary flow carry the bubbles along until they condense in the flow. With the condensation, the cross-section of the liquid flow is reduced and the conservation of momentum causes an acceleration of the flow as in a convergent nozzle. It could even be observed that bubbles sometimes come to a halt, standing still in the flow, or migrate backwards against the bulk flow (see sketch of Fig. 61). Again, a thermocapillary flow develops around the condensing bubble, caused by a temperature gradient at the bubble's interface with the cold side at the top and the warm side at the stagnation point toward the heater. Therefore, this thermocapillary flow is also directed along the main stream, and so it accelerates this flow, thereby causing a reaction force in the opposite direction, which holds the bubbles standing in the flow or even moves them backwards to the heater.

b. Medium Subcooling   At medium subcooling between $10 < \Delta T_{sub} < 30$ K, the observations are generally similar to those described above. But now many bubbles collapse immediately at the surface and only a few depart. The thermocapillary flow velocity is reduced, as shown before, but the liquid transferred from the bulk to the interface is cold enough to condense the vapor rapidly. A periodic process sets in, determined by bubble generation and growth, induction of thermocapillary flow, condensation and collapse. Sometimes bubbles are also observed to be swept along with thermocapillary flow and condense.

c. High Subcooling, Cavitation Boiling   At high subcooling $\Delta T_{sub} > 30$ K, a high heat flux is necessary to raise the wall temperature above nucleation temperature so that bubbles may be generated. Otherwise heat conduction at μ-g or convection at 1-g is sufficient to cool the heater and keep the surface temperature below nucleation temperature. If onset of boiling occurs, the high superheat and heat flux causes a rapid bubble growth, which consumes the surrounding superheat energy immediately. Because of evaporation the vapor volume expands and the liquid interface extends. Now the vapor gets in touch with subcooled liquid and condenses immediately. The rapid periodic vapor expansion and collapse pump the warm condensed liquid away at a high frequency, like a piston. During the short period in which the interface exists, thermocapillary convection cannot be developed. At direct visual observation more or less nothing could be seen because of the microscopic size and the high frequency of this process. Only by inspection with an interferometer can a slowly moving plume of warm liquid be detected, which is identified with the pumped liquid, whereas at 1-g strong convection prevails.

D. Dynamics and Instability of CHF

Experimental studies of critical heat flux performed under microgravity conditions are presented and compared with correlations in Section VII. Although the number of experiments that could be conducted to date in μ-g has been limited, all of them correspond in the statement that, in contradiction to the results in nucleate boiling, the experimental values are considerably lower than those at 1-g, but higher than the correlations extrapolated to μ-g predict.

The generally accepted correlations for CHF are based on hydrodynamic instability models relying on the assumption of a vapor film that becomes unstable in the gravitational field. Applied under terrestrial situations, these relations are rather successful. Under microgravity pool boiling, however, they lose their reliability as the hydrodynamic forces caused by gravity tend

to zero. Only surface tension force, momentum forces due to bubble growth, drag force, coalescence dynamics, and the reaction force of the evaporating liquid at the microlayer remain, which may be considered only in a lump sum of the heat flux itself. The critical heat flux expressed in the correlations is not clearly determined, because for an exact determination a second parameter would be necessary, which may be (local) surface temperature as an indication of the wetting conditions.

The appearance of CHF starts as a local event at the heater surface, mostly beginning at a location where the temperature becomes somewhat higher than the average. This is mostly caused at a dry spot in the center underneath a larger bubble or under a vapor volume generated by the coalescence of several bubbles, whereby the vapor volume cannot rise or move fast enough away from the heater and prevents the supply of liquid to the heating surface. Depending on the heat and mass balance and the induced momentum balance, at the line where the three phases — heater surface, liquid, vapor — coexist, the dry spot may extend to a dry area or may even shrink. If at the three-phase line the evaporating mass flow is larger than the liquid mass support to it, this will lead directly to an extension of the dry area, which may spread rapidly below the bubble or the accumulated vapor volume pushing the liquid away. If the heater temperature cannot be reduced fast enough, the temperature of the dry area may increase up to the melting temperature of the heater material.

The model presented in Section X with Fig. 49 and the flow conditions in Fig. 50 can be applied for the understanding and modeling of the critical heat flux as well. With high evaporation rate at the bubble center, a dry spot will appear. Now the adhesion forces between liquid and surface material take effect and, together with the capillary force, take care of the liquid supply to the interface line [Eq. (34)]. But with increasing heat flux, the evaporating mass flow increases and the liquid supply becomes insufficient. The three-phase line is developing backward, pushed by the reaction force of the evaporating mass and additionally supported by thermocapillary flow caused by the high temperature gradients at the liquid interface of the microwedge (Fig. 50c), which is directed opposite to the liquid supply of capillary-adhesion flow. At the three-phase line the local mass balance with the liquid flow to and the evaporating mass flow (indicated by the index r, Fig. 66) determines the stability of the evaporation, as long as Eq. (40) is balanced with Eq. (30):

If $\dot{m}_r = \dot{m}_{r,ev} = \dfrac{\dot{q}_r}{\Delta h}$, stable situation;

If $\dot{m}_r < \dot{m}_{r,ev} = \dfrac{\dot{q}_r}{\Delta h}$, unstable situation $\rightarrow$ dry area extends, burnout.
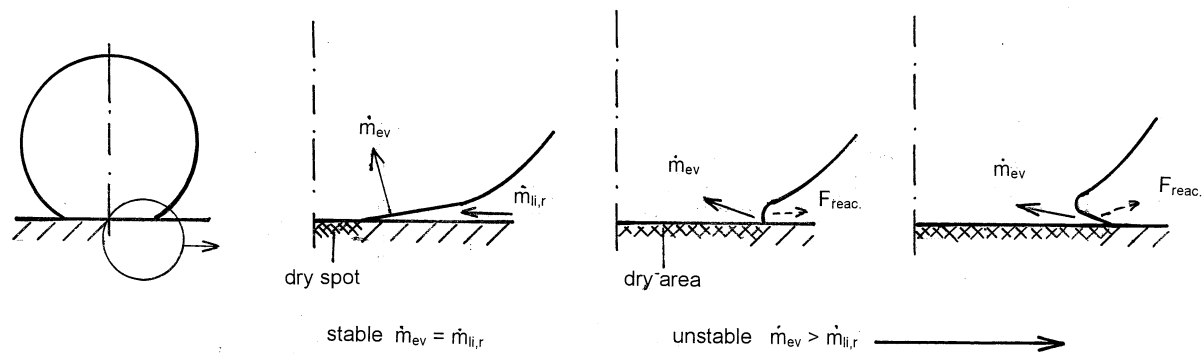
FIG. 66. Sketch of the development of the boiling crisis.

At the heat flux balance the transient heat support from the heater surface must also be considered; it must be high enough to maintain even locally the high heat flux values. The change to unstable mass balance may happen at a heat flux or temperature only a little higher, indicated by sudden change of the gradient of the temperature rate to a positive value as $d^2 T_w/dt^2 > 0$, leading to overall extension of CHF. In Figs. 31 and 40 the dry area extended below the bubble, indicated by the slow increase of the heater temperature, but the gradient of the temperature rate was still $d^2 T_w/dt^2 < 0$, which suggests that finally a quasi-stable situation may be obtained at a certain heat flux, with $dT_w/dt = 0$.

The appearance of CHF may not be a consequence of only one effect, as confirmed by the experiments. It will rather be influenced by a combination and interaction of macroscopic hydrodynamic events, with obstruction of the liquid transport to the heater surface and pushing away of liquid by vapor expansion on one side, and — even more important — of microscopic effects, which happen at the three-phase interface line, described earlier. If the liquid transport to the three-phase line is insufficient, a dry spot extends to an area where the temperature increases and prevents rewetting, which in turn fosters further rise of surface temperature [70]. In the present CHF models these microscopic events, with mass flow into the microlayer and wetting and rewetting conditions, are generally ignored.

There are some new models to explain onset of the boiling crisis by the recoil pressure only [43, 44, 58]. They show that at some typical time the dry spot under the bubble begins to grow rapidly under the action of vapor recoil. The authors of the new models did not verify their results on real measurements of CHF values. If in such a model the bubble expansion, the capillary-adhesion flow, dynamic forces, and external forces such as gravity may be included, it will be a step forward to understand the onset of the boiling crisis and its influence on gravity.

XII. Why Enhancement? Why Diminution?

A. Reasons for Heat Transfer Enhancement

1. *Influence of Bubble Size*

A conspicuous observation during boiling under microgravity was that the size of the bubble attached to the heater surface and the size of the departing bubbles increased with the reduction of the gravity level. Let us discuss the question: What is the influence of the bubble size on the heat transfer? A simple geometrical consideration is treated. At a heater of a

square surface with side length D, a large bubble with diameter D is attached with a base area of the diameter $D_b = D \sin \psi$ to the surface, where ψ may be regarded as an apparent contact angle. The attached surface may be regarded as the active heat transfer surface with the area as $\frac{1}{4}\pi(D \sin \psi)^2$. The same square surface is now occupied by N^2 small bubbles with a size of $d = D/N$. If we assume that these small bubbles are attached at the surface with the same apparent contact angle ψ, then their base diameter is $d_b = d \sin \psi$. Further, it may be assumed that the active heat transfer surface of the bubbles is determined by the base area defined by the base diameter. Then the comparison of the active area of the large bubble and the areas of the N^2 small bubbles results in

$$(D \cos \psi)^2 \pi = N^2(d \cos \psi)^2 \pi \rightarrow D^2 = (Nd)^2 \qquad \text{with } N = D/d. \quad (62)$$

Consequently, as long as the apparent contact angle is equal and independent of the bubble size, the active heat transfer area may even be regarded as independent of the bubble size. This is in relatively good agreement with the observation at moderate heat fluxes that the average heat transfer intensity is independent of bubble size as long as the heat transfer mode is nucleate boiling. Naturally, this is only a simple relation, which considers neither the three-dimensional heat conduction in the heater wall underneath the bubbles nor the different forces on the bubbles influencing the size and form the apparent contact angle.

The overall heat transfer intensity is determined by the bubble departure size, the departure frequency, and the number of active nucleation sites. A number of relations for the prediction of mean departure diameter and frequency are presented by Carey [8]. Under microgravity and saturation conditions, if almost all heat is transported by the latent heat of the bubbles, then the departure size and frequency are related to each other as first proposed by Jakob and Fritz [22]:

$$f D_d = \text{constant}. \tag{63}$$

2. Influence of Low Heat Flux

The general observation has been that at lower heat fluxes the microgravity heat transfer is enhanced compared to terrestrial measurements under identical conditions. It is often assumed that the total heat flux in boiling is partly due to the latent heat of the boiling process itself, and due in a substantial part to convection due to gravity or forced convection. The part of the boiling heat transfer process includes the evaporation itself, the

microconvection caused by bubble growth and dynamics, and the liquid exchange by bubble departure. These mechanisms will be effective in microgravity as well as at 1-g.

Boiling onset is initiated if the temperature for bubble nucleation or activation is reached at the heater surface. This happens at μ-g much more evenly, because before boiling onset occurs, the heat to the liquid is transferred by conduction only. With free convection the surface is generally better cooled; thus, nucleation happens at a higher heat flux. Free convection develops a certain flow structure at the heater surface, such as the Bénard-like structure over a heated flat plate, or at circumferential flows around tubes, wires, and spheres with an upper and lower stagnation point, whereas the lower stagnation point is generally better cooled than the upper one. Therefore, a heated surface at low heat flux exposed into a fluid with free convection does not have a constant evenly distributed surface temperature; on the contrary, the temperature adjusts itself according to the flow structure. Boiling onset will occur at those parts of the surface where the cooling by the flow is not as efficient, and where the nucleation temperature will be reached. Consequently, at low heat fluxes parts of the surface are still cooled by free convection, whereas others are already cooled by boiling. With increasing heat flux and increasing temperature of the superheated liquid boundary layer, the areas of the surface that are boiling controlled increase as well. It must be emphasized that usually only average values of surface temperatures $\Delta \bar{T}_{\text{sat}}$ and heat fluxes are measurable, which are considered here. At low heat flux a simple model will be considered. The total heat flux at the heater surface will be composed of a boiling part and a convection part, where the total heat transfer area A is shared respectively $A = A_{\text{boil}} + A_{\text{con}}$:

$$\dot{Q} = \dot{Q}_{\text{boil}} + \dot{Q}_{\text{con}} = \bar{\alpha} \cdot A \cdot \Delta \bar{T}_{\text{sat}} = \alpha_{\text{boil}} \cdot A_{\text{boil}} \cdot \Delta T_{\text{boil}} + \alpha_{\text{con}} \cdot A_{\text{con}} \cdot \Delta T_{\text{con}}. \quad (64)$$

The local temperature difference at the area where convection governs the heat transfer is ΔT_{con}, depending on the intensity of the convection flow. This temperature may be lower or even higher as $\Delta \bar{T}_{\text{sat}}$; however, it will be below the temperature of boiling onset. ΔT_{boil} may be close to the average $\Delta \bar{T}_{\text{sat}}$. For simplicity, let us assume that $\Delta \bar{T}_{\text{sat}} \approx \Delta T_{\text{sat}} \approx \Delta T_{\text{boil}} \approx \Delta T_{\text{con}}$. Then it follows, for the average heat transfer coefficient $\bar{\alpha}_{1\text{g}}$, that

$$\bar{\alpha}_{1\text{g}} = \frac{A_{\text{boil}}}{A} \alpha_{\text{boil}} + \left(1 - \frac{A_{\text{boil}}}{A} \right) \alpha_{\text{con}}. \quad (65)$$

For μ-g conditions the second term can be neglected, because the heat transfer by conduction is lower than that by convection $\alpha_{\text{cond}} < \alpha_{\text{con}}$. The

heat transfer coefficient of free convection is with $\alpha_{\text{con}} \propto \Delta T^{0.25}$ smaller than for boiling $\alpha_{\text{boil}} \propto \Delta T_{\text{sat}}^n$ with $n \geqslant 2$. Thus, it is obvious that at low heat fluxes, as long as at 1-g a mixed mode with both convection and boiling governs the heat transfer, the microgravity efficiency can be $\alpha_{\mu g}/\alpha_{1g} > 1$. With this consideration, the surprising experimental results may be justified. Differences will arise at subcooled boiling if the driving temperature difference for the convection part is increasing to $\Delta T_{\text{con}} = \Delta T_{\text{sat}} + \Delta T_{\text{sub}}$.

With increasing heat flux the part of the surface occupied by boiling increases as well; up to fully developed nucleate boiling. At μ-g larger bubbles are formed than at 1-g at the same heat flux. The bubbles touch each other and coalesce; therefore, they hinder themselves and form dry spots beneath them, which leads to higher surface temperatures and a lower heat transfer efficiency compared to 1-g data at the same heat flux.

3. *Influence of Buoyancy at the Microlayer Thickness*

In Section X it was stated that the local heat transfer reversal depends on the thickness of the microlayer below the bubble [Eq. (25)]. This thickness is influenced by gravity as long as a microlayer beneath the bubbles exists. The bubbles are lifted by buoyancy if the heater is directed during the growth period opposite to the gravity vector. By that the thickness of the microlayer increases, $\delta(r, t)_{1g} > \delta(r, t)_{\mu g}$, which results in an increase of the thermal resistance to the bubble between heater surface and bubble interface and may contribute to the heat transfer enhancement in microgravity. The situation changes with the gravity vector. A confirmation that this lifting mechanism influences the heat transfer intensity may be seen in the fact that boiling at 1-g and at a surface inclined by about 60° to a downward-facing surface enhanced the heat transfer by about 15% compared with an upwardly facing surface. This effect is generally attributed to a gliding effect of the bubbles along the heater surface and must therefore depend on the gliding length. But this observation was also made during reference measurements on a small, flat circular heater of 3 mm diameter with inclined surface from 0 to 180°, where the gliding effect was small and can probably be neglected [64].

B. Influencing Factors for Deterioration

Naturally, especially under saturated conditions in microgravity pool boiling, bubbles are missing the important force of gravity, which transports the bubble and with that the latent heat away from the surface. Therefore, it is inevitable that at μ-g vapor volume collects preferably close to the

heater surface, and that bubbles coalesce directly at the heater. This is also known in terrestrial boiling, if most nucleate sites are activated and the vapor production is increasing so intensively that the bubbles coalesce directly at the surface. This region at the boiling curve is often called the "coalesce boiling region" and is connected with a deterioration of the heat transfer intensity. The same happens at microgravity, but, at a lower heat flux than under terrestrial conditions. The vapor transport is maintained as long as there is free space for coalesced bubbles to detach and hover at a certain distance above the heater surface and absorb new formed bubbles from the surface. But at a larger vapor production, bubbles remain attached at the surface and grow by coalescence, forming dry spots. With increasing heat flux, the dry spots increase in number and size, and they decrease the overall heat transfer coefficient, leading finally to the boiling crisis.

Important for the maintenance of the nucleate boiling process is the thermal oscillation of the heater surface with the frequency of the departing bubbles. If that is not possible, as discussed in the interpretation of the experiments with the direct-heated flat plate, the dry area increases even at relatively low heat fluxes.

XIII. Application of Boiling in Microgravity

The results of the presented boiling research demonstrate clearly that boiling is an efficient mode of heat transfer and is applicable in a microgravity environment, even under saturated liquid-state conditions, if a proper design for the heater surface is selected. In the subcooled liquid state, the self-induced thermocapillary convection produce a liquid flow that may be used for a small thermosiphon loops for cooling of small high-powered electronic devices. The thermosiphon effect often used for heat exchangers under terrestrial conditions naturally cannot operate in microgravity at saturated boiling. But with the induction of a relatively slow liquid motion, even saturated boiling could be maintained, which would carry the vapor with it and transport it to the cold part of the loop, where condensation may occur. There is no question that flow boiling will be applicable under microgravity in loops if special arrangements for vapor separation and condensation are provided and the heat transfer and flow conditions are adjusted.

For the design of heat transfer systems for space applications; the correlations applied for terrestrial use can be employed regarding the factor of safety, but the maximum expected heat flux must be reduced, and care must be taken for the transport and recondensation of the vapor.

XIV. Conclusions and Future Perspectives

The results from microgravity boiling research and the direct comparison with terrestrial heat transfer indicate that the real heat transfer mechanisms in both environments are similar, or even identical. Gravity and the convection caused by it mask the true mechanisms of boiling. The dominant mechanism for boiling heat transfer is governed by the evaporation process in the wedge-shaped liquid microlayer, which is formed by the rapid bubble growth beneath the bubble interface and the solid wall. In a microgravity environment, bubble detachment is caused by surface tension forces and bubble reformation after the superheated energy around the bubble is consumed, and when the forces due to bubble growth are slowed down, this is called "bubble ripeness." Further detachment and vapor transport processes at saturated conditions are caused by horizontal and vertical coalescence mechanisms. Additionally, in subcooled boiling the bubbles act as small heat pipes with evaporation at the base and condensation at the top, which is maintained by self-induced thermocapillary convection. This convection results from the change of partial pressure of inert gases, which remain and accumulate when the vapor condenses in the upper part of the bubbles. Inert gases are always dissolved in the liquids even if they are sold as very pure. The thermocapillary convection carries the warm liquid from the interface into the bulk and cold liquid from the bulk to the interface. By that means, the transport of heat from the heating surface into the bulk subcooled liquid is maintained. At high subcooling the transport process is determined by the pumping effect caused by rapid bubble growth and immediate collapse.

From the present studies, the conclusion can be drawn that boiling, and also pool boiling, can be used as a heat transfer mechanism for technical applications in space vehicles. But this is out of the sphere of influence of the author. At present, however, he recommends the use of a microgravity environment for careful and well-prepared studies of boiling phenomenon without buoyancy force; such studies are of eminent importance for the better understanding of its complex physics. These studies should be performed in close international cooperation and coordination, because even if the International Space Station can be used, each single experiment will still be expensive, and the problems to be solved are numerous and the questions to be answered manifold. In order to study the influence of thermophysical properties, two characteristic liquids should be selected and the investigations should cover a wide range of saturated and subcooled states from low saturated pressure to near critical. Likewise, direct and indirect heater systems of various geometries, material properties, and surface qualities such as roughness, textures, fins, and coatings should be

applied. For technical application, enhanced heat transfer structures as already used should be carefully investigated, in order to learn about the effective mechanism responsible for the enhancement. The objective of these studies is to optimize those structures for heat transfer utilization and higher thermal efficiency. Simultaneously with the studies of the overall heat transfer, skillful heaters should be developed to investigate details of the temperature and flow field around single bubbles. Advanced optical and electronic diagnostic techniques should be applied to investigate bubble dynamics, bubble interactions, and interrelation with neighboring bubbles and with the heater surface itself. These studies are the conditions for a better understanding of the complex physics of the boiling phenomenon and are the conditions for the development of a more rigorous boiling theory, of better physical-based models, and of correlations for space and terrestrial application.

Acknowledgments

Nomenclature

A	area	K	Kutateladse number
A	dispersion constant	K	curvature
a	acceleration	k	Boltzmann constant
a	thermal diffusivity	L	Laplace coefficient
B	size	M	molar mass
Bo	Bond number	Ma	Marangoni number
C	constant	m	exponent
c	concentration	$\dot{m}$	mass flow density
c_p	isobaric specific heat capacity	m^*	mass per molecule
		n	exponent
D	bubble diameter	N	number of nucleate sites
F	force	Nu	Nusselt number
f	frequency	Pr	Prandtl number
g	gravity acceleration	p	pressure
h	enthalpy	$p^* = p/p_c$	reduced pressure
Δh	phase change enthalpy	$\dot{Q}$	heat flow rate
Ja	Jakob number	$\dot{q} = \dot{Q}/A$	heat flux density

Q_B	enthalpy per bubble
R	bubble radius
R	orbital radius
R_λ	thermal resistance
$R' = Bo^{1/2}$	dimensionless radius
Ra	Rayleigh number
r	radius coordinate
T	temperature
t	time
u	velocity in r direction
w	velocity
z	coordinate

GREEK SYMBOLS

α	heat transfer coefficient
β	evaporation coefficient
β	contact angle
Δ	difference
δ	thickness of microlayer
ε	gravity efficiency
ϕ	angle
λ	thermal conductivity
μ	dynamic viscosity
v	kinematic viscosity
ρ	density
σ	surface tension

τ	shear stress
ψ	apparent contact angel
ξ	mass concentration

INDICES

B	bubble
c	critical
CHF	critical heat flux
con	condensation
d	departure
dy	dynamic
ev	evaporation
ex	external
f	fluid
g	gas, vapor
i	interface
l and li	liquid
rea	reaction
R	recoil
sat	saturation
sub	subcooled
v	vapor
w	wall, heater
1g	$1g$, earth gravity
μg	μg, microgravity

References

1. Abe Y., Oka T., Mori Y. H., Toshiharu M., and Nagashima A, (1994). *Int. J. Heat Mass Transfer* **37** 2405.
2. Beer H., Burow P., and Best R. (1977). Bubble growth, bubble dynamics, and heat transfer in nucleate boiling, viewed with a laser interferometer. In *Heat Transfer in Boiling* (E. Hahne and U. Grigull, Eds.), pp. 21–52. Academic Press, New York.
3. Betz, J. (1997). Strömung und Wärmeübergang bei thermokapillarer Konvektion an Gasblasen. Dissertation, TU München 1997. Herbert Utz Verlag Wissenschaft, München.
4. Betz, J., and Straub, J. (2001). Numerical and experimental study of the heat transfer and fluid flow by thermocapillary convection around gas bubbles. *J. Heat Mass Transfer*, in press.
5. Borishanskij, V. M. (1969). Correlation of the effect of pressure on the critical heat flux and heat transfer rates using the theory of hydrodynamic similarity. In *Problems of Heat Transfer and Hydraulics at Two-Phase Media* (S. S. Kutateladse, Ed.), pp. 16–37. Pergamon Press, Oxford.
6. Borishanskij, V. M., Danilova, G. N., Gotovskiy, M. A., Borishanskij, A. V., Danilova, G. P., and Kupriyanova, A. V. (1981). Correlation of data on heat transfer in an elementary characteristics of the nucleate boiling mechanism. *Heat Transfer Sov. Res.* **13**(1), 100–116.
7. Bromley, L. A. (1950). Heat transfer in stable film boiling. *Chem. Eng. Prog.* **46**, 221–227.

8. Carey, V. (1992). *Liquid–Vapor Phase-Change Phenomena*, Series in Chemical and Mechanical Engineering. Hemisphere Publishing, New York.

9. Clark, J. A. (1968). Gravic and agravic effects in cryogenic heat transfer. *Adv. Cryogen. Heat Transfer 87*, **64**, 93–102.

10. Cooper, M. G. (1969). The microlayer and bubble growth in nucleate pool boiling. *Int. J. Heat Mass Transfer* **12**, 915–933.

11. Cooper, M. G., and Lloyd, A. J. P. (1969). The microlayer in nucleate pool boiling. *Int. J. Heat Mass Transfer* **12**, 895–913.

12. Ded, J., and Lienhard, J. (1972). The peak pool boiling heat flux from a sphere. *AIChE J.* **18**, 337–342.

13. Derjaguin, B. V. (1955). Definition of the concept of and magnitude of the disjoining pressure and its role in the static and kinetics of thin layers of liquid. *Kolloidnyi Zh.* **17**, 191–197.

14. Dhir, V. K. (1990). Nucleate and transition boiling heat transfer under pool boiling and external flow conditions. In *Proc. Ninth Int. Heat Transfer Conf., Jerusalem 1990* (G. Hetsrony, Ed.), Vol. 1, pp. 91–112. Hemisphere, New York.

15. Forster, H. K., and Zuber, N. (1955). Dynamics of vapor bubbles and boiling heat transfer. *AIChE J.* **1**, 531–535.

16. Frederking, T. H. K., and Clark, J. A. (1963). Natural convection film boiling on a sphere. *Adv. Cryogen. Eng.* **8**, 501.

17. Fritz, W. (1934). Berechnungen des Maximalvolumens von Dampfblasen. *Z. Phys.* **36**, 379–384.

18. Fujita, Y., and Bai, Q. (1998). Numerical simulation of the growth for an isolated bubble in nucleate boiling. In *Heat Transfer 1998, Proc. of 11th IHTC, Kyongju, Korea*, Vol. 2, pp. 437–442.

19. Golobic, I., Pavloic, E., Strgar, S., and Kenning, D. B. R. (1996). Wall temperature variation during bubble growth on a thin plate: Computation and experimentations. In *Proc. Eurotherm Seminar No. 48, Paderbom, Germany, Sept. 1996*. Edizioni ETS, Pisa, Italy.

20. Hammer, J. (1996). Einfluss der Mikrozone auf den Wärmeübergang beim Blasensieden. *Fortschr. Ber VDI*, Düsseldorf, Ser. 19, No. 96.

21. Haramura, Y., and Katto, Y. (1983). A new hydrodynamic model of critical heat flux, applicable widely to both pool and forced convection boiling on submerged bodies in saturated liquids. *Int. J. Heat Mass Transfer* **26**, 389–399.

22. Jakob, M., and Fritz, W. (1931). Versuche über den Verdampfungsvorgang. *Fortschr. Geb. Ingenieurw.* **2**, 435.

23. Jawurek, H. H. (1969). Simultaneous determination of microlayer geometry and bubble growth in nucleate boiling. *Int. J. Heat Mass Transfer* **12**, 843–848.

24. Katto, Y., and Yokoya, A. (1968). Principal mechanism of boiling crisis in pool boiling. *Int. J. Heat Mass Transfer* **11**, 993–1002.

25. Keshock, E. G., and Siegel, R. (1964). Forces acting on bubbles in nucleate boiling under normal and reduced gravity conditions. NASA Tech. Note TN D-2299. National Aeronautics and Space Administration, Washington, DC.

26. Kutateladse, S. S. (1959). Heat transfer in condensation and boiling. AEC-tr-3770.

27. Kutateladse, J. J. (1963). *Fundamentals of Heat Transfer*. Edward Arnold, Ltd. Translated from Russian.

28. Kutateladse, S. S., and Gogonin, I. I. (1979). Growth rate and departure diameter of a vapor bubble in free convection boiling of a saturated liquid, Udc 536.248.2. Translation from *Teplofizika Vysokikh Temperature* **17**(4), 792–797.

29. Lay, J. H., and Dhir, V. K. (1994). A nearly theoretical model for fully developed nucleate boiling of saturated liquids. In *Proc. 10th Int. Heat Transfer Conference, Brighton, UK, 1994*, 10-PB-17, pp. 105–110.

30. Lay, J. H., and Dhir, V. K. (1995). Shape of a vapor stem during nucleate boiling of saturated liquids. *J. Heat Transfer* **117**, 394–401.
31. Lee, H. S., and Merte, H. (1998). The origin of the dynamic growth of vapor bubbles related to vapor explosion. *J. Heat Transfer* **120**, 174–182.
32. Lee, H. S., and Merte, H. (2000). Pool boiling mechanisms in microgravity. In *Proc. United Engineering Foundation Conference: Microgravity Fluid Physics and Heat Transfer, Sept. 1999, Kahuku, Oahu, Hawaii.* Ed. Dhir, 126–135.
33. Lee, H. S., Merte, H., and Chiaramonte, F. (1997). Pool boiling curve in microgravity. *J. Thermophys. Heat Transfer* **11**(2), 216–222.
34. Lee, H. S., Merte, H., and Chiaramonte, F. (1998). Pool boiling phenomena in microgravity. In *Heat Transfer, 1998, Proc. of the 11th Int. Heat Transfer Conf., August 1998, Kyongyu, Korea*, Vol. 2, pp. 395–399.
35. Lienhard, J. H., and Dhir, V. K. (1973). Hydrodynamic prediction of peak pool boiling heat fluxes from finite bodies. *J. Heat Transfer* **95**, 152–158.
36. Lioy, I. (1989). Bubble, drop, particle unit (BDPU), a multi-user microgravity facility. In *Proc. 40th Congr. of the Astronautical Federation, Spain, IAF.*
37. Marco, P. Di, and Grassi, W. (2000). Pool boiling in reduced gravity. In *Boiling 2000: Phenomena & Emerging Applications, Anchorage, AK, April 30 – May 5, 2000.*
38. Marek, R. (1996). Einfluess thermokapillarer Konvektion und inerter Gase beim Blasensieden in unterkühlter Flüssigkeit. Dissertation, TU München.
39. Marek, R., and Straub, J. (2001). The origin of thermocapillary convection in subcooled nucleate pool boiling. *Int. J. Heat Mass Transfer* **44**, 39–53.
40. Merte, H., and Clark, J. A. (1964). Boiling heat transfer to a cryogenic fluid at standard, fractional, and near-zero gravity. *Int. J. Heat Mass Transfer* **86**, 351–359.
41. Micko, S. (2000). Sieden am Heizdraht unter reduzierter Schwerkraft. Dissertation, TU München.
42. Moissis, R., and Berenson, P. J. (1963). On the hydrodynamic transition in nucleate boiling. *J. Heat Transfer Trans. ASME Ser. C* **85**, 221–229.
43. Nikolayev, V. S., and Beysens, D. A. (1999). Boiling crisis and non-equilibrium drying transition. *Europhys. Lett.* **47**, 345–351.
44. Nikolayev, V. S., Beysens, D. A., Lagier, G. L., and Hegseth, J. (2000). Growth of a dry spot under a vapor bubble at high heat flux and high pressure. Submitted.
45. Nishikawa, A., and Urakawa, K. (1960). An experiment of nucleate boiling under reduced pressure. *Mem. Fac. Eng. Kyushu Univ.* **19**, 63–71.
46. Noyes, R. C. (1963). An experimental study on sodium pool boiling heat transfer. *J. Heat Transfer Trans. ASME Ser. C* **85**, 125–131.
47. Nukiyama, S. (1934). The maximum and minimum values of the heart Q transmitted from metal to boiling water under atmospheric pressure. *Trans. JSME* **37**, 357.
48. Ohta, H. (2000). Boiling experiments under microgravity conditions by using transparent heaters. In *Proc. United Engineering Foundation Conference: Microgravity Fluid Physics and Heat Transfer, Sept. 1999, Kahuku, Oahu, Hawaii.* Ed. Dhir, 151–159.
49. Ohta, H., Kawaji, M., Azuma, M., Inoue, K., Kawasaki, K., Tamaoki, H., Ohta, K., Takada, T., Okada, S., Yoda, S., and Nakamura, T. (1997). TR-1A rocket experiment on nucleate pool boiling heat transfer under microgravity. ASME HTD-Vol. 354, 249–256.
50. Picker, G. (1998). Nicht-Gleichgewichts-Effekte beim Wachsen und Kondensieren von Dampfblasen. Dissertation, TU München 1998. Herbert Utz Verlag, München.
51. Picker, G., and Straub, J. (2000). Interfacial mass transfer studies on vapor bubbles in microgravity. In *Proc. United Engineering Foundation Conference, Sept. 1999, Kahuku, Oahu, Hawaii.* Ed. Dhir, 72–79.
52. Pitschmann, P., and Grigull, U. (1970). Film boiling on horizontal cylinders. *Wärme und Stoffübertragung* **3**, 75–84.

53. Plesset, M. S., and Sadhal, S. S. (1979). An analytical estimation of the microlayer thickness in nucleate boiling. *J. Heat Transfer* **101**, 180–182.
54. Plesset, M. S., and Zwick, S. A. (1954). Growth of vapor bubbles in superheated liquids. *J. Appl. Phys.* **25**, 493–500.
55. Qiang, B., and Fujita, Y. (2000). Numerical simulation of bubble growth in reduced gravity. In *Proc. United Engineering Foundation Conference, Sept. (1999), Kahuku, Oahu, Hawaii*. Ed. Dhir, 136–142.
56. Rohsenow, W. M. (1952). A method of correlating heat transfer data for surface boiling of liquids. *Trans. ASME, Ser. C, J. Heat Transfer* **74**, 969–976.
57. Scriven, L. E. (1959). On the dynamics of bubble growth. *Chem. Eng. Sci. Genie Chim.* **10**, 1–13.
58. Sefiane, K., Benielli, D., and Steinchen, A. (1998). A new mechanism for pool boiling crises, recoil instability and contact angle influence. *Colloids Surf.* **142**, 361–373.
59. Siegel, R. (1967). Effects of reduced gravity on heat transfer. In *Advances in Heat Transfer*, Vol. 4 (T. F. Irvine, Ed.), pp. 143–228. Academic Press, New York.
60. Singh, S., and Dhir, V. K. (2000). Effect of gravity, wall superheat, and liquid subcooling on bubble dynamics during nucleate boiling. In *Proc. United Engineering Foundation Conference, Sept. (1999) Kahuku, Oahu, Hawaii*. Ed. Dhir, 106–113.
61. Son, G., and Dhir, V. K. (1998). Numerical simulation of a single bubble during partial nucleate boiling on an horizontal surface. In *Heat Transfer 1998, Proceedings of 11th IHTC, Kyongju, Korea*, Vol. 2, pp. 533–538.
62. Son, G., Dhir, V. K., and Ramanujapu, N. (1999). Dynamics and heat transfer associated with a single bubble during nucleate boiling on a horizontal surface. *J. Heat Mass Transfer* **121**, 1–9.
63. Steinle, H. F., and Schwartz, E. W. (1959). An experimental study of the transition from nucleate to film boiling under zero gravity conditions. Convair Astronautics Report No. AZJ-55-009.
64. Steinbichler, M. (2000). Experimentelle Untersuchung des gesättigten und unter-kühlten Siedens an Miniaturheizflächen unter Mikrogravitation. Dissertation, TU München.
65. Steinbichler, M., Micko, S., and Straub, J. (1998). Nucleate boiling heat transfer on small hemispherical heaters and a wire under microgravity. In *Heat Transfer 1998, Proc. of the 11th IHTC, Kyongju, Korea*, Vol. 2, pp. 539–544.
66. Stephan, K., and Abdelsalam, M. (1980). Heat transfer correlation for natural convection boiling. *Int. J. Heat Mass Transfer* **23**, 73–87.
67. Stephan, P. C. (1992). Wärmedurchgang bei Verdampfung aus Kapillarrillen in Wärmerohren. *Fortschr. Ber. VDI*, Series 19, No. 59. VDI Verlag, Düsseldorf.
68. Stephan, P., and Hammer, J. (1994). A new model for nucleate boiling heat transfer. *Heat Mass Transfer* **30**, 119–125.
69. Stralen, S. van, and Cole, R. (1972). *Boiling Phenomena I, II*. Hemisphere Publishing, London.
70. Straub, J. (1993). The role of surface tension for two-phase heat and mass transfer in the absence of gravity. In *Third World Conference on Experimental Heat Transfer, Fluid Mechanics, and Thermodynamics, Honolulu, Hawaii, October 1993; Exp. Therm. Fluid Sci.* **9**, 253–273 (1994).
71. Straub, J. (1995). The micro wedge model: A physical description of nucleate boiling without external forces. In *Materials and Fluids under Low Gravity* (L. Ratke, Ed.). European Symposium on Gravity Dependent Phenomena in Physical Sciences. Springer, Berlin, 1996.
72. Straub, J. (2000). Microscale boiling heat transfer under 0g and 1g conditions. *Int. J. Therm. Sci.* **39**, 490–497.

73. Straub, J., and Micko, S. (1996). Boiling on a wire under microgravity conditions — First results from a space experiment, performed in May 1996. In *Proc. Eurotherm. Seminar No. 48, Paderbom, Germany*, pp. 275–282. Edizioni ETS, Pisa, Italy.

74. Straub, J., Winter, J., Picker, G., and Zell, M. (1995). Boiling on a miniature heater under microgravity — A simulation for cooling of electronic devices. In *Proc. 30th National Heat Transfer Conf., Portland, OR, 1995*. ASME HDT 1995, Vol. 305, pp. 61–69.

75. Straub, J., Zell, M., and Vogel, B. (1990). Pool boiling in a reduced gravity field. In *Proc. 9th Int. Heat Transfer Conf.* (G. Hetserony, Ed.), pp. 129–155. Hemisphere, New York.

76. Straub, J., Zell, M., and Vogel, B. (1992). Boiling under microgravity conditions. In *Proc. First European Symposium Fluids in Space, Ajaccio, France, 1991*, ESA SP-353.

77. Sun, K. H., and Lienhard, J. H. (1970). The peak pool boiling heat flux on horizontal cylinders. *Int. J. Heat Mass Transfer* **13**, 1425–1439.

78. Suzuki, K., Koyama, Y., and Kawamura, H. (1999). A contribution towards burnout heat flux in microgravity. In *Proc. United Engineering Foundation Conference: Microgravity Fluid Physics and Heat Transfer, Sept. 1999, Kahuku, Oahu, Hawaii*. Ed. Dhir, 144–150.

79. Vogel, B. (1994). Analyse der Energieströme beim Sieden unter Schwerelosigkeit. Dissertation, TU München.

80. Walter, H. U. (Ed.) (1987). *Fluid Science and Material Science in Space*. Springer-Verlag, Berlin.

81. Wayner, P. C., Tung, C. Y., Tirumala, M., and Yang, J. H. (1985). Experimental study of evaporation at the contact line region of a thin film of Hexan. *J. Heat Transfer* **107**, 182–189.

82. Wayner, P. C. (1992). Evaporation and stress in the contact line region. In *Proc. Engineering Foundation Conference on Pool and Flow Boiling, Santa Barbara, CA* (V. K. Dhir and A. E. Bergles, Eds.), pp. 251–256.

83. Weinzierl, A. (1984). Untersuchung des Wärmeübergangs und seiner Transport-mechanismen bei Siedevorgängen unter Schwerelosigkeit. Dissertation, TU München.

84. Weinzierl, A., and Straub, J. (1982). Wärmeübergang mit Blasenbildung-Ergebnisse des TEXUS-IIIb-Experiments. *Z. Flugwiss. Weltraumf.* **6**, 339–343.

85. Winter, J. (1998). Kinetik des Blasenwachstums. Dissertation, TU München.

86. Yagov, V. V., and Zudin, Y. B. (1994). Mechanistic model for nucleate boiling crisis at different gravity fields. *Heat Transfer 1994*. In *Proc. IHTC-10*, Vol. 5, pp. 189–195.

87. Zell, M. (1991). Untersuchung des Siedevorgangs unter reduzierter Schwerkraft. Dissertation, TU München.

88. Zell, M., and Straub, J. (1987). Microgravity pool boiling-TEXUS and parabolic flight experiments. In *Proc. 6th European Symposium on Material Sciences under Microgravity Conditions, Bordeaux, France, 1986*, ESA SP-256, pp. 155–160.

89. Zell, M., Straub, J., and Vogel, B. (1989). Pool boiling under microgravity. *J. Physico-Hydrodynamics* **11**, 813–823.

90. Zeng, L. Z., Klausner, J. F., and Mei, R. (1993). A unified model for the prediction of bubble detachment diameters in boiling systems: I. Pool boiling. *Int. J. Heat Mass Transfer* **36**, 2261–2270.

91. Zuber, N. (1959). Hydrodynamic aspect of boiling heat transfer. Dissertation AECU-4439, Research Laboratory Los Angeles and Ramo-Woolbridge Corporation, UCLA.

92. Zuber, N., Tribus, M., and Westwater, J. W. (1961). Hydrodynamic crisis in pool boiling of saturated and subcooled liquids. In *IHTC, Boulder*, pp. 230–236.

Heat Transfer and Fluid Flow in Rotating Sealed Cavities

WEI SHYY and MICHAEL P. EBERT*

Department of Aerospace Engineering, Mechanics, and Engineering Science
University of Florida
Gainesville, Florida 32611

Abstract

Fluid flow and heat transfer between rotating disks is of practical engineering interest. It is also a topic that has attracted longstanding interest and debate in the research community. We first review the basic studies for infinite rotating disk flows, especially the different speculations reached by Batchelor, i.e., non-zero bulk flow velocity, and by Stewartson, i.e., zero bulk flow velocity. Then, we present the analytical, numerical, and experimental studies reported in the literature for both finite unshrouded and sealed disk flows. Geometric configurations, flow parameters (Reynolds and rotational Grashof numbers) and flow regimes considered in these studies are investigated. It is found that depending on the flow regimes (turbulent versus laminar) and the end-wall effect (shrouded versus unshrouded), either Batchelor or Stewartson type of flow exists. Scaling and correlations of the velocity and temperature length scales as well as heat transfer effectiveness are also discussed in terms of Reynolds and rotational Grashof numbers. Issues related to turbulence modeling for treating rotational effects are also presented.

I. Introduction

Fluid flow and heat transfer between rotating disks is of great interest to the gas turbine industry. In a quest for higher thermal efficiencies, turbine inlet temperatures have steadily increased. These high temperatures compromise the overall durability of the mechanical components in gas turbine engines. Specifically, engineers are concerned with material stresses, fatigue life, and radial growth of turbine disks. In order to address these issues,

*Present address: Naval Surface Warfare Center, Carderock, Division, West Bethesda, Maryland 20817.

knowledge of the temperaure and heat flux distribution inside the disks is needed. Accurate disk temperature distributions can be obtained only when the boundary conditions to which the disk is subjected are known. These thermal boundary conditions depend on the fluid dynamic and heat transfer characteristics of the gas-filled cavities that surround the turbine disks. Gas turbine engines contain gas-filled cavities between turbine disks and a stationary casing or another rotating disk. Figure 1 shows a typical cross-section of a gas turbine and the cavity that is formed between two rotating turbine disks, the shaft and the hub. Typically, air extracted from the compressor is passed through these disk cavities and then used to cool the turbine blades that are located downstream of the combustor. The extraction of this cooling air from the compressor imposes a performance penalty on the engine from the point of view of fuel economy. It is therefore desirable to minimize the amount of cooling air needed to ensure proper performance of the turbine blades. Optimizing the amount of compressed air again requires an understanding of the flow and heat transfer characteristics in the turbine disk cavities.

The prediction of fluid flow and heat transfer in rotating cavities in real gas turbine geometries is a complicated task. Before undertaking such an effort, it is useful to first understand the physical mechanisms underlying simple cavity systems. The essential features of the flow and heat transfer can be modeled using rotating disk systems in which plane disks represent the more complex turbine disk geometries found in actual engines. Prediction of such basic flows will assist in the development of suitable physical models for the more complex flows and geometries occurring in real gas turbines, and guide the development of computational algorithms for such applications. Model geometries used in many theoretical, experimental, and numerical investigations of turbine disk cavities include plane cylindrical or annular cavities. Figure 2 shows a schematic of the general geometric layout for such a cavity. The figure depicts an annular cavity characterized by an inner radius of $r_{\min}$, an outer radius of R, and an axial width designated as h. The axis of rotation is customarily coincident with the z-axis with part of or the whole system rotating with angular speed Ω. The cylindrical cavity can be viewed as a special case of the annular cavity where the inner radius $r_{\min}$ is allowed to go to zero. The walls that form the cavity consist of two disks that are perpendicular to the z-axis and one or two cylindrical walls, often called shrouds, for a cylindrical and annular cavity, respectively. The axis system indicated in Fig. 2 is the familiar Cartesian system, which may or may not rotate with the cavity. It is often convenient to use a cylindrical coordinate system with r defined as the radial coordinate and z remaining as the axial coordinate. In the cylindrical coordinate system the geometry can often be simplified even further, because of its axisymmetry, to the two-dimensional geometry defined to be the cross-section (rz-plane) of the cavity.
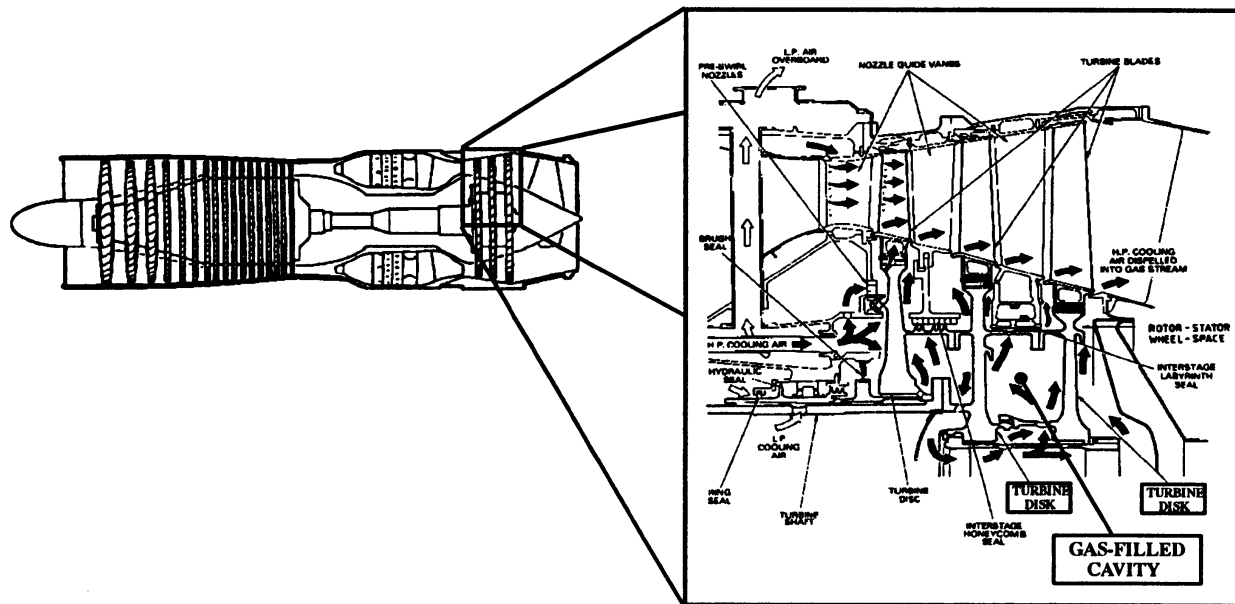
FIG. 1. Sketch of a gas turbine engine with detailed view of a cavity found between two rotating turbine disks.
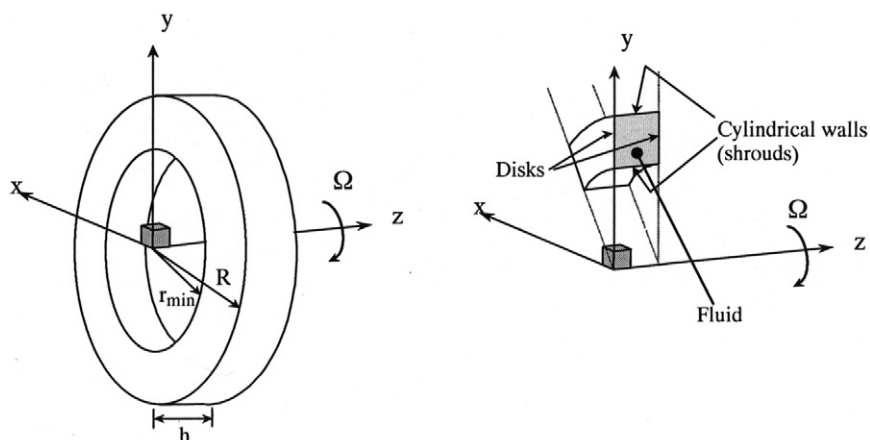
FIG. 2. Schematic of simplified rotating cavity geometry.

A large number of situations can be developed based solely on the velocity boundary conditions specified for the confining walls of the cavity. These situations can in general be classified into three types: (1) fully rotating, (2) rotor–stator, and (3) differentially rotating. The most straightforward of these is the fully rotating type in which all the confining walls rotate at the angular speed Ω. The rotor–stator type consists of one of the disks rotating at the angular speed Ω while the other disk remains stationary. For the rotor–stator disk system many different conditions can be imposed on the cylindrical confining walls, the most common of which are illustrated in Fig. 3. In Fig. 3a the cylindrical walls are held completely stationary; in Fig. 3b the cylindrical confining walls are split into a portion that rotates with the rotating disk and a portion that is held stationary. Another possibility, which is depicted in Fig. 3c, is that the whole of the cylindrical confining walls rotate with angular speed, Ω, of the rotor. The differentially rotating type of configuration can be further broken down into two categories, corotating and contrarotating. For the differential corotating configuration, the two disks rotate in the same direction but at different angular speeds, whereas the differential contrarotating configuration is established when the two disks are rotating in opposite directions. Situations analogous to those depicted in Fig. 3 can be conceived for the cylindrical walls for both of these differentially rotating configurations. The fluid confined within the cavity is set in motion relative to an inertial reference frame in all the cases just discussed because of the viscous property of the fluid combined with the motion of one or more of the confining walls. The most fundamental of flows results in the case of a fully rotating configur-
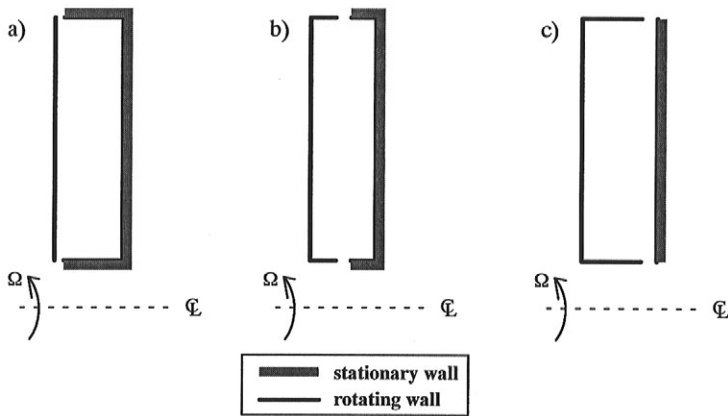
FIG. 3. Cavity cross-sections for three common situations encountered for rotor–stator-type configurations: (a) fully stationary cylindrical walls, (b) partially rotating, partially stationary cylindrical walls, and (c) fully rotating cylindrical walls.

ation. An isothermal fluid confined in such a cavity tends to a state of solid body rotation.

To introduce the effects of forcing cooling air through these cavities, a number of superimposed throughflow configurations can be devised. The throughflow configuration is chosen such that the simplified cavity problem will model the major characteristics of an actual configuration found inside a turbine engine. Some of the common throughflow configurations for cylindrical and annular cavities are illustrated in Fig. 4. These configurations can be identified as ones that are typically used either for simplified models of turbine cavities or for simplified models of compressor cavities. For modeling of turbine disk cavities, cooling air is generally forced through the cavity in a radially outward fashion, thereby allowing the cooling air exiting the cavity to be easily routed through the turbine blades. Figures 4a and 4b illustrate cylindrical cavities that are characterized by axial inlets and radial outlets; Figs. 4d and 4e illustrate annular cavities that have radial inlets for the superimposed cooling air. A common configuration used to model the flow inside a compressor cavity, formed between two compressor disks, in which cooling air is extracted from the mainstream, is shown in Fig. 4f. This configuration is characterized by a radial inlet through the outer shroud of the cavity and a uniform radial outlet through the inner cylindrical boundary. Sometimes the cooling air flows axially through radial clearances between compressor disks and the shaft in the process of being transported to the turbine stage of the engine. Figure 4c illustrates a
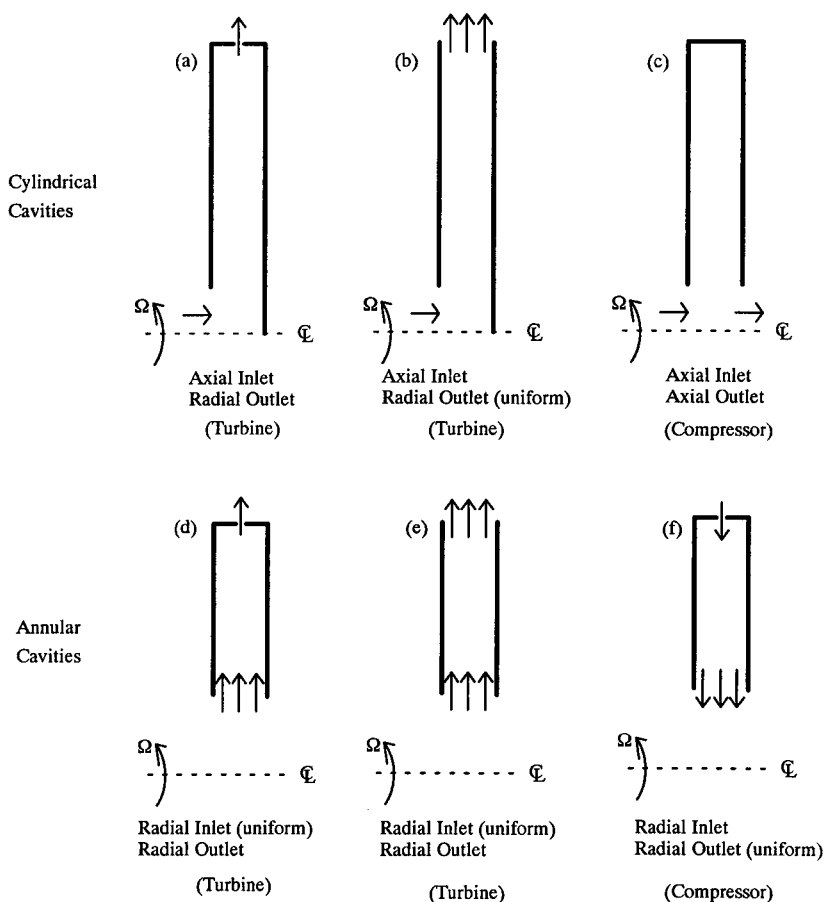
FIG. 4. Schematic of some common turbine and compressor cavity throughflow configurations.

simplified model that is often used for modeling flows in these cavities and is characterized by an axial inlet and outlet adjacent to the axis of rotation and a solid shroud.

The situations and configurations discussed so far can be used to investigate cavities with isothermal and nonisothermal boundary conditions. With heat transfer imposed on the fluid, variations in density will give rise to buoyancy forces in the presence of an acceleration field, which for rotating flows is always present in the form of centripetal acceleration. The coupled effects of buoyancy and rotation can produce complex phenomena

in situations that would otherwise be fairly benign. As an example of this, consider the case when a fluid is confined in a completely rotating cavity. As discussed previously, an isothermal fluid will tend to a state of solid body rotation. However, if a thermal gradient is imposed along the axis of rotation, convection, relative to the solid body motion of the fluid, will be induced by the action of buoyancy forces that result from the accompanying density gradient normal to the centripetal acceleration field. Imposed thermal gradients can usually be classified in studies of rotating cavities as being either axial or radial. Figure 5 summarizes the various configurations and possible combinations of thermal boundary conditions and throughflow arrangements.

In this review, we summarize the existing literature on both fluid flow and heat transfer characteristics inside rotating disk systems without a superimposed throughflow (i.e., the left-hand branch of Fig. 5). Both shrouded and unshrouded configurations are considered because the end wall (shroud) affects the fundamental flow structure. In Section II, we discuss the outstanding issues related to the well-known infinite rotating disk flows. In Section III, we summarize the findings for finite unshrouded disk systems. Then, we turn attention to the sealed configurations, including both isothermal sealed cavities (Section IV) and sealed cavities with imposed thermal
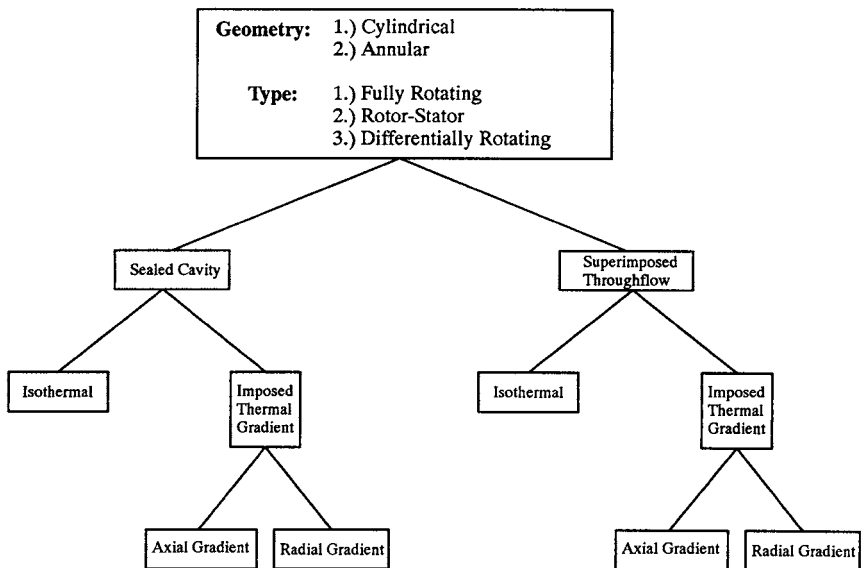
Fig. 5. Classification of rotating disk systems.

gradients (Section V). Turbulence modeling is important for handling the high Reynolds/Grashof number flows typically encountered in practice. In Sections VI and VII, we review the issues and possible concepts for handling the near wall and Reynolds number effects, as well as rotational effects with emphasis on the two-equation turbulence model. Numerical issues related to flows with substantial body force terms, such as the present ones, are assessed in Section VIII. Configurations with throughflows, although practically important, are not addressed here to confine our scope.

II. Infinite Rotating Disk Flows

Most of the earliest published work, regarded as relevant to flows in rotating turbine disk cavities, actually dealt with flow between two infinite rotating disks or even more fundamentally the flow in the neighborhood of a single rotating disk of infinite extent. In 1921 von Kármán [25] showed that for an infinite flat disk rotating at a constant angular speed, Ω, in a nonrotating viscous fluid, with constant properties, the complete set of Navier–Stokes equations can be reduced by a similarity transformation to a set of nonlinear ordinary differential equations that describes the steady flow of the fluid. The set of equations obtained are still not solvable in closed analytical form; however, they are considerably more amenable to numerical or series solution than the full set of nonlinear partial differential equations. Cochran [11] is credited with the first solution of these equations, which he solved using a series expansion. Comprehensive discussions on the solutions to this problem can be found in the books by Owen and Rogers [36] and Schlichting [41]. As described in [41] and illustrated in Fig. 6, a disk of infinite extent rotating with angular speed Ω about an axis perpendicular to its plane will carry a layer of fluid immediately adjacent to its surface. Just above the surface of the disk centifugal forces produce a secondary flow that is directed radially outward. The velocity boundary layer thus has a circumferential and a radial component. In order to replace the mass of fluid driven radially outward by the centrifugal force, an axial flow directed toward the disk is produced, which, from the solution of the ordinary differential equations, graphically depicted in Fig. 7, is found to be of order $(v\Omega)^{1/2}$ far from the disk, where v is the kinematic viscosity. The axial velocity toward the disk, as reported in [36], approaches $0.8845(v\Omega)^{1/2}$. A scaling analysis that balances the viscous and centrifugal forces in the velocity boundary layer described earlier shows that the thickness δ of the velocity boundary layer is proportional to $(v/\Omega)^{1/2}$ and hence independent of the radial distance from the axis of rotation. Also from the solution of the ordinary differential equations, it can be seen that the circumferential
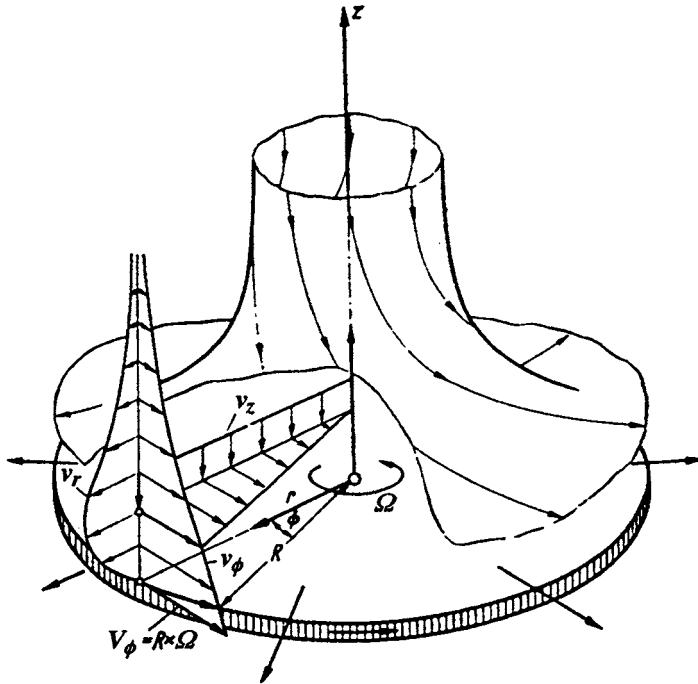
FIG. 6. Flow in the neighborhood of a disk rotating at an angular speed Ω in a fluid at rest. (Velocity components: v_r radial, v_ϕ, circumferential, v_z, axal).
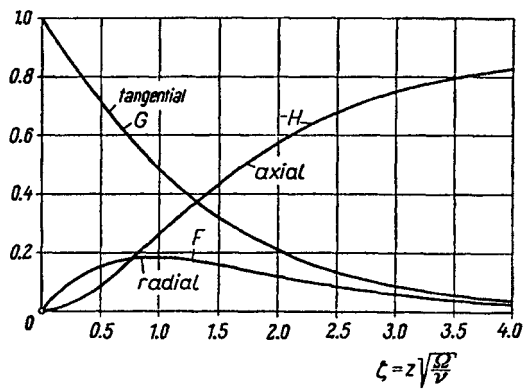
FIG. 7. Velocity distribution near a disk rotating at an angular speed Ω in a fluid at rest ($F = v_r/r\Omega$, $G = v_\phi/r\Omega$, $H = v_z/(v\Omega)^{1/2}$).

velocity is reduced to 50% of the value at the wall at a distance of about $(v/\Omega)^{1/2}$ and that the peak radial velocity is also found at approximately this distance. Schlichting also notes that for Reynolds numbers (Re_r) up to 3.0×10^5, based on the radial distance from the axis of rotation and circumferential velocity of the disk at this radial position, there is excellent agreement between the theoretical solution and the experimental measurements of Theodorsen and Regien [46]; however, at larger Reynolds numbers the flow becomes turbulent. It should be noted that the solution described earlier for the infinite rotating disk in a stationary fluid is not a unique solution to the governing set of nonlinear ordinary differential equations. For further discussion on this point refer to Zandbergen and Dijkstra [53].

In 1951 Batchelor [2] showed that the same similarity transforms used by von Kármán, along with the appropriate set of boundary conditions, could also be used to reduce the equations governing flow between two coaxial infinite rotating disks to a set of nonlinear ordinary differential equations. Batchelor presents qualitative observations about the general nature of the flow between two infinite rotating disks based on physical arguments and general properties of the reduced set of equations. In his paper, Batchelor considers the full range of cases characterized by the ratio of rotating speeds of the two disks $(-1 \leqslant \Gamma = \Omega_2/\Omega_1 \leqslant 1$, where Ω_1 is the faster of the two angular speeds) and in particular discusses situations when the Reynolds number (Re_h), defined as $h^2\Omega_1/v$ where h is the axial distance between the two disks, becomes very large. For the cases where $0 \leqslant \Gamma \leqslant 1$ (i.e., both disks rotate in the same direction) Batchelor explains that the radial velocity will be directed inward near the slower rotating disk and directed outward near the faster disk. He also explains, when considering the circumferential velocity component at large Reynolds numbers, that there would exist a core of fluid between the layers of viscous action adjacent to each disk (boundary or Ekman layers) that behaves like an inviscid body of fluid rotating uniformly at an angular speed somewhere between Ω_1 and Ω_2. Batchelor considered the particular case when $\Gamma = 0$ (i.e., one stationary and one rotating disk) as representative for the range $0 \leqslant \Gamma \leqslant 1$ and developed a sketch of the predicted streamlines for this case. These streamlines are shown in Fig. 8a.

Stewartson [45] acknowledged that experimentally it is found that when the disks are rotating in the same direction, the main body of the fluid does indeed rotate with an angular speed somewhere between Ω_1 and Ω_2. However, for the rotor–stator case $(\Gamma = 0)$, Stewartson presents experimental and theoretical evidence that indicate that the main body of fluid has essentially zero angular velocity. This demands the existence of only one Ekman layer adjacent to the rotating disk and is hence substantially different from the flow described by Batchelor. A sketch of the flow

(a)

Streamlines   Circumferential velocity   Radial velocity

(b)

Streamlines   Circumferential velocity   Radial velocity
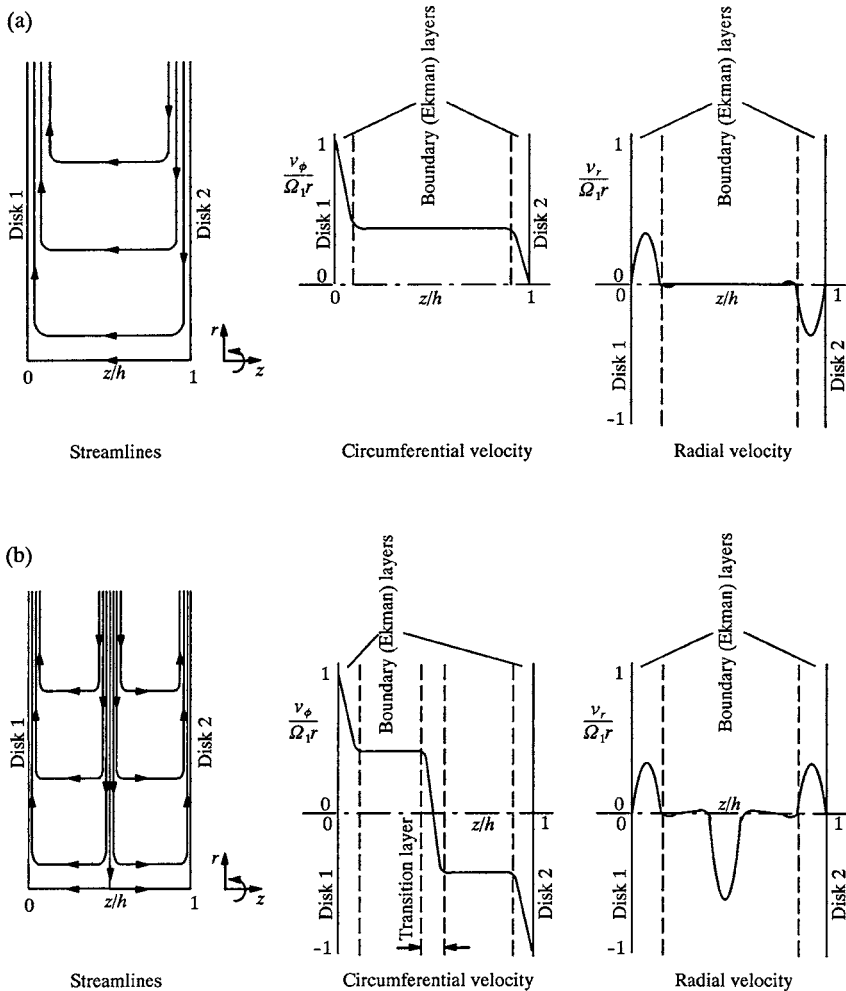
FIG. 8. Streamlines, circumferential velocity, and radial velocity as predicted by Batchelor for large Reynolds number flow between two infinite disks: (a) $\Gamma = 0$; (b) $\Gamma = -1$.

predicted by Stewartson for $\Gamma = 0$ is given in Fig. 9a.

For the cases where $-1 \leqslant \Gamma < 0$ (i.e., the disks rotate in the opposite direction) Batchelor [2] describes a flow in which the radial flow adjacent to each disk is directed outward, with an inward radial flow in the interior of the fluid. Since the flow is radially outward on each disk, the axial velocity
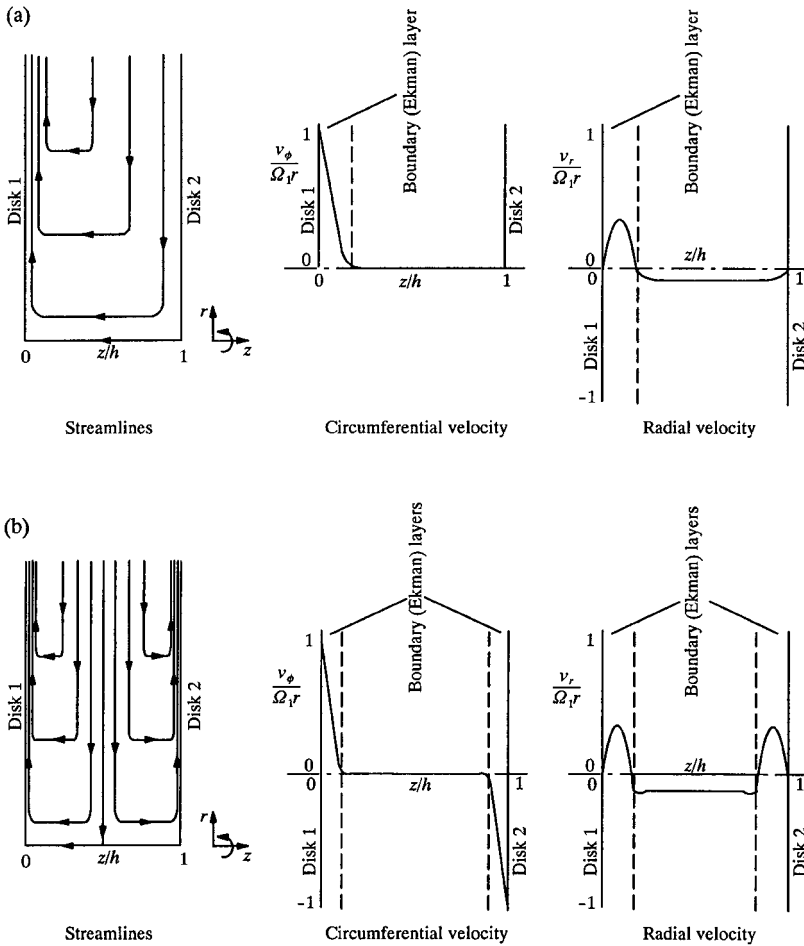
FIG. 9. Streamlines, circumferential velocity, and radial velocity as predicted by Stewartson for large Reynolds number flow between two infinite disks: (a) $\Gamma = 0$; (b) $\Gamma = -1$.

must be directed toward both disks in their immediate neighborhood. Batchelor reasons that two contrarotating cores of fluid exist separated by a viscous transition layer. The flow predicted by Batchelor for $\Gamma = -1$ at large Reynolds numbers is sketched in Fig. 8b.

Stewartson [45] contends that this type of flow is not in agreement either with his series solution of the reduced set of equations for small Reynolds numbers or with the available experimental evidence, which indicate that

again the main body of fluid has essentially no angular velocity. A sketch of the flow predicted by Stewartson for $\Gamma = -1$ is given in Fig. 9b. The conflicting predictions described previously for the flow between two coaxial infinite rotating disks has become known as the Batchelor–Stewartson controversy and has been the subject of many theoretical, experimental, and numerical investigations found in the literature. A review of the research done on this subject up to 1987 has been published by Zandbergen and Dijkstra [54], and a general historical overview of the Batchelor-Stewartson controversy can be found in [36]. The major finding has been that theoretically the structure of the flow between two infinite coaxial rotating disks is not unique, and in fact both Batchelor- and Stewartson-type flows can be found to satisfy the governing set of ordinary differential equations, along with a host of other solutions.

III. Finite Unshrouded Disk Systems

The flow between two infinite disks, though interesting from a theoretical standpoint, is of little practical importance. A considerably more practical problem is that of the flow between two finite coaxial disks. This topic can be subdivided into unshrouded and shrouded disk systems. The unshrouded configuration was crudely studied by Stewartson [45] experimentally using two smooth cardboard disks attached to a lathe. The findings supported his theoretical predictions for the infinite two-disk problem already discussed, in that he found that the fluid core between the two disks rotated for $0 < \Gamma \leqslant 1$, but did not rotate for the rotor–stator case or for the counter-rotating case. In 1958 Picha and Eckert [39] experimentally studied the core flow between two unshrouded coaxial disks with aspect ratios G (axial gap to disk radius, $G = h/R$) between 0.11 and 0.78, and Reynolds numbers (Re_R) between 2.6×10^5 and 11.9×10^5, based on the radius of the disks and the circumferential velocity at the edge of the slower disk. The results confirmed Stewartson's findings. Picha and Eckert also thoroughly studied the circumferential velocity field between two unshrouded disks that are rotating at the same speed and in the same direction. Since the infinite disk solution yields pure solid body rotation for this system, the influence of having only finite disks can easily be observed. It was found that solid body rotation occurred only for small radii and that the circumferential velocity decreased wth increasing radius in the outer portion of the disks, as shown in Fig. 10.

In 1987 Brady and Durlofsky [8] used asymptotic analysis to develop a set of equations applicable to laminar flow between finite disks of arbitrarily small aspect ratio G, as defined earlier. By numerically solving these
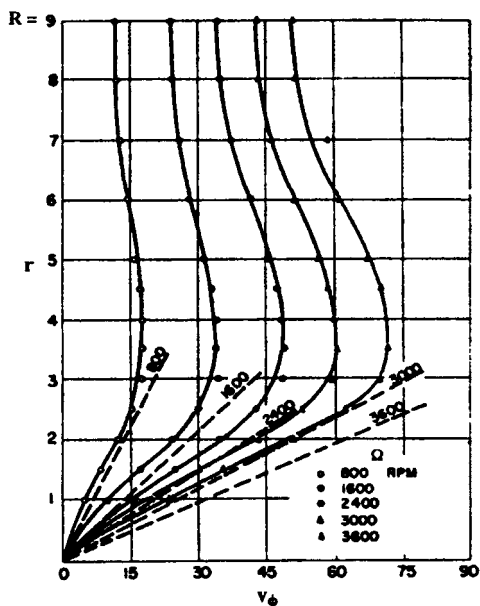
Fig. 10. Circumferential velocity (ft/sec) versus radial distance (in.) from the axis of rotation of the fluid core between two free disks. The two disks rotate with equal angular speed and have a gap to radius ratio (G) of 0.22. (Source: Picha and Eckert [39].)

equations for Reynolds numbers (Re_h) up to 500, they were able to relate their solutions for the velocity and pressure fields to those for the infinite disk problem. The aim of the work was to determine which, if any, of the similarity solutions for the infinite problem (essentially Batchelor-type or Stewartson-type) describes the flow over a portion of the domain between finite rotating disks. They found that their solutions also agreed with Stewartson-type flow in regions close to the axis of rotation for the rotor–stator and contrarotating cases. Near the outer edge, the effect of the end, as expected, is important and the flow is not of similarity form. They found, however, that this effect of the finite end boundary condition is not confined to a region near the outer portion of the disks and that the solutions are only quantitatively in agreement with Stewartson's infinite disk solution in a small region near the axis of rotation. The influence of the end condition was found to penetrate further inward from the edge with increasing Reynolds number.

In 1992 Bhavnani *et al.* [3] published experimental measurements of the

velocity field for an unshrouded rotor–stator configuration at a Reynolds number (Re_R) of 9.6×10^5 and an aspect ratio of 0.072. The results given indicate that at this Reynolds number the flow is of the type described by Batchelor. The connection between the Stewartson-type flow found in the works discussed earlier and the Batchelor-type flow seemingly found by Bhavnani *et al.*, for the finite, unshrouded, rotor–stator case is unclear. However, it seems likely to be tied together with the transition from laminar to turbulent flow. It should also be pointed out that the aspect ratio used by Bhavnani was smaller than that for any of the results reported by Picha and Eckert.

IV. Isothermal Sealed Cavities

This section reviews the work that has been done for cavities (i.e., shrouded disk systems) in which there is no fluid forced through the cavity and for which no thermal gradients are imposed across the cavity. These flows correspond to the leftmost branch of Fig. 5. The most basic configuration of this type is the fully rotating cavity, for which the confined fluid obtains a state of solid body rotation at steady-state conditions. This configuration is not considered any further. Picha and Eckert [39] considered the flow inside a cavity that consisted of two coaxial disks rotating at the same speed and in the same direction and a completely stationary cylindrical shroud. Clearly secondary flows develop due to the no-slip condition on the shroud and the disks. It was observed that the radial extent of the inner core where solid body rotation occurred was larger with the stationary shroud than in the corresponding experiment previously discussed without the shroud. Morse [35] also considered this configuration in a numerical study of laminar–turbulent transition in closed rotating disk geometries. It is organizationally convenient and helpful in generating comparisons between similar studies to divide the remaining discussion of isothermal sealed cavities into the following two sections: (1) rotor–stator and (2) contrarotating.

A. Rotor–Stator

Picha and Eckert [39] also studied the flow inside a cavity that consisted of one stationary disk, one rotating disk, and a completely stationary cylindrical shroud. For this configuration they found that a definite core rotation was established near the axis of rotation. This is in contrast with their findings for the unshrouded case discussed earlier and indicates that the presence of a stationary shroud promotes Batchelor-type flow for the
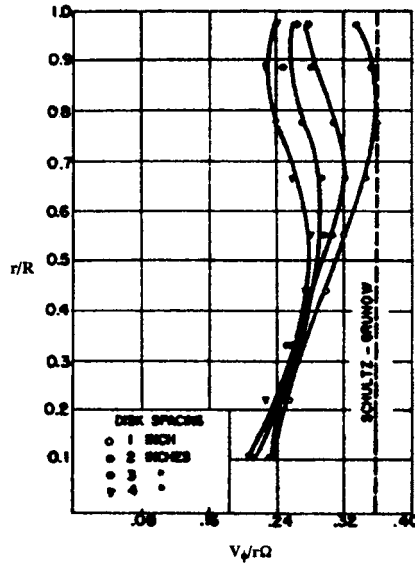
FIG. 11. Nondimensional circumferential velocity of the fluid core versus nondimensional radial distance from the axis of rotation between two shrouded disks, one rotating with angular speed Ω and one stationary. The shroud at $r = R$ is stationary. (Source: Picha and Eckert [39].)

rotor–stator case. The measured circumferential velocity in the fluid core, normalized by the local velocity of the rotor, as a function of the normalized radial distance from the axis of rotation is given in Fig. 11. It was found that for a given disk spacing the measured nondimensional circumferential core velocity when Ω, the angular speed of the rotating disk, was 1600, 2400, 3000, and 3600 rpm essentially correlated onto a single curve.

In 1960 Daily and Nece [13] also investigated enclosed rotor–stator flows with a completely stationary shroud. They performed theoretical and experimental studies of cavities with aspect ratios between 0.0127 and 0.217. The experiments concentrated on measuring disk-friction torque for Reynolds numbers (Re_R) in the range of 10^3–10^7 with the goal of developing theoretical predictions for the effect of cavity proportions on disk friction. They identified four different modes of flow that are possible depending on the combination of aspect ratio and Reynolds number: (I) laminar flow, merged boundary layers, (II) laminar flow, separate boundary layers, (III) turbulent flow, merged boundary layers, and (IV) turbulent flow, separate boundary layers. Figure 12 shows representative results from the experimental measurements of the rotor torque coefficient, C_m, versus Reynolds

number for a fixed aspect ratio. The different modes discussed earlier are identified by comparing the experimental data with theoretical predictions for the C_m versus Reynolds number corresponding to each of the four modes individually. For the case when $G = 0.0255$, Fig. 12a indicates that all four modes can be achieved; however, Fig. 12b indicates that for $G = 0.115$ only modes II and IV are present. On the basis of their experimental data, Daily and Nece developed an empirical relationship for the torque coefficient for each mode. Using these empirical expressions, Owen and Rogers [36] developed a graphical map of these four modes in the two-parameter space of Reynolds number and aspect ratio. This map is shown in Fig. 13 and indicates that for separate boundary layers, the transition to turbulent flow in the rotor boundary layer is predicted to occur at a Reynolds number of about 1.5×10^5. For modes II and IV, Daily and Nece found that core rotation was confirmed, again indicating that Batchelor-type flow existed. For mode IV it was found that boundary layer thicknesses increase with radius on both the rotor and stator and that the angular speed of the core rotation decreased as the aspect ratio decreases and the Reynolds number is held constant.

Numerical investigations of rotor–stator configurations were conducted by Pao [37], Lugt and Haussling [34], and Dijkstra and van Heijst [15] using stream-function vorticity methods to solve the full system of governing partial differential equations. In 1970 Pao [37] computed the flow field for a configuration in which the cylindrical shroud was attached to the rotor. The numerical procedure used by Pao was only able to compute the steady-state solution for Reynolds numbers (Re_h) up to 200, but some results are shown for time-dependent calculations at early times for Reynolds numbers up 5000. Lugt and Haussling [34] and Dijkstra and van Heijst [15] extended Pao's work and obtained numerical results for laminar flow in the same configuration. Dijkstra and van Heijst, in particular, have given a relatively extensive computational and experimental study of the rotor–stator case for an aspect ratio of 0.07 and for Reynolds numbers (Re_h) up to 1000. The general character of the flow as described by Dijkstra and van Heijst inside an enclosed rotor–stator disk system can be outlined as follows. For sufficiently high Reynolds numbers, boundary or Ekman layers form on each disk. The fluid in the layer adjacent to the rotating disk is carried radially outward owing to centrifugal action. As this fluid approaches the enclosing shroud, it is forced to produce a thin layer of fluid adjacent to the shroud that moves axially across the cavity toward the stationary disk. The fluid in the Ekman layer adjacent to the stationary disk moves radially inward while, through the core region of the cavity, fluid moves axially toward the rotating disk in order to replace the fluid that is being carried radially outward. From this description it is clear that Batchelor-type flow
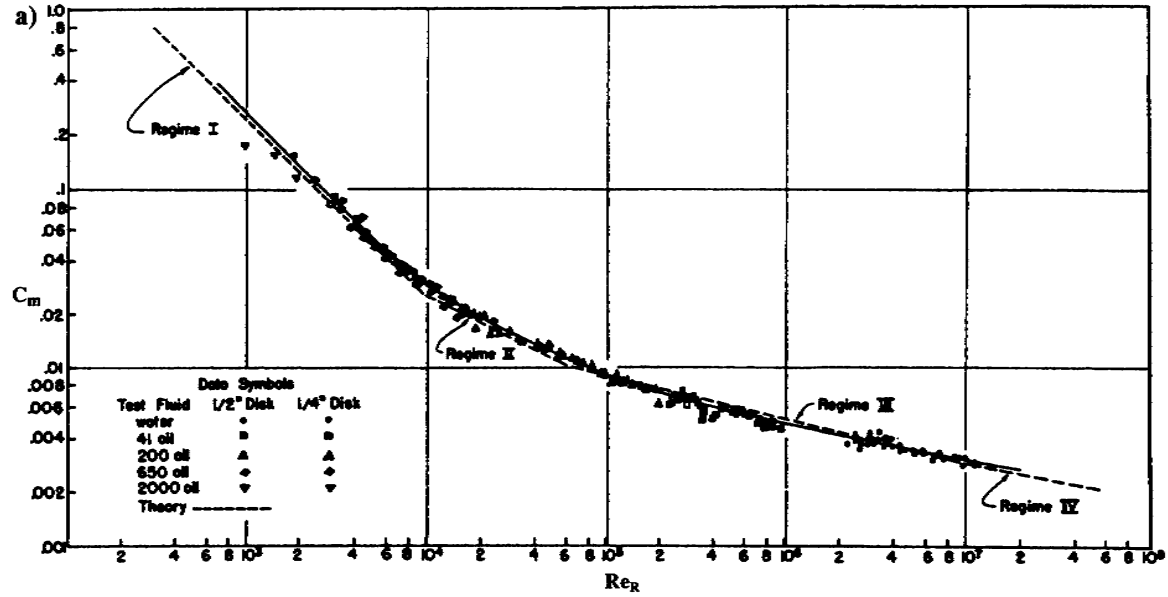
FIG. 12. Torque coefficient data versus Reynolds number for a smooth rotor disk that forms one wall of a rotor–stator cavity of aspect ratio (a) $G = 0.0255$, (b) $G = 0.115$ (shown on following page). (Source: Daily and Nece [13].)
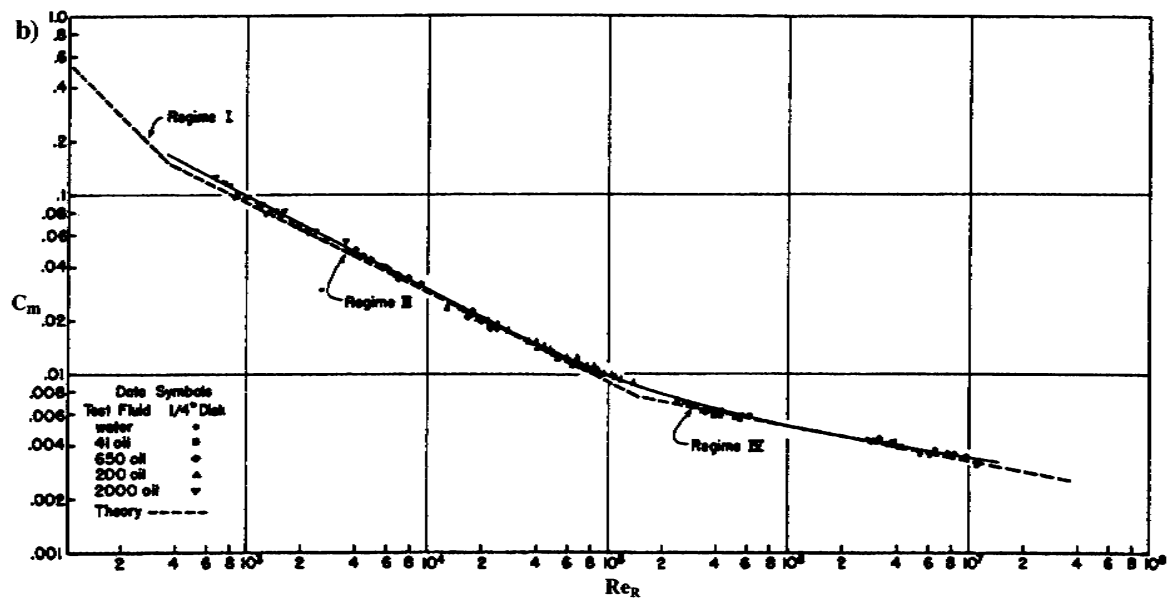
FIG. 12b.
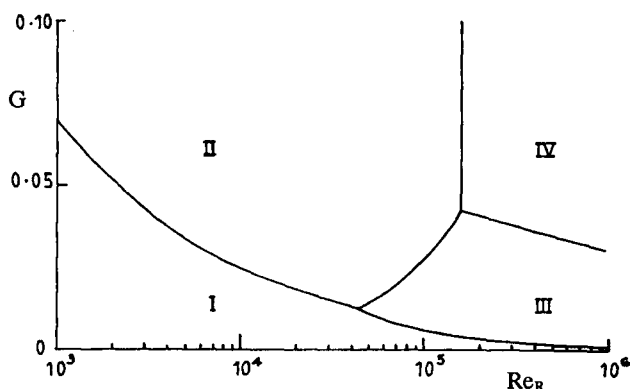
FIG. 13. Map of the four regions for which the flow between a shrouded rotor–stator system may be classified: (I) laminar flow, merged boundary layers, (II) laminar flow, separate boundary layers, (III) turbulent flow, merged boundary layers, and (IV) turbulent flow, separate boundary layers.

was found. Figure 14 shows the numerical results of Dijkstra and van Heijst for the stream-function, vorticity, and azimuthal velocity at a Reynolds number of 100 based on the axial gap distance; the corresponding results for Reynolds number of 1000 are given in Figure 15. Figure 16 gives a comparison between Dijkstra and van Heijst's numerically calculated circumferential velocity profiles and their experimental data. The experimental data is given for small radius intervals because the experimental technique, in which small tracer particles were randomly distributed in the cavity and resulted in an insufficient number of particles at a given radius.

More recent computational work in the study of sealed cavities has applied numerical methods based on the primitive variable formulation of the full set of partial differential equations. In 1991 Williams *et al* [51] studied rotor–stator systems with various aspect ratios using such a method for both laminar ($Re_R = 4.2 \times 10^4$) and turbulent ($Re_R = 4.4 \times 10^6$) flows. Williams *et al.* used the experimental results of Daily and Nece [13] for validation of their numerical technique and applied both a standard high and a low Reynolds number k–ε turbulence model for closure. Figure 17 indicates results for the circumferential and radial velocity variation in cavities with aspect ratios of 0.0255 and 0.0637 at $Re_R = 4.4 \times 10^6$. From this figure it can be seen that both turbulence models do a reasonable job of predicting the tangential and radial velocity profiles. However, Fig. 18 shows that the low Reynolds number turbulence model tended to over-predict the disk torque coefficient by more than 30%, while the prediction
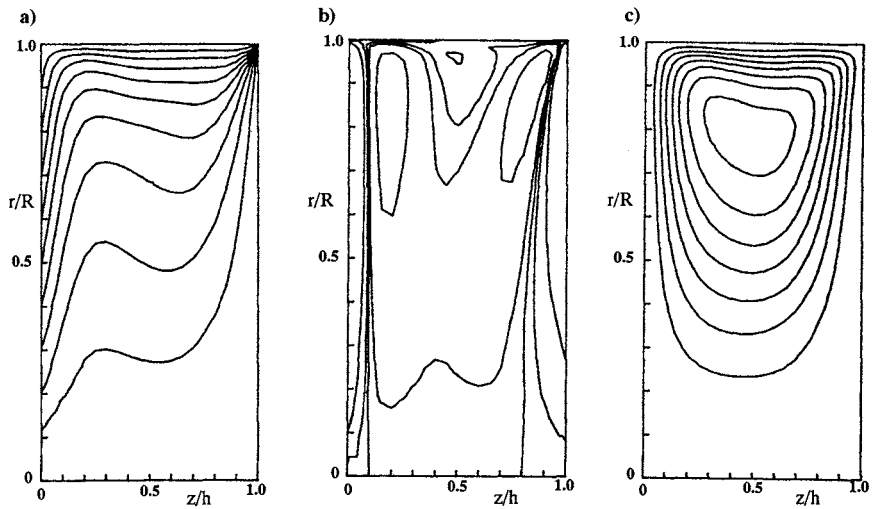
FIG. 14. Numerical results for an enclosed rotor–stator system. The disk at $z/h = 0$ and the shroud at $r/R = 1.0$ rotate about the z-axis with angular speed Ω while the disk at $z/h = 1.0$ remains stationary in an inertially fixed reference frame. The results are for $Re_h = 100$ (based on the axial gap). (a) Lines of constant circumferential velocity; (b) lines of constant vorticity; (c) streamlines. (Source: Dijkstra and van Heijst [15], with permission of Cambridge University Press.)

of C_m with the high Reynolds number model is within 10% of the experimentally determined values. Williams *et al.* also found that for the cases they studied the high Reynolds number turbulence model was more efficient in terms of computing and grid point costs than the low Reynolds number model.

In 1991, Morse [35] published a numerical study of a rotor–stator configuration for which the main focus was to investigate the transition from laminar to turbulent flow that occurs with increasing Reynolds number, and also with increasing radius for a given Reynolds number, and how to accurately model this transition. To facilitate this study, Reynolds numbers (Re_R) in the range of 10^5–10^7 were simulated for cavities with aspect ratios, G, of 0.0685 and 0.11. Morse used an anisotropic low-turbulence Reynolds number k–ε model that included an artificial energy source based on a mixing length model to effect transition. Predicted profiles of the radial and circumferential velocities including comparisons with experimental data for a Reynolds number of 6.9×10^5 are shown in Fig. 19 and indicate the behavior of the transition from laminar to turbulent flow along the rotor. In this figure, the numerical results obtained for purely laminar flow are
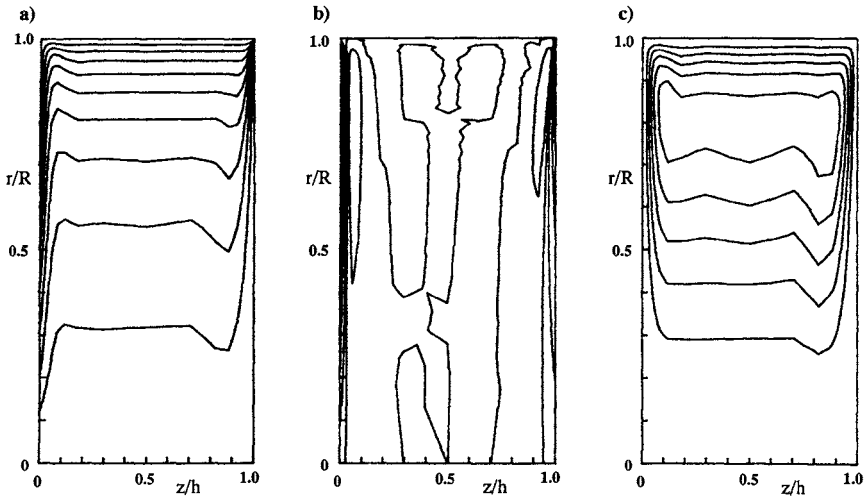
FIG. 15. Numerical results for an enclosed rotor–stator system. The disk at $z/h = 0$ and the shroud at $r/R = 1.0$ rotate about the z-axis with angular speed Ω while the disk at $z/h = 1.0$ remains stationary in an inertially fixed reference frame. The results are for $Re_h = 1000$ (based on the axial gap). (a) Lines of constant circumferential velocity; (b) lines of constant vorticity; (c) streamlines. (Source: Dijkstra and van Heijst [15], with permission of Cambridge University Press.)
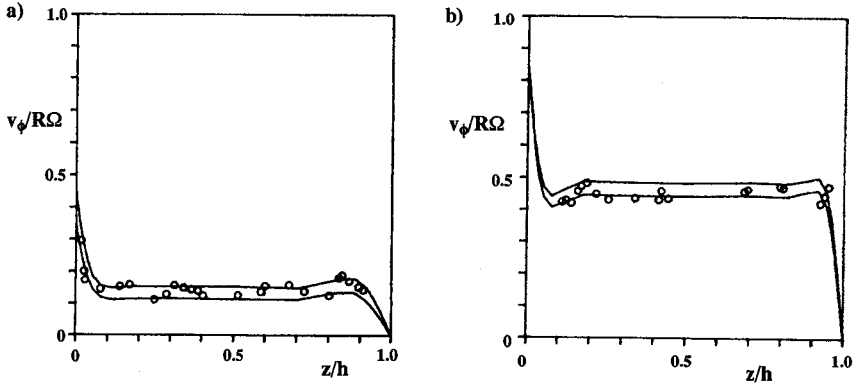
FIG. 16. Comparison between experimental ($\bigcirc$) and numerical (——) results for the circumferential velocity in a rotor–stator system in which the disk at $z/h = 0$ and the shroud at $r/R = 1.0$ rotate about the z-axis with angular speed Ω while the disk at $z/h = 1.0$ remains stationary in an inertially fixed reference frame. The results are for $Re_h = 1000$ at (a) $0.36 \leqslant r/R \leqslant 0.45$ and (b) $0.84 \leqslant r/R \leqslant 0.87$. (Source: Dijkstra and van Heijst [15], with permission of Cambridge University Press.)
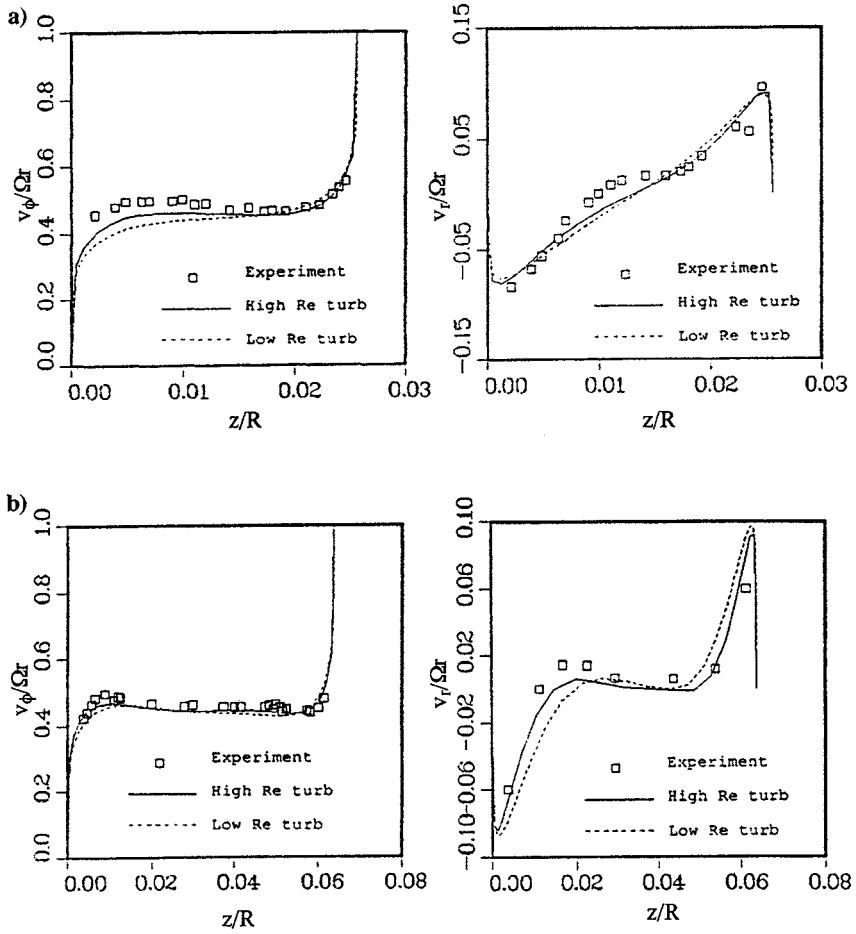
FIG. 17. Comparison between experimental and numerical results for the circumferential (v_ϕ) and radial (v_r) velocities in a rotor–stator system in which the disk at axial location $z/R = 0$ and the shroud at $r = R$ remain stationary and the disk at (a) $z/R = 0.0255$ and (b) $z/R = 0.0637$ rotates about the x-axis with angular speed Ω. The results are for $Re_R = 4.4 \times 10^6$ at a radial location given by $r/R = 0.765$. (Source: Williams et al. [51].)

shown by the dashed lines and serve as a guide to assess transition effects. It can be seen that at the nondimensional radial location $r/R = 0.47$, Morse's turbulence model just begins to show signs of transition along the rotor, located at $z/h = 1.0$, while turbulence appears to be already well established, and well captured by the model, in the boundary layer adjacent
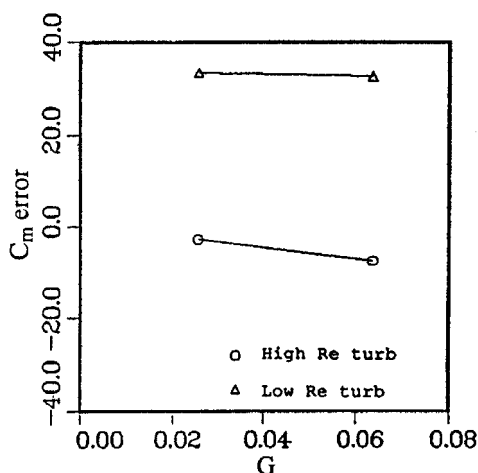
FIG. 18. Comparison of error in the numerical predictions of the rotor torque coefficient (C_m) in a rotor–stator disk system. The error between experimentally determined torque coefficients and the predicted values using high and low Reynolds number turbulent models are shown. The results given are for simulations performed for cavities with aspect ratios of 0.0255 and 0.0637. The Reynolds number (Re_R) is 4.4×10^6. (Source: Williams et al. [51].)

to the stator, located at $z/h = 0$. Because of the existence of turbulence, the boundary layer adjacent to the stator is appreciably thicker and the region of reversed flow, which is quite distinct in the laminar result, is much less pronounced. At the two larger values of r/R shown in Fig. 19 the flow appears to have become fully turbulent along the rotor. The overall agreement with the experimental data is good. To study the effect of Reynolds number, Morse presented results for the variation with Reynolds number of the angular velocity of the fluid midway between the two disks, from which he determined that the first definite signs of transition to turbulent flow over the rotor occurred at $Re_R = 4 \times 10^5$.

Gan and MacGregor [19] have published an experimental investigation of a rotor–stator disk system using laser-Doppler anemometry. For their investigation the shroud was split midway between the rotor and stator disks, allowing half to rotate with the rotor and the other have to remain stationary. The results are consistent with previous investigations using hot-wire anemometry and with theoretical predictions. It was observed that the inviscid core has an angular speed of approximately 40% of the rotor speed in the majority of the cavity for both laminar and turbulent flow. This can also be seen by examining Fig. 17.

• Data of Daily, Ernst and Asbedian [12]
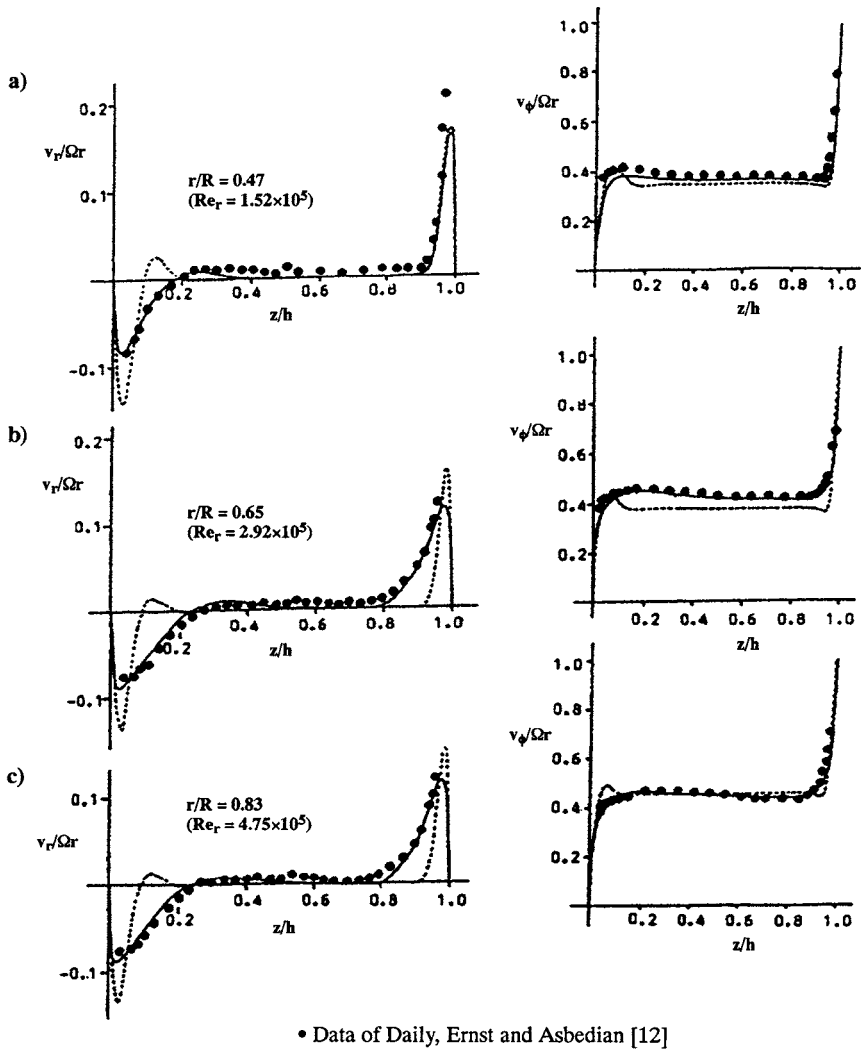
FIG. 19. Comparison between experimental data and numerical results (- - -, laminar) for the radial (v_r) and circumferential (v_ϕ) velocities in a rotor–stator system in which the disk at axial location $z/h = 0$ and the shroud at $r = R$ remain stationary and the disk at $z/h = 1.0$ rotates about the z-axis with angular speed Ω. $G = 0.0685$ and $r_{min}/R = 0.11$. The results are for $Re_R = 6.9 \times 10^5$ at (a) $r/R = 0.47$, (b) $r/R = 0.65$, and (c) $r/R = 0.83$. Re_r is the local Reynolds number based on r. (Source: Morse [35].)

B. CONTRAROTATING

Picha and Eckert [39] made the experimental observation that there was no circumferential component of velocity in the core region between two disks that rotated in opposite directions and were enclosed by a stationary shroud. This of course indicates Stewartson-type flow. Dijkstra and van Heijst [15] numerically studied contrarotating cases with $Re_h = 100$. The results for $\Gamma = -0.3$ and $\Gamma = -0.825$ are shown in Figs. 20 and 21, respectively. It was found that a two-cell structure appeared with a stagnation streamline and a corresponding stagnation point separating the two cells on the slower disk. The circulation of the secondary flow was found to be in opposing directions for these two cells. As Γ approached -1 the stagnation point moved radially outward along the slower disk. This two-cell structure is explained by Dijkstra and van Heijst on the basis that the flow induced by the disk with the larger-magnitude angular speed dominates the weaker flow induced by the disk with smaller-magnitude angular speed. Each disk induces a radially outward flow in its Ekman layers close to the axis of rotation. The radially outward flow adjacent to
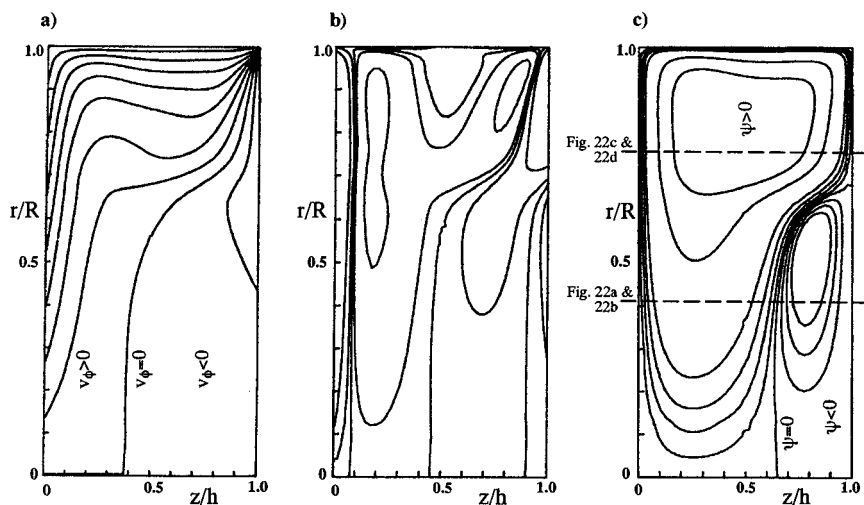
FIG. 20. Numerical results for an enclosed disk system with $\Gamma = -0.3$ and $Re_h = 100$ (based on Ω_1). The disk at $z/h = 0$ and shroud at $r/R = 1.0$ rotate at an angular speed of Ω_1 while the disk at $z/h = 1.0$ rotates in the opposite direction at an angular speed of $0.3\Omega_1$. The results are for (a) lines of constant circumferential velocity (v_ϕ); (b) lines of constant vorticity; (c) streamlines. (Source: Dijkstra and van Heijst [15], with permission of Cambridge University Press.)
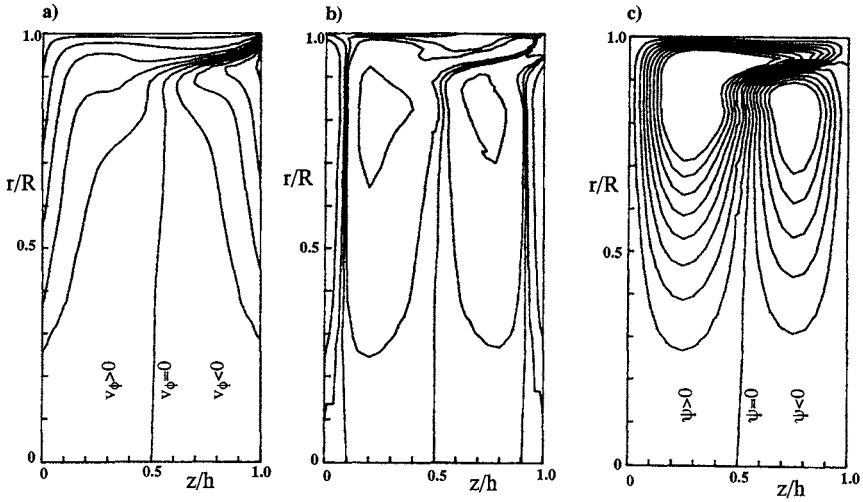
FIG. 21. Numerical results for an enclosed disk system with $\Gamma = -0.825$ and $Re_{\mathrm{h}} = 100$ (based on Ω_1). The disk at $z/h = 0$ and shroud at $r/R = 1.0$ rotate at an angular speed of Ω_1 while the disk at $z/h = 1.0$ rotates in the opposite direction at an angular speed of $0.825\Omega_1$. The results are for (a) lines of constant circumferential velocity (v_ϕ); (b) lines of constant vorticity; (c) streamlines. (Source: Dijkstra and van Heijst [15], with permission of Cambridge University Press.)

the disk with the larger-magnitude angular speed is diverted across the cavity by the shroud and eventually results in a radially inward flow along the outer portion of the disk with smaller-magnitude angular speed. The radially outward flow near the axis of rotation meets the radially inward flow and forms a stagnation point on the slow disk. Representative numerical and experimental profiles for the circumferential and radial velocities are shown in Fig. 22 for $\Gamma = -0.3$. Both experimental and numerical data indicate that at radial locations that fall within the two-cell structure, as in Figs. 22a and 22b, the flow is distinctly of Stewartson type, while at radial locations outside the two cell structure, as in Figs. 22c and 22d, the flow is of Batchelor type. The experimental setup used by Dijkstra and van Heijst prohibited them from obtaining data for the case when both disks rotate with the same angular speed but in opposite directions, $\Gamma = -1.0$.

Morse [35] computed flows, using the same numerical method as discussed in the rotor–stator section, for a system with contrarotating disks, a stationary shroud, and an aspect ratio of 0.1. The predicted axial variation of the circumferential velocity at a Reynolds number (Re_{R}) of 10^6, for various values of Γ, at a nondimensional radius of $r/R = 0.75$, is shown in
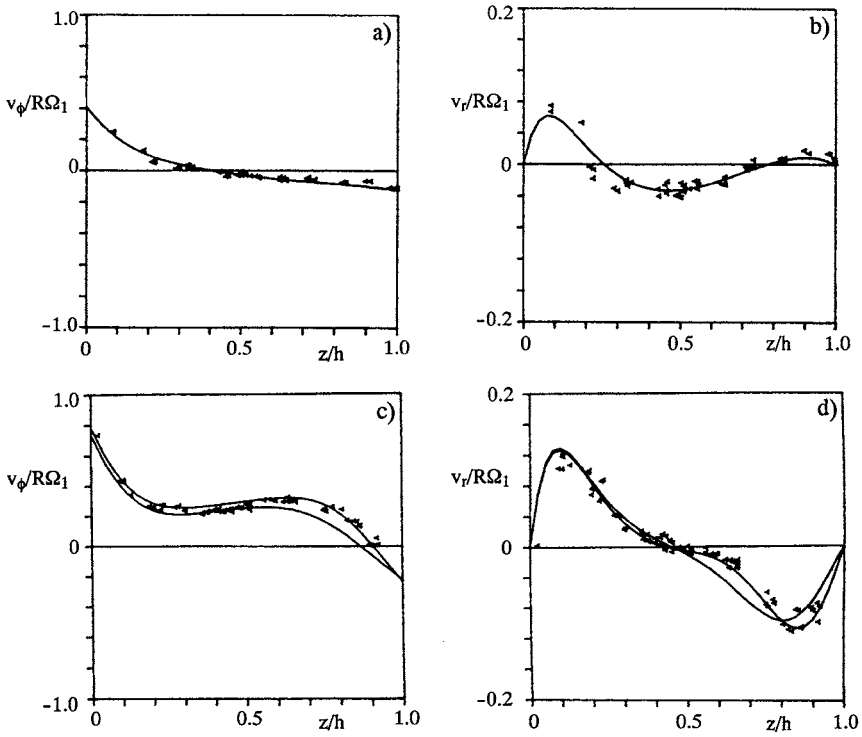
FIG. 22. Comparison between experimental (◆) and numerical results for the circumferential velocity (v_ϕ) profile (a,c) and the radial velocity (v_r) profile (b,d) in a contrarotating disk system in which the disk at $z/h = 0$ and the shroud at $r/R = 1.0$ rotate about the z-axis with angular speed Ω_1 while the disk at $z/h = 1.0$ rotates in the opposite direction at an angular speed of $0.3\Omega_1$. The results are for $Re_h = 100$ (based on Ω_1) at (a,b) $r/R = 0.41$ and (c,d) $0.74 < r/R < 0.78$. (Source: Dijkstra and van Heijst [15], with permission of Cambridge University Press.)

Fig. 23. Figure 24 shows the corresponding predicted values of the circumferential velocity midway between the two disks versus radial location for various values of Γ. Figure 25 shows Morse's predicted influence of the value of Γ on the disk moment coefficient at $Re_R = 10^6$ for the primary disk and for the secondary disk, which rotate with angular speed Ω_1 and $\Omega_2 = \Gamma\Omega_1$, respectively. As expected, the disk moment coefficient increases with decreasing Γ and the value of the moment coefficient for both disks is the same when $\Gamma = -1$.

Gan *et al.* [18, 19] and Kilic *et al.* [26, 27] have published experimental and numerical studies on flows between contrarotating disks, for both
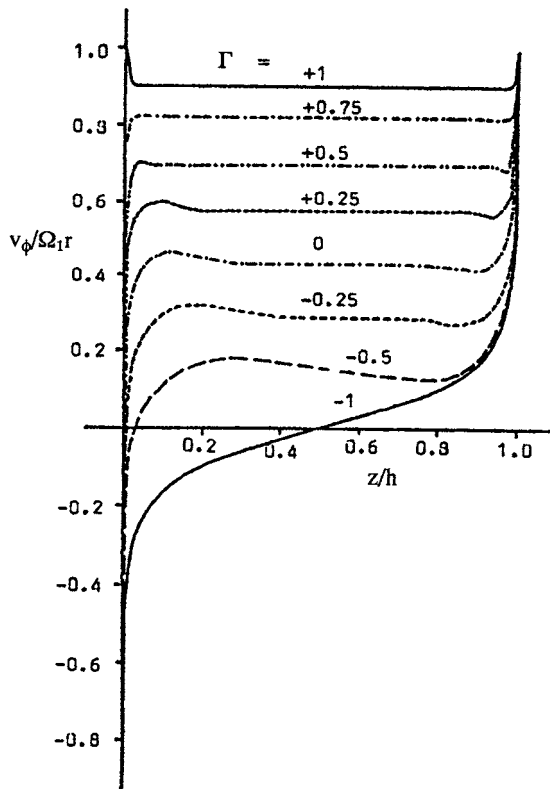
FIG. 23. Numerical prediction of the circumferential velocity (v_ϕ) profile for various values of the disk rotation ratio (Γ) in a rotating disk system in which the disk at $z/h = 0$ rotates about the z-axis at angular speed of $\Omega_2 = \Gamma\Omega_1$ and the disk at $z/h = 1.0$ rotates at an angular speed of Ω_1. The shroud at $r/R = 1.0$ remains stationary. The profiles are for $Re_R = 10^6$ (based on Ω_1) at $r/R = 0.75$, and the aspect ratio (G) is 0.1. (Source: Morse [35].)

laminar and turbulent flows. Gan *et al.* [18] studied only the case when $\Gamma = -1$ for $Re_R = 2.31 \times 10^5$, 7.26×10^5, and 1.17×10^6. At a Reynolds number of 2.31×10^5, comparisons made between experimental measurements and computations for laminar and turbulent flow, shown in Fig. 26, indicate that the flow in the core was turbulent, but the flow in both disk boundary layers remained laminar up to a radial location corresponding to a local Reynolds number of 1.1×10^5 and was found to be fully turbulent for radial locations beyond those corresponding to a local Reynolds number of 1.7×10^5. This is similar to the prediction of $Re \approx 1.5 \times 10^5$ for the transition along the rotor of the rotor–stator configuration studied by Daily
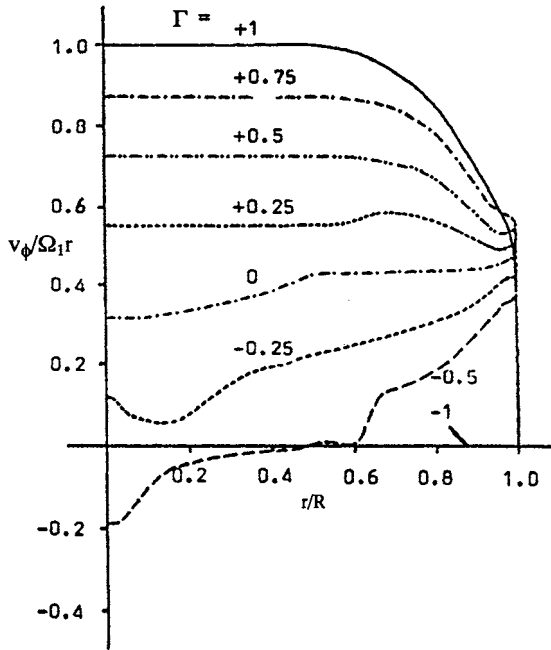
Fig. 24. Numerical prediction of the circumferential velocity (v_ϕ) versus radial position for various values of the disk rotation ratio (Γ) in a rotating disk system in which the disk at $z/h = 0$ rotates about the z-axis at angular speed of $\Omega_2 = \Gamma\Omega_1$ and the disk at $z/h = 1.0$ rotates at an angular speed of Ω_1. The shroud at $r/R = 1.0$ remains stationary. The profiles are for $Re_R = 10^6$ (based on Ω_1) at $z/h = 0.5$, and the aspect ratio (G) is 0.1. (Source: Morse [35].)

and Nece [13]. Computations performed using a low-Reynolds-number $k-\varepsilon$ model agreed well with the experimental measurements of velocity except in regions of the boundary layers, which were found to be laminar. The results clearly indicate that Stewartson-type flow exists for $\Gamma = -1$ at these Reynolds numbers. Although it is clear that the comparison between experimental results and the turbulent computations shown in Fig. 26 indicate that the flow is essentially turbulent and of Stewartson-type under the stated conditions, it is interesting to note that the results of the laminar computations given in Fig. 26 strongly resemble the flow structure predicted by Batchelor. This suggests that for $\Gamma = -1.0$, a transition from Batchelor-type flow to Stewartson-type flow may occur as the Reynolds number is increased. Gan and MacGregor [19] performed a purely experimental investigation of the contrarotating case where $\Gamma = -1$. The experiments were performed at $Re_R = 6 \times 10^4$, 2.31×10^5, and 4×10^5. It was again found
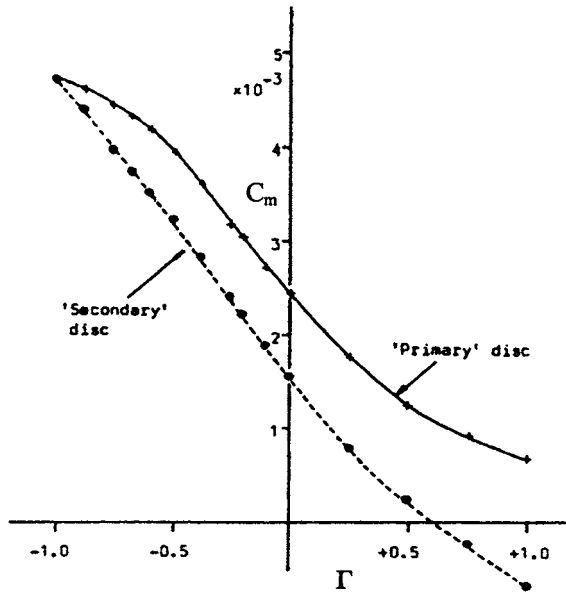
FIG. 25. Numerical predictions of the primary (Ω_1) and secondary (Ω_2) disk torque coefficient (C_m) for various values of the disk rotation ratio (Γ) in a rotating disk system in which the disk at $z/h = 0$ rotates about the z-axis at angular speed of $\Omega_2 = \Gamma\Omega_1$ and the disk at $z/h = 1.0$ rotates at an angular speed of Ω_1. The shroud at $r/R = 1.0$ remains stationary. The results are for $Re_R = 10^6$ (based on Ω_1) and an aspect ratio (G) of 0.1. (Source: Morse [35].)

that the flow in the core is turbulent for a local Reynolds number as low as 2.16×10^4 but remains laminar in the boundary layers for local Reynolds numbers up to 1.1×10^5, and that Stewartson-type flow exists for $\Gamma = -1$.

Kilic et al. [26] studied the transition from Batchelor-type flow for the rotor–stator case ($\Gamma = 0$) to Stewartson-type flow found to exist for the case when $\Gamma = -1$. The study is performed for $Re_R = 1.25 \times 10^6$, which is known to be in the turbulent regime. The computations utilized a low-Reynolds-number k–ε model. Transition from complete Batchelor-type flow at $\Gamma = 0$ to complete Stewartson-type flow at $\Gamma = -1$ was found to take place by development of a two-cell structure in which Batchelor-type flow occurs in the outer radial region and Stewartson-type flow in the inner radial region. This two-cell structure is the same as that described by Dijkstra and van Heijst [15]. Comparisons with experimental data were found to agree well with the computational results. Kilic et al. [27] performed an identical study of this transition from Batchelor-type flow at $\Gamma = 0$ to Stewartson-type flow at $\Gamma = -1$; however, this time the experiments and computations were
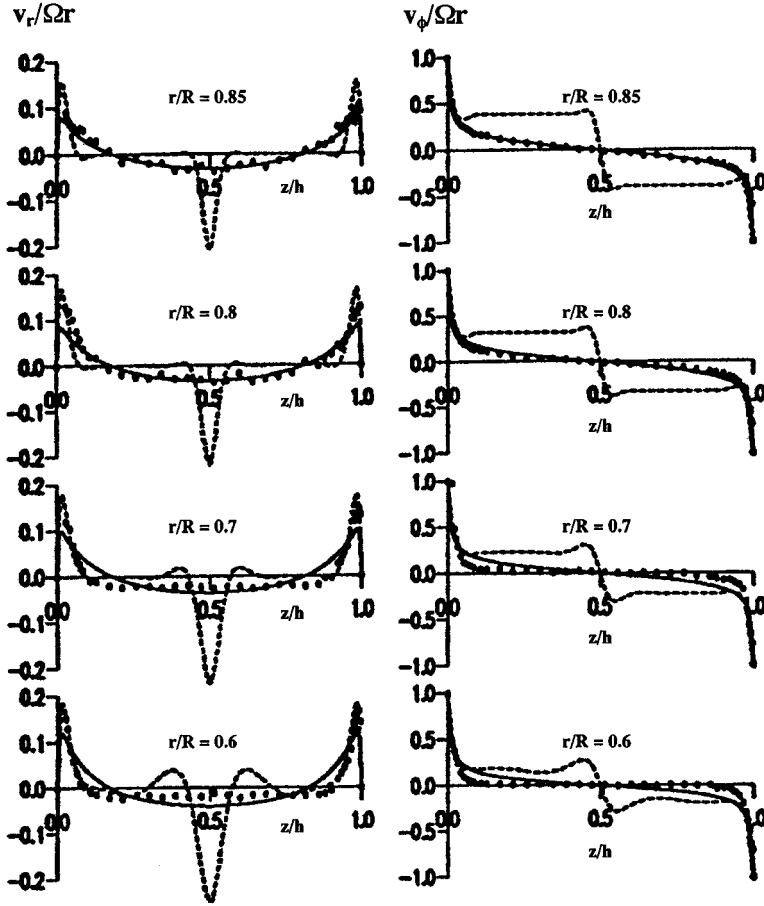
FIG. 26. Comparison between experimental data and numerical results (- - -, laminar) for the axial variation of the radial (v_r) and circumferential (v_ϕ) velocities in a contrarotating system in which the disks at axial locations $z/h = 0$ and $z/h = 1.0$ rotate about the z-axis with angular speed Ω, but in opposite directions (i.e., $\Gamma = -1.0$). The shroud at $r = R$ is split at the mid-axial location so that half of it rotates with each disk. The results are for $Re_R = 2.31 \times 10^5$ at various radial locations defined by r/R. The aspect ratio is 0.12. (Source: Gan *et al.* [18].)

performed at $Re = 10^5$, for which there is also a transition from laminar to turbulent flow as Γ is reduced. This situation revealed that the version of the low-Reynolds-number k–ε model used had a tendency to predict larger regions of laminar flow than were measured experimentally in the cavity at a particular value of Γ. It was also mentioned that previous studies using
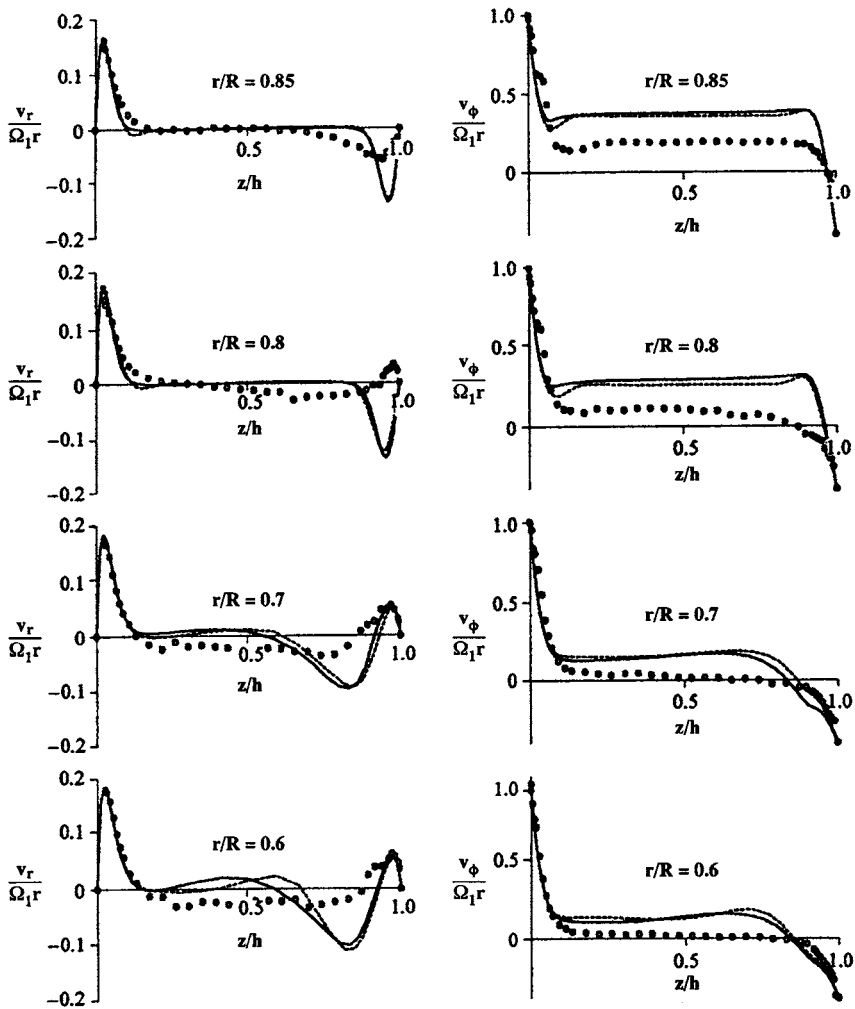
FIG. 27. Comparison between experimental data and numerical results (- - -, laminar) for the axial variation of the radial (v_r) and circumferential (v_ϕ) velocities in a contrarotating system in which the disk at axial location $z/h = 0$ rotates about the z-axis with angular speed Ω_1 while the disk at $z/h = 1.0$ rotates with an angular speed of $-0.4\Omega_1$ (i.e., $\Gamma = -0.4$). The shroud at $r = R$ is split at the midaxial location so that half of it rotates with each disk. The results are for $Re_R = 10^5$ at various radial locations defined by r/R. The aspect ratio is 0.12. (Source: Gan et al. [18].)

Morse's turbulence model showed no significant overall improvement with respect to this issue. "Both models captured the main features of the 'double transition' but neither achieved accurate predictions near the slower disk during the transition process." This is illustrated in Fig. 27, which gives the computational results for both laminar and turbulent simulations in comparison to experimental results for $\Gamma = -0.4$. The results for both computations and measurements show radial inflow for $r/R = 0.85$ and radial outflow for $r/R = 0.6$ and $r/R = 0.7$; for $r/R = 0.8$, the computations show inflow that is in contrast with the experimentally measured outflow. The general characteristic of these results correspond well with the two-cell structure found by Dijkstra and van Heijst [15]; however, the location of the stagnation point predicted by both laminar and turbulent computations can be seen to be between $r/R = 0.7$ and $r/R = 0.8$ while in reality the stagnation point falls between $r/R = 0.8$ and 0.85. In addition, the experimental measurements of the axial variation of the circumferential velocity at $r/R = 0.6$ and 0.7 reveal essential zero core rotation while the computations predict a definite core rotation.

V. Sealed Cavities with an Imposed Thermal Gradient

This section discusses the secondary flows, in sealed cavities, whose confining walls all rotate at an angular speed Ω about the axis of symmetry, that develop because of the driving force of buoyancy. If the fluid were isothermal it would be in solid-body rotation; however, the coupling of the temperature, and therefore density, gradients with the centrifugal acceleration may produce secondary convection. In 1969 Homsy and Hudson [20] studied the thermally induced convection in a rotating cylinder of fluid using a perturbation expansion and reviewed work done in this area up to that time. The two disks forming the ends of the cylinder were held at constant uniform, but different, temperatures, while both an insulated and perfectly conducting condition for the cylindrical wall was considered. It was determined that the secondary flow that developed because of this axially imposed thermal gradient considerably enhanced the heat transfer through the cavity.

In 1978 Hudson et al. [22] published experimental results for centrifugally driven thermal convection in a circular cylinder. Their goal was to determine the dependence of the mean Nusselt number on the system parameters and to compare these experimentally determined relationships with those predicted by the theory developed by Homsy and Hudson [20]. The Nusselt number is defined by the ratio of the heat flux through the cylinder to that heat flux which would occur in the pure conduction state of solid body

rotation. Their investigation can be separated into two regimes. The first regime corresponds to large Reynolds numbers, or equivalently when the Ekman number ($Ek = 2/Re_h$) is small. For large Reynolds numbers a boundary layer flow occurs similar to that found for isothermal rotor–stator systems. The other regime corresponds to small Reynolds numbers for which boundary layers do not form and the viscous forces are influential throughout the cavity. In order to investigate the two regimes, Hudson *et al.* performed experiments using two different silicone oils having nominal kinematic viscosities and Prandtl numbers of $3.5 \times 10^{-4}\,m^2/s$, 3120 and $6.5 \times 10^{-7}\,m^2/s$, 7.2. The cavity, which rotated at angular speeds of up to 89.6 rad/sec about its vertical axis, had a radius of 13.98 cm and a height that could be adjusted to either 0.97 cm or 2.0 cm. This produced Reynolds numbers (Re_h) up to 4.69×10^4 for the low-viscosity oil and up to 95 for the high-viscosity oil. Water was used to heat and cool the upper and lower disks, respectively; the cylindrical shroud was made of an insulating plastic.

From the low-Reynolds-number experiments with the high-viscosity oil it was found that the mean Nusselt number depends on the aspect ratio ($G = h/R$) and a rotational Grashof number (Gr_r). The Grashof number plays a role similar to that of the Reynolds number in that it is an indication of the ratio of the buoyancy force, which drives the natural convection, to the viscous forces and indicates the "vigor" of the buoyancy-induced flow. For gravitationally induced buoyancy flow in a cavity, the Grashof number is typically defined as

$$Gr = \frac{g\beta\Delta T h^3}{v^2},\tag{1}$$

where g is the gravitational acceleration, β is the coefficient of thermal expansion, and ΔT is the temperature difference across the cavity. For centrifugally induced buoyancy flows, the rotational Grashof number is typically defined by replacing the gravitational acceleration in Eq. (1) by the centripetal acceleration at the outer edge of the cylinder ($\Omega^2 R$):

$$Gr_r = \frac{\Omega^2 R\beta\Delta T h^3}{v^2}.\tag{2}$$

Based on the experimental data collected, Hudson *et al.* found that the mean Nusselt number is given by the following empirical relationship for small Reynolds numbers and $Gr_r \geqslant 2.0$:

$$\overline{Nu} = 1.13 Gr_r^{0.267} G^{0.054}.\tag{3}$$

The empirical relationship for large Reynolds numbers as determined by the experiments with the low viscosity oil, for which boundary layers

develop, is given by

$$\overline{Nu} = 0.533(\beta\Delta T)^{0.822} Re_R^{0.499} G^{0.825}. \qquad (4)$$

The empirical relationships given by these two equations were found by Hudson *et al.* to be consistent with the previously established theory of Homsy and Hudson.

In 1985 Chew [10] published numerical solutions of the full governing equations for the thermally driven laminar flow in cavities filled with a high-viscosity oil and air-filled cavities. Chew compared his results for the high-viscosity oil-filled cavities with the experimentally determined heat transfer rates given by Hudson *et al.* [22]. The relevance of various similarity solutions for the flow between two infinite disks at different uniform temperatures is also investigated. The results shown in Fig. 28 indicate that Chew's numerical predictions of the mean Nusselt number for the high-viscosity oil are in good agreement with the experimentally measured correlation, Eq. (3), obtained by Hudson *et al.* [22]. Streamline and isotherm data computed for an air-filled cavity ($G = 0.267$) with a Reynolds number (Re_R) of 1.0×10^4 and $\beta\Delta T = 0.228$ are presented in Fig. 29. The streamlines indicate that Ekman layers have formed on both disks along with a boundary layer on the cylindrical wall through which fluid is channelled from the cold disk to the hot disk. In the core of the fluid away from the outer cylindrical wall, there exists an axial flow of fluid from the hot disk to the cold disk. It can be seen that this type of centrifugally driven thermal convection is qualitatively similar to the secondary flow that develops in a rotor–stator system. Chew also found that the local Nusselt
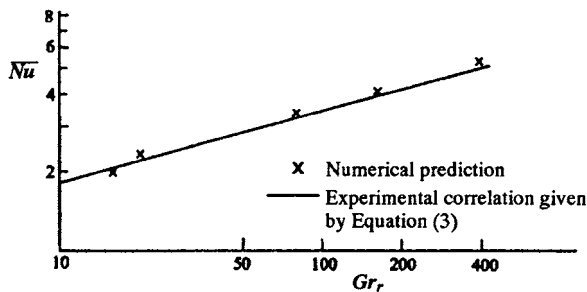
FIG. 28. Comparison between numerically predicted values of the mean Nusselt number for a sealed cylindrical cavity filled with a high-viscosity silicone oil ($v = 3.5 \times 10^{-4}\,\mathrm{m^2/s}$) for various rotational Grashof numbers. The two disks were held at uniform but different temperatures, and the cylindrical shroud was assumed adiabatic in the numerical calculations. (Source: Chew [10], with permission of Cambridge University Press.)
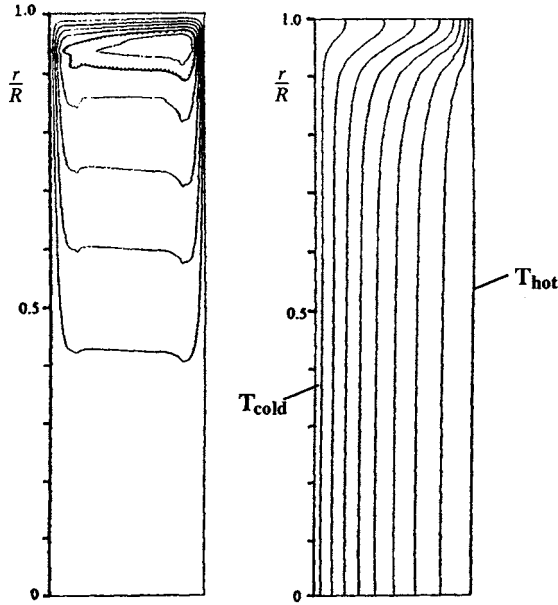
Fig. 29. Numerically computed (a) streamlines at intervals of $1.5 \times 10^{-6}\, \mathrm{m^3/s}$ and (b) isotherms at intervals of 10 K for the thermally driven flow of air inside a rotating cylindrical cavity with an aspect ratio of 0.267. The left-hand disk is held at a constant, uniform temperature T_{cold} while the right-hand disk is held at a constant, uniform temperature T_{hot} ($Re_{\mathrm{R}} = 1.0 \times 10^4$ and $\beta \Delta T = 0.228$). (Source: Chew [10], with permission of Cambridge University Press.)

numbers on the disks were strongly dependent on the radial position and that the mean Nusselt number for the hot disk was strongly dependent on the thermal boundary conditions imposed on the cylindrical wall of the cavity.

Bohn et al. [5] present numerical results for laminar, buoyancy-induced heat transfer and fluid flow in a sealed air-filled rotating annulus with a square cross-section using a finite volume scheme. The annulus is characterized by an inner (r_{min}) and outer (R) radius and an axial gap (h) . The heat flux is imposed through the cavity in the axial direction by means of isothermal side walls (disks) of different, uniform temperature. The inner and outer cylindrical walls of the cavity are modeled as adiabatic. The numerical scheme was validated in two ways. Reducing r_{min} to zero allowed simulations to be performed that corresponded to the results reported by Chew [10]. The second method of validation involved allowing the $r_{\mathrm{m}}/\Delta r$ ratio to

become very large, where r_m is the mean radius and $\Delta r = R - r_{min}$. Theoretically, for $r_m/\Delta r = \infty$ the nondimensional governing equations become identical to those for gravity-induced natural convection in a stationary cavity with the gravitational acceleration replaced by the centripetal acceleration. In this limit the Coriolis forces disappear and the centrifugal buoyancy term in the radial momentum equation is the only remaining body force. Utilizing this limiting behavior, Bohn *et al.* found good agreement with the benchmark solutions of De Vahl Davis [14].

To study the influence of the ratio $r_m/\Delta r$ more completely, Bohn *et al.* [5] computed the mean Nusselt number variation with $r_m/\Delta r$ at constant Reynolds and rotational Grashof numbers. The results corresponding to a rotational Gershof number $(Gr_r = \Omega^2 r_m \beta \Delta T h^3/v_0^2)$ of 1.51×10^5 and two Reynolds numbers $(Re_h = \Omega r_m h/v_0)$ of 6.14×10^3 and 2.46×10^4 are shown in Fig. 30. The monotonic manner in which the heat transfer rate approaches the value for a stationary square cavity under the influence of gravity at the same Grashof number is clearly illustrated. Thus, it can be seen that the heat transfer rate is maximum for conditions when the Coriolis forces are zero, and in general it can be shown that the secondary fluid motion, which is driven by the centrifugal buoyancy force, is damped by the Coriolis forces. Increasing the Reynolds number at constant rotational
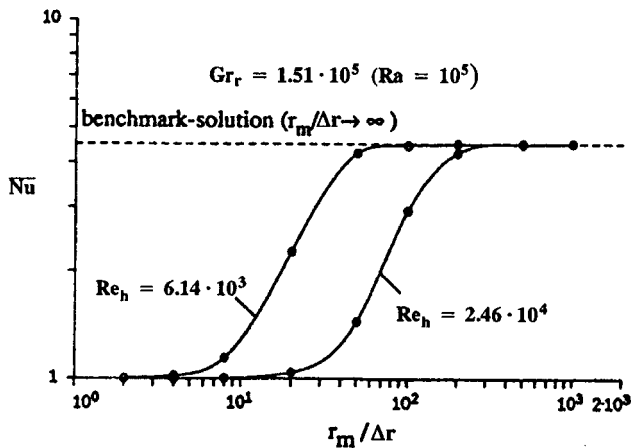
FIG. 30. Numerically computed variation of the mean Nusselt number with $r_m/\Delta r$ for a rotating annular cavity with a square cross-section filled with air. The Nusselt numbers are computed for a constant rotational Grashof number $(Gr_r = \Omega^2 r_m \beta \Delta T h^3/v_0^2)$ of 1.51×10^5 and Reynolds numbers $(Re_h = \Omega r_m h/v_0)$ of 6.14×10^3 and 2.46×10^4. The Nusselt number is shown to approach the value found for natural convection in a stationary square enclosure at the same Grashof number. (Source: Bohn *et al.* [5].)
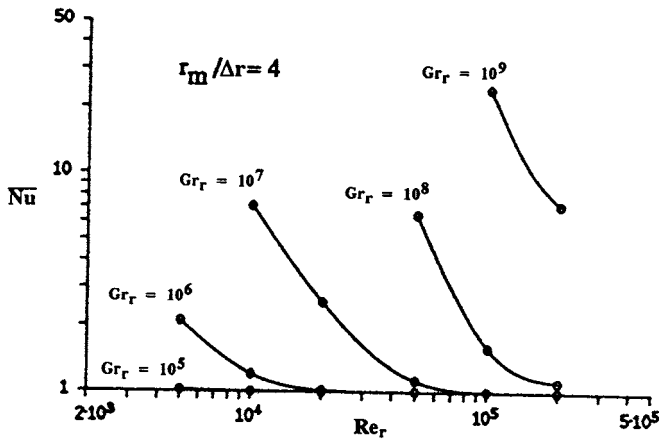
FIG. 31. Numerically computed variation of the mean Nusselt number with rotational Grashof number ($Gr_r = \Omega^2 r_m \beta \Delta T h^3 / v_0^2$) and Reynolds number ($Re_h = \Omega r_m h / v_0$) for a rotating annular cavity with a square cross-section filled with air. The results are for a constant $r_m/\Delta r$ ratio of 4.0. (Source: Bohn *et al.* [5].)

Grashof number strengthens the Coriolis forces compared to the buoyancy force, which leads to a reduction of the flow circulation between the hot and the cold walls and therefore a reduction of the heat transfer by convection. This behavior is also illustrated in Fig. 30, in which it can be seen that the limiting Nusselt number is reached earlier for the lower Reynolds number simulation. Figure 31 maps the influence of Reynolds number and rotational Grashof number on the variation of the mean Nusselt number for a constant $r_m/\Delta r$ ratio of 4.0. As expected from the earlier discussion, the mean Nusselt number rises as the rotational Grashof number is increased at constant Reynolds number, and an increase in the Reynolds number at a constant rotational Grashof number attenuates the heat transfer. Bohn *et al.* [5] also investigated the fully three-dimensional flow and heat transfer in a radially sectored annulus. The radial walls are intended to reduce the relative circumferential velocity of the fluid and thus reduce the Coriolis forces. It was found that a significant increase in the mean Nusselt number can be obtained for an annular cavity with section angles of less than 30°.

The results presented by Bohn *et al.* [5] are obtained using a potentially low-order convection scheme and modest grid resolutions that may not adequately resolve the thin layer structure observed in the flow field. Ebert *et al.* [16] have conducted a systematic investigation to assess the numerical accuracy for such computations and have documented differences observed from solutions with varying grid resolutions and discretization schemes.

Noticeable differences can be observed from different treatments. Ebert *et al.* have also presented a scaling analysis to help gain additional physical insight. For example, as the Reynolds and rotational Grashof numbers increase, the velocity gradient in the wall region increases, but not necessarily so for the temperature gradient and mean Nusselt number. Based on an order-of-magnitude investigation of the governing equations, one can identify the various velocity and wall layer thickness scales. They have deduced that whereas the wall layer velocity scales with $(\Omega r_{\mathrm{m}} \Delta T/T_{\mathrm{m}})$, the velocity layer thickness scales with $(\nu/\Omega)^{1/2}$, or Gr/Re and $1/Re^{1/2}$, respectively, for a given fluid and cavity geometry. Furthermore, the thermal wall layer thickness, or the inverse of the Nusselt number, scales as $Re^{3/2}/Gr_{\mathrm{r}}$ for a given fluid and cavity geometry. These scaling laws are confirmed by several cases, including both annular and cylindrical geometries.

To help illustrate the scaling relations, Ebert *et al.* considered the annular cavity with square cross-section computed by Bohn *et al.* [5]. Two different flow conditions, corresponding to Reynolds numbers ($Re_{\mathrm{h}} = \Omega r_{\mathrm{m}} h/\nu_0$) of 10^4 and 10^5 and rotational Grashof numbers ($Gr_{\mathrm{r}} = \Omega^2 r_{\mathrm{m}} \beta \Delta T h^3/\nu_0^2$) of 10^7 and 10^8, respectively, were studied for this configuration. Figure 32 depicts the computed isotherm distributions for the two cases and shows that the thermal wall layer thickness increased from Fig. 32a to Fig. 32b. Qualitatively the ratio of the thermal wall layer thickness in Figure 32a to 32b, can be predicted based on the scaling analysis results to be approximately 3.2. Figure 33 shows the computed radial and axial velocity profiles for these two cases along with comparisons between the predicted ratios of maximum velocity magnitudes and the velocity wall layer thicknesses, using both the numerical computations and the scaling relations. Figure 34 shows the local Nusselt number distribution along the hot and cold walls for both cases as well as the results of the mean Nusselt number comparison between numerical and scaling predictions. It is clear that scaling relations can provide useful insight into the trend of the various aspects related to the velocity and temperature fields.

In Bohn *et al.* [4], experimental and numerical results of heat transfer and fluid flow in a rotating air-filled annular cavity with an imposed radial heat flux are presented. The imposed radial heat flux is in the opposite direction to the centifugal force, setting up an unstable stratification. Measurements of the mean Nusselt number were performed while varying Rayleigh number in a range that might be encountered in gas-filled cavities of actual gas turbine rotors ($10^7 < Ra < 10^{12}$). It was found that in the case of radially directed heat flux, the heat transfer showed a strong dependence on the Rayleigh number with only a weak dependence on the Reynolds number. This is in contrast to the results described previously for an axially directed heat flux where it was shown that the Reynolds number is an influential

(a)

min temp = 600 K
max temp = 900 K

Level	temp (K)
16	900.0
15	880.0
14	860.0
13	840.0
12	820.0
11	800.0
10	780.0
9	760.0
8	740.0
7	720.0
6	700.0
5	680.0
4	660.0
3	640.0
2	620.0
1	600.0

(b)

min temp = 735 K
max temp = 765 K

Level	temp (K)
13	765.0
12	762.5
11	760.0
10	757.5
9	755.0
8	752.5
7	750.0
6	747.5
5	745.0
4	742.5
3	740.0
2	737.5
1	735.0
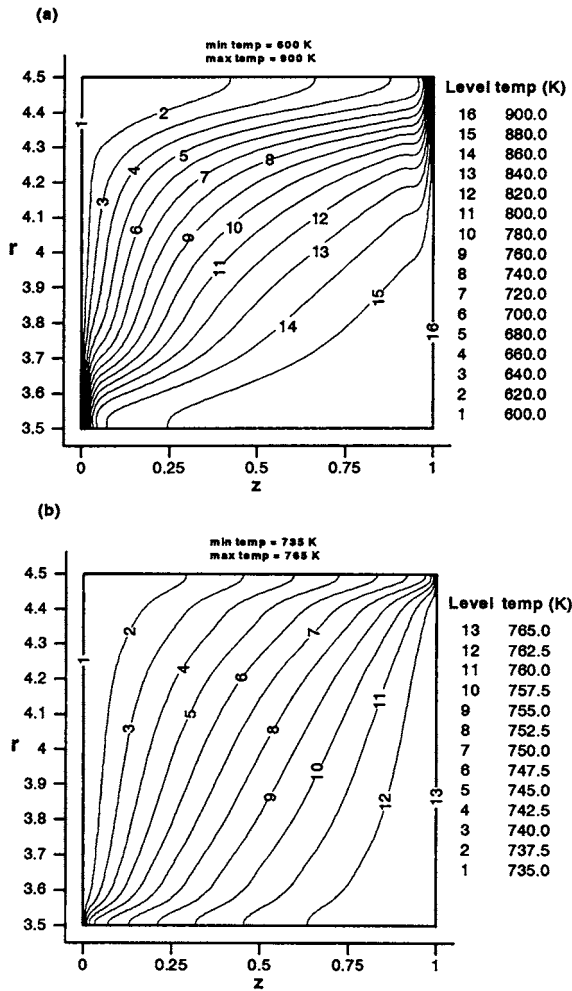
FIG. 32. Temperature contours computed for the cross-section of an annular cavity. (a) $Re_h = 10^4$, $Gr_r = 10^7$. (b) $Re_h = 10^5$, $Gr_r = 10^8$. ($Re_h = \Omega r_m h / v_0$ and $Gr_r = \Omega^2 r_m \beta \Delta T h^3 / v_0^2$.) (Source: Ebert et al. [16].)

parameter. Steady-state numerical simulations were found to give accurate predictions of the heat transfer rate in the cavity. Numerical results from unsteady numerical simulations, however, suggest that the flow may be affected by a time-dependent instability phenomenon. The experimental data collected was insufficient for determining the character of the flow field.
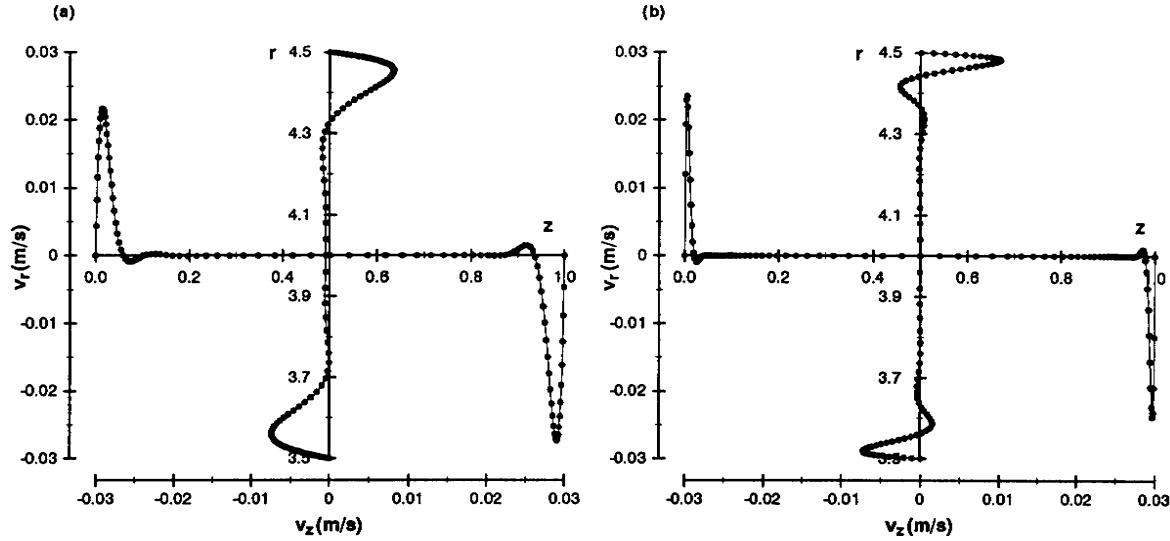
	scaling prediction	numerical prediction
velocity magnitude	$\dfrac{\text{case(a)}}{\text{case(b)}} \Rightarrow \dfrac{Gr_r/Re_h}{Gr_r/Re_h} = \dfrac{1000}{1000} = 1.0$	$\dfrac{\text{case(a)}}{\text{case(b)}} \Rightarrow \dfrac{(v_r)_{max}}{(v_r)_{max}} = .96$
velocity wall layer thickness	$\dfrac{\text{case(a)}}{\text{case(b)}} \Rightarrow \dfrac{1/Re_h^{\frac{1}{2}}}{1/Re_h^{\frac{1}{2}}} = \dfrac{.01}{.0032} = 3.2$	$\dfrac{\text{case(a)}}{\text{case(b)}} \Rightarrow \dfrac{\delta_{zv}}{\delta_{zv}} = 2.8$

FIG. 33. Radial and axial velocity profiles computed for the cross-section of an annular cavity. (a) $Re_h = 10^4$, $Gr_r = 10^7$; (b) $Re_h = 10^5$, $Gr_r = 10^8$ ($Re_h = \Omega r_m h/v_0$ and $Gr_r = \Omega^2 r_m \beta \Delta T h^3/v_0^2$). (Source: Ebert et al. [16].)

	scaling prediction	numerical prediction
mean Nusselt number	$\dfrac{\text{case(a)}}{\text{case(b)}} \Rightarrow \dfrac{Gr_r/Re_h^{3/2}}{Gr_r/Re_h^{3/2}} = \dfrac{10}{3.2} = 3.1$	$\dfrac{\text{case(a)}}{\text{case(b)}} \Rightarrow \dfrac{\overline{Nu}}{\overline{Nu}} = \dfrac{7.44}{2.56} = 2.9$
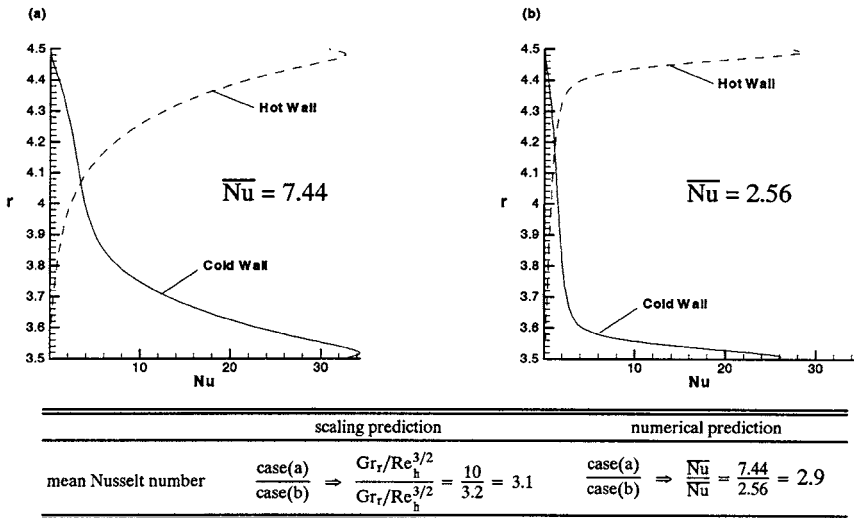
FIG. 34. Local Nusselt number variation along the hot and cold walls as computed for an annular cavity. (a) $Re_h = 10^4$, $Gr_r = 10^7$; (b) $Re_h = 10^5$, $Gr_r = 10^8$ ($Re_h = \Omega r_m h/v_0$ and $Gr_r = \Omega^2 r_m \beta \Delta T h^3/v_0^2$). (Source: Ebert et al. [16].)

In 1996, Bohn et al. [6] returned to an experimental and numerical investigation of the heat transfer and fluid flow in rotating air-filled annular cavities with an imposed axial heat flux. The experimental setup allowed for heat transfer measurements of flows with Rayleigh numbers in the range $2 \times 10^7 < Ra < 5 \times 10^{10}$. However, because of a limit on the experimentally obtainable values of $\Delta T/T_m$, the influence of the Reynolds number separate from the Rayleigh number could not be explored empirically. For fixed cavity geometry and Prandtl number, the experiments produced a relationship between the mean Nusselt number and the Rayleigh number given by

$$\overline{Nu} = 0.346Ra^{0.124}. \tag{5}$$

Comparison is made between this result and results obtained from the radial heat flux investigation of Bohn et al. [4]. Figure 35 shows that for this range of Rayleigh numbers the heat transfer rate is substantially larger for a cavity with radial heat flux than for a cavity with axial heat flux, indicating that for cavities with a heat flux in both directions the radial heat transfer is dominant.

To compare the influence of the Reynolds number on the heat transfer rate in cavities with pure axial and pure radial heat fluxes, two-dimensional numerical simulations were performed. Figure 36 contains plots of the
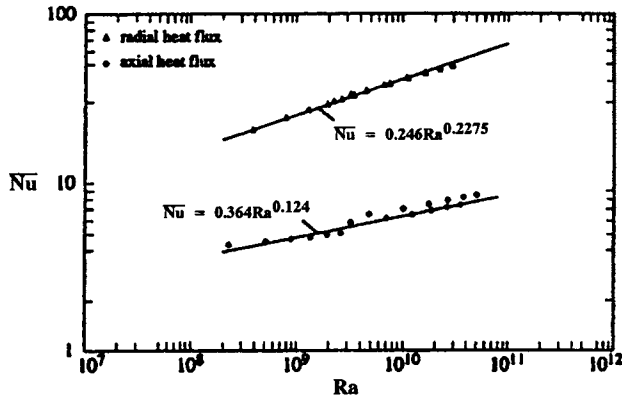
FIG. 35. Numerically computed variation of the mean Nusselt number with Rayleigh number for a rotating annular cavity with an axially and radially directed heat flux. (Source: Bohn *et al.* [6].)

predicted mean Nusselt number as a function of the Rayleigh number for different Reynolds numbers and confirms that the influence of the Reynolds number is small for a cavity with a radially directed heat flux, but significant for cavities with an axially directed heat flux. It was found that the two-dimensional numerical predictions for the heat transfer rate for Rayleigh numbers less than 2×10^9 were consistent with the experimental measurements. However, as the Rayleigh number increased, differences between the two-dimensional numerical prediction and the experimental measurements were reported. A likely contribution to the discrepancy is the occurrence of a radial heat flux in the experiments due to imperfect insulation on the cylindrical walls that was not accounted for in the numerical simulations. Another possible source for this discrepancy may be the development of a three-dimensional flow structure within the cavity. A comparison between two-dimensional and three-dimensional simulations for a cavity with an axial heat flux shows that for Reynolds numbers $(Re_h = \Omega r_m h / v_0)$ greater than 1.457×10^4, differences begin to appear.

VI. Two-Equation Turbulence Model and Low Reynolds Number Effects

To date the most commonly used turbulence models have been two-equation turbulence schemes in which two partial differential equations are used to describe the development of the turbulent kinetic energy and of a quantity related to the turbulence length scale. The standard $k-\varepsilon$ model
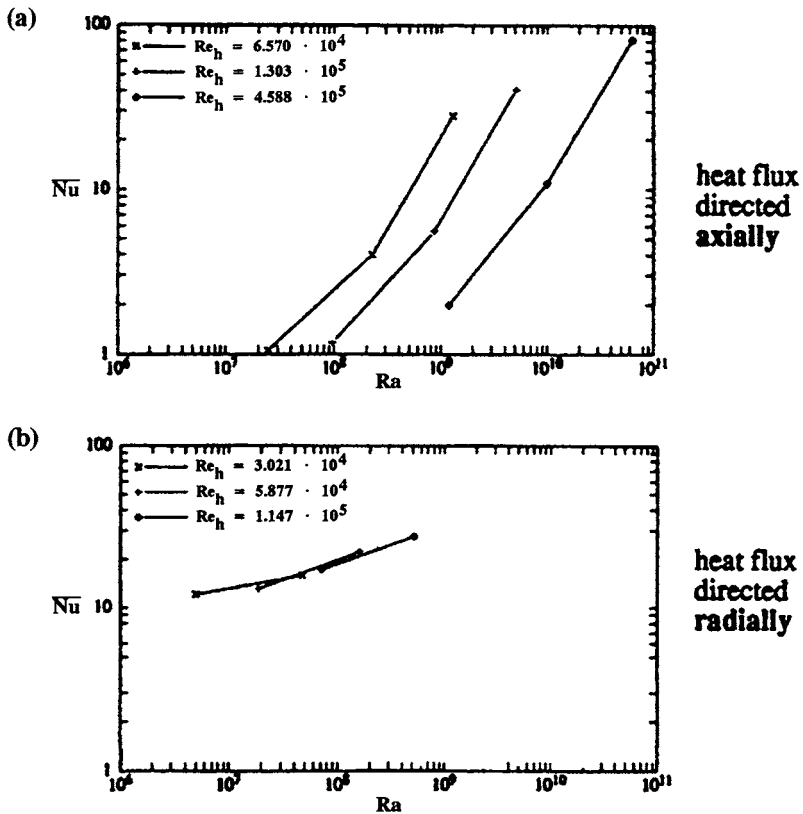
FIG. 36. Numerically computed variation of the mean Nusselt number with Rayleigh number for a rotating annular cavity with an (a) axially directed heat flux and (b) a radially directed heat flux at various Reynolds numbers ($Re_h = \Omega r_m h/v_0$). (Source: Bohn *et al.* [6].)

(Jones and Launder [24]; Launder and Spalding [32]) is the most widely used and validated turbulence model for many different types of problems. It has achieved notable successes in calculating a wide variety of engineering applications. Despite this fact, the original $k-\varepsilon$ model has known deficiencies for certain types of flows, especially when the production and dissipation of the turbulent kinetic energy are not close to equilibrium. Also, this model is only valid for fully turbulent regions and, for wall-bounded flows, requires additional modeling of near-wall regions, such as the wall function (Jones and Launder [24]). This treatment is suitable for high Reynolds flows only and is inadequate when the local Reynolds number becomes low.

The eddy viscosity model is based on the assumption that the Reynolds stresses are a local property of the mean flow and are related to the mean flow gradients via a turbulent viscosity as

$$-\rho \overline{u_i' u_j'} = \mu_t \left(\frac{\partial u_i}{\partial x_j} + \frac{\partial u_i}{\partial x_j} \right), \tag{6}$$

where μ_t is some turbulent viscosity which needs to be modeled. Modeling of μ_t requires specification of local length and time scales. The $k-\varepsilon$ models provide the velocity scale via the turbulent kinetic energy k and the length scale via a combination of k and the rate of viscous dissipation of turbulent kinetic energy ε. The dimensionless analysis yields the turbulent viscosity as

$$\mu_t = \rho C_\mu \frac{k^2}{\varepsilon}, \tag{7}$$

where C_μ is a proportionality coefficient, k is turbulent kinetic energy $k = 1/2(\overline{u'^2} + \overline{v'^2} + \overline{w'^2})$, and ε is dissipation rate,

$$\varepsilon = v \frac{\overline{\partial u_j'}}{\partial x_i} \frac{\overline{\partial u_j'}}{\partial x_i}.$$

The transport equations for k and ε, after the modeling assumptions, can be expressed as

$$\frac{\partial}{\partial t} \rho k + \frac{\partial}{\partial x_i} (\rho u_i k) = \frac{\partial}{\partial x_i} \left[\left(\mu + \frac{\mu_t}{\sigma_k} \right) \frac{\partial k}{\partial x_i} \right] + \Pi - \rho \varepsilon \tag{8}$$

$$\frac{\partial}{\partial t} \rho \varepsilon + \frac{\partial}{\partial x_i} (\rho u_i \varepsilon) = \frac{\partial}{\partial x_i} \left[\left(\mu + \frac{\mu_t}{\rho_\varepsilon} \right) \frac{\partial \varepsilon}{\partial x_i} \right] + \frac{C_1 \varepsilon \Pi}{k} - C_2 \rho \frac{\varepsilon^2}{k}. \tag{9}$$

Note that Π is the generation (production) of k from the mean flow shear stresses:

$$\Pi = \tau_{ij} \frac{\partial u_i}{\partial x_j} = \mu_t \left(\frac{\partial u_i}{\partial x_j} + \frac{\partial u_j}{\partial x_i} \right) \cdot \frac{\partial u_i}{\partial x_j}. \tag{10}$$

As formulated by Launder and Spalding [32], the various constants used in the standard $k-\varepsilon$ model have the following values:

$$C_\mu = 0.09, \quad C_1 = 1.44, \quad C_2 = 1.92, \quad \sigma_k = 1.0, \quad \sigma_\varepsilon = 1.3$$

For a fully developed turbulent flow near a no-slip wall, the normalized near-wall tangential velocity, assuming a two-layer structure (viscous sub-

layer followed by the log layer), can be written as (White [50])

$$u^+ = Y^+, \qquad Y^+ \leqslant 11.63$$

$$u^+ = \frac{1}{\kappa} \log(EY^+), \qquad Y^+ > 11.63$$

where

$$u^+ = \frac{u^t}{u_\tau}, \qquad Y^+ = \frac{\rho Y_P u_\tau}{\mu}, \qquad u_\tau = \sqrt{\frac{\tau_{wall}}{\rho}}.$$

The van Karman constant κ has the value 0.4187. The quantity E is assigned the value 9.793 for smooth walls. Note that Y_P is the coordinate normal to the wall and Y^+ defines local Reynolds number.

Assuming local equilibrium between production and dissipation and constant stress layer near the wall, the shear stress can be related to the turbulent kinetic energy as

$$\frac{\tau_{wall}}{\rho} = \sqrt{C_\mu k}. \tag{11}$$

Hence, from the preceding equations we obtain

$$Y^+ = \frac{\rho C_\mu^{1/4} k^{1/2} Y_P}{\mu} \tag{12}$$

and

$$\tau_{wall} = \frac{\mu Y^+}{Y_P u^+} u^t. \tag{13}$$

The validity of this procedure is, of course, restricted to situations in which the Reynolds number is sufficiently high for the viscous effects to be unimportant or where universal wall functions are well established. Many suggestions have been made for the extension of the turbulence closure models to enable their use at low Reynolds numbers and to describe the flow close to the solid wall. The low-Reynolds-number models approximate the governing equations all the way to the wall and thus obviate the need to make any assumptions about the nature of turbulence or the velocity profile near solid walls.

A summary of the low-Reynolds-number flow structures has been presented by Patel *et al.* [38]. Figure 37a shows the variations of $k^+(=k/u_\tau^2)$. In spite of the rather large scatter, it is seen that k^+ becomes maximum around $y^+ = 15$. In the interval $60 < y^+ < 150$, k^+ becomes almost constant and takes a value around 3.3. Figure 37b shows the distribution of the shear
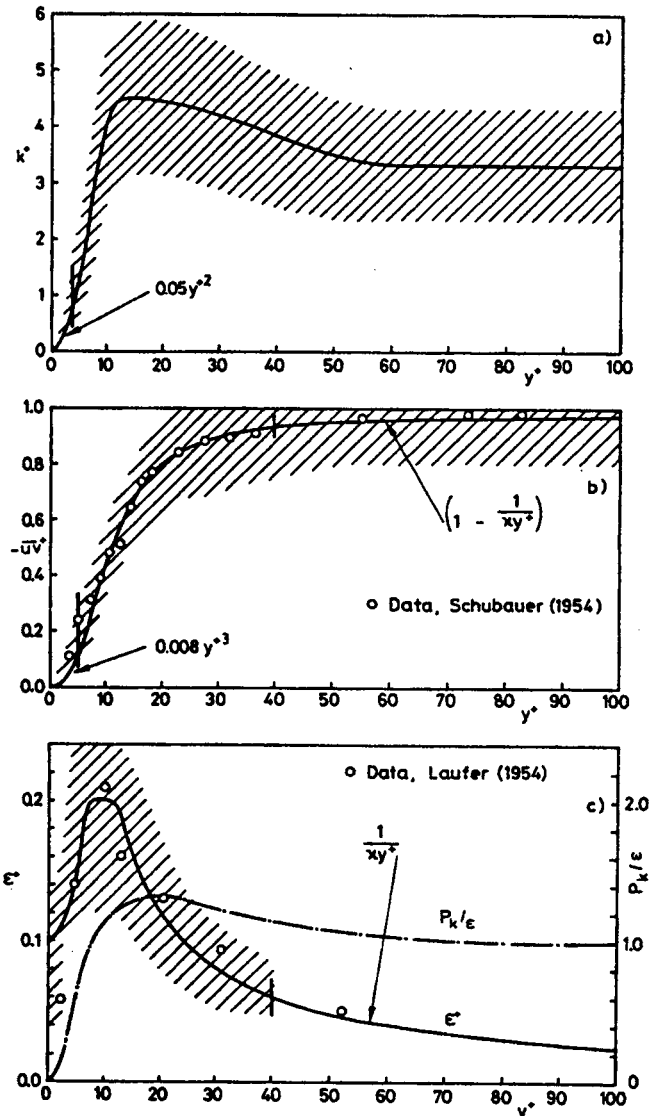
FIG. 37. Near-wall variations of the turbulent quantities (a) turbulent kinetic energy k; (b) Reynolds stress $-\overline{uv}$; (c) dissipation rate. (Source: Patel *et al.* [38].)

stress $-\overline{uv}^{+}$ ($-\overline{uv}/u_{\tau}^{2}$) in the near wall region. Note that the Reynolds stress accounts for approximately 50% of the total stress at $y^{+} \approx 10$ and $-\overline{uv}^{+} \propto y^{+3}$ very close to the wall. Figure 37c shows dissipation rate $\varepsilon^{+} = v\varepsilon/u_{\tau}^{4}$. Note that in the log region $30 < y^{+} < 100$, say, production of k is roughly equal to the dissipation and region $0 < y^{+} < 30$ is subject to a large measurement uncertainty.

The low Reynolds number models may be summarized by the following set of equations:

$$\mu_{t} = \rho C_{\mu} f_{\mu} \frac{k^2}{\tilde{\varepsilon}} \tag{14}$$

$$\varepsilon = \tilde{\varepsilon} + D \tag{15}$$

$$\frac{\partial}{\partial t} \rho k + \frac{\partial}{\partial x_i} (\rho u_i k) = \frac{\partial}{\partial x_i} \left[\left(\mu + \frac{\mu_t}{\sigma_k} \right) \frac{\partial k}{\partial x_i} \right] + \Pi - \rho \varepsilon \tag{16}$$

$$\frac{\partial}{\partial t} \rho \tilde{\varepsilon} + \frac{\partial}{\partial x_i} (\rho u_i \tilde{\varepsilon}) = \frac{\partial}{\partial x_i} \left[\left(\mu + \frac{\mu_t}{\sigma_\varepsilon} \right) \frac{\partial \tilde{\varepsilon}}{\partial x_i} \right] + \frac{C_1 f_1 \tilde{\varepsilon} \Pi}{k} - C_2 f_2 \rho \frac{\tilde{\varepsilon}^2}{k} + E \tag{17}$$

$$R_{\mathrm{T}} = k^2 / v\tilde{\varepsilon}. \tag{18}$$

Table I summarizes the low Reynolds number functions. The first line in the table is the parent high-Reynolds-number model. The other two represent low-Reynolds-number models proposed by Chien [9] and Launder and Sharma [31], which are used later in the discussion.

TABLE I
CONSTANTS AND FUNCTIONS FOR THE $k-\varepsilon$ MODELS

Model	D	$\bar{\varepsilon}_w - $ B.C.	C_μ	C_1	C_2	σ_k	σ_ε
Standard	0	Wall functions	0.09	1.44	1.92	1.0	1.3
Chien	$2v\dfrac{k}{y^2}$	0	0.09	1.35	1.8	1.0	1.3
Launder–Sharma	$2v\left(\dfrac{\partial \sqrt{k}}{\partial y}\right)^2$	0	0.09	1.44	1.92	1.0	1.3

Model	f_μ	f_1	f_2	E
Standard	1.0	1.0	1.0	0
Chien	$1 - \exp(-0.0115 y^+)$	1.0	$1 - 0.22 \exp[-(R_{\mathrm{T}}/6)^2]$	$-2v(\bar{\varepsilon}/y^2)\exp(-0.5y^+)$
Launder–Sharma	$\exp\left[\dfrac{-3.4}{(1+R_{\mathrm{T}}/50)^2}\right]$	1.0	$1 - 0.3\exp(-R_{\mathrm{T}}^2)$	$2vv_t\left(\dfrac{\partial^2 U}{\partial y^2}\right)^2$

$R=1.0$

$a=0.13$

$s=0.12$

$s_c=0.016$

$\Omega_1 = 1.0$

$\Omega_2 = 0... - 1.0$

$\Gamma = \Omega_2/\Omega_1 = 0... - 1.0$

$\nu = 1.0 \times 10^{-5}$

$Re_R = \Omega_1 R^2/\nu = 100,000$
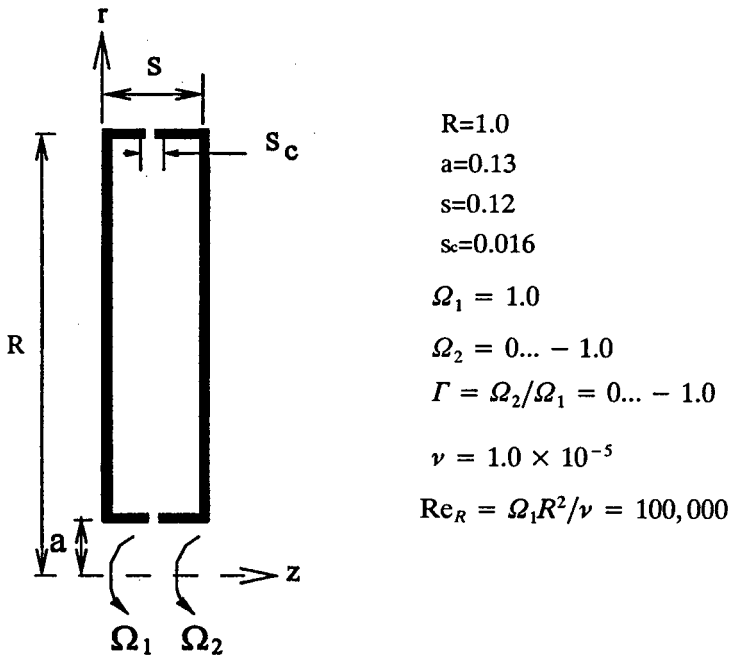
FIG. 38. Schematic of cavity flow experimentally and numerically studied by Kilic *et al.* [27].

We choose, as an example, to demonstrate the performance of two equation models and the effect of low-Reynolds-number, cases reported by Kilic *et al.* [27]. The paper describes a combined computational and experimental study of the flow between contrarotating discs. A schematic of the case is shown in Fig. 38. Results are presented for $-1 \leqslant \Gamma \leqslant 0$ and $Re_R = 10^5$, where Γ is the ratio of the speed of the slower disk to that of the faster one and Re_R is the rotational Reynolds number of the faster disk.

This sample case at a relatively low Reynolds number shows the transition from Batchelor-type flow at $\Gamma = 0$ to Stewartson-type flow at $\Gamma = -1$ with a transition point at about $\Gamma = -0.4$. The transition is associated with transition from laminar to turbulent flow, and consequently the accuracy of the computations depends strongly on the transitional characteristics of the turbulence model used.

Figure 39 shows a comparison between computations and experiment for the velocities for $\Gamma = 0$, the rotor–stator case. The low Reynolds number model of Chien [9] and the standard k–ε model using 71×71 grid are adopted. The grid was slightly stretched toward the center, so that the first
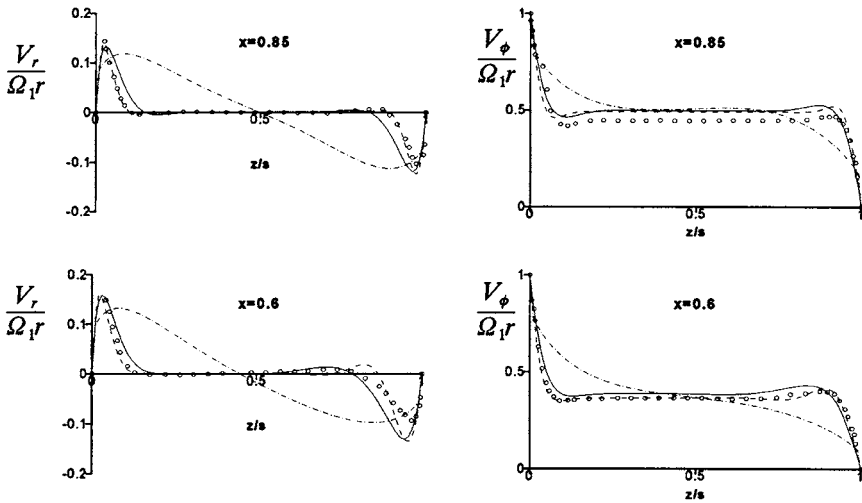
FIG. 39. Comparisons between computed and measured velocities for $\Gamma = 0$, $Re_R = 10^5$: (---) laminar flow; (——), (–·–) turbulent flow by low Re and standard models; ($\bigcirc$) measurements.

node was at the distance $Y_P = 2.56 \times 10^{-4}$. The results show good performance by laminar computations and low-Reynolds-number models, but the standard k–ε model, known to perform well for high-Reynolds-number flows, fails to capture flow features in this case. The measurements and computations show laminar Batchelor-type flow structure.

The results in Fig. 40 for $\Gamma = -0.6$ show evidence of the double transition from Batchelor-type flow (laminar) to Stewartson-type flow (turbulent). The flow regime may be characterized as too turbulent for laminar computations, but still not turbulent enough to use the standard k–ε model with wall functions.

As mentioned earlier, the wall functions are applicable for, say, $y^+ \geqslant 30$. This may be achieved by choosing the first computational node at a sufficient distance from the wall. This gives correct behavior of the flow in the regions far from the wall, but loses resolution of predicting the near-wall velocity field, which is usually important, for example, in the rotating cavity cases.

Figure 41 shows a comparison between eddy viscosity predicted by the standard and Chien's low-Reynolds-number models. The figure shows that the standard model significantly overpredicts turbulence intensity levels, having the highest discrepancy in the near-wall region, as expected according to the preceding discussion.
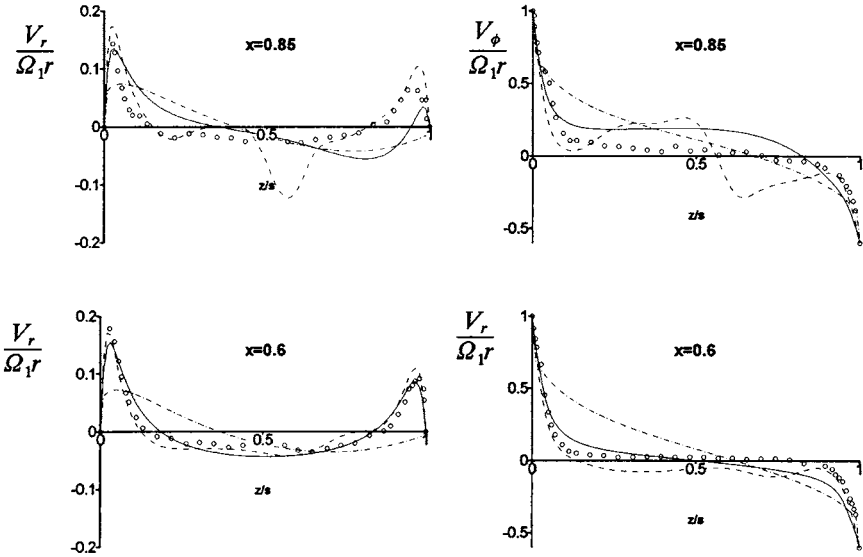
FIG. 40. Same as Fig. 39, but for $\Gamma = -0.6$.
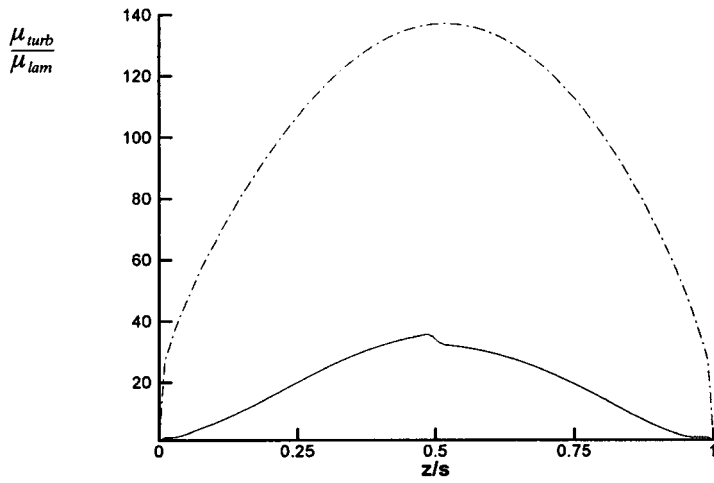
FIG. 41. Comparison between eddy viscosity predicted by low Reynolds number (——) and standard $k-\varepsilon$ models ($-\cdot-$); $\Gamma = -0.6$, $x = 0.6$.

VII. Turbulence Modeling for Rotational Effects

In this section, we review the issues related to turbulence modeling for treating the rotational effect. It is known from both experiment and direct numerical simulation data that for homogeneous flows, the system rotation can change the turbulence dissipation rate (Bardina *et al.* [1], Shimomura [42]). However, as will be discussed, the conventional two-equation turbulence model fundamentally cannot account for the presence of the rotation-induced body force effect. Additional modeling concepts need to be introduced to reflect the presence of rotation [44]. We start with the governing equations then summarize the key modeling issues and possible treatments in the context of the two-equation closure.

When the axis of rotation is perpendicular to the plane of mean shear, rotation induces Coriolis force, which can have a considerable effect on the mean flow pattern as well as the turbulence structure. It was pointed out by Johnston *et al.* [23] that there are two basic effects associated with boundary layers on rotating surfaces: (i) If components of the Coriolis acceleration exist parallel to the solid surface on which the layers are growing, three-dimensionality, i.e., secondary flows will tend to develop in the mean flow field of the layers; (ii) if a component of the Coriolis acceleration is perpendicular to a solid surface, stabilizing effects are observed in the turbulence structure. Both effects are important in the flow fields of centrifugal impellers.

Three different stability-related phenomena in bounding rotating shear flows have been observed by Johnston *et al.* [23]: (i) Rotation can, by a change in the wall-layer streak burst rate, modify the rate of turbulence production relative to dissipation and thereby modify the profiles of turbulence energy, stress, and mean velocity across the layer; (ii) rotation can increase or decrease the tendency of a hydrodynamically unstable laminar layer to undergo transition to a turbulent state, i.e., rotation can promote or suppress turbulent transition; (iii) finally, for laminar boundary layers and laminar channel flows, rotation may induce instability of the flow to large-scale disturbances, for example, the development of large cellular vortical models of the Taylor–Gortler type. The effect of the Coriolis force on turbulence structure of shear flows has been analyzed by Johnston *et al.* [23], and the role of the gradient Richardson number has been identified. The stability-related phenomena of rotating flows have also been analyzed by Bradshaw [7] with the examination of other turbulent shear flows with analogous nonconservative body forces (curved-streamline flows with centrifugal forces and density stratified flows with buoyant forces normal to the plane of flow), and by Tritton [47] with the "displaced particle analysis."

Direct and large-eddy simulations of turbulence, which require the solution of the three-dimensional time-dependent Navier–Stokes equations, may complement experimental investigation of rotating shear flows in a fruitful way, and thereby promote our understanding of the influences of rotation on the turbulence structure. The direct and large-eddy simulation of flow in a rotating channel (Kim [28], Kristoffersen and Andersson [29]) reproduced many of the experimentally observed effects of the Coriolis forces on the mean flow and its turbulence structure. However, these flow simulations are only obtained at relatively low Reynolds numbers. For simulating high-Reynolds-number rotating turbulence flows, turbulent models with rotating effect are needed.

A number of computational studies using the Reynolds-averaged approach have been done to predict the effect of rotation on turbulence as well as mean flow quantities. The simplest turbulence model is based on the mixing length formula (Bradshaw [7]):

$$l/l_0 = 1/(1 + \beta R_i). \tag{19}$$

Here β is a constant determined from experiments, l_0 is the mixing length at zero rotation, and R_i is the Richardson number, which is the local stability parameter; a negative value of R_i denotes an unstable region while a positive value denotes a stable region. Howard *et al.* [21] and Younnis [52] used a two-equation k–ε model with modifications based on the value of the turbulent Richardson number to incorporate the effect of rotation on turbulence structure and on the mean flow. Galmes and Lakshminarayana [17] and Warfield and Lakshminarayana [49] used algebraic Reynolds-stress models to account for the rotational effect and the anisotropy of the turbulence. Launder *et al.* [33] used a full second moment closure to calculate fully developed rotating channel flow. In general, these methods have been successful in capturing the mean characteristics of the flow and in some cases also the turbulent quantities. However, the computational expense depends on the extent of the complexity of the turbulence models.

In the following, the rotational effect on turbulence modeling within the context of the k–ε model is investigated. First, the turbulent transport equation for Reynolds stress in the rotational frame is presented. The rotational effect analysis with the k–ε model is detailed. Second, a physical analysis of effect of rotation on turbulence structure is conducted. Based on these analyses, a k–ε model with rotational effects in general three-dimensional coordinates is presented. Then, numerical assessment of the rotational modeling is made.

A. The Turbulent Transport Equations with Rotational Effects

If the coordinate system is attached with the rotational system, then the momentum equation is expressed as

$$\rho \frac{\partial \vec{q}}{\partial t} + \rho \vec{q} \cdot \nabla \vec{q} = -\nabla P + \mu \nabla^2 \vec{q} - 2\rho \vec{\Omega} \times \vec{q} - \rho \vec{\Omega} \times (\vec{\Omega} \times \vec{r}). \quad (20)$$

Here, $\vec{q}$ is the velocity vector, and $\vec{\Omega}$ is the angular velocity of the coordinate system. Eqution (20) can be written in the nondimensional form

$$\frac{\partial \vec{q}}{\partial t} + \vec{q} \cdot \nabla \vec{q} = -\nabla P + \frac{1}{Re} \nabla^2 \vec{q} - 2R_0 \vec{\Omega} \times \vec{q} - R_0^2 \vec{\Omega} \times (\vec{\Omega} \times \vec{r}). \quad (21)$$

Here, for simplicity, the same symbols are used for both the dimensional and nondimensional variables. $R_e = \rho U_0 l_0 / \mu$ is the Reynolds number, U_0 is the velocity scale, and l_0 is the length scale. $R_0 = \Omega_0 l_0 / U_0$ is the rotational number, and Ω_0 is the angular velocity scale. Clearly, if $R_0 \sim O(1)$, then the Coriolis force and centrifugal force will have noticeable effects on flows through the momentum equation.

For turbulent flows, the system rotation not only affects flow fields through the momentum equation, it also affects flow fields by modifying the turbulent transport process. This can be seen through the Reynolds-stress equation. If the momentum equation, Eq. (20), is written in the tensor form

$$\rho \frac{\partial u_i}{\partial t} + \rho u_k \frac{\partial u_i}{\partial x_k} = -\frac{\partial p}{\partial x_i} + \mu \frac{\partial^2 u_i}{\partial x_k \partial x_k} - 2\rho e_{ipk} \Omega_p u_k - \rho e_{irs} \Omega_r (e_{spk} \Omega_p r_k), \quad (22)$$

the corresponding Reynolds-stress equations can be written as

$$\frac{\partial \tau_{ij}}{\partial t} + \bar{u}_k \frac{\partial \tau_{ij}}{\partial x_k} = -\tau_{ik} \frac{\partial \bar{u}_j}{\partial x_k} - \tau_{jk} \frac{\partial \bar{u}_i}{\partial x_k} + \varepsilon_{ij} - \Pi_{ij} + \frac{\partial}{\partial x_k} \left[v \frac{\partial \tau_{ij}}{\partial x_k} + C_{ijk} \right] + Rot_{ij}$$

$$(23)$$

where

$$Rot_{ij} = -2e_{ipk} \Omega_p \overline{\rho u_i' u_k'} - 2e_{jpk} \Omega_p \overline{\rho u_i' u_k'}. \quad (24)$$

Here, Rot_{ij} is the extra term caused by Coriolis force. It can be seen that the Reynolds-stress component τ_{ij} is affected by the interaction between the angular velocity and other Reynolds-stress components, and τ_{ij}, in turn, affects the velocity field. Whereas nominally centrifugal force has no direct effect on τ_{ij}, as indicated by Eq. (23), it can affect τ_{ij} by changing the mean flow field through the momentum equations.

The turbulence kinetic energy equation can be obtained by taking the trace of Eq. (23). In fact, the trace of term (i) in Eq. (24) is

$$
\text{trace of } (i) = -2\rho[e_{123}\Omega_2\overline{u_1'u_3'} + e_{132}\Omega_3\overline{u_1'u_2'} + e_{231}\Omega_3\overline{u_2'u_1'} + e_{213}\Omega_1\overline{u_2'u_3'}
$$
$$
+ e_{312}\Omega_1\overline{u_3'u_2'} + e_{321}\Omega_2\overline{u_3'u_1'}]
$$
$$
= -2\rho[\Omega_2\overline{u_1'u_3'} - \Omega_3\overline{u_1'u_2'} + \Omega_3\overline{u_2'u_1'} - \Omega_1\overline{u_2'u_3'}
$$
$$
+ \Omega_1\overline{u_3'u_2'} - \Omega_2\overline{u_3'u_1'}]
$$
$$
= 0. \tag{25}
$$

Similarly, the trace of term (ii) in Eq. (24) is also zero. Accordingly, the turbulent kinetic equation is seemingly unchanged by the system rotation:

$$
\rho\frac{\partial K}{\partial t} + \rho\bar{u}_j\frac{\partial K}{\partial x_j} = \mathcal{P} - \rho\varepsilon + \frac{\partial}{\partial x_j}\left[\mu\frac{\partial K}{\partial x_j} - \frac{1}{2}\overline{\rho u_i'u_i'u_j'} + \overline{p'u_j'}\right]. \tag{26}
$$

Although the system rotation has no direct effect on the turbulent kinetic energy equation, its effect is implicitly included in the $\mathcal{P}$ and $(\frac{1}{2}\overline{\rho u_i'u_i'u_j'} + \overline{p'u_j'})$ terms.

With system rotation, the equation for the turbulent kinetic energy dissipation rate is

$$
\rho\frac{\partial\varepsilon}{\partial t} + \rho\bar{u}_j\frac{\partial\varepsilon}{\partial x_j} = \mathcal{P}_\varepsilon - \Phi_\varepsilon + \mathcal{D}_\varepsilon + \mu\nabla^2\varepsilon + Rot(\varepsilon), \tag{27}
$$

where

$$
Rot(\varepsilon) = -4ve_{ipk}\Omega_p\frac{\overline{\partial u_i'}}{\partial x_j}\frac{\overline{\partial u_k'}}{\partial x_j} \tag{28}
$$

is the term caused by system rotation. Expanding this term, we get

$$
Rot_{123} = -4v\Omega_2\frac{\overline{\partial u_1'}}{\partial x_j}\frac{\overline{\partial u_3'}}{\partial x_j} \tag{29}
$$

$$
Rot_{132} = 4v\Omega_2\frac{\overline{\partial u_1'}}{\partial x_j}\frac{\overline{\partial u_2'}}{\partial x_j} \tag{30}
$$

$$
Rot_{231} = -4v\Omega_3\frac{\overline{\partial u_2'}}{\partial x_j}\frac{\overline{\partial u_1'}}{\partial x_j} \tag{31}
$$

$$
Rot_{213} = 4v\Omega_1\frac{\overline{\partial u_2'}}{\partial x_j}\frac{\overline{\partial u_3'}}{\partial x_j} \tag{32}
$$

$$
Rot_{312} = -4v\Omega_1\frac{\overline{\partial u_3'}}{\partial x_j}\frac{\overline{\partial u_2'}}{\partial x_j} \tag{33}
$$

$$Rot_{321} = 4v\Omega_2 \frac{\overline{\partial u'_3}}{\partial x_j} \frac{\partial u'_1}{\partial x_j} \tag{34}$$

$$Rot(\varepsilon) = Rot_{123} + Rot_{132} + Rot_{231} + Rot_{213} + Rot_{312} + Rot_{321} = 0. \tag{35}$$

Interestingly, the system rotation has seemingly no direct effect on the turbulence dissipation rate equation, either. From the preceding analysis, it can be seen that the original $K-\varepsilon$ model does not explicitly account for the rotational effect on turbulence transport process. To simulate rotating turbulent flows with the $K-\varepsilon$ model, modifications have to be made to account for the explicit effect of Coriolis force on the turbulent transport process. In the next section, theoretical analyses are conducted to investigate the mechanisms of Coriolis force affecting the fluid flow stability character-istics and the turbulent transport process, and to identify the key parameter in the process.

B. Displaced Particle Analysis

The role of rotation on the stability of a shear flow is given by Tritton [47] with the so-called "displaced particle analysis." His argument related orig-inally to the stability of laminar flows. However, it may also be an indication of the processes occurring with turbulent flows.

The specific configuration under consideration is a unidirectional shear flow in a rotational reference frame, with the vorticity associated with the shear parallel to that of the system rotation. We choose Cartesian coordi-nates, so that the mean flow is in the x direction with the speed varying in the y-direction, $\boldsymbol{u} = (u(y), 0, 0)$. The system rotates with an angular velocity Ω about the z-axis. The shear vorticity is

$$\zeta = -\frac{\partial u}{\partial y} \tag{36}$$

and the effect of the rotation is indicated by the ratio of the background vorticity to the shear vorticity:

$$S = \frac{2\Omega}{\zeta}. \tag{37}$$

This can be seen in Fig. 42 with positive $\partial u/\partial y$ and positive Ω so that S is negative. Suppose that a small perturbation leads to a fluid particle being displaced a small distance δ in the y-direction. In its undisplaced position it has longitudinal velocity u_1 and when displaced it has velocity u'_1. There is a Coriolis force $2\rho\Omega u'_1$ acting on it as shown in Fig. 42 (ρ is fluid density)
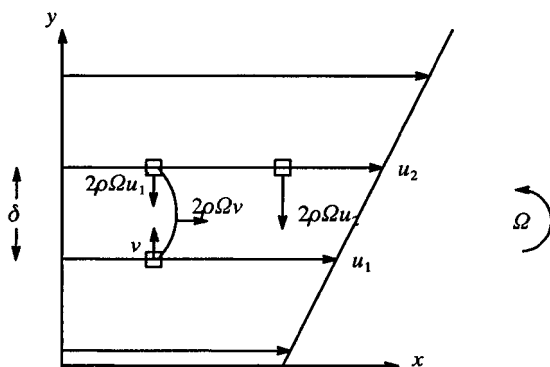
FIG. 42. Forces on displaced and undisplaced "particles."

Similar Coriolis force $2\rho\Omega u_2$ acts on an undisplaced particle at its new position and thus will be balanced by a pressure gradient in the y-direction. That pressure gradient also acts on the displaced particle. Hence, the net force tends to displace the particle further if $u_1' < u_2$ and to return it toward its original position if $u_1' > u_2$, $u_1' \neq u_1$ because of the Coriolis force that acted while the particle was moving with velocity v in the y-direction:

$$u_1' - u_1 = \int 2\Omega v dt = 2\Omega\delta. \qquad (38)$$

Hence,

$$u_1' - u_2 = u_1' - u_1 + u_1 - u_2$$

$$= 2\Omega\delta - \frac{\partial u}{\partial y}\delta$$

$$= -\frac{\partial u}{\partial y}(S + 1)\delta$$

$$= \zeta(S + 1)\delta. \qquad (39)$$

The net effect of the Coriolis and pressure forces on the displaced particle is a force

$$2\rho\Omega(u_2 - u_1') = -\rho\zeta S(S + 1)\delta. \qquad (40)$$

Remembering that we are considering negative ζ (positive $\partial u/\partial y$) and negative S, we see that the particle tends to be displaced further if $S > -1$, and restored if $S < -1$. Corresponding considerations for positive S show that the particle always tends to be restored in this case. Thus, there is a

destabilizing mechanism, to which the shear and Coriolis effects are both intrinsic, occurring in the range $-1 < S < 0$.

Bradshaw [7] defined an equivalent gradient "Richardson number" as

$$B = S(S + 1) = \frac{-2\Omega(\partial u/\partial y - \Omega)}{(\partial u/\partial y)^2}. \tag{41}$$

He first recognized the role of this dimensionless parameter in rotating flows by making an analogy with system rotation, streamline curvature, and buoyancy in turbulent shear flows. Although Tritton's analysis was initially related to the stability of laminar shear flows rather than to turbulence, both lines of argument led to the same main result, showing that this fluid particle stability mechanism could be an indication of the effect of Coriolis force on turbulent shear flows. In summary, the effect of rotation is destabilizing when

$$-1 < S < 0, \tag{42}$$

i.e.,

$$B < 0. \tag{43}$$

Maximum destabilization occurs at $S = -\frac{1}{2}$ (i.e., $B = -\frac{1}{4}$), and restabilization of the flow may be expected when $S < -1$. On the other hand, positive S is always associated with stabilized flow.

C. SIMPLIFIED REYNOLDS-STRESS ANALYSIS

The rotational effect on turbulent flow has been analyzed with the simple boundary-layer type flow (Johnston *et al.* [23]). It is useful to consider the rotation effect by looking at the equations for the rates of increase of the turbulent correlations $\overline{u'^2}$, $\overline{v'^2}$, $\overline{w'^2}$ and $-\overline{u'v'}$ as we follow time-mean particle motion. For the two-dimensional boundary layer case, the Reynolds-stress equations are

$$D(-\overline{u'v'})/Dt = \overline{v'^2}\partial\bar{u}/\partial y + (\overline{u'^2} - \overline{v'^2})2\Omega + [\text{O.T.}] \tag{44}$$

$$D(\overline{u'^2})/Dt = -\overline{u'v'}w\partial\bar{u}/\partial y - (-\overline{u'v'})4\Omega + [\text{O.T.}] \tag{45}$$

$$D(\overline{v'^2})/Dt = +0 + (-\overline{u'v'})4\Omega + [\text{O.T.}] \tag{46}$$

$$D(\overline{w'^2})/Dt = +0 + 0 + [\text{O.T.}]. \tag{47}$$

The terms on the left-hand sides are the "advection" or "mean transport" terms. Just to the right of the equals sign are the production terms appearing in a nonrotating frame. Next on the right are the rotation "production" terms, which enter the Eqs. (44)–(47) for rotating flows as a result of

Coriolis acceleration. Finally, all other terms are lumped together and designated [O.T.]. These terms include rate of viscous transport and dissipation, diffusion and convection by turbulence, and the fluctuating pressure–strain interaction terms. All the [O.T.] terms are identical to their respective zero-rotation forms.

The equation for development of turbulent kinetic energy

$$K = \tfrac{1}{2}(\overline{u'^2} + \overline{v'^2} + \overline{w'^2}) \tag{48}$$

is

$$\frac{DK}{Dt} = (-\overline{u'v'}) \frac{\partial \bar{u}}{\partial y} + [\text{O.T.}] = P + [\text{O.T.}]. \tag{49}$$

Production of turbulence energy P is not explicitly dependent on Ω, but is implicitly affected by rotation through the effects Ω has on Reynolds stress and mean shear.

For boundary layers and channel flows, peak levels of turbulence energy and stress are achieved in the regions close to the solid walls, i.e., the wall layers. In the wall layers the production and dissipation terms in Eqs. (44)–(47) are very large. The excess energy or stress produced locally is diffused by the nondissipation parts of the [O.T.] terms. The advection terms are usually very small and may be neglected in the wall layers. Therefore, the production terms are the only terms that can cause a local gain in the level of energy or stress. It is reasonable to assume, as a first approximation, that effects which increase (decrease) the approximate net production rates will also lead to an increase (decrease) in levels of turbulence energy and stress.
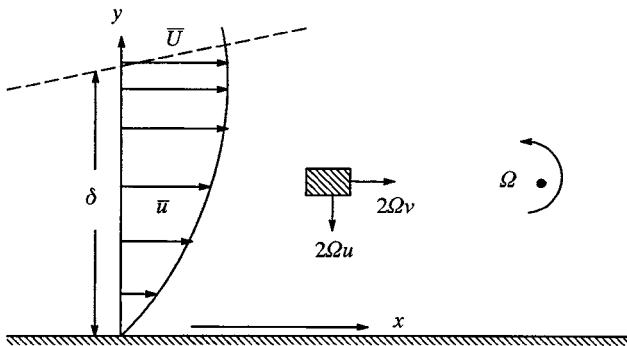
Fig. 43. Mean velocity for a two-dimensional boundary layer on a rotating surface. Vectors on particle are Coriolis forces.

Let us apply this idea to the rotation-boundary layer case (see Fig. 43) where $\partial \bar{u}/\partial y$ is positive and the usual condition exists, i.e., $-\overline{u'v'} > 0$ and $\overline{u'^2} - \overline{v'^2} > 0$. Also assume, for the moment, that the rotation rate is positive, $\Omega > 0$. It is seen from the rotation production terms in Eq. (44) that a positive rotation causes an increase in the net rate of production of turbulence stress. Consequently, we expect that a layer with positive rotation will have a higher level of stress $-\overline{u'v'}$ than an otherwise equivalent stationary layer. If $-\overline{u'v'}$ is increased with positive rotation, then the production of turbulence energy P will be higher and consequently the level of energy K will increase. The direction of rotation is arbitrary. If it is negative, $\Omega < 0$, the same line of argument will indicate that rates of production of $-\overline{u'v'}$ and K will tend to decrease relative to conditions that would exist in an equivalent stationary flows.

In summary, the examination of the production terms in Eq. (44)–(47) leads to the conclusion that in wall layers the sign, and the magnitude, of rotation effects might be controlled by the local dimensionless parameter

$$S = -\frac{2\Omega}{(\partial \bar{u}/\partial y)} \tag{50}$$

so that when $S > 0$, decrease of $-\overline{u'v'}$ and K is expected, but when $S < 0$, increase of $-\overline{u'v'}$ and K is expected.

Note that, in the preceding analysis, the effect of [O.T.] terms is neglected. From the direct numerical simulation data (Kristoffersen and Andersson [29]), it can be seen that for the three-dimensional turbulent duct flow, [O.T.] terms have some effects on turbulent structure, which is obvious for the correltion $\overline{w'^2}$ in the third direction. It is also clear that $-\overline{u'v'}$ and Ω affect each other. However, the result of the direct numerical simulation largely confirmed the foregoing analysis. In the next section, the same analysis will be used to modify the $K-\varepsilon$ equations to accommodate the system rotation effect.

D. MODELING CONCEPTS FOR TREATING ROTATIONAL EFFECTS

From the preceding theoretical analyses, it can be seen how rotation affects the turbelence kinetic energy and Reynolds stress, and the role of the Richardson number. A consistent approach with the $k-\varepsilon$ model is to make the coefficients of the cource terms in turbulent transport equations depend on the Richardson number. Except for the energy diffusion term, the turbulent kinetic energy equation is treated exactly in the $K-\varepsilon$ model. The dissipation equation seems to be the obvious place to affect adjustments to the transport of length scales. The ε equation itself is heuristically derived

and therefore offers some room for refinement. On the grounds of seeking the simplest possible form, Launder *et al.* [30] have assumed that the effects of streamline curvature on the length scale can be accommodated by making the effective value of $C_{\varepsilon 2}$ depend on the Richardson number. Howard *et al.* [21], using the Bradshaw analogy [7] between streamline curvature and system rotation, adopted the model of Launder *et al.* [30] for streamline curvature to rotating straight duct flow, making $C_{\varepsilon 2}$ depend on the rotational Richardson number. They used two forms of Richardson number,

$$\text{(i)} \qquad R_i = \frac{-2\Omega(\partial u/\partial y - 2\Omega)}{(\partial u/\partial y)^2} \tag{51}$$

or

$$\text{(ii)} \qquad R_i = \frac{-2\Omega}{\partial u/\partial y}. \tag{52}$$

Following Launder *et al.* [30], the turbulent Richardson number is defined by replacing the mean flow time scale represented by the denominator ($\partial u/\partial y$) with a turbulent time scale (K/ε). Thus, the corresponding Richardson number is

$$\text{(i)} \qquad R_{it} = -2\Omega \left(\frac{K}{\varepsilon}\right)^2 \left(\frac{\partial u}{\partial y} - 2\Omega\right) \tag{53}$$

or

$$\text{(ii)} \qquad R_{it} = -2\Omega \left(\frac{K}{\varepsilon}\right)^2 \frac{\partial u}{\partial y}. \tag{54}$$

Accordingly,

$$C_{\varepsilon 2} = 1.93(1 + C_c), \tag{55}$$

where

$$C_c = 0.2R_{it}. \tag{56}$$

The coefficient of 0.2 is from Launder *et al.* [30]. However, the preceding formulation is tested only for straight channel/duct flows. It is not coordinate invariant. In the present work, it is generalized to

$$R_{it} = -2\Omega \left(\frac{k}{\varepsilon}\right)^2 \left(\frac{\partial u}{\partial y} - \frac{\partial v}{\partial x}\right). \tag{57}$$

Here, $\left(\dfrac{\partial u}{\partial y} - \dfrac{\partial v}{\partial x}\right)$ is the mean vorticity. For three-dimensional flow,

$$R_{it} = -2(K/\varepsilon)^2 \left[\Omega_x \left(\frac{\partial v}{\partial z} - \frac{\partial w}{\partial y}\right) + \Omega_y \left(\frac{\partial w}{\partial x} - \frac{\partial u}{\partial z}\right) + \Omega_z \left(\frac{\partial u}{\partial y} - \frac{\partial v}{\partial y}\right) \right] \tag{58}$$

or

$$R_{it} = 2 \left(\frac{K}{\varepsilon} \right)^2 e_{ipj} \Omega_p \frac{\partial u_i}{\partial x_j}. \tag{59}$$

The final forms of the modified K–ε equations are

$$\frac{\partial K}{\partial t} + \bar{u}_i \frac{\partial K}{\partial x_i} = P - \varepsilon + \frac{\partial}{\partial x_i} \left(\frac{v_T}{\sigma_K} \frac{\partial K}{\partial x_i} \right) \tag{60}$$

$$\frac{\partial \varepsilon}{\partial t} + \bar{u}_i \frac{\partial \varepsilon}{\partial x_i} = C_{\varepsilon 1} \frac{\varepsilon}{K} P - C_{\varepsilon 2}(1 + C_c) \frac{\varepsilon^2}{K} + \frac{\partial}{\partial x_i} \left(\frac{v_T}{\sigma_\varepsilon} \frac{\partial \varepsilon}{\partial x_i} \right). \tag{61}$$

E. NUMERICAL ASSESSMENT OF ROTATIONAL EFFECT

Numerical results have been obtained using the assumption that the flow field is periodic in the circumferential direction. This assumption allows us to discretize only a small portion of the complete cavity. A two-dimensional planar grid was constructed to discretize the cross-sectional plane of the cavity. This mesh was constructed in a way that resembles a Cartesian grid that has been stretched toward the center from the four walls that form the cross-section of the cavity, leaving more points directly adjacent to these walls. This planar grid was then used to form a three-dimensional sector-shaped computational domain by sequentially rotating the cross-sectional planar grid about the axis of symmetry, placing copies of the planar grid at $5°$ and $10°$ away from the original planar grid. This is done to allow the general three-dimensional flow solver to compute gradients in the circumferential direction, which for this investigation will be zero because of the periodic assumption. Two cross-sectional planar grids have been used for this study, an 81×31 and an 121×51 grid.

Figure 44 shows the numerically predicted variation of the normalized circumferential velocity profile versus the experimentally measured profile at a nondimensional radial location of approximately $r/R = 0.675$ for the 81×31 grid. Figure 45 is the same plot for the results on the finer, 121×51 grid. It can be seen that both set of results are in reasonable agreement with the experimental data. Figure 46 shows the numerically predicted radial velocity profile versus the experimentally measured profile at this radial location for both grids. All of the numerical predictions are seen to be very similar. Figure 47 indicates the predicted variation of the eddy viscosity and the turbulent Reynolds number, i.e., using the local eddy viscosity value to replace the laminar viscosity for the definition of the Reynolds number. Figure 48 indicates the predicted variation of the eddy viscosity and the turbulent Reynolds number. Figure 49 indicates the regions of the flow field
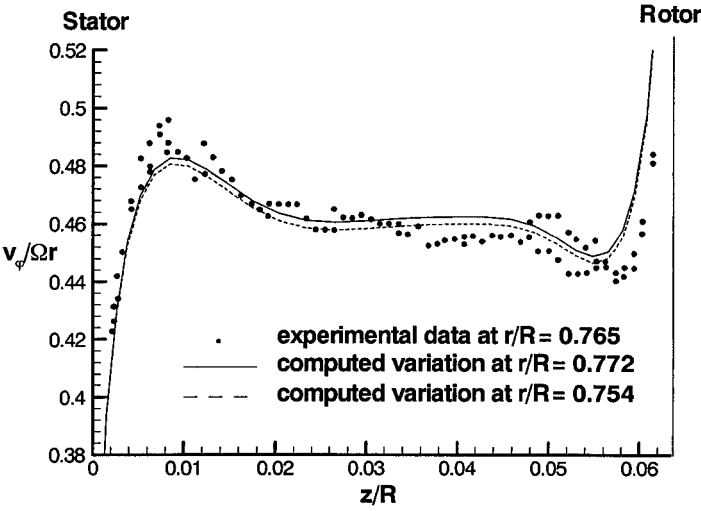
FIG. 44. Comparison between the experimentally measured circumferential velocity profile and the numerically predicted profile at $r/R \approx 0.765$ for $Re_R = 4.4 \times 10^6$ using the 81×31 grid.
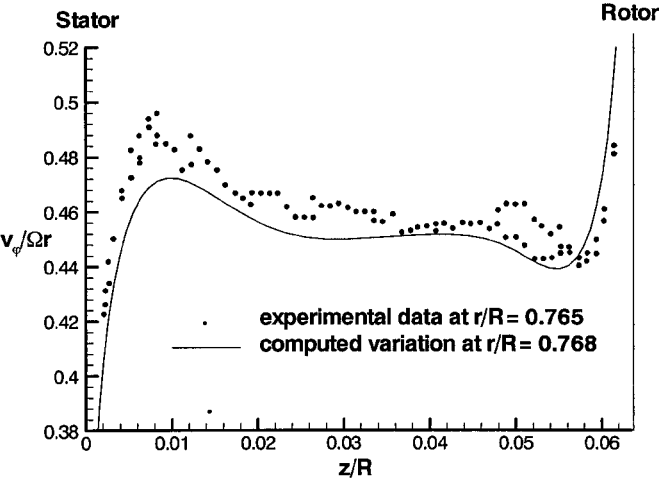
FIG. 45. Comparison between the experimentally measured circumferential velocity profile and the numerically predicted profile at $r/R \approx 0.765$ for $Re_R = 4.4 \times 10^6$ using the 121×51 grid.
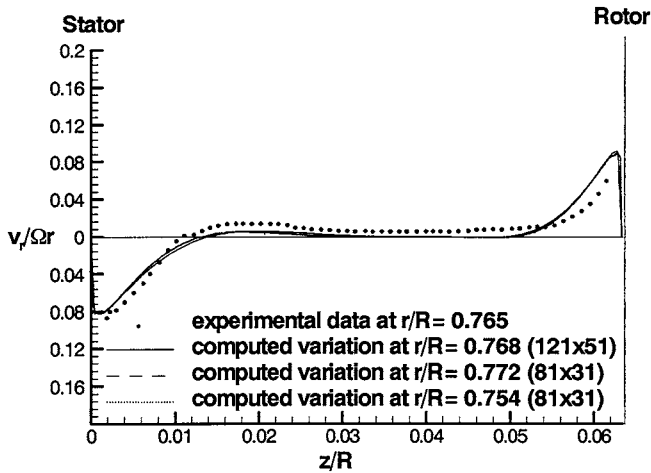
FIG. 46. Comparison between the experimentally measured radial velocity profile and the numerically predicted profile at $r/R \approx 0.765$ for $Re_R = 4.4 \times 10^6$ for both the 81×31 and the 121×51 grids.

for which there is a net production or a net dissipation of turbulent kinetic energy. Figure 50 compares the results obtained using the standard $k-\varepsilon$ model and the Richardson number correction model.

For this flow configuration, there is no open boundary and the turbulent flow structure is established strictly because of the balance between local
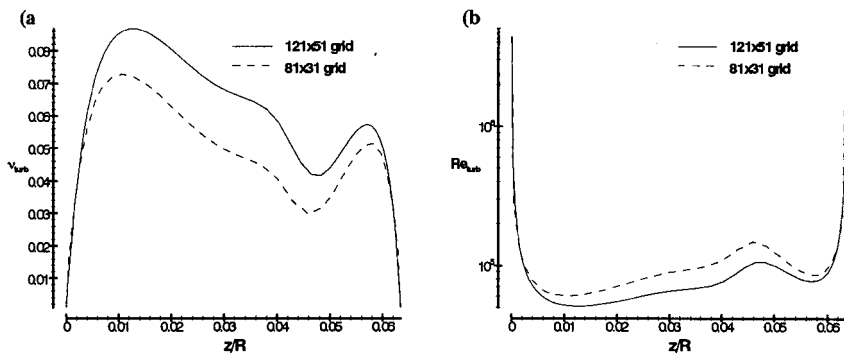
FIG. 47. Plot of the numerically predicted variation of (a) the eddy viscosity and (b) the turbulent Reynolds number at $r/R \approx 0.765$ for $Re_R = 4.4 \times 10^6$ for both the 81×31 and the 121×51 grids.
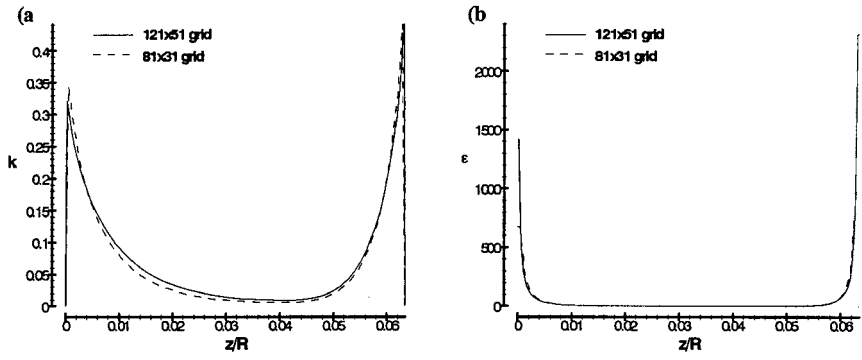
FIG. 48. Plot of the numerically predicted variation of (a) the turbulent kinetic energy and (b) the turbulent dissipation rate at $r/R \approx 0.765$ for $Re_R = 4.4 \times 10^6$ for both the 81×31 and the 121×51 grids.
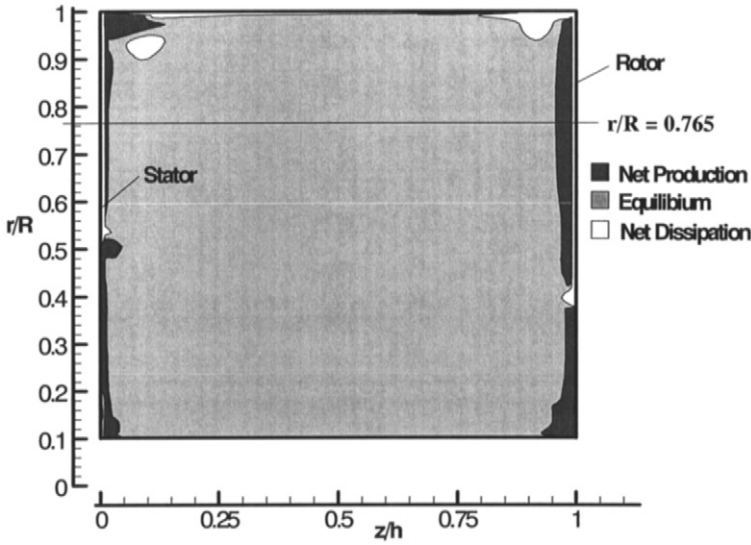
FIG. 49. Plot of the numerically predicted regions of net production and net dissipation of turbulent kinetic energy for $Re_R = 4.4 \times 10^6$ for the 121×51 grid.
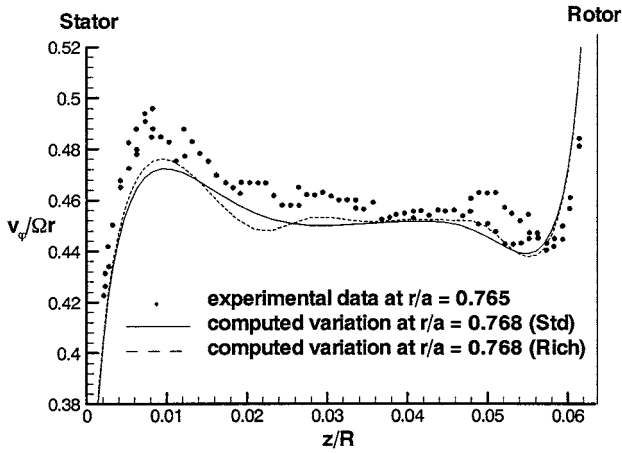
FIG. 50. Comparison between the experimentally measured circumferential velocity profile and the numerically predicted profile using both the standard k–ε model and the Richardson number correction model at $r/R \approx 0.765$ for $Re_R = 4.4 \times 10^6$ using the 121×51 grid.

production, dissipation, and convective/diffusive transport mechanisms of the key turbulence variables: k and ε. For k, the wall boundary value is zero everywhere, whereas for ε, the conventional extrapolated equilibrium treatment is applied [44]. Since the production and dissipation mechanisms are confined in the wall region, as evidenced in Fig. 48, the variations of both k and ε appear largely in the wall region also. As depicted in Fig. 47, there are substantial variations in both eddy viscosity and turbulent Reynolds number, both in the flow domain and between two different grid systems. However, these variations are mainly caused by the relatively small values of k and ε. An inspection of the *balance* between local production and dissipation in the k-equation, as shown in Fig. 49, reveals that away from the wall region, the flow is in essence in equilibrium and hence the variations in eddy viscosity and turbulent Reynolds number are not influential in terms of the flow and heat transfer characteristics.

The modified turbulence model that accounts for the Richardson number correction has been adopted in the computation, and the comparison between the standard model and this modified model is highlighted in Fig. 50. From this figure it can be seen that only minor differences between the two solutions exist. As already discussed, the Richardson number affects the sink term of the ε-equation in a manner that tends to reduce ε when $Ri_t > 0$. Figures 51 and 52 indicate that although the magnitude of the Richardson
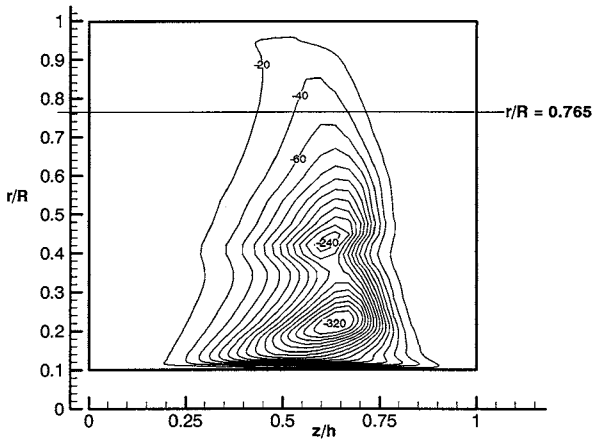
FIG. 51. Cross-sectional plane contour plot of the turbulent Richardson number for the rotor–stator disk system.

number becomes large in a portion of the flow field, it has little effect because of the already low values of ε in that region. The region that would be most sensitive to the rotational effect is the wall region. However, from Fig. 50 it is clear that this modified k–ε turbulence model has only modest effects on the flow in this type of rotor–stator configuration.
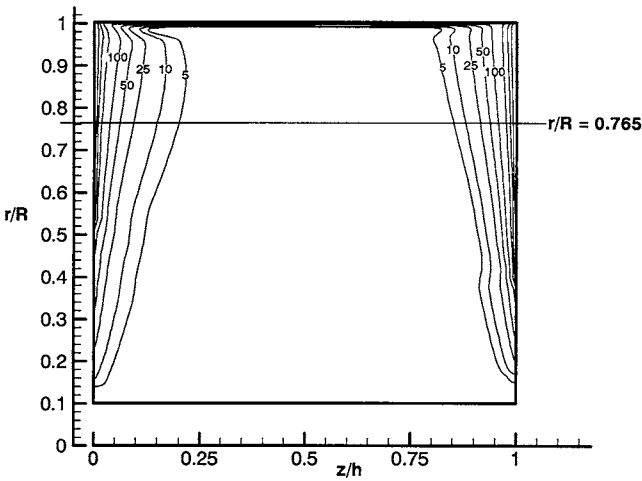
FIG. 52. Cross-sectional plane contour plot of the dissipation rate of turbulent kinetic energy (ε) for the rotor–stator disk system.

The modified turbulence model, by accounting for the Richardson number correction, has been adopted in the computation, and the comparison between the "original" Launder–Spalding model [32] and this modified model is highlighted in Fig. 50. As already discussed, the Richardson number affects the sink terms in the ε-equation. Consequently, local balance between k and ε changes, depending on the balance between the local mean strain rate, turbulent kinetic energy, dissipation rate of the turbulent kinetic energy, and overall system rotational speed. The most sensitive region to be affected by the rotational effect is the wall region. In the present rotor–stator system, the mean strain rate of the flow field is positive on both rotor and stator wall regions. The Richardson number correction causes the mean velocity to exhibit more variations in accordance with the modification to the ε-equation.

VIII. Numerical Convergence Considerations

Convergence of numerical solutions for rotating cavity geometries is notoriously slow. One known cause for the slow rate of convergence is the existence of extra source terms in the governing equations that occur because of the rotation. These additional source terms are of a form that interlink or couple the momentum equations over and above the usual coupling due to the convection terms and continuity condition. To illustrate this more clearly, the viscous, incompressible, steady-state equations governing the conservation of mass and the time rate of change of linear momentum with respect to a Cartesian frame of reference that rotates about the z-axis with constant angular speed Ω are given:

$$\frac{\partial(u)}{\partial x} + \frac{\partial(v)}{\partial y} + \frac{\partial(w)}{\partial z} = 0 \tag{62}$$

$$\frac{\partial(uu)}{\partial x} + \frac{\partial(uv)}{\partial y} + \frac{\partial(uw)}{\partial z} = -\frac{1}{\rho}\frac{\partial p}{\partial x} + v\left[\frac{\partial^2 u}{\partial x^2} + \frac{\partial^2 u}{\partial y^2} + \frac{\partial^2 u}{\partial z^2}\right] + 2\Omega v + \Omega^2 x$$
$$\tag{63}$$

$$\frac{\partial(uv)}{\partial x} + \frac{\partial(vv)}{\partial y} + \frac{\partial(vw)}{\partial z} = -\frac{1}{\rho}\frac{\partial p}{\partial y} + v\left[\frac{\partial^2 v}{\partial x^2} + \frac{\partial^2 v}{\partial y^2} + \frac{\partial^2 v}{\partial z^2}\right] - 2\Omega u + \Omega^2 y$$
$$\tag{64}$$

$$\frac{\partial(uw)}{\partial x} + \frac{\partial(vw)}{\partial y} + \frac{\partial(ww)}{\partial z} = -\frac{1}{\rho}\frac{\partial p}{\partial z} + v\left[\frac{\partial^2 w}{\partial x^2} + \frac{\partial^2 w}{\partial y^2} + \frac{\partial^2 w}{\partial z^2}\right]. \tag{65}$$

The most common methods used to solve this set of equations implement an algorithm that sequentially solves the individual equations [40, 44, 48]. These sequential algorithms artificially decouple the set of governing equations and rely on an iterative solution technique to obtain the final converged solution. A typical sequential solution algorithm would begin by solving Eq. (63) for u using guessed values for v, w, and the pressure field. Then Eq. (64) would be used to solve for v using the calculated values for u and the guessed values for w and the pressure field. Similarly, Eq. (65) would then be solved for w using calculated values for u and v and the guessed values for the pressure field. At this point the computed values for u, v, and w would not necessarily satisfy the continuity equation. To enforce the continuity condition on the flow field, a pressure correction equation is often developed from Eq. (62) that corrects the velocities and pressure field. This sequence is repeated in order to update the decoupled variables in the individual equations until a specified convergence tolerance is met.

As stated earlier, for the rotating cavity flows there exist additional source terms that couple the momentum equations over and above the usual coupling due to the convection terms and continuity condition. In Eqs. (63) and (64) these additional terms are the Coriolis accelerations $2\Omega v$ and $-2\Omega u$, respectively. In order to provide a measure of additional coupling within the solution algorithm and hence, we hope, improve the convergence characteristics, we have altered the sequence used in the solution algorithm. The modified algorithm attempts specifically to improve coupling between the Coriolis source terms of the u and v momentum equations. This has been accomplished by adding an inner iteration cycle between these two equations. The number of inner iterations, n, can be optimized for the specific problem being solved. To illustrate the effectiveness of this technique, the computation presented in the previous section has been performed utilizing values of n between 1 and 8. Figure 53 shows the residual trace for the u-momentum equation for various values of n. This figure clearly shows that the rate of convergence can be significantly improved using this modified algorithm. The largest step improvement in convergence was found to occur when n was increased from 1 to 2, with less dramatic step improvements as n was further increased. Plots of the v-momentum equation residual trace showed a similar trend, whereas residual traces for the w-momentum and pressure correction equations showed relatively little effects. To further assess the effectiveness of this method, Fig. 54 shows the normalized CPU time needed to reach a specified level of convergence versus n. From this figure it can be seen that the optimum value for n was 7, based on a criterion of minimizing CPU time for this computation.
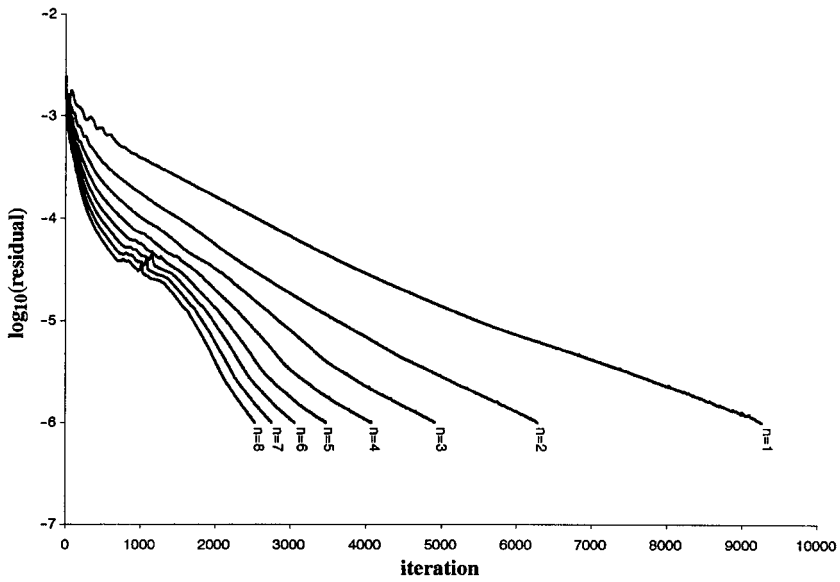
FIG. 53. Trace of the u-momentum equation residual for various values of n.
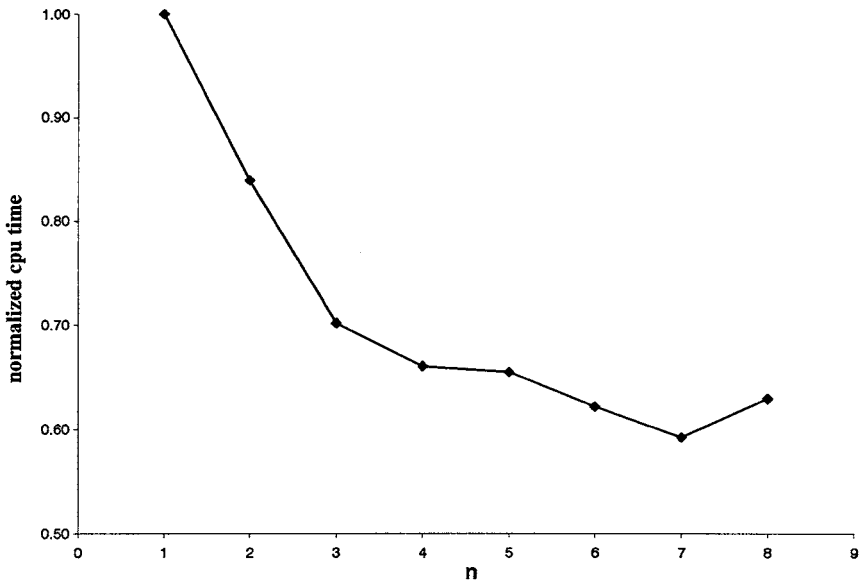
FIG. 54. Normalized CPU time required to reach a specified level of convergence versus n.

IX. Concluding Remarks

The fluid flow and heat transfer in rotating disk systems is a very interesting and challenging topic that involves a number of geometric and flow parameters and has been found to be very difficult to analyze for many cases of direct practical interest. In this review, we have summarized the various aspects related to both infinite and finite disk flows. Depending on the flow regime and geometric configuration, predictions made by both Batchelor and Stewartson can be observed. Several main directions have been identified for future activity. For example, in much of the published literature, insufficient attention has been given to establish the required numerical accuracy. The issue of turbulence modeling is a long-standing one; however, it is particularly important and unresolved for the current rotating flow problems. Current modeling concepts have been reviewed to encourage future efforts. The experimental information is also often of insufficient detail to enable a comprehensive assessment of the analytical and numerical solutions. Much remains to be done before we gain satisfactory understanding of this topic to guide turbomachinery design.

Appendix

Summary of Sealed Cavity Investigations

TABLE I

Isothermal Sealed Cavity Investigations Found in the Literature
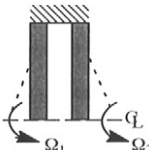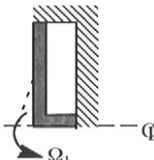
Ref.	Geometry	$G = h/R$	$\Gamma = \Omega_2/\Omega_1$	Reynolds number	Type
Picha, Eckert [39]		0.11 to 0.78	$-1 \leqslant \Gamma \leqslant 1$	2.92×10^5 $\leqslant Re_R$ $\leqslant 1.31$ $\times 10^5$	Experimental
Daily, Nece [13]		0.0127 to 0.217	$\Gamma = 0$	1.0×10^3 $\leqslant Re_R$ $\leqslant 1.0$ $\times 10^7$	Experimental and theoretical

TABLE I *Continued*
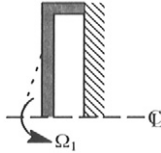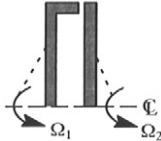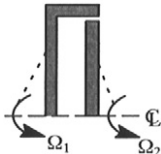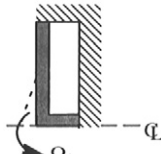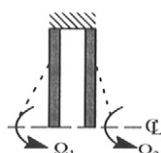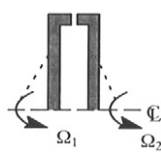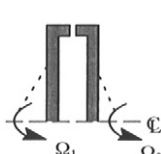
Ref.	Geometry	$G = h/R$	$\Gamma = \Omega_2/\Omega_1$	Reynolds number	Type
Pao [37]		1.00	$\Gamma = 0$	1 $\leqslant Re_{\text{h}}$ $\leqslant 5000$	Numerical and experimental
Lugt, Haussling [34]		1.00	$\Gamma = 0$, -0.11, -0.33	$Re_{\text{h}} = 100$, 1000, 5000	Numerical
Dijkstra, Heijst [15]		0.07	-0.825 $\leqslant \Gamma \leqslant 0$	100 $\leqslant Re_{\text{h}}$ $\leqslant 1000$	Numerical and experimental
Williams *et al.* [51]		0.0255 to 0.217	$\Gamma = 0$	$Re_{\text{R}} = 4.2$ $\times 10^4$ and 4.4×10^6	Numerical
Morse [35]		0.0685 and 0.1	$-1 \leqslant \Gamma$ $\leqslant 1$	$Re_{\text{R}} = 1.0$ $\times 10^5$ to 1.0×10^7	Numerical
Gan *et al.* [19]		0.12	$\Gamma = 0, -1$	$Re_{\text{R}} = 10^5$ and 10^6 $(\Gamma = 0)$ $Re_{\text{R}} = 6 \times 10^4$, 2.31×10^5 and 4×10^5 $(\Gamma = -1)$	Experimental
Gan *et al.* [18]		0.12	$\Gamma = -1$	$Re_{\text{R}} = 2.31$ $\times 10^5$, 7.26×10^5, and 1.17×10^6	Experimental and numerical

TABLE I   *Continued*
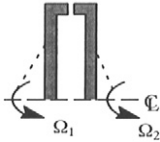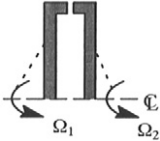
Ref.	Geometry	$G = h/R$	$\Gamma = \Omega_2/\Omega_1$	Reynolds number	Type
Kilic *et al.* [26]		0.12	$-1 \leqslant \Gamma \leqslant 0$	$Re_R = 1.25 \times 10^6$	Numerical and experimental
Kilic *et al.* [27]		0.12	$-1 \leqslant \Gamma \leqslant 0$	$Re_R = 1.0 \times 10^5$	Numerical and experimental

TABLE II

SUMMARY OF FLOW TYPES FOUND IN ROTATING DISK SYSTEMS

	Configuration	Laminar flow type	Turbulent flow type
Unshrouded	Rotor–stator ($\Gamma = 0.0$)	Stewartson	Batchelor
	Contrarotating ($\Gamma = -1.0$)	Stewartson	unclear
Shrouded	Rotor–stator ($\Gamma = 0.0$)	Batchelor	Batchelor
	Contrarotating ($\Gamma = -1.0$)	Batchelor	Stewartson

References

1. Bardina, J., Ferziger, J. H., and Rogallo, R. S. (1985). Effect of rotation on isotropic turbulence; computation and modeling. *J. Fluid Mech.* **154**, 321–336.
2. Batchelor, G. K. (1951). Note on a class of solutions of the Navier–Stokes equations representing steady rotationally-symmetric flow. *Quart. J. Mech. Appl. Math.* **4**, Part 1, 29–41.
3. Bhavnani, S. H., Khodadadi, J. M., Goodling, J. S., and Waggott, J (1992). An experimental study of fluid flow in disk cavities. *J. Turbomachinery* **114**, 454–461.
4. Bohn, D., Deuker, E., Emunds, R., and Gorelitz, V. (1995). Experimental and theoretical investigations of heat transfer in closed gas-filled rotating annuli. *J. Turbomachinery* **117**, 175–183.
5. Bohn, D., Dibelius, G. H., Deuker, E., and Emunds, R. (1994). Flow pattern and heat transfer in a closed rotating annulus. *J. Turbomachinery* **116**, 542–547.
6. Bohn, D., Emunds, R., Gorelitz, V., and Krüger, U. (1996). Experimental and theoretical investigations of heat transfer in closed gas-filled rotating annuli II. *J. Turbomachinery* **117**, 175–183.

7. Bradshaw, P. (1969). The analogy between streamline curvature and buoyancy in turbulent shear flow. *J. Fluid Mech.* **36**, 177–191.

8. Brady, J. F., and Durlofsky, L. (1987). On rotating disk flow. *J. Fluid Mech.* **175**, 363–394.

9. Chien, K. (1982). Predictions of channel and boundary-layer flows with a low-Reynolds-number turbulence model. *AIAA J.* **20**, 33–38.

10. Chew, J. W. (1985). Computation of convective laminar flow in rotating cavities. *J. Fluid Mech.* **153**, 339–360.

11. Cochran, W. G. (1934). The flow due to a rotating disk. *Proc. Camb. Phil. Soc.* **30**, 365–375.

12. Daily, J. W., Ernst, W. D., and Asbedian, V. V. (1964). Enclosed rotating disks with superposed throughflow: mean steady and periodic unsteady characteristics of induced flow. *Hydrodynamics Lab. Rept. 54*, Massachusetts Institute of Technology, Cambridge, MA.

13. Daily, J. W., and Nece, R. E. (1960). Chamber dimension effects on induced flow and frictional resistance of enclosed rotating disks. *J. Basic Eng.* **82,** 217–232.

14. De Vahl Davis, G. (1983). Natural convection of air in a square cavity: A benchmark numerical solution. *Int. J. Num. Methods Fluids* **3**, 249–264.

15. Dijkstra, D., and van Heijst, G. J. F. (1983). The flow between two finite rotating disks enclosed by a cylinder. *J. Fluid Mech.* **128**, 123–154.

16. Ebert, M., Shyy, W., Thakur, S., Segal, C., and Liou, M. (1999). Heat transfer and fluid flow in rotating cavities. *AIAA Paper No. 99-0737*.

17. Galmes, J. M., and Lakshminarayana, B. (1984). Turbulence modeling for three-dimensional shear flows over curved rotating bodies. *AIAA J.* **22**, 1420–1428.

18. Gan, X. P., Kilic, M., and Owen, J. M. (1995). Flow between contrarotating disks. *J. Turbomachinery* **117**, 298–305.

19. Gan, X. P., and MacGregor, S. A. (1995). Experimental study of the flow in the cavity between rotating disks. *Exp. Thermal Fluid Sci.* **10**, 379–387.

20. Homsy, G. M., and Hudson, J. L. (1969). Centrifugally driven thermal convection in a rotating cylinder. *J. Fluid Mech.* **35**, Part 1, 33–52.

21. Howard, J. H. G., Patankar, S. V., and Bordynuik, R. M. (1980) Flow prediction in rotating ducts using Coriolis-modified turbulence models. *J. Fluids Eng.* **102**, 456–461.

22. Hudson, J. L., Tang, D., and Abell, S. (1978). Experiments on centrifugally driven thermal convection in a rotating cylinder. *J. Fluid Mech.* **86**, Part 1, 147–159.

23. Johnston, J. P., Halleen, R. M., and Lezius, D. K. (1972). Effects of spanwise rotation on the structure of two-dimensional fully developed turbulent channel flow. *J. Fluid Mech.* **56**, 533–557.

24. Jones, W. P., and Launder, B. E. (1972). The prediction of laminarization with a 2-equation model of turbulence. *Int. J. Heat Mass Transfer* **15**, 301–314.

25. von Kármán, T. (1921). Über laminare und turbulent reibung. *Zeits. f. angew. Math. u. Mech.* **1(4)**, 233–252. Also, *NACA TM 1092* for English translation (1946).

26. Kilic, M., Gan, X. and Owen, J. M. (1996). Turbulent flow between two disks contrarotating at different speeds. *J. Turbomachinery* **118**, 408–413.

27. Kilic, M., Gan, X., and Owen, J. M. (1994). Transitional flow between contra-rotating disks. *J. Fluid Mech.* **281**, 119–135.

28. Kim, J. (1983). The effect of rotation on turbulence structure. *Proc. 4th Symp. on Turbulent Shear Flows, Karlsruhe,* 6.14–6.19.

29. Kristoffersen, R., and Andersson, H. I. (1993). Direct simulation of low-Reynolds-number turbulent flow in a rotating channel. *J. Fluid Mech.* **256**, 163–197.

30. Launder, B. E., Priddin, C. H., and Sharma, B. I. (1979). The calculation of turbulent boundary layers on spinning and curved surfaces. *J. Fluids Eng.* **102**, 231–239.

31. Launder, B. E., and Sharma, B. I. (1974). Application of the energy dissipation model of turbulence to the calculation of flow near a spinning disc. *Lett. Heat Mass Transfer* **1**, 131–138.
32. Launder, B. E., and Spalding, D. B. (1974). The numerical computation of turbulent flows. *Comput. Meths. Appl. Mech. Eng.* **3**, 269–289.
33. Launder, B. E., Tselepidakis, D. P., and Younnis, B. A. (1987). A second-moment closure study of rotation channel flow. *J. Fluid Mech.* **183**, 63–75.
34. Lugt, H. J., and Haussling, H. J. (1973). Development of flow circulation in a rotating tank. *Acta Mech.* **18**, 255–272.
35. Morse, A. P. (1991). Assessment of laminar-turbulent transition in closed disk geometries. *J. Turbomachinery* **113**, 131–138.
36. Owen, J. M., and Rogers, R. H. (1989). *Flow and Heat Transfer in Rotating-Disc Systems*, Vol. I, *Rotor–Stator Systems*. Wiley, New York.
37. Pao, H.-P. (1970). Numerical computation of a confined rotating flow. *J. Appl. Mech.* **37**, 480–487.
38. Patel, V. C., Wolfgang, R., and Scheuerer, G. (1985). Turbulence models for near-wall and low Reynolds number flows: A review. *AIAA J.* **23**, 1308–1319.
39. Picha, K. G., and Eckert, E. R. G. (1958). Study of the flow between coaxial disks rotating with arbitrary velocities in an open or enclosed space. *Proc. U.S. Natl. Congr. Appl. Mech.*, *3rd*, 791–798.
40. Rhie, C. M., and Chow, W. L. (1983). Numerical study of the turbulent flow past an airfoil with trailing edge separation. *AIAA J.* **21**, 1525–1532.
41. Schlichting, H. (1979). *Boundary-Layer Theory*. McGraw Hill, New York.
42. Shimomura, Y. (1993). Turbulence modeling suggested by system rotation. In *Near-Wall Turbulence* (R. M. C. So, C. G. Speziale, and B. E. Launder, Eds.), pp. 115–123. Elsevier, Amsterdam.
43. Shyy, W. (1994). *Computational Modeling for Fluid Flow and Interfacial Transport*. Elsevier, Amsterdam, (revised printing 1997).
44. Shyy, W., Thakur, S. S., Ouyang, H., Liu, J. and Blosch, E. L. (1997). *Computational Techniques for Complex Transport Phenomena*. Cambridge University Press, New York.
45. Stewartson, K. (1953). On the flow between two rotating coaxial disks. *Proc. Camb. Phil. Soc.* **49**, 333–341.
46. Theodorsen, T., and Regier, A. (1944). Experiments on drag of revolving discs, cylinders, and streamline rods at high speeds. *NACA Rep. 793*.
47. Tritton, D. J. (1992). Stabilization and destabilization of turbulent shear flow in a rotating fluid. *J. Fluid Mech.* **241**, 503–523.
48. Udaykumar, H. S., Kan, H.-C., Shyy, W., and Tran-Son-Tay, R. (1997). Multiphase dynamics in arbitrary geometries on fixed Cartesian grids. *J. Comp. Phys.* **137**, 366–405.
49. Warfield, M. J., and Lakshminarayana, B. (1987). Computation of rotating turbulent flow with an algebraic Reynolds stress model. *AIAA J.* **25**, 957–964.
50. White, F. M. (1974). *Viscous Fluid Flow*. McGraw Hill, New York.
51. Williams, M., Chen, W. C., Baché, G., and Eastland, A. (1991). An analysis methodology for internal swirling flow systems with a rotating wall. *J. Turbomachinery* **113**, 83–90.
52. Younnis, B. A. (1993). Prediction of turbulent flows in rotating rectangular ducts. *J. Fluids Eng.* **115**, 646–652.
53. Zandbergen, P. J., and Dijkstra, D. (1977). Non-unique solutions of the Navier–Stokes equations for the Karman swirling flow. *J. Eng. Math.* **11**, 167–188.
54. Zandbergen, P. J., and Dijkstra, D. (1987). Von Kármán swirling flows. *Ann. Rev. Fluid Mech.* **19**, 465–491.

Recent Advances in the Modeling and Applications of Nonconventional Heat Pipes

SURESH V. GARIMELLA

Cooling Technologies Research Consortium,
School of Mechanical Engineering,
Purdue University,
West Lafayette, Indiana 47907-1288

C. B. SOBHAN

Department of Mechanical Engineering,
Regional Engineering College,
Calicut, Kerala 673601, India

I. Introduction

The use of heat pipes and thermosyphons is becoming widespread in a large number of applications, as these devices are generally passive in their operation and provide effective heat transport with minimal losses. Practical applications range from aerospace engineering to energy conversion devices, and from electronics cooling to biomedical engineering. One of the drivers for heat pipe development has been the need to reliably manage thermal dissipation in increasingly miniaturized and higher-density microelectronic components, while maintaining device temperatures to specification. Many different types of heat pipes have been developed in recent years to address electronics thermal management problems, as well as a host of other applications, and have shown promising results.

Extensive research on heat pipes and thermosyphons has been reported during the past decade. Effective design of heat pipes, based on their operating limitations and depending on analytical and experimental results

and parametric studies, has been the object of attention of many investigators. Various new concepts involving miniature forms of heat pipes and thermosyphons, micro heat pipes, and other nonconventional designs have been proposed, and the operation of these devices has been analyzed and tested. Increasingly realistic assumptions have been used in the modeling of heat pipes, supported by experimental investigations.

Although the vapor flow and heat transfer processes in heat pipes have been studied in the past, the analysis of these processes coupled with liquid flow in the wick structure has received much attention more recently. Simplified conduction models and transport equations have been used for the liquid flow in heat pipe wicks, with the wick structure generally being treated as a porous medium. Theoretical and experimental approaches have been employed for computing, visualizing, and measuring the capillary meniscus at the wick–vapor boundaries. In addition, efforts to identify the major limitations of heat pipe operation and to quantify the maximum heat transport capabilities theoretically and experimentally have been reported. A number of recent publications have dealt with transient analyses and heat pipe startup. Thermodynamic aspects of heat pipe operation, including meniscus formation, have also been explored. Analyses of vapor and liquid flow dynamics in heat pipes incorporating thermodynamic considerations have been presented.

Flat-plate and other nonconventional designs such as disk-shaped, rotating, and reciprocating heat pipes, as well as thermosyphons, have also received attention. Multidimensional analyses of the vapor and wick regions in such heat pipes have been reported wherein the temperature, pressure, and velocity fields in the vapor and liquid as well as the maximum heat transport capabilities are obtained. Miniature forms of heat pipes and thermosyphons for use in electronics cooling applications have also been explored.

Micro heat pipes have been suggested as effective devices for cooling electronics, and methods for the development, analysis, and testing of micro heat pipes have been discussed in detail in the literature. Fundamental studies of the fluid flow and heat transfer mechanisms in micro channels and their application to understanding the physics of micro heat pipes are also available.

Recent advances in the analysis and understanding of heat pipes are reviewed here, with a special emphasis on investigations reported over the past decade. Although conventional heat pipes are briefly discussed, the focus is on nonconventional designs, including heat pipes that are flat, concentric annular, rotating, disk-shaped, reciprocating, or gas-loaded. Both experimental and theoretical approaches are included. Special conditions such as startup transients and operation with discrete heat sources at the

evaporator are discussed. A majority of the studies have been aimed at electronics cooling applications, although a number of other applications have also been studied. Micro heat pipes, thermosyphons, and capillary pumped loops are surveyed. This review also includes a discussion of the recent patents and inventions in this area.

II. Thermal Analysis

Theoretical and experimental investigations that provide insight into the physics, design considerations, and operating limits of various types of conventional heat pipes as well as nonconventional designs such as annular, flat, and disk-shaped, and gas-loaded, rotating, and reciprocating heat pipes (where novel methods are used to achieve or improve fluid transport) are discussed in this section.

A. Conventional Designs

A variety of theoretical analyses in the literature have provided temperature, pressure, and velocity distributions in transient and steady-state operation of heat pipes. Transient, compressible one-dimensional vapor flow in a cylindrical heat pipe was analyzed by Jang *et al.* [1]. Transient vapor flow dynamics were predicted at subsonic, sonic, and supersonic speeds, and at high mass flow rates and high temperatures. Friction coefficients at the interface were incorporated from existing two-dimensional numerical results. Injection and suction terms were included in the governing equations. Solutions were obtained using the implicit noniterative Beam Warming finite difference method. The numerical results as shown in Fig. 1 for a sodium heat pipe were compared with experimental data [2] on vapor flow in a cylindrical heat pipe simulated using a porous pipe with injection and suction of air, and also with data on actual vapor flow in cylindrical heat pipes [3].

Bowman *et al.* [4] presented a one-dimensional model in which the vapor flow, treated as a saturated vapor and not an ideal gas, was assumed to be incompressible in space but compressible in time. This model was improved by Bowman and Beran [5], who used a more accurate closure relationship between vapor density and vapor temperature in solving the mass conservation equation. This relationship expressed the density as a series function of the saturated vapor temperature with the coefficients having been obtained by curve-fitting saturated vapor data. An implicit solution method was used for solving the governing equations.
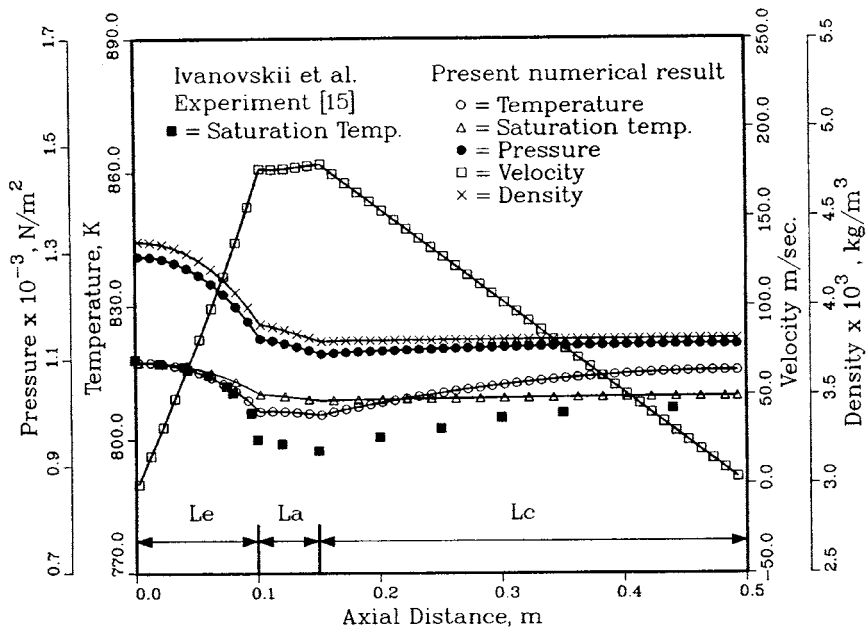
FIG. 1. Axial variations of temperature, pressure, velocity, and density in a sodium heat pipe at steady state [1].

Issacci *et al.* [6] used a two-dimensional, transient, compressible viscous flow model and a finite-difference solution to analyze the vapor dynamics during heat pipe startup. Transient variations of pressure, velocity, and friction factor were obtained. The calculated pressure drops for the transient period were found to be significantly higher than the steady-state values, exhibiting a nearly periodic oscillation while converging toward a steady state. This phenomenon was explained in terms of the multiple wave reflections observed in the evaporator and adiabatic regions during the startup transient. The transient variations of the vapor temperature and pressure are shown in Fig. 2. The average friction factor at the liquid–vapor interface was found to be significantly higher during the transient than at steady state, especially for higher input fluxes. A reversal of flow was noticed in the adiabatic region during the transient period. High heat fluxes on the order of 100 W/cm^2 were used in the analysis.

Zuo and Faghri [7] developed a heat pipe model with quasi-steady, one-dimensional vapor flow and transient, two-dimensional heat conduction in the wall and wick. The vapor flow was solved using the SIMPLE algorithm and the wick and wall regions were solved using the boundary
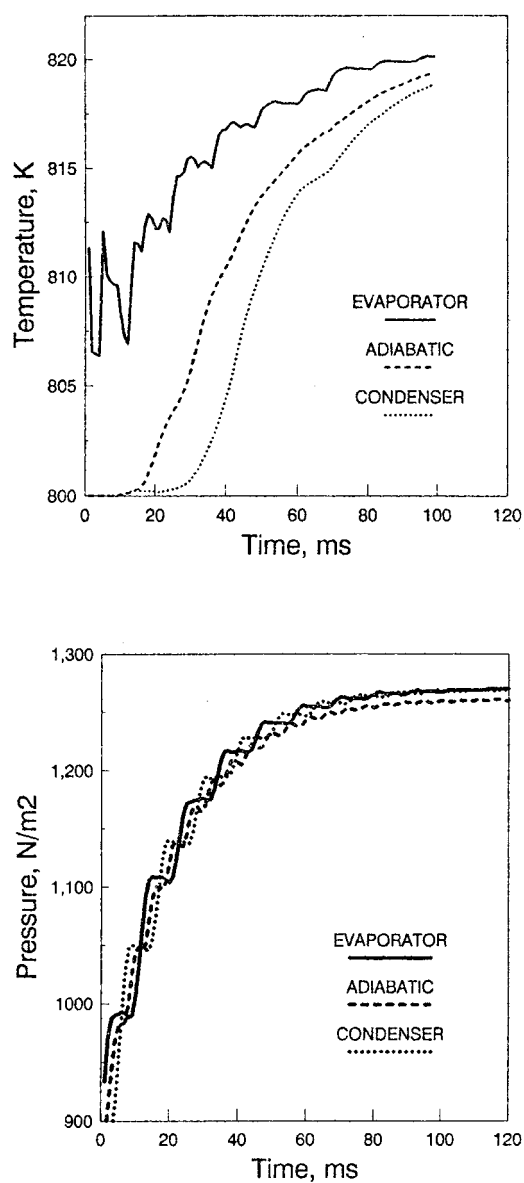
FIG. 2. Transient variation of the averaged vapor temperature and pressure during heat pipe startup [6]; periodic oscillations in transient pressure variation are noted.

element approach. This work essentially compared the effectiveness of using finite differences versus boundary elements for the solution of heat conduction in the wall and wick regions. A hybrid FDM/BEM method was found to offer a significant reduction in the computational time. A two-dimensional numerical analysis of the transient behavior of a cylindrical heat pipe was performed by Cao and Faghri [8]. Conservation equations were solved using an effective thermal conductivity for the screen wick. The saturation temperature was obtained from the saturation pressure at the liquid–vapor interface using the Clausius–Clapeyron equation; the equation of state for an ideal gas was applied in the vapor core.

A two-dimensional heat pipe transient analysis model was developed by Tournier and El-Genk [9]. Liquid compressibility, energy, and momentum discontinuities at the liquid–vapor interface and determination of the radius of curvature of the liquid meniscus at the interface were incorporated into the model, in addition to the effects of liquid pooling. Conservation equations were solved in the vapor region, while the Brinkman–Forchheimer extended Darcy flow model was employed for the wick region. The vapor in the core was assumed to be saturated, obviating the need for a consideration of the energy equation. At the liquid–vapor interface, conservation of mass was enforced along with a no-slip condition and an enthalpy jump due to evaporation/condensation. Numerical solutions were obtained by a predictor–corrector method. Variations of the effective thermal power throughput and vapor temperature with time were obtained. Axial variations of the wall and vapor temperatures and the normalized void fraction in the wick at various locations were computed. An important contribution of this paper was the identification of the formation and disappearance of the liquid pool, shown in the plots for the early transient response. The extent of the liquid pool, along with the evaporation and condensation rates, were determined with respect to axial position as a function of time. Figure 3 shows the transient variation of the extent of the liquid pool at the condenser from [9].

Chang and Chow [10] analyzed the transient response of a liquid metal heat pipe using a three-dimensional model for the wall and the wick, under the assumption that the liquid velocity in the wick was low, and the heat transfer through the wick was by conduction only. A one-dimensional model was used for the vapor flow. Transient variations of the surface temperature were compared with experimental results performed on a sodium heat pipe. The condenser was operated under transient conditions, and a reverse heat load was used in some of the experiments.

Experimental studies in the literature have generally attempted temperature and pressure measurements and visual observation of the fluid flow phenomena in heat pipes. Experimental verification of predicted maximum
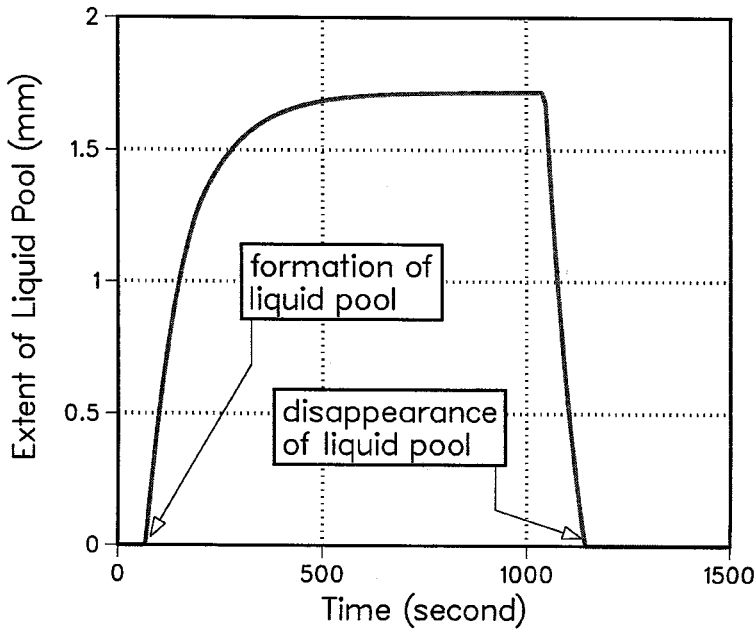
FIG. 3. Transient variation of the extent of liquid pool at the end of the condenser section in a water heat pipe [9].

heat transport limits and evaluation of the performance of heat pipes under various operating conditions have also been presented.

Yamamoto *et al.* [11] conducted transient experiments on stainless steel–mercury heat pipes, with the evaporator heated in a furnace. Results were presented in terms of temperature distributions and boiling and condensation curves. The mercury heat pipe was found to exhibit good performance except during startup. However, the material compatibility between the stainless steel container and mercury was not satisfactory, as revealed by visual observation using SEM and X ray microanalysis.

Copper–water heat pipe systems with double-layered copper screen wicks were investigated by El-Genk and Huang [12] to determine their transient response to step changes in input power. The evaporator section was uniformly heated and the condenser section was convectively cooled at different cooling rates. Spatial and temporal variations in the temperature of the wall as well as in the vapor were measured in addition to the effective power throughput. Time constants for transients in the vapor temperature and power throughput were determined as functions of the power input and

the liquid mass flow rate in the cooling jacket of the condenser. El-Genk *et al.* [13] performed experiments on a cylindrical copper–water heat pipe in an inclined position. The effect of the inclination angle at various power inputs and cooling rates was assessed, using the time constants during heat-up and cool-down. The time-dependent vapor and wall temperature data were used to benchmark their two-dimensional heat pipe transient analysis model.

Experiments were performed by Huber and Bowman [14] on copper–water heat pipes at various inclination angles to determine the effect of vibration on the capillary limit. Temperatures, vibration characteristics, and coolant flow rates were measured. Longitudinal vibration was found to cause a decrease in the capillary heat transport limit at certain amplitudes and frequencies.

A transient experimental and numerical study of the performance of a circular stainless steel–ammonia loop heat pipe was reported by Wirsch and Thomas [15]. The heat transfer coefficient at the evaporator was experimentally determined. A two-dimensional conduction model for the evaporator wall was solved using finite elements, and the characteristics of the loop heat pipe explored.

The evaporative heat transfer in a cylindrical grooved heat pipe was studied by Kobayashi *et al.* [16]. The liquid meniscus was divided into a macro and a micro region in the theoretical analysis: the macro region covered the liquid meniscus where conventional heat and mass transfer were expected to take place, while the micro region included the narrow meniscus region close to and in contact with the wall where intermolecular forces would affect transport. The thickness of the micro region was measured by optical means and its magnitude was explained in terms of the proposed theory. An interesting result was that one-third of the total heat supplied was transported though the micro region even though this region occupied only 1% of the total meniscus area.

B. Nonconventional Designs

1. *Flat Heat Pipes*

Flat heat pipes are especially useful in applications where space considerations are important as they can effectively replace a number of cylindrical heat pipes. Asymmetrical heating of the flat heat pipe (from one side only) was analyzed using an integral method by Vafai and Wang [17] to obtain the pressure, temperature, and velocity distributions. A nondimensional formulation of the governing equations was used with the porous wick represented by Darcy's law. Calculations were performed for heat pipes with
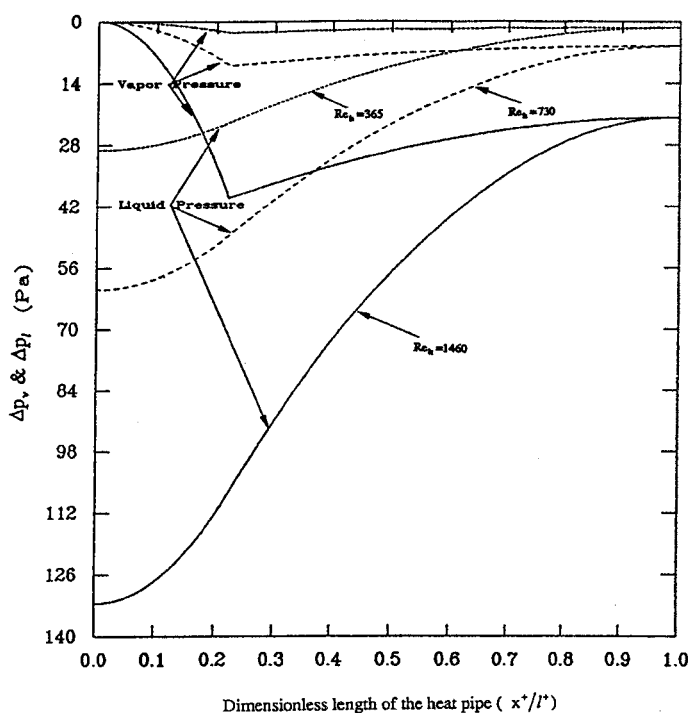
FIG. 4. Distributions of the vapor and liquid pressure along an asymmetrical flat plate heat pipe heated only from one side [17].

the container and wick made from aluminum and with heavy water as the working fluid. Axial distributions of the vapor and liquid pressures obtained by this analysis are shown in Fig. 4. Zhu and Vafai [18] studied the startup transient characteristics of an asymmetrical flat plate heat pipe, using transient heat conduction equations for the heat pipe wall and wick regions, and a pseudo-three-dimensional approximation for the vapor region.

A transient two-dimensional analysis of the vapor core and wick regions of a flat heat pipe was performed by Unnikrishnan and Sobhan [19]. For modeling the porous wick, the momentum equations were modified to account for the effect of the solid boundary and the inertial forces on the fluid flow [20]. The energy equation for the porous wick region included convection terms. Transient and steady-state variations of temperature, pressure and velocity were presented to illustrate the effect of different wick porosities. Figure 5 shows two typical plots of the transient distribution of the field variables obtained from this analysis, which demonstrate that the
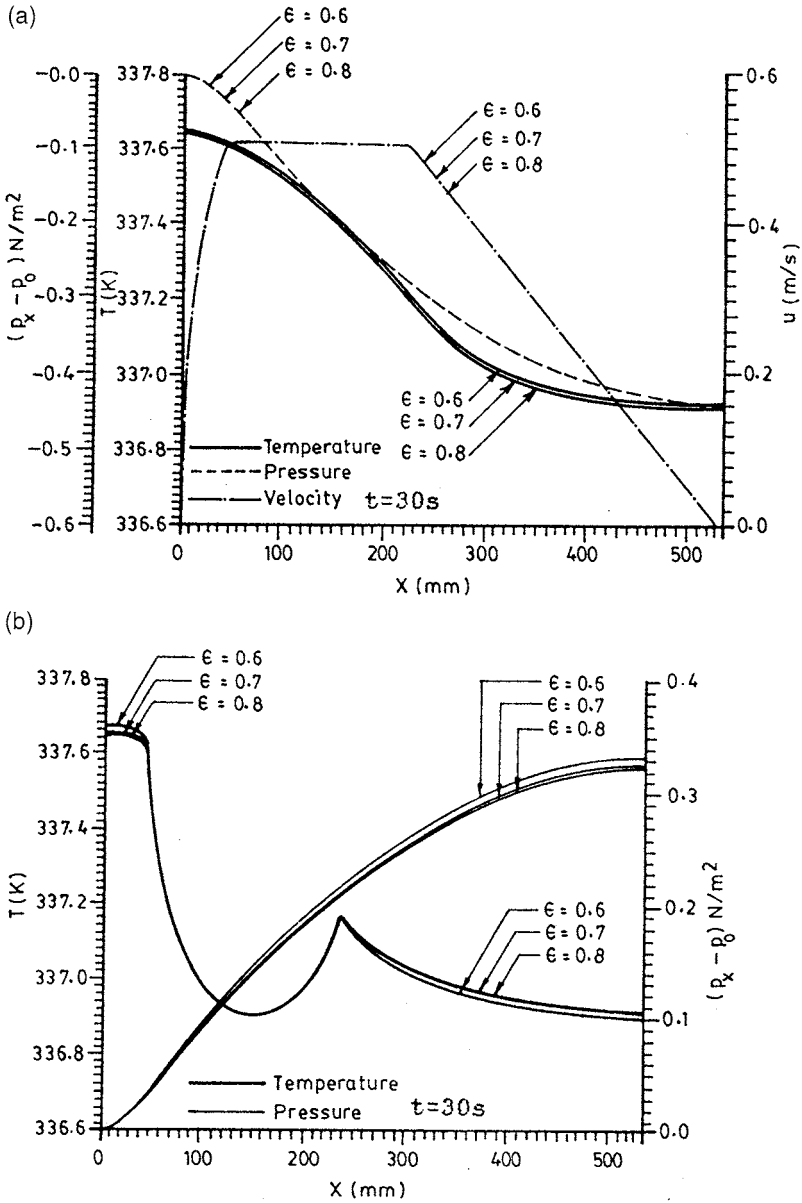
FIG. 5. Transient analysis of a flat heat pipe [19]: (a) distributions of the vapor temperature, pressure, and velocity for various wick porosities; (b) distributions of temperature and pressure in the wick for various wick porosities.

effect of wick porosity in the vapor core is of secondary importance, whereas this effect is more pronounced in the wick, especially in the evaporator and condenser regions.

A computational model for the analysis of flat heat pipes was developed by Sobhan *et al.* [21], which took into account the effects of conduction through the wall and wick that in turn result in heat flow into the interior through the externally adiabatic section and affect the velocity distributions in the wick and vapor. The heat removal capability of the heat pipe was contrasted to that of a copper heat sink with dimensions equivalent to those of the heat pipe wall, and it was found that the temperature drop along the heat pipe was reduced by 83% compared to the copper heat sink. The effects of variations in the wall thickness, wick porosity, and evaporator heat flux on the performance of the flat heat pipe were explored using this model by Vadakkan *et al.* [22].

Khrustalev and Faghri [23] discussed the boiling and capillary limitations of a miniature, axially grooved flat heat pipe, with its performance enhanced by applying a porous copper coating on the surface between the grooves. The maximum heat transport capacity, incorporating heat transfer coefficients for the enhanced surfaces, was computed. Variations of the maximum heat flow rate with respect to the operating temperature, with and without the porous coating, were compared as shown in Fig. 6, showing a significant enhancement predicted due to the presence of the porous coating.

Experiments on a flat plate heat pipe used as an alternative to a solid metal heat sink for electronics cooling were reported by Um *et al.* [24]. An aluminum heat pipe with a glass top and stainless steel screen wick on one side was considered, with a dielectric fluid (FC-72) as the working medium. Effects of gravity on the temperature distribution and heat transport capacity were studied.

2. *Concentric Annular Heat Pipes*

A concentric annular heat pipe utilizes the annulus between two concentric tubes as the vapor space and features a capillary wick on either side of the annulus. The advantage is that both the inside and outside walls can be used for transferring heat into the evaporator. The design, testing, and analysis of the capillary limit in copper–water concentric annular heat pipes was discussed by Faghri and Thomas [25]. The axial temperature variation and maximum heat transport capacity in such a design were compared with those for a conventional heat pipe. Experimental measurements revealed that the annular heat pipe was capable of providing a maximum heat transport capacity as high as two times that of a conventional cylindrical heat pipe at comparable operating temperatures. The temperature variation
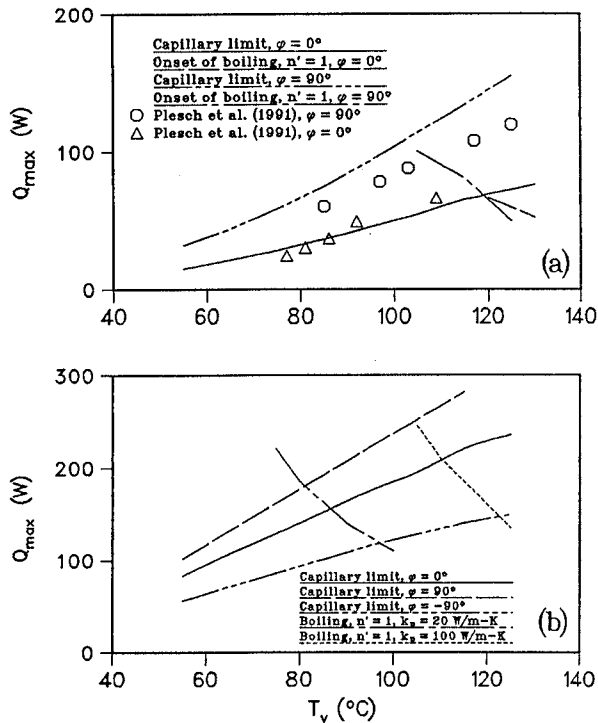
FIG. 6. Effect of application of a porous copper coating (b) on the intergroove region of a flat miniature heat pipe for enhancement of its performance, shown in comparison with the performance of a similar heat pipe without the coating (a) variation of the maximum heat transfer with respect to the operating temperature [23].

in the evaporator section was found to be lower for the concentric annular heat pipe, whereas in the condenser section, the temperature drop was larger for the annular case. The evaporator and condenser performance characteristics from this work are shown in Fig. 7. The variation of maximum heat input as a function of tilt angle was also reported in the paper. Two analyses of the concentric annular heat pipe were presented by Faghri [26]: A one-dimensional model was developed for compressible flow to arrive at the axial variations of Mach number, pressure, and temperature; and a two-dimensional approach was used for treatment of the vapor as an incompressible flow in which uniform blowing and suction rates were assumed over the heating and cooling sections, which were then related to the local heat transfer rates per unit length.
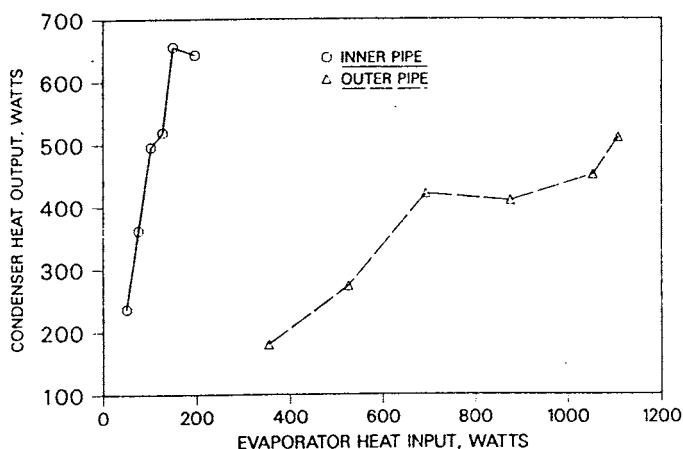
FIG. 7. Evaporator and condenser performance for a concentric annular heat pipe from experiments on a copper–water system [25].

3. Rotating Heat Pipes

Rotating heat pipes utilize centrifugal force to accomplish the transport of the liquid phase. Laminar, steady, incompressible vapor flow in axially rotating heat pipes was analyzed by Faghri *et al.* [27]. Normalized velocity components and temperature variations along the radius and length were obtained. The axial coefficient of friction was plotted along the length and was found to decrease with an increase in the rotational speed; as the radial Reynolds number increased, the magnitude of friction coefficients decreased. The tangential coefficient of friction remained almost constant along the axial direction at low radial Reynolds numbers, but increased rapidly in the condenser section at high Reynolds numbers. The rotational speed and radial Reynolds number were found to have a strong influence on the predicted velocities and pressures. At high rotational speeds, a central core with reversed flow in the axial direction was observed and was attributed to the reduced pressure at this location. A transient, two-dimensional simulation of the rotating heat pipe, with an axisymmetric formulation that accounted for the thin liquid condensate film on the inner surface of the wall, was used by Harley and Faghri [28] to arrive at transient variations of the temperatures and velocities.

Lin and Groll [29] performed a two-dimensional analysis of the stability of annular flow in a rotating heat pipe with a cylindrical wall. The mismatch between the asymptotic solutions obtained for the Froude number and the

experimental data in certain ranges was explained in terms of the axial wave observed at the interface between the two phases. A modified expression was proposed for the critical Froude number for the collapse of the annular liquid layer in inviscid flow, based on visual observation of the axial wave crest:

$$\text{Fr} = \frac{3}{(1 - D_r)^2}. \tag{1}$$

A theoretical analysis of the steady-state operation of a rotating miniature heat pipe with a grooved inner wall was reported by Lin and Faghri [30]. The momentum equation for the liquid was modified to incorporate a centrifugal force term. The conservation equations were solved using finite elements and an expression for the liquid friction coefficient in the groove was obtained. It was observed that the heat pipe performance improved with an increase in the rotational speed and the operating temperature.

Lin and Faghri [31] conducted experiments on a rotating stepped-wall heat pipe to study the region of hysteretic annular flow, which is the rotational-speed range between the onset and collapse of annular flow. Condensation heat transfer coefficients were obtained as a function of heat rate and rotational speed and compared with values predicted theoretically. It was concluded that the hysteretic annular flow was a stable flow pattern and resulted from secondary flow in the liquid pool. The condensation coefficients in the hysteretic annular flow region were found to be lower relative to those in the other regions. Variation of the condensation coefficient with respect to the heat rate was found to be significantly more pronounced at the higher rotational speeds, as seen in Fig. 8.

An axially rotating miniature heat pipe with a polygonal inner wall featuring axial triangular grooves was analyzed by Lin and Faghri [32]. Effects of the disjoining pressure, surface tension, and centrifugal force on the flow were discussed. The influence of superheat on the apparent contact angle and the evaporative heat transfer coefficient in the micro region was explored. The centrifugal force was found not to significantly affect the liquid film flow and evaporator heat transfer into the micro region.

Ponnappan and He [33] experimented with high-speed rotating heat pipes with methanol and water as working fluids, to study the performance at various rotational speeds. The axial temperature profiles were obtained for air and oil cooling of the condenser at various coolant flow rates. The performance of the heat pipe was found to be inferior to design values, and this was attributed to the poor efficiency of condenser cooling. Theoretical and experimental heat transfer capacities of the water and methanol heat pipes were compared. It was found that the agreement between theoretical predictions of [34] and the experimental results was poor, the deviation
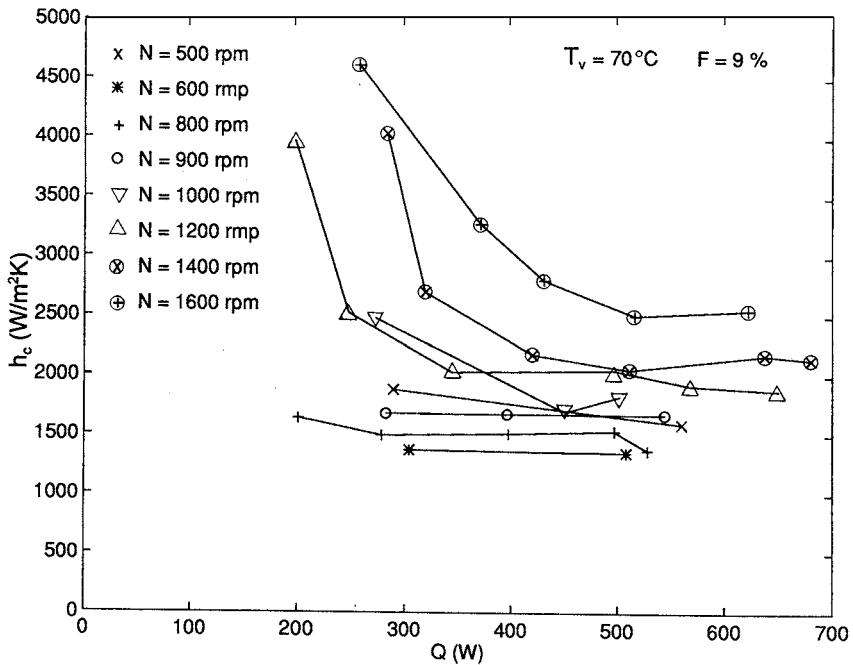
FIG. 8. Condensation heat transfer coefficient as a function of heat transfer rate and rotational speed, in a rotating stepped wall heat pipe with hysteretic annular flow [31].

being greater in the case of the water heat pipe. The deviation was explained as being due to the experimental limitation caused by the oil cooling at the condenser that does not match with the design heat transport, and also due to the limitations from the Nusselt-type condensation theory used in the theoretical predictions, which may not be applicable for the high-speed flow regime of the experiments.

4. Disk-Shaped Heat Pipes

Disk-shaped heat pipes for application in boron neutron capture therapy have been investigated in a series of papers. Steady incompressible vapor and liquid flow in a disk-shaped heat pipe with divergent vapor channels and a vertical as well as lateral wick structure were analyzed by Vafai *et al.* [35]. Continuity and momentum equations were used to model the vapor flow with the assumption of a parabolic profile for the radial velocity, while the mass conservation equation and Darcy's law were utilized to solve for flow in the wick region. The maximum heat transport capacity based on the

capillary limitation was obtained. The effects of varying the thickness of the vapor channel and the wick on the performance of a disk-shaped and a rectangular flat heat pipe were compared. The disk-shaped heat pipe showed more uniform temperature distributions in the vapor. The results showed that the disk-shaped heat pipe, while utilizing a smaller surface area, increased the heat transfer capability by up to 15% when compared to the rectangular heat pipe. The analytical model developed for the vapor and liquid flow in the disk-shaped heat pipe was used to study the influence of several design parameters by Zhu and Vafai [36]. The criteria for capillary and boiling limitations were established for the disk-shaped heat pipe, and the maximum heat transfer capacity was predicted based on the capillary limitation. The influence of the number of internal channels and the thickness and shape of the top, bottom, and vertical wicks on the performance was investigated. Variations in the maximum heat transfer rate as a function of the divergence angle of the vapor flow channel and the physical parameters of the wick were presented.

Disk-shaped heavy water heat pipes were investigated using a boundary layer approximation by Zhu and Vafai [37]. The vapor flow was considered to be steady and incompressible, and it was assumed that vapor injection and suction in the vertical wick were negligible. For the analytical solution, the radial velocity profile was approximated by a third-order polynomial; the analysis was performed for different values of disk radius, divergent flow channel angle, and injection Reynolds number to obtain the vapor velocity and pressure variations. It was found that the pressure variations in the angular and transverse directions for a disk-shaped heat pipe were small. Back flow was observed at the top entrance of the condensation zone for injection Reynolds numbers (based on vapor injection velocity and vapor channel height) of 50 and more.

An analytical model for the startup transients in disk-shaped heat pipes with asymmetrical heating was proposed by Zhu and Vafai [18]. Integral solutions were obtained in the wall and wick with an approximation for the temperature distribution in the form of a second-order polynomial function. The differential equations for mass and momentum conservation were numerically integrated in the vapor region, assuming a liquid–vapor interface temperature at each time step. The vapor phase was assumed to be saturated and did not require the solution of an energy equation. Transient temperature, velocity, and pressure distributions were obtained. Variations of the power throughput with respect to time were also plotted. Transient variations of the power throughput and temperature for the disk-shaped heat pipe obtained in this work are shown in Figs. 9 and 10.
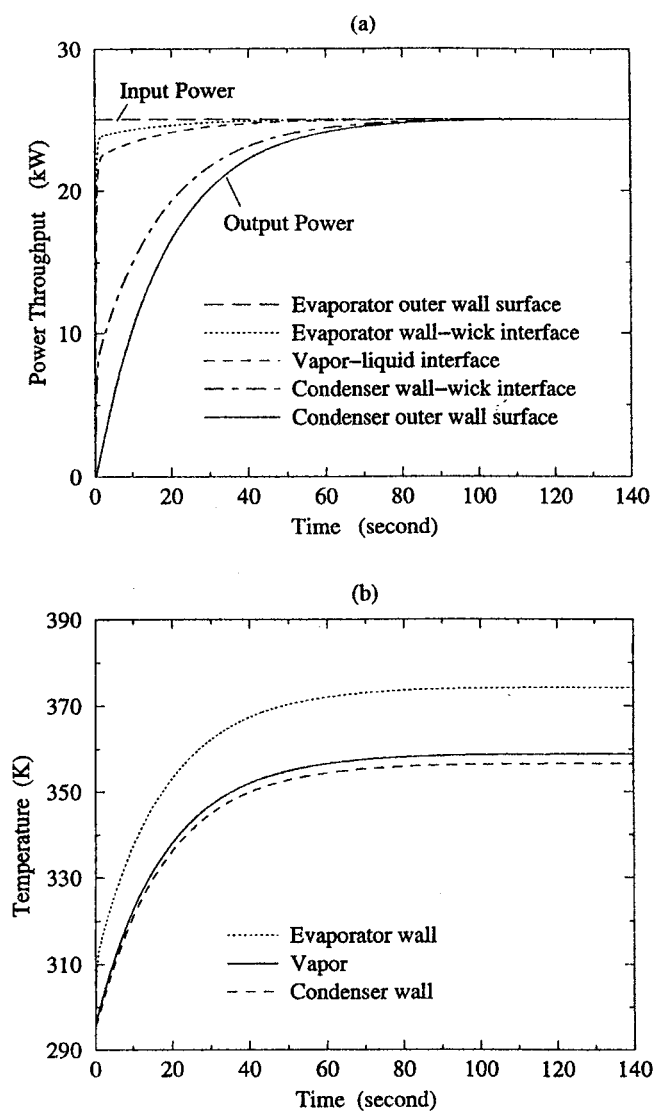
FIG. 9. Transient variations of the power throughput and the vapor and wall temperatures in a disk-shaped heat pipe [18].
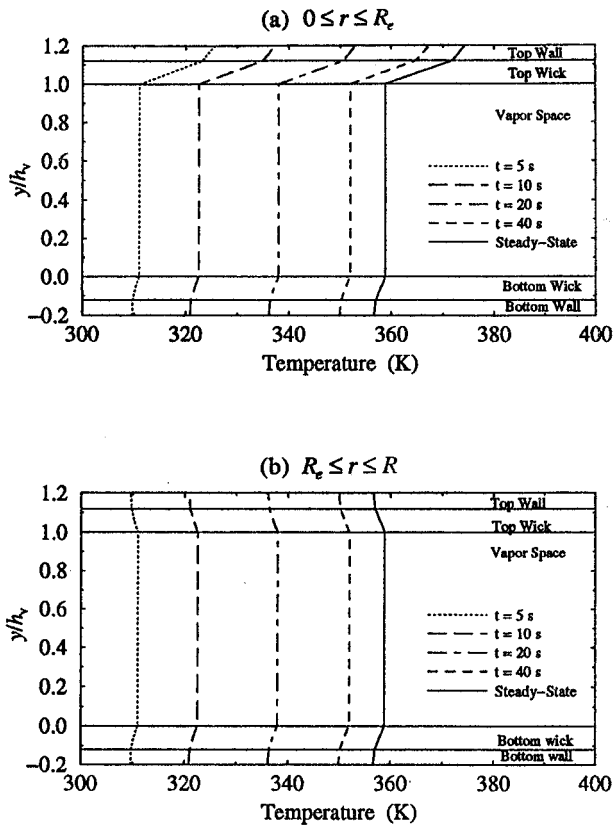
FIG. 10. Transient variation of the predicted vertical temperature distribution in a disk-shaped heat pipe during startup [18].

5. *Reciprocating Heat Pipes*

A reciprocating heat pipe utilizes the impinging effects of the working fluid brought about by reciprocal motion to enhance performance. The application of a reciprocating heat pipe in cooling the piston of heavy-duty diesel engines and its thermal analysis were discussed by Cao and Wang [38]. Experimental observations were made with a transparent heat pipe without heat input in order to demonstrate the liquid impingement against the top wall as well as the liquid motion inside the reciprocating heat pipe. Thermal tests were conducted on copper–water reciprocating heat pipes. It was concluded that a much lower piston temperature could be obtained with the piston cooled by a reciprocating heat pipe than under normal
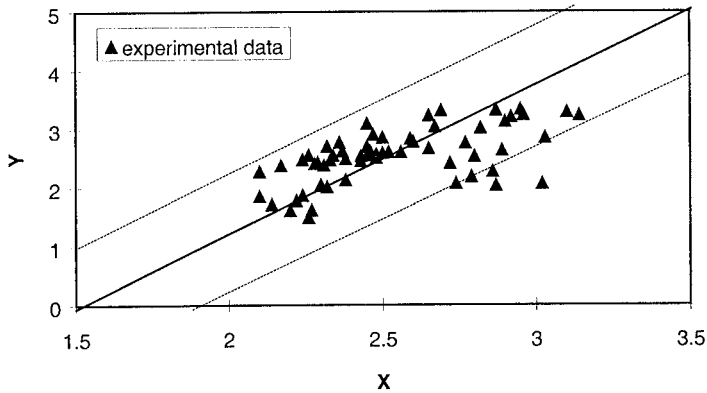
FIG. 11. Comparison of a semiempirical correlation and experimental results for a reciprocating heat pipe [39].

$$Y = \ln\left(\frac{\Delta T - \Delta T_w}{T_m}\right), \quad X = \ln\left[0.0052\, Pr^{0.87}\left(\frac{V_l}{V_{hp}}\right)^{-0.14}\left(1 - \frac{V_l}{V_{hp}}\right)^{-0.39} Re_v^{0.028} I_m^{0.5}\right]$$

operating conditions for the same amount of heat dissipation; the use of a reciprocating heat pipe yielded a heat dissipation rate that was eight times higher at the same temperature level.

A theoretical and experimental investigation of reciprocating heat pipes was reported by Ling *et al.* [39], who presented semiempirical correlations for their dimensionless temperature distribution and effective thermal conductance. It was found that the liquid impingement had a significant effect on the temperature drop along the length of the heat pipe. A liquid impingement number was defined, which takes a larger value when the temperature drop along the heat pipe is larger. Effects of the fluid charge ratio (ratio of liquid charge volume to heat pipe volume) on the heat pipe performance (temperature and effective conductance) were determined experimentally. The influence of the frequency of the reciprocating motion on the temperature drop and effective thermal conductance, as well as their dependence on heat pipe diameter and heat input value, were also obtained. A comparison of the semiempirical correlation and the experimental data from this work is shown in Fig. 11. It was found that the experimental data were collected to within 30% by the correlation.

6. *Gas-Loaded Heat Pipes*

Inclusion of a noncondensible gas in the vapor core of a heat pipe provides a means to control its performance, through control of the amount

of gas included. Gas-loaded heat pipes are variable-conductance devices that offer a nearly constant heat flux and isothermal operation as heat load increases, because of the compression of the noncondensible gas in the condenser and the resulting increase in the surface area for heat transfer. Analysis of gas-loaded heat pipes involves a solution of the appropriate vapor–gas diffusion model in addition to the governing equations for flow and heat transfer.

Double-diffusive convection in a variable-conductance, gas-loaded heat pipe due to the combined effects of temperature and concentration gradients was analyzed by Peterson and Tien [40]. A dimensionless species equation based on molar properties, but independent of average molar velocity, was derived and, along with dimensionless conservation equations, was used to analyze a two-dimensional planar heat pipe. The boundary conditions for the conservation equations were obtained by a solution of the species equation. The results of the analysis included velocity and concentration fields and the variation with Rayleigh number of the gas flux at the gas–vapor interface. The effect of Rayleigh number on the total heat transfer was obtained for different values of inclination angle and nondimensional molecular weight of the gas. The redistribution of the gas within the condenser did not have a significant effect on the overall condensation heat transfer. Results from the numerical simulation were presented along with experimental measurements on a cylindrical helium–water system. The isoconcentration profiles obtained from the numerical simulation of a planar heat pipe were compared with experimental results for a cylindrical case as shown in Fig. 12.

A transient two-dimensional analysis of a gas-loaded heat pipe was presented by Harley and Faghri [41]. A simplified conduction model was used in the wick region, and the vapor core was analyzed using conservation equations for a mixture of sodium vapor and argon. A self-diffusion model was used to account for the interspecies heat transfer occurring by means of vapor–gas mass diffusion. The liquid–vapor interface was assumed to be impermeable to the noncondensible gas. The Clausius–Clapeyron equation was used to determine the interface temperature as a function of pressure. The interfacial velocity was determined from the imposed heat transfer rate at the evaporator. Transient wall temperatures as well as the temperature, pressure, and axial velocity profile at the centerline of the vapor core were obtained. The addition of the noncondensible gas was seen to increase the transient startup period. It was concluded that the steady-state operation of gas-loaded heat pipes depends heavily on the mass of the noncondensible gas introduced; a reduction in the wall and vapor temperatures in the condenser resulted as the mass of the gas was increased.
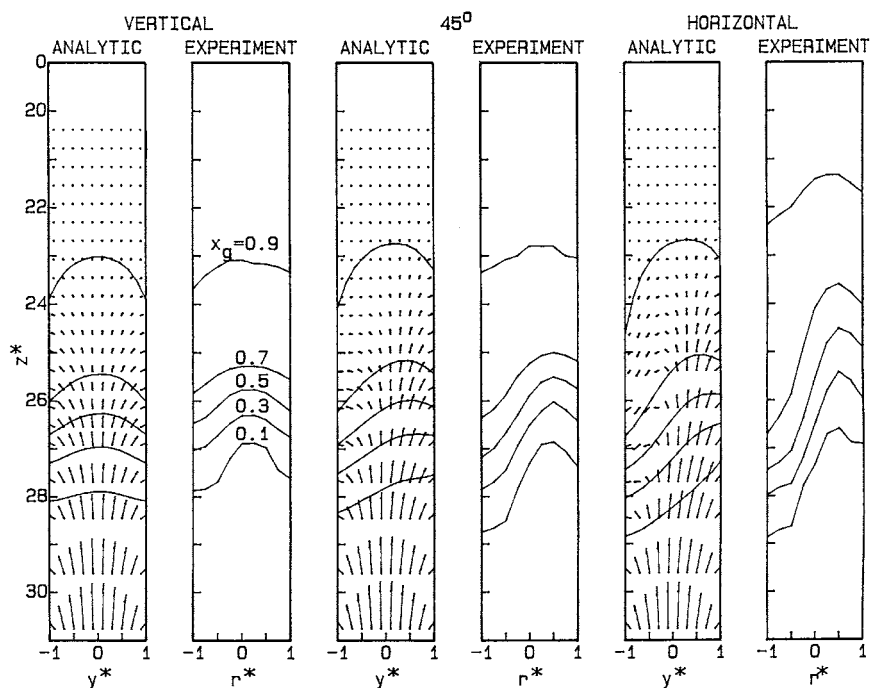
FIG. 12. Mixed double-diffusive convection in a cylindrical gas loaded heat pipe [40]: comparison of the isoconcentration profiles from computations and experiments for a helium–water system, at various inclination angles.

Ponnappan and Chang [42] experimentally studied the startup perform-ance of a liquid metal heat pipe in a gas-loaded mode of operation, using argon gas. The startup behavior in the gas-filled mode was found to be smooth (no temperature spikes at the evaporator) compared to the near-vacuum operation of the heat pipe. Chung and Edwards [43] presented a theoretical analysis of the moving gas-vapor fronts in a gas-loaded heat pipe. Axial temperature profiles were derived and incorporated into the model for transient operation. Experiments were performed on a stainless steel–ammonia system with an actively controlled gas reservoir, and the startup transient temperature history was compared with analytical predic-tions. The theoretical results were found to agree fairly well with the experimental data, except at the point where the gas front entered the condenser from the adiabatic section; at this location, the model showed a more abrupt variation. The motion of the gas front during the transient

period was found to have a significant effect on the axial temperature profile, and it was suggested that the influence of this varying profile on axial conduction should be included in heat pipe transient models.

7. Other Designs

Besides the designs discussed in the foregoing, various nonconventional designs of heat pipes suitable for specific applications have also been considered in the literature. Special shapes and methods of operation are employed in these heat pipes.

Heat pipes designed for transferring heat from the leading edge of hypersonic-vehicle wings, which are subjected to intense aerodynamic heating, were analyzed by Cao and Faghri [44]. These heat pipes transfer the intense aerodynamic heating at the leading edge of the wings to a condenser where the heat is rejected by radiation or convection. The numerical simulation included a consideration of capillary and sonic limits in the wick structure. The vapor flow was modeled as being transient, compressible, and quasi-one-dimensional with radial injection and suction velocities included; the mass flux of vapor was evaluated using an interfacial energy balance. Friction coefficients for the evaporator and condenser were expressed as functions of the cross-sectional geometry. The wick was considered as isotropic and homogeneous, and its temperature distribution was considered to be independent of the liquid flow. Extensions to this work on the analysis of the wing leading edge as well as nose-cap heat pipes with a generalized finite-difference computational model were reported by Cao and Faghri [45]. The analysis considered a design in which, in addition to the radiation heat transfer from the outer wall to space, the inner wall of the vapor chamber also transferred heat to a hydrogen-cooled heat exchanger by radiation. Expressions for capillary and boiling limits were derived. Transient variations of the surface temperature of the outer shell and the axial vapor flow Mach numbers were obtained. Steady-state pressure distributions were also presented.

Helically grooved copper heat pipes with ethanol as the working fluid were tested under centrifugal motion by Thomas *et al.* [46] in order to study the effects on the capillary limit of body forces induced by transverse acceleration. Information on the dry-out, circumferential temperature uniformity, heat loss to the environment, thermal resistance, and capillary limit was obtained. As shown in Fig. 13, the measured thermal resistance was found to generally decrease with an increase in heat transport; at the commencement of dry-out ($Q_t \approx 50$ W), however, the resistance was seen to increase. There was also a fivefold increase in the capillary limit when the radial acceleration was increased from 0 to $6g$, which was attributed to the faster return of the working fluid to the evaporator section. A qualitative
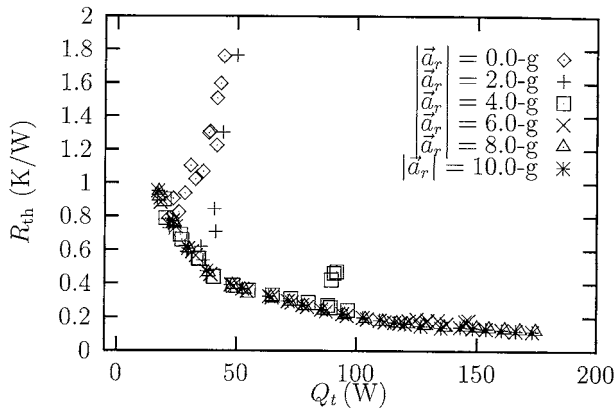
FIG. 13. Variation of thermal resistance with heat transport, for different values of radial acceleration, for a helically grooved copper–ethanol heat pipe [46].

study on a copper–ethanol heat pipe with straight axial grooves with radial accelerations of zero and $10g$ and a heat input of 10 W revealed that there was no significant improvement in the performance with an increase in radial acceleration. A mathematical model was developed to predict the capillary limit of the helically grooved heat pipe subjected to a transverse body force. The effects of temperature-dependent coolant properties and the geometry of the heat pipe and grooves were considered in the model. The capillary limit predicted by the model was found to overpredict experimental data by up to 50%, even though the trends were qualitatively similar.

Experiments were performed by Bryan and Seyed-Yagoobi [47] on the enhancement using electrohydrodynamic (EHD) pumping of the heat transport capacity of a monogroove heat pipe (with the vapor and liquid channels interconnected to form a single groove). The EHD pump was located in the liquid channel in the adiabatic section of the heat pipe. Refrigerant R-123 was used as the working medium. Enhancements of the order of 100% were achieved in the heat transport capacity using the EHD pump. Transient variations of the vapor and liquid temperatures in the evaporator were obtained as shown in Fig. 14, depicting the effects of EHD pumping.

III. Thermodynamics and Fundamental Aspects

A thermodynamic approach to analyzing transport in heat pipes has been employed in several studies in the literature. Richter and Gottschlich [48] represented the operation of the heat pipe as a thermodynamic cycle, in
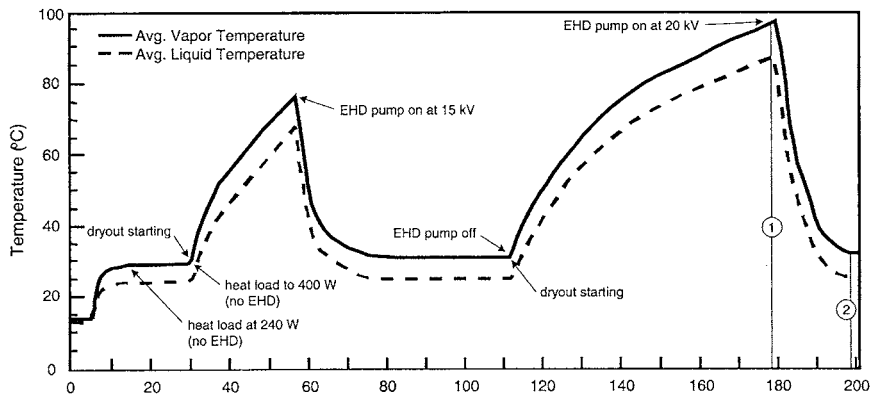
FIG. 14. Typical variation of the average evaporator vapor and liquid temperatures with time for a monogroove heat pipe with electrohydrodynamic pumping [47]; the effect of pumping in bringing down the temperature at dry-out is illustrated.

which thermal energy is converted into kinetic energy. The basic cycle is shown as a temperature–entropy diagram (Fig. 15). For given physical parameters, the temperature difference and the operating temperature were identified as the key operating variables. Zuo and Faghri [49] presented a network thermodynamic analysis where the transient heat pipe behavior was described by first-order, linear ordinary differential equations. The heat pipe was cast as a thermal network of various components and analyzed in terms of a properties group and a dimensions group. A dimensionless number was proposed to evaluate the thermal compatibility of the dimensions with the materials used,

$$\Psi = \frac{\Phi}{\Theta} \geqslant 1, \tag{2}$$

in which

$$\Phi = \frac{\delta}{D} \frac{R_v^4}{L_c(L_e + 2L_a + L_c)} \quad \text{and} \quad \Theta = 2k_{\text{eff}} \frac{T_{\text{HP}}\mu_v}{\rho_v^2 h_{\text{fg}}^2}.$$

A thermodynamic model of the vapor–liquid interface in micro heat pipes, including axial temperature and pressure differences, changes in the local interfacial curvature, disjoining pressure, and Marangoni effects, was developed by Swanson and Peterson [50]. The vapor–liquid interface was subdivided in this model into three regions—the intrinsic meniscus, the transition region, and the thin film region—and treated separately.
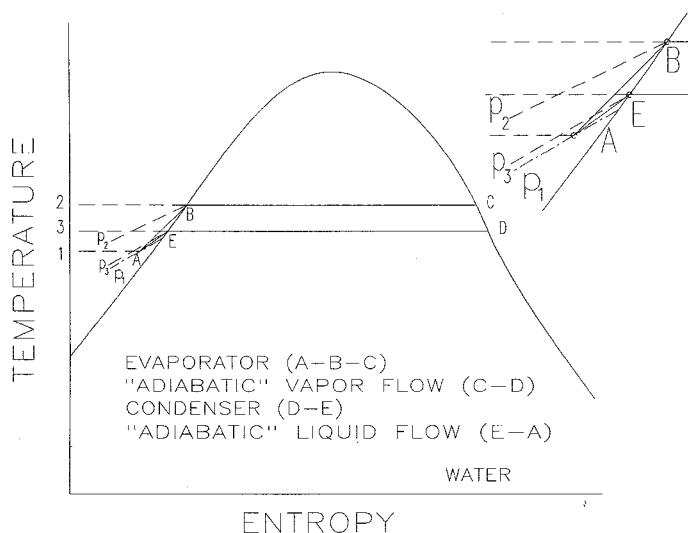
FIG. 15. Basic thermodynamic cycle of heat pipe operation on a temperature–entropy diagram [48].

Fundamental aspects of the fluid flow and heat transfer through liquid films in heat pipes, such as capillary flow, fluid friction, and an analysis of the meniscus, have been explored in several papers. Khrustalev and Faghri [51] proposed a mathematical model for heat transfer through thin liquid films in the evaporator section of heat pipes with capillary grooves. The heat conduction in the metallic fin between the grooves and the liquid film was modeled using an energy balance. The free surface temperature of the liquid film was determined using the extended Kelvin equation relating the vapor pressure over the thin evaporating film to the saturation pressure, while the interfacial resistance was obtained from kinetic theory. The film surface curvature was expressed in terms of solid surface curvature and film thickness. The heat flow in the liquid film was modeled in distinct regions: equilibrium film, micro film, transition, and meniscus regions. In addition to distributions of the field variables, axial variations of the local heat flux and the heat transfer coefficient were obtained with respect to the roughness size and the input heat flux at the evaporator.

An augmented Laplace–Young equation was presented by Schonberg et al. [52] to describe the steady meniscus formed during high flux evaporation from a micro channel. Using a kinetic-theory model for interfacial heat flux, dimensionless temperature distributions were obtained.

Pratt *et al.* [53] investigated thermocapillary effects in heated menisci formed by volatile liquids in capillary-pumped heat transfer devices and established a criterion for instability of the evaporating meniscus. An analysis based on conservation equations and stress balances was followed in this work by a stability analysis to obtain a critical wave number above which the system becomes unstable. The critical interfacial temperature difference, over a length scale defined as $x_c = (rh_{tr})^{1/2}$, where $h_{tr} = [\bar{A}r/(2\sigma)]^{1/3}$, was expressed as

$$\Delta T_c = \frac{2}{r}\left(\frac{2\bar{A}^{1/2}\sigma}{r}\right)^{2/3}. \tag{3}$$

Two different configurations of capillary-pumped phase change loops were experimentally investigated to examine the stability of a heated, evaporating meniscus within a porous medium and to understand the effect of instabilities. Good agreement was obtained between the theoretical predictions of the critical interfacial temperature gradient and the experimental data at the onset of instability.

Heat transfer characteristics of evaporating thin liquid films in V-shaped micro grooves with nonuniform imposed heat flux were analyzed by Ha and Peterson [54]. Combined liquid conduction and interfacial vaporization were used to describe the local interfacial mass flux, based on which a local heat transfer coefficient was defined. An expression was developed for the evaporating film profile. Ha and Peterson [55] further investigated the axial flow of an evaporating thin film through a V-shaped micro channel, taking into account a gravity term to incorporate the effect of small tilt angles. Solutions to the resulting nonlinear governing equations were obtained using a perturbation method.

Experiments were conducted by Ma *et al.* [56] to determine the influence of the air flow on the friction factor in countercurrent flow of water and air through triangular channels. The dependence of the product of liquid friction factor and Reynolds number on the air velocity was obtained for different channel angles and was found to increase with the air flow Reynolds number. The influence was found to be more predominant in grooves with larger channel angles as shown in Fig. 16. A mathematical model for the friction factor for flow in triangular grooves was developed by Peterson and Ma [57]. The model considered interfacial shear stresses due to liquid–vapor frictional interactions in countercurrent flow, and thus is particularly applicable in cases where the liquid surface is strongly influenced by the vapor flow direction and velocity. An analytical approach and approximate algebraic model for the radius of curvature of the meniscus in capillary flow along a micro groove channel was presented by Peterson
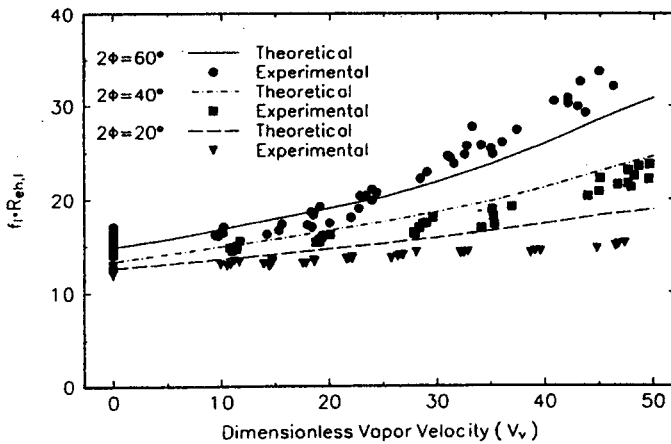
FIG. 16. Experimental and predicted friction factors in a countercurrent air–water heat pipe for various channel angles [56].

and Ha [58]. A nondimensional expression for the dry-out location was developed as a function of a parameter that consisted of the Bond number, capillary number, and dimensionless groove geometry.

Peng *et al.* [59] studied the rewetting characteristics of capillary-induced liquid flow in circular channels with micro grooves on the inside surface. Results from experiments were applied in a transient theoretical model to determine the location of the rewetting front in the evaporator as a function of the applied heat flux. Ochterbeck *et al.* [60] developed a model to analyze the depriming/rewetting characteristics of external-artery heat pipe designs (featuring a separate arterial channel for liquid flow) subjected to externally induced accelerations. The model considered the effects of longitudinal accelerations, the repriming time after termination of acceleration, and the rewetting characteristics of the circumferential grooves. The analytical results were compared with results of space flight experiments and found to agree well with the microgravity test results.

The entrainment phenomenon in two-phase parallel flows was studied by Kim and Peterson [61], using wave instability theories. Theoretical criteria for entrainment were compared with experimental observations on air–water and steam–water systems, and a modified theoretical criterion was developed. The onset of entrainment was detected visually with a high-speed video camera. Various instability criteria were compared and their dependence on temperature was discussed. Variations in critical vapor velocity were presented with respect to the liquid film thickness, vapor temperature, and viscosity number N_{vi}. Kihm *et al.* [62] experimentally investigated the

parameters governing liquid entrainment caused by a high-speed air stream passing over a saturated screen mesh interface. They developed correlations for critical velocity for dry-out and for droplet mean diameter. The critical Weber number for various models of entrainment was compared by Kim and Peterson [61, 63]. Capillary and boiling limits that affect entrainment were theoretically investigated and compared with experimental data from a copper heat pipe. The characteristics of the wave-induced, intermediate, and shear-induced modes of entrainment, as well as the thermal detection of entrainment, were discussed. Experimental results on the variation of the critical Weber number at the onset of entrainment with vapor temperature, and the dependence of the critical Weber number on the viscosity number for various mesh sizes were compared with theoretical predictions. A dimensionless correlation for the critical Weber number was developed based on the experimental data [63]:

$$\mathrm{We}_{vc} = 10^{-1.163} N_{vi}^{-0.744} \left(\frac{\lambda_c}{d_1}\right)^{-0.509} \left(\frac{D_h}{d_2}\right)^{0.276}. \tag{4}$$

Imura *et al.* [64] proposed a geometric model for the effective pore radius of screen wicks based on observation of the screen geometry through a microscope. Effective pore radii were calculated using this model and compared to those calculated from experimental data on the capillary height. The effects of surface treatment on the radius of curvature of the meniscus at the liquid–vapor interface were also studied. The experiments in this work were performed with water, ethanol, and R-113. McCreery [65] investigated the liquid flow and vapor formation phenomena in a flat heat pipe with a two-dimensional heat pipe apparatus. Experimental observations made with 2-propanol as the working fluid were used to explain the nature of the liquid–vapor interface, the vapor formation mechanism, and the oscillatory mode of operation.

IV. Heat Pipe Startup from the Frozen State

The transient problem of heat pipe startup from the frozen state has been addressed in the literature. Jang *et al.* [66] studied a cylindrical heat pipe, considering conduction in the wall and wick (neglecting liquid-flow effects) and employing a one-dimensional model for vapor flow. An equivalent heat capacity method was used to model phase change in the working fluid during the startup period. The effect of the boundary condition imposed on the outer wall on the startup from a frozen state was studied in terms of time-dependent temperature distributions at the wall and the liquid–vapor

interface, and axial variations of the vapor temperature, pressure, density, and Mach number.

The freeze–thaw characteristics of a copper–water heat pipe were studied experimentally by Ochterbeck and Peterson [67]. The freezing and restart characteristics corresponding to different initial working fluid distributions were discussed. The effect of variations in the amount of noncondensible gas present in the working fluid was also studied experimentally. The freezing blow-by phenomenon during startup was considered in a subsequent experimental investigation [68]. This phenomenon occurs when frozen working fluid that blocks vapor and liquid flow is melted, producing a pressure difference between the evaporator and condenser regions. Upon break-through of the blockage, liquid may be driven from the evaporator into the condenser, resulting in a sudden depletion of liquid in the wick in the evaporator and subsequent dry-out. The depressurization caused after break-through of the blockage was found to lead to an increase in the heat transport rate beyond the existing evaporator power input, leading to dry-out in the evaporator. A theoretical analysis was also presented to calculate the evaporating mass flow rate during the blow-by phenomenon.

A free-molecular, transition, and continuum vapor flow model based on the dusty gas model was developed by Tournier and El-Genk [69], as an extension of their transient two-dimensional model previously discussed [9], to analyze the startup of a liquid metal heat pipe from the frozen state. The startup was simulated by incorporating a two-dimensional freeze and thaw model which employed a volume-averaged homogeneous enthalpy method to predict the melt progression during startup. The computed wall temperature during the transient period was found to be in good agreement with measurements on a radiatively cooled sodium heat pipe [70]. The freeze and thaw model was verified by comparing with analytical solutions for one-dimensional conduction and two-dimensional freezing in a corner, with good agreement.

Faghri [71] analyzed the time-dependent wall and vapor temperature variations of a low-temperature copper–water heat pipe during startup from a frozen state and freeze-out from the normal operating conditions. Wall-temperature predictions from a two-dimensional numerical model were used to identify the failure of startup; experimental results for startup failure were in excellent agreement with the predictions. A method of starting up a frozen heat pipe using a pulsed heat input was also discussed. Cao and Faghri [72] proposed a "flat-front model" for the startup process of a high temperature heat pipe, which treated the transient propagation of the axial wall temperature distribution as a moving hot zone with a steep front. Approximate closed-form solutions for the transient temperature distribution in the hot zone as well as its length were found to agree well with experimental data

for stainless steel–sodium systems [70, 73, 74]. A heat pipe limitation related to startup was identified; the criterion proposed for startup from frozen conditions without dry-out occurring in the evaporator, was

$$\frac{\varphi \rho_1 A_w h_{fg}}{C(T_m - T_a)} \geqslant 1. \tag{5}$$

A more detailed simulation of the early startup transient in a liquid metal (sodium) heat pipe from the frozen state by Cao and Faghri [75] considered five distinct periods within the startup process. A rarefied gas flow self-diffusion model was proposed for the early startup period, when rarefied flow is dominant. Separate solutions to the wall, wick, and vapor regions were formulated and coupled via interface mass fluxes. Predictions were compared with experimental measurements of the outer wall temperature [70, 73] with generally good agreement. The analysis revealed the existence of large vapor density gradients along the heat pipe at startup. The criterion for the establishment of continuum flow, which delineated the early startup period from the subsequent periods, was based on the Knudsen number (continuum for Kn < 0.01). In further work, Cao and Faghri [76] coupled a continuum vapor flow model for a transient, compressible, laminar vapor flow analysis with the rarefied vapor self-diffusion model in a "two region model" to describe the coexistence of continuum and rarefied vapor flow for most of the startup period. The outside wall temperature from the numerical computation compared well with experimental data from various sources. It was concluded that the high-temperature heat pipe startup process was characterized by a moving hot zone with relatively steep fronts; in this moving hot zone, the temperature front in the vapor was steeper than in the wall, as shown for a typical case in Fig. 17.

Jang [77] studied the startup of liquid metal heat pipes. The transition temperatures during the change from a free-molecular flow to a continuum flow for these heat pipes were determined for different vapor space diameters. A potassium heat pipe was tested in a vacuum chamber and the surface temperature was compared with theoretically calculated values of the transition temperatures, which showed that the heat pipe was inactive until it reached the transition temperature, thus validating the prediction.

Ponnappan and Chang [42] experimentally studied the startup performance of a liquid metal heat pipe in near-vacuum and gas-loaded conditions. A sodium heat pipe with an arterial wick was tested; argon gas was used for loading in the gas-filled mode, as discussed in Section II.B. In the vacuum mode, large temperature spikes were observed at the evaporator during the frozen startup. In comparison, startup was found to be smoother in the gas-filled mode.
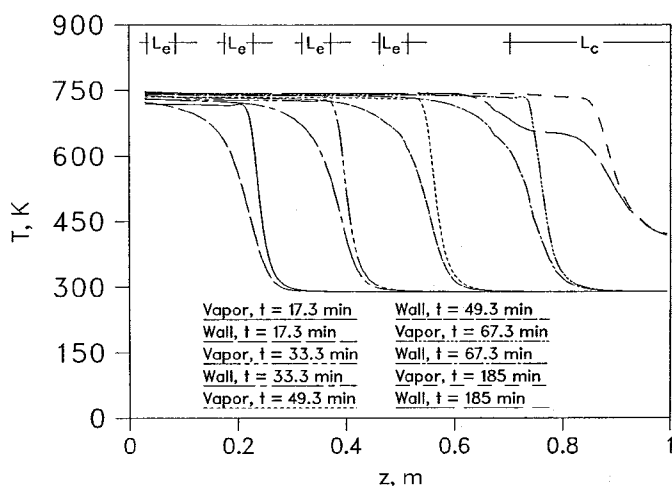
FIG. 17. Propagation of the moving hot zone during high-temperature heat pipe startup process, indicated by the vapor and wall temperatures [76]; the temperature front is steeper in the vapor than in the wall.

Analysis of heat pipe startup from the frozen state is important because of the existence of large thermal gradients and associated thermal stresses during the startup period, and the possibility of dry-out following the breakdown of the blockage, described as the blow-by phenomenon. As seen from the discussion in this section, the transient problem of heat pipe startup from the frozen state has been analyzed, mostly in the case of conventional cylindrical designs. Analysis of frozen startup in a variety of nonconventional heat pipes, however, has yet to be undertaken.

V. Discrete Heat Sources at the Evaporator

In place of a uniformly distributed heat input at the evaporator, multiple discrete heat sources may be present. Such a situation has been analyzed as a conjugate heat transfer problem in a single domain, with a generalized energy conservation equation applicable in all regions of the heat pipe [78]. Laminar, subsonic, steady flow in low-temperature cylindrical heat pipes with multiple heat sources was considered. In the core, the ideal gas law was used to account for vapor compressibility. The wick was treated as an isotropic porous medium saturated with liquid, with the velocities being volume-averaged. The single-domain approach used in this work incorpor-

ated a source term in the momentum equation for the wick to account for porosity, as well as modified density and pressure variables for different regions of the heat pipe. Latent heat was added as a source term in the energy equation at the interface. The results included temperature distributions in the heat pipe wall and vapor, with different evaporator sections operating at different input levels. It was concluded that the heat transport capacity of the heat pipe could be increased by an optimized redistribution of the heat load. Numerical results were compared with results from experiments on a copper–water system with multiple heat sources, with excellent agreement.

Faghri *et al.* [70, 73] conducted transient experiments on a sodium–stainless steel heat pipe with multiple heat sources and sinks. Behavior during startup from a frozen state was investigated under various heat loads and input locations, with different heat rejection rates at the condenser. Numerical simulations for the transient heat pipe performance were compared with experimental results. Through experiments conducted in a vacuum environment, the effect of surface emissivity on the steady-state axial distribution of vapor temperature was studied. The effect of startup pressure on the temperature distribution was also explored. An interesting observation from this work was that the annular gap between the wick and the heat pipe wall and between adjacent layers of the wick generally enhanced the maximum heat transport capacity of the heat pipe.

Schmalhofer and Faghri [79, 80] experimentally and theoretically investigated a low-temperature copper–water heat pipe under uniform circumferential heating, as well as block heating over either the upper or the lower half of the evaporator surface (with the heat pipe held horizontal). Transient wall and vapor temperatures were measured under various step heat input rates. Under similar conditions, the uniform and block-heating modes were found to exhibit almost equal times to undergo a given temperature rise. Numerical and experimental results of the variation of the capillary limit with vapor temperature were also obtained. Temperature profiles and velocity maps were predicted (as shown in Figs. 18 and 19, respectively) and were found to agree well with experimental results. The experimental values for the capillary limit were found to agree with the theoretical predictions to within $\pm 25\%$.

VI. Heat Pipe Applications

Studies of heat pipes in the literature have been directed at a number of diverse applications, some of which have been discussed in the foregoing. For instance, the application considered by Vafai and Wang [17] was the
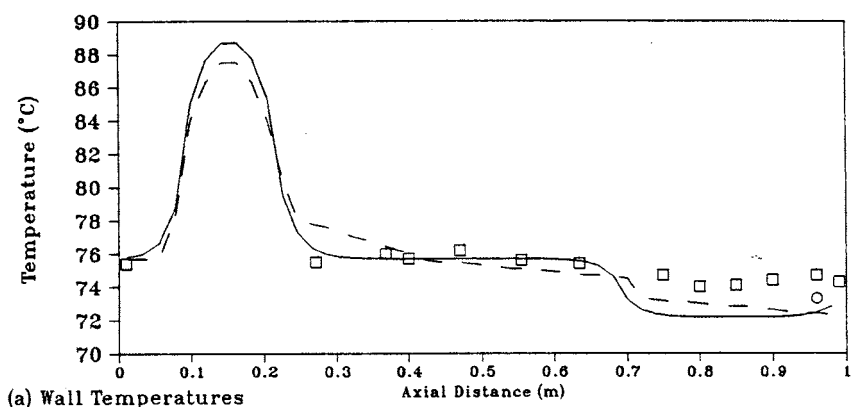
(a) Wall Temperatures
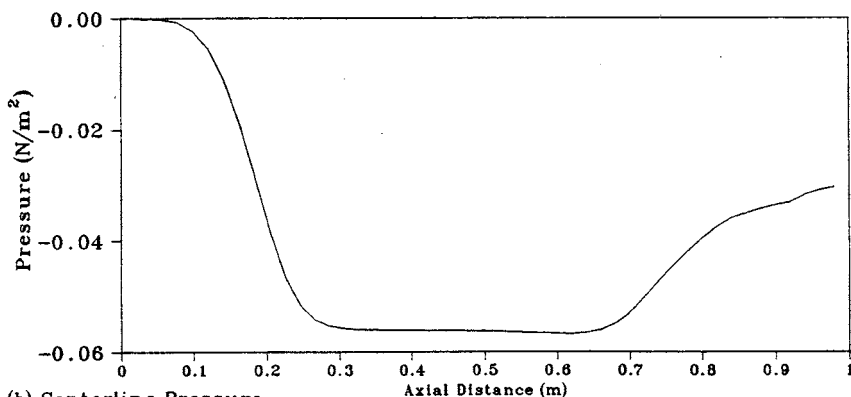
(b) Centerline Pressure

Numerical Model, Top of Pipe

□ Experimental Data, Top of Pipe

Numerical Model, Bottom of Pipe

○ Experimental Data, Bottom of Pipe

Fig. 18. Axial distribution of the wall temperature (experiment and prediction) and centerline pressure in a block-heated heat pipe [80].

cooling of a lithium target used in neutron production and in moderating the production of neutrons, for the treatment of brain tumors. Additional examples of application-oriented investigations are covered in this section.

The technical feasibility of applying heat pipes in the extraction of heat from the ground in volcanic zones was explored by Tanaka et al. [81]. A network analysis was used to obtain the temperature distribution in the heat

(a)

(a) NZ 5/50

(b) NZ 6/50

(c) NZ 8/50

(d) NZ 10/50
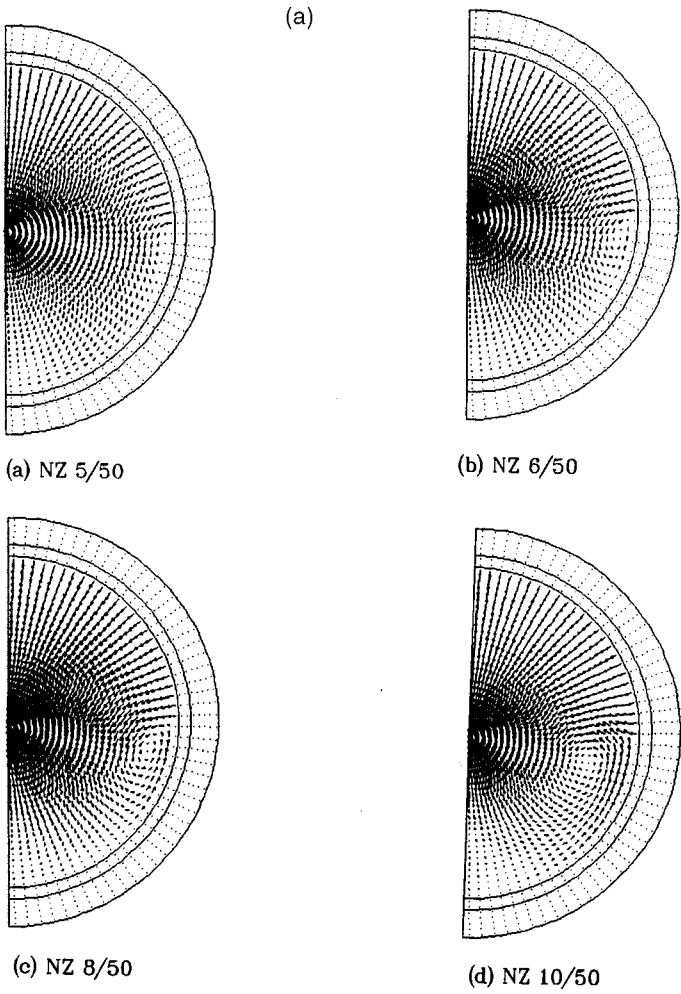
FIG. 19a. Predicted velocity variation in the radial and circumferential directions in a block-heated heat pipe [80]: (A) evaporator section.

pipe and the surrounding earth; the results were also compared to experimental data. McGuinness [82] analyzed heat pipes for geothermal applications and obtained steady-state solutions; maximum possible lengths of heat pipes were calculated for geothermal applications.

Modifications to heat pipes for application in spacecraft thermal control systems were investigated by Schlitt [83]. The use of composite wick designs

(b)

(a) NZ 11/50

(b) NZ 15/50

(c) NZ 20/50

(d) NZ 25/50
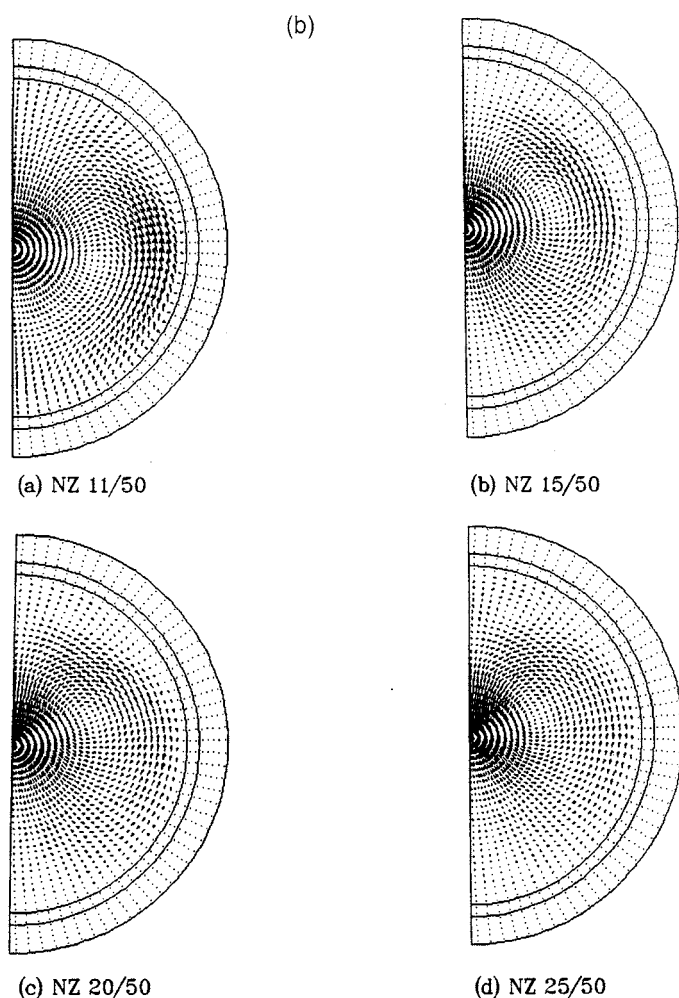
FIG. 19b. Predicted velocity variation in the radial and circumferential directions in a block-heated heat pipe [80]: (B) adiabatic section.

with large liquid cross sections and designs with circumferential grooves in the evaporator to handle high heat loads was investigated. Configurations with liquid fillets and axially tapered liquid channels were proposed for improving the performance of composite wicks. The design, development, and testing of a pumped heat pipe cold plate for high heat flux space applications was reported by Ambrose *et al.* [84]. This heat pipe was designed to integrate detachable spacecraft payloads to a pumped thermal
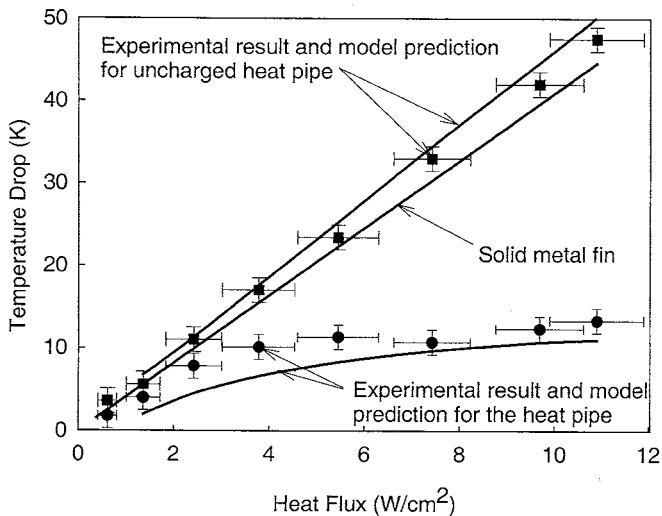
FIG. 20. Comparison of the performance of an uncharged and charged planar heat pipe used as a cooling fin, from experiment and analysis [86].

control loop, using ammonia as the working fluid. Experimental studies were conducted on stainless steel–potassium heat pipes under space flight and ground test conditions by Dickinson *et al.* [85], to characterize the startup behavior, compare in-flight and ground performance under startup, operation, and shut-down conditions, and assess the design in terms of the measured energy throughput and evaporator temperatures as well as calculated thermal resistances.

Wei *et al.* [86] performed experimental and analytical studies on a planar heat pipe used as a cooling fin in the dissipation of high heat fluxes. The configuration used consisted of a main fin (a vertically oriented plate) with heat pipes used as subfins protruding horizontally from the main fin. A simple two-dimensional model was used assuming a uniform saturated temperature and pressure for the vapor and liquid; the axial wall temperature gradient was neglected. Correlations were used to represent the convective heat transfer coefficients outside as well as the evaporation and condensation inside the heat pipe. The experimental and calculated temperature variations were compared for charged and uncharged heat pipes, as shown in Fig. 20. Zhao and Avedisian [87] compared the heat dissipation due to an array of copper plate fins mounted on a cylindrical copper heat pipe, with an identical array mounted on a solid copper rod. The heat pipe used a sintered copper wick and water as the working fluid. The main

parameter investigated was the module height. It was found that under forced convection, fins supported by the heat pipe dissipated heat transfer rates that were higher by as much as three times compared to fin arrays supported by the copper rod, under identical conditions. This improvement in heat transfer rate decreased as the height of the fin stack decreased.

VII. Micro Heat Pipes

An important class of nonconventional heat pipes is the micro heat pipe. A micro heat pipe essentially consists of micro channels of polygonal cross section. While vapor flows through the interior of the micro channels, liquid flows back by capillary action along the corners of the channels. Micro heat pipes do not require a wick for liquid flow. They are especially promising in cooling microelectronic devices because of their small size and high thermal conductance.

The literature on miniature and micro heat pipes was reviewed by Cao *et al.* [88]. The capillary limit for micro heat pipes was analyzed, and the existence of a "vapor continuum limitation" for micro heat pipes was discussed, in addition to the other limits for conventional heat pipes.

Theoretical modeling of micro heat pipes in the literature has been based on a solution of the conservation equations for fluid flow in the micro channels. Problems associated with the modeling have included the incorporation of frictional effects and the variation in meniscus radius along the flow direction. Experimental studies, on the other hand, have been mostly confined to external temperature measurements and determination of heat transport limits.

One of the more widely cited studies on modeling and testing of micro heat pipes was performed by Babin *et al.* [89]. This paper discussed the fundamental concepts of micro heat pipes and presented combined experimental and analytical investigations to understand the phenomena that govern the performance limitations and operating characteristics of the micro heat pipe. A micro heat pipe made of copper or silver with a single channel of trapezoidal cross section was studied with water as the working fluid. An expression for the capillary limit was derived and the limits of operation computed. The variation of pressure and the dependence of heat transfer limits on the operating temperature and tilt angle were presented. Experiments were conducted in the charged and uncharged states, under vacuum as well as under cooling at the condenser. Variations of thermal conductance (as shown in Fig. 21), input power, and temperature distribution with changes in the evaporator temperature were measured under steady-state operation. A transient numerical model was developed by Wu
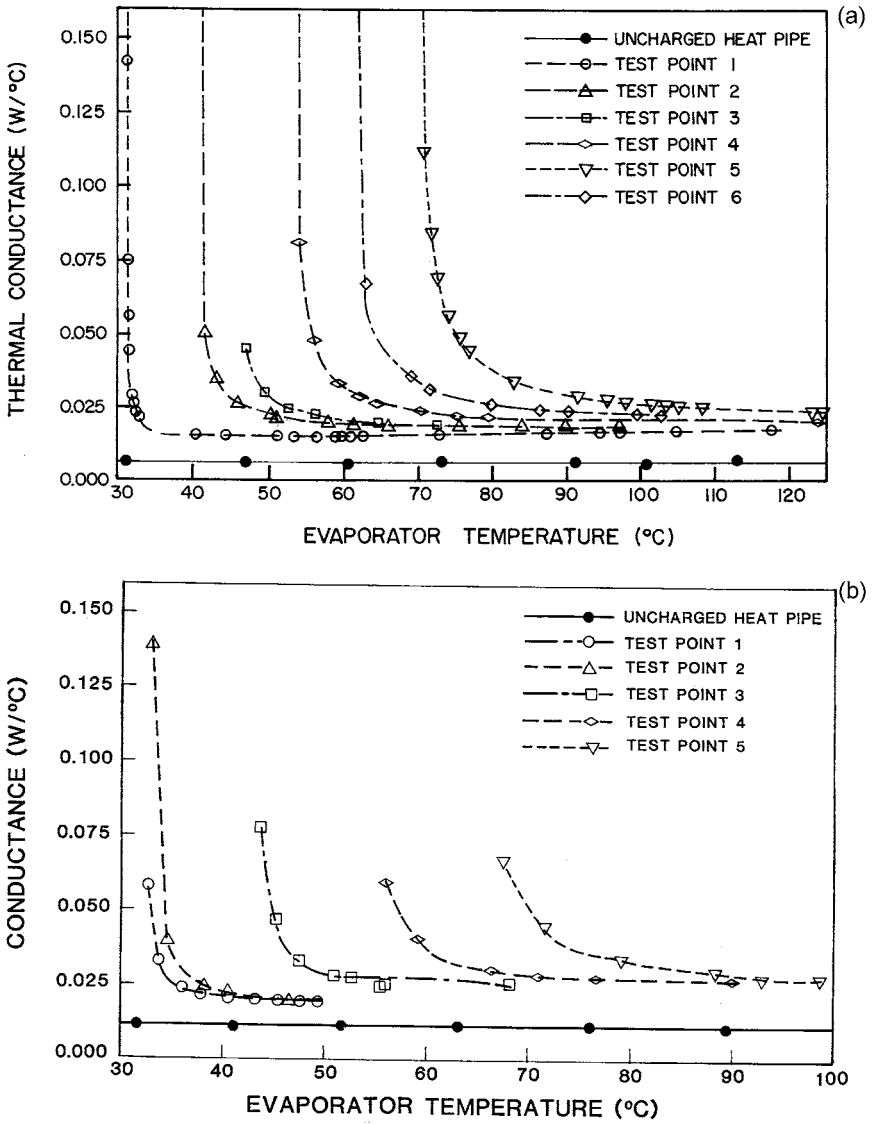
FIG. 21. Measured thermal conductance of a trapezoidal (a) copper–water and (b) silver–water micro heat pipe as a function of evaporator temperature [89].

and Peterson [90] to analyze this heat pipe. Expressions for free molecular flow mass flux of evaporation and condensation [91] were employed, along with the Laplace–Young equation for the variation of meniscus radius. An important observation from this work was a reversal of liquid flow during the early transient period, explained as being due to a pressure imbalance. It was also concluded that the wetting angle was one of the most important factors contributing to the transport capacity of micro heat pipes. The numerical model was found to predict accurately the steady-state experimental results of [89]. Transient measurements of the wall temperature and the maximum transport capacity in tapered micro heat pipes were reported by Wu *et al.* [92], who tested charged and uncharged silver heat pipes at a constant condenser temperature. The numerical model was found to predict the steady-state results well, but underestimated the transient response.

Micro heat pipes fabricated as an integral part of silicon wafers have also been studied, since the problems with thermal contact resistance between the heat pipe and device can be circumvented by this means, leading to very effective heat removal. Peterson *et al.* [93] compared temperature variations in a silicon wafer with and without micro heat pipe grooves. At a power level of 4 W/cm^2, the wafer with the integral heat pipe showed a reduction in maximum chip temperature of as much as 11°C, as well as an increase in effective thermal conductivity by up to 25%, compared to the ungrooved wafer. Some of the details of fabrication and charging were discussed. Peterson [94] further discussed various aspects of the fabrication, operation, modeling, and testing of integral micro heat pipes in silicon. More extensive work on similar micro heat pipes with triangular and rectangular grooves was reported in Peterson *et al.* [95]. Figure 22 shows a comparison of the maximum temperature and effective thermal conductivity of wafers with and without micro heat pipe arrays obtained in this work and illustrates the improvement in performance due to the micro heat pipe array. A discussion of the use of micro heat pipes as an integral part of semiconductor devices was also presented by Mallik *et al.* [96].

Parametric studies on a micro heat pipe array fabricated in silicon using vapor deposition were performed by Mallik and Peterson [97], with the number of heat pipes in the array and the heat input as parameters. The maximum heat transport capability of the micro heat pipe was found to vary inversely with its length and as the cube of its hydraulic diameter. This work was extended to include transient performance by Peterson and Mallik [98]. An analytical model was developed by Duncan and Peterson [99] for a triangular, etched micro heat pipe, with predictive capabilities for the capillary limit of operation, the curvature of the meniscus in the evaporator, and the optimal value of the liquid charge.
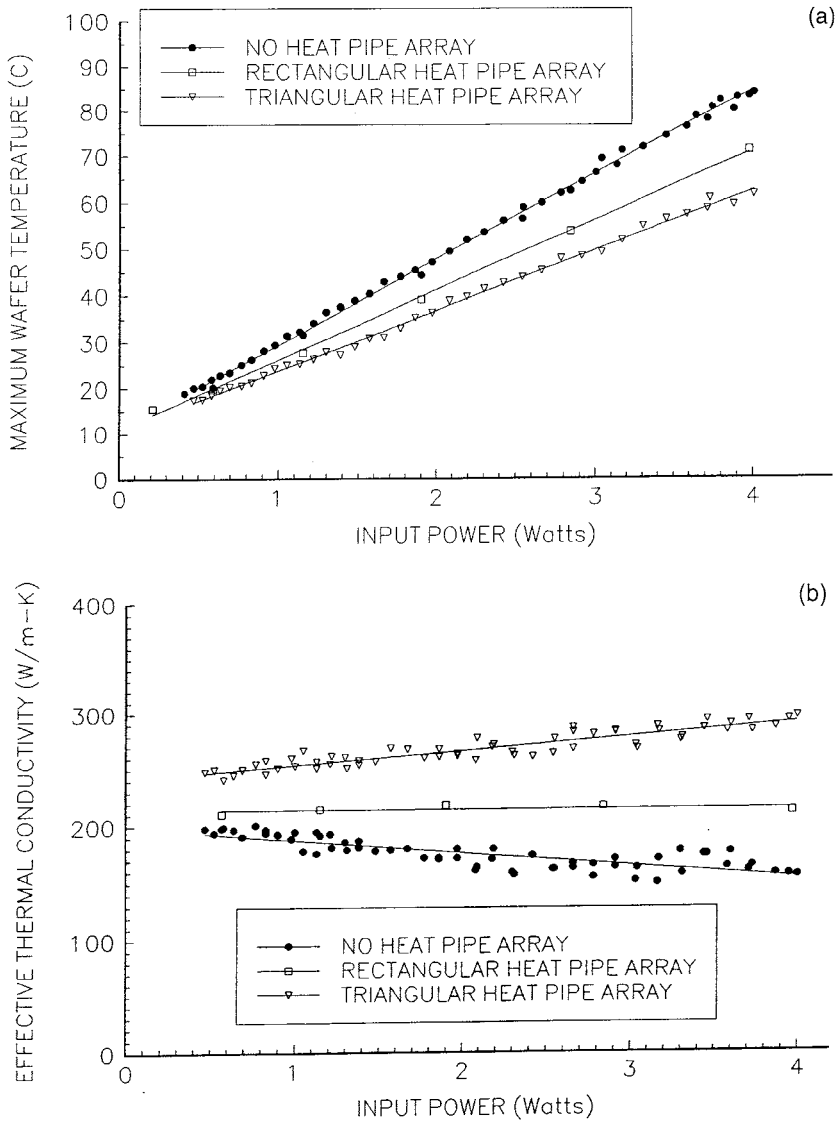
FIG. 22. (a) Maximum chip temperature and (b) effective thermal conductivity for silicon wafers with and without integral micro heat pipes [95], as a function of input power.

The maximum heat transfer capabilities of flat copper-water micro heat pipes were explored by Hopkins *et al.* [100]. The maximum heat load for various operating temperatures was determined experimentally, in trapezoidal and rectangular micro grooves in vertical and horizontal orientations, as was the dry out condition. The experimental results showed that the effective thermal resistance decreased with an increase in heat transport, as shown in Fig. 23. A one-dimensional model describing the fluid flow in a miniature grooved heat pipe was used to predict the capillary limitation on heat transport. The analysis employed two different regions based on the liquid–vapor meniscus behavior: one at the beginning of the evaporator where the contact angle was constant, and a second in the adiabatic and condenser sections where the contact angle varied along the axis.

A detailed mathematical model for the analysis of a micro heat pipe, which described the liquid distribution and thermal characteristics in relation to the liquid charge and heat load, was developed by Khrustalev and Faghri [101]. The variation in curvature of the free liquid surface as well as the interfacial shear stress due to liquid–vapor frictional interaction were represented in the model. Correlations from the literature were utilized for friction, while heat transfer in the condenser and evaporator were incorporated through mean heat transfer coefficients estimated analytically. The importance of the liquid fill, contact angle, and interfacial shear stress in predicting the maximum heat transfer capacity and the thermal resistance was demonstrated. The liquid cross-sectional area and the meniscus curvature and contact angle were obtained. The predicted results were compared to existing experimental data [90] for copper–water and silver–water systems. Good agreement was obtained between the experimental results and numerical predictions for the onset of dry-out. A new flat micro heat pipe configuration with an increased liquid cross-sectional area was proposed for electronics cooling applications.

Longtin *et al.* [102] presented a steady-state, one-dimensional model of the evaporator and adiabatic sections of a micro heat pipe with triangular channels, incorporating local variations in the channel cross-sectional area through geometric coefficients. The formulation assumed a nearly isothermal device with the vapor temperature being almost constant; the energy equation was solved in the liquid phase. The Laplace–Young equation was used at the meniscus. The conservation equation for mass included an influx term for evaporation, and the interfacial velocity was incorporated through an energy balance at the interface. A comparison of the predicted results from this model with heat transfer rate data from copper–water and silver–water systems [89] is shown in Fig. 24.

A transient theoretical analysis of one-dimensional vapor and liquid flow in a micro heat pipe of triangular cross section was performed by Sobhan
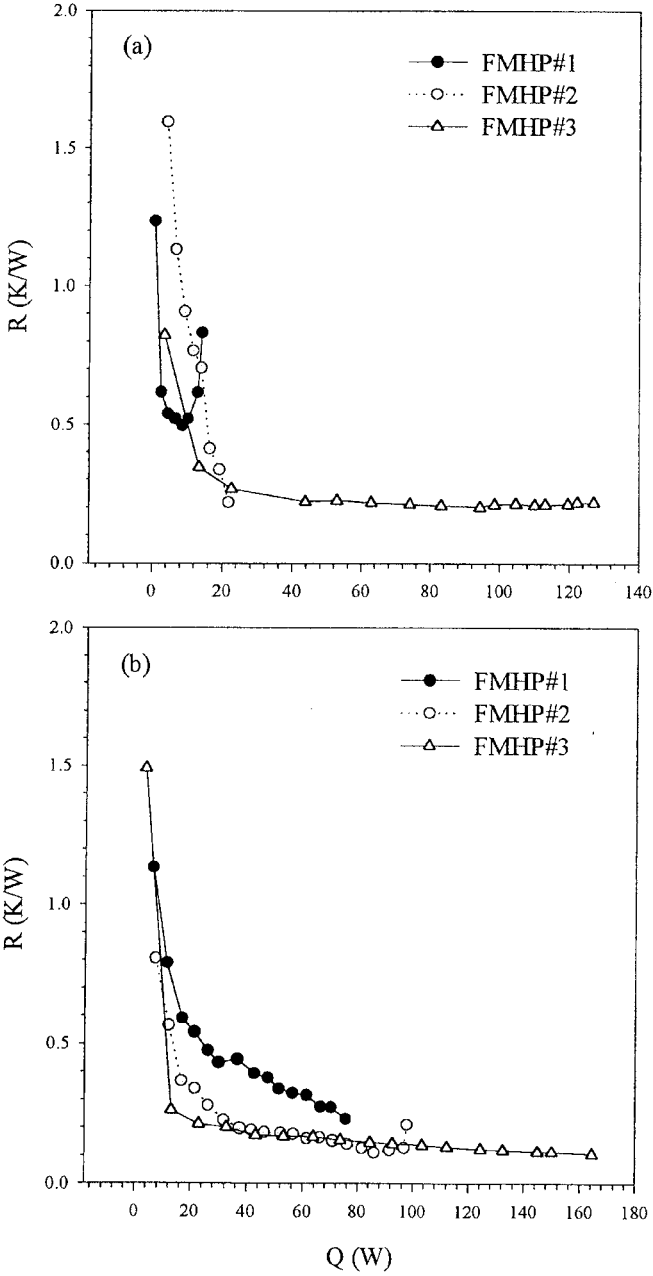
FIG. 23. Effective thermal resistance of a flat miniature heat pipe with micro capillary grooves [100] at an operating temperature of 90°C in the (a) horizontal and (b) vertical orientations.

(a)

(b)
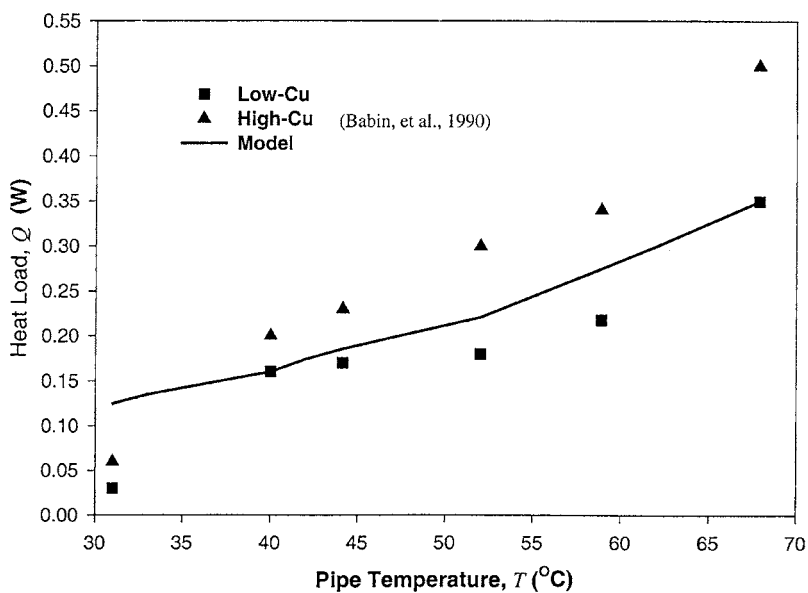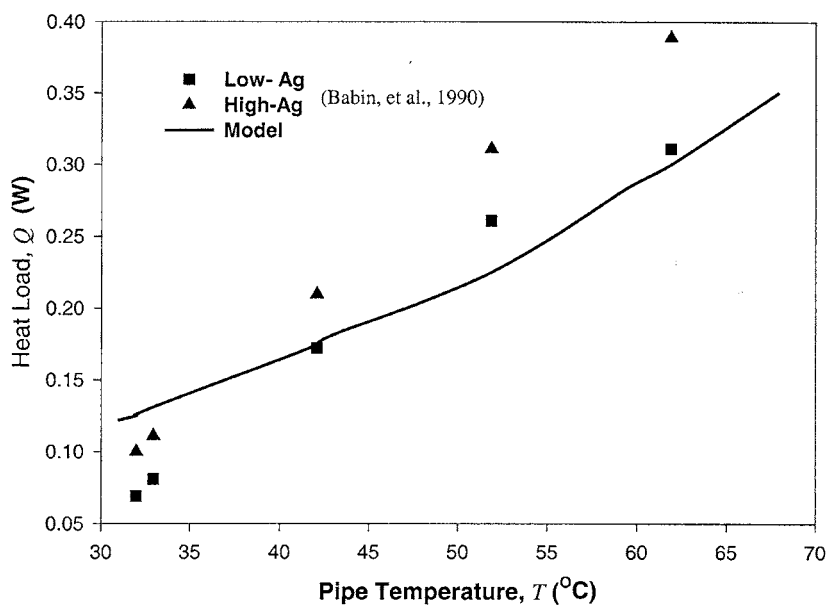
FIG. 24. Comparison of the calculated [102] and measured [89] heat transport capacity for a (a) silver–water, (b) copper–water micro heat pipe.

et al. [103]. A micro heat pipe with evaporator and condenser sections was analyzed. The formulation solved the energy equation in the vapor as well as the liquid. The resulting vapor temperature distributions provided a means for calculating the overall effective thermal conductivity of the heat pipe. Variations of the instantaneous effective thermal conductivity and the steady-state effective thermal conductivity with respect to heat input were obtained as shown in Fig. 25.

Peterson and Ma [104] proposed a model for predicting the minimum meniscus radius and the maximum heat transport in triangular grooves. A hydraulic diameter incorporating the effect of frictional liquid–vapor interactions was defined and used in the modeling. The results indicated that the heat transport capacity of the micro heat pipe depended strongly on the apex channel angle of the liquid arteries, contact angle of liquid flow, length of the heat pipe, vapor flow velocity, and tilt angle. Analytical expressions for the minimum meniscus radius and maximum capillary heat transport limit in micro heat pipes were presented by Ma and Peterson [105]. Comparisons with experimental data from triangular grooves and micro heat pipes were made for the maximum capillary heat transport predicted, which indicated that the analytical expressions can be used to predict the maximum capillary heat transport with a high degree of accuracy.

Ma and Peterson [106] conducted experiments to measure the capillary heat transport limit and a "unit effective area heat transport," defined for small triangular grooves as $Q_{eff} = Q/A_{eff}$, where $A_{eff} = D_{eff}L_e$. Methanol was the working fluid in grooved copper. It was found that there was an optimum geometry for which the unit effective area heat transport was a maximum, and that this maximum depended on the tilt angle and the effective length of the heat pipe.

A semiempirical correlation was developed by Ha and Peterson [107] for predicting the maximum heat transfer capacity in micro heat pipes. This was achieved by modifying the analytical model for the maximum heat capacity developed by Cotter [108] to obtain better agreement between the experimental and predicted results. The modified model incorporated the effects of the temporal intrusion of the evaporator section into the adiabatic section of the heat pipe occurring near dry-out.

Visualization experiments were conducted by Chen *et al.* [109] with glass micro heat pipes fabricated by attaching a wire insert to the inner wall of a glass capillary tube. The heat pipe was also modeled as a porous medium experiencing two-phase flow. A comparison of the predicted and experimental values for maximum heat flow in the horizontal and vertical orientations revealed that the effect of gravity was significant. A number of other studies on micro heat pipes (for example, [110, 111]) have considered the effect of system parameters such as tilt angle, condenser side heat removal, and quantity of charge on the maximum heat transport limits.
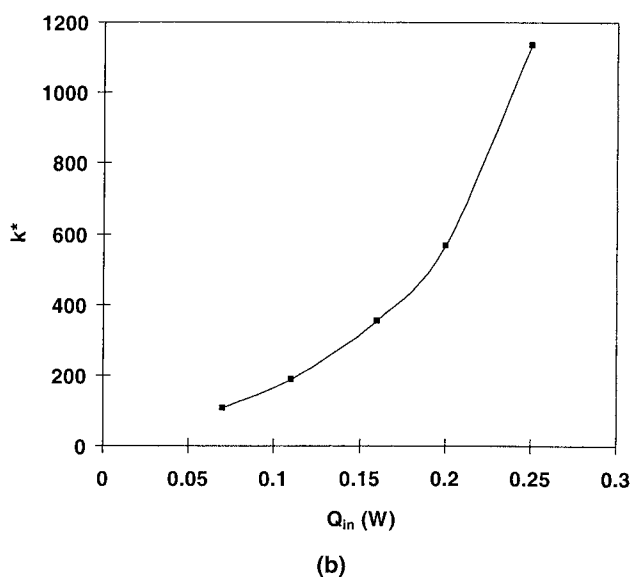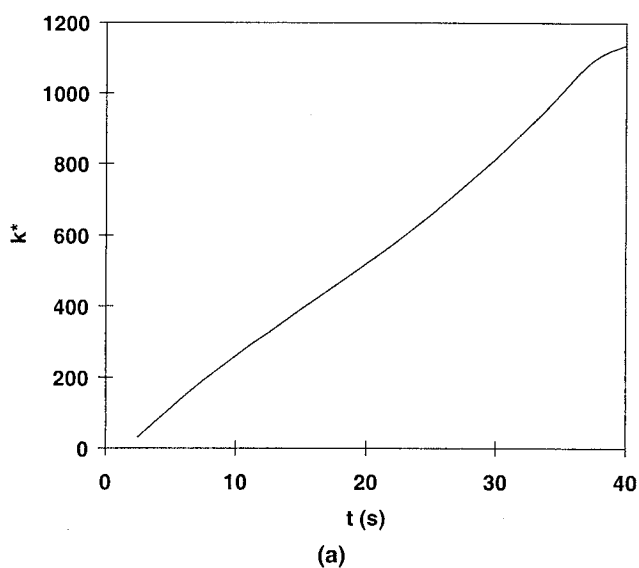
FIG. 25. (a) Transient variation of the instantaneous effective thermal conductivity ratio and (b) dependence of the steady-state effective thermal conductivity ratio on the heat input at a constant heat transfer coefficient at the condenser, for a micro heat pipe of triangular cross section [103].

VIII. Thermosyphons

Two-phase thermosyphons, or "wickless heat pipes," utilize the counter-current flow of the liquid and vapor phases for heat transfer. The essential difference between a heat pipe and a thermosyphon is that the latter does not use a wick structure for the return of the condensed fluid to the heated region, but instead achieves this by gravity or by mechanical means. A closed two-phase thermosyphon consists of a liquid pool contained in the heated section or evaporator, an adiabatic section, and a cooled or condenser section. Conventional and miniature forms of thermosyphons have been developed for use as heat exchangers in applications ranging from energy conversion systems to electronics cooling. Studies of thermosyphons, both theoretical and experimental, have explored the operational limits, as well as the effects of important parameters such as the nature and filling ratio of the working fluid, tilt angle, and geometric dimensions on the maximum heat transport. Several nonconventional shapes and special applications have also been investigated.

Bezrodny and Podgoretskii [112] studied the flooding and heat transfer limits in two-phase thermosyphons. The effect of inclination angle, filling ratio, pressure, and working fluid on the limiting axial flux were studied. An optimum filling ratio was obtained as a function of the inclination angle.

The flooding limit in a closed two-phase thermosyphon was determined by Shatto et al. [113] by monitoring the thermal resistance for different fluids with high fill ratio. Visual observations revealed that the transition from annular to churn flow took place well below the flooding limit.

Numerical modeling of a closed two-phase thermosyphon under steady-state operation was performed by Zuo and Gunnerson [114]. The effect of the axial normal stress in the liquid film was considered in the analysis, in addition to the interfacial shear. Harley and Faghri [115] modeled the operation of a thermosyphon under transient conditions by treating the falling condensate film using a quasi-steady state Nusselt-type analysis. The effects of vapor compressibility and conjugate heat transfer at high temperatures were examined. The numerical predictions were compared with experiments and good agreement was observed at low temperatures.

El-Genk and Saber [116] proposed correlations to calculate the expanded (due to the vapor voids inside the liquid pool) liquid pool height in the evaporator of a closed thermosyphon based on numerical modeling. An interfacial shear stress analysis was used to determine the liquid film thickness in the evaporator, immediately above the expanded boiling pool. The calculated liquid pool heights were compared to experimentally determined values for acetone, ethanol, and water and were found to agree within $\pm 8\%$. The influence of the lengths of the adiabatic and condenser sections
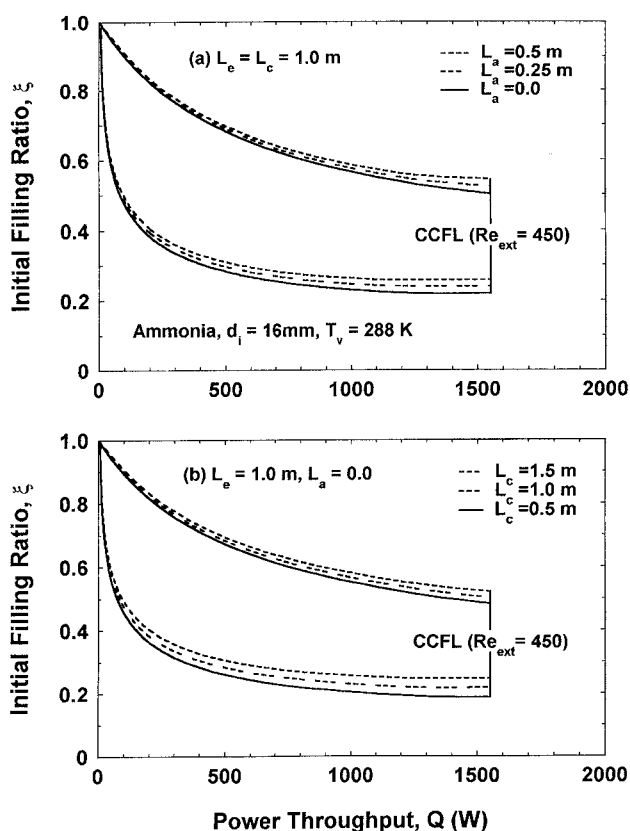
FIG. 26. Effect of the adiabatic and condenser section lengths on the operation envelope of a closed two-phase thermosyphon [116].

on the operation of the thermosyphon as obtained in this study are shown in Fig. 26.

Inclined two-phase thermosyphons have been analyzed in numerical and experimental studies. Zuo and Gunnerson [117] developed a model that could predict the occurrence of dry-out when the liquid film thickness or axial liquid film velocity became zero at any location on the evaporator wall. The mean and maximum heat transfer rates, the minimum evaporator charging ratio, the liquid–vapor interfacial shear stresses, and the effects of working fluid inventory were all studied as a function of inclination angle. Visual observations of the effect of inclination angle on the flow patterns in an inclined thermosyphon were reported by Shiraishi et al. [118]. Flow phenomena were recorded and the corresponding heat transfer rates mea-

sured. The flow patterns were classified into annular and stratified flow regimes. In the case of stratified flow, it was found that dry-out occurred due to the depletion of the working fluid from the evaporator section following the development of an interfacial liquid wave.

Peterson *et al.* [119] discussed flow instability and bifurcation in gas-loaded thermosyphons, utilizing the Clausius–Clapeyron equation at the liquid–vapor interface and Dalton's law for determining the gas concentration. Experimental results were also presented showing the variations in the gas flow pattern as the Rayleigh number was increased. Zhou and Collins [120] carried out theoretical and experimental studies on condensation in a cylindrical, two-phase thermosyphon containing a noncondensible gas.

The application of a two-phase thermosyphon in cooling high-power multichip modules in a switching system for broadband ISDN was discussed by Kishimoto and Harada [121]. The cold-plate temperatures were experimentally mapped, and the influence of tilt angle on the thermal resistance studied.

The heat flux density, vapor temperature, and overall heat transfer coefficient for a two-phase, right-angled elbow thermosyphon were obtained by Lock and Fu [122]. A horizontal orientation for the evaporator and condenser was found to lead to a holdup in the condenser coupled with dry-out, which could stop the thermosyphon operation. Experimental studies on a two-phase thermosyphon with a "cranked" configuration (where the evaporator and condenser sections are offset from each other) was also reported by Lock and Fu [123]. Experiments with distilled water as the working fluid revealed that the heat transfer rates were much higher than those obtained for single-phase thermosyphons [124] and also that the critical heat fluxes were lower than those in a linear (not offset or "cranked") system [125].

Lin *et al.* [126] considered a thermosyphon with a built-in crossover flow separator. The crossover flow separator helps to collect the condensate flow and route it to the liquid pool through a feed tube, thus avoiding flooding that could be caused when the liquid film flows down the heated wall. The analysis incorporated an empirical correlation for wall friction; water, ethanol, Freon 11, and Freon 113 were the working fluids studied. Expressions were derived for the critical heat flux resulting from a flow instability. The calculated maximum heat transfer was compared with experimental data and was found to agree within ±15%.

Islam *et al.* [127] conducted experiments on an open concentric-tube thermosyphon to understand the effects of the geometric parameters (tube diameter and heated length) on the critical heat flux. The existence of an optimum diameter for the inner tube, for which the critical heat flux was a maximum, was demonstrated for a given diameter of the heated outer tube and working fluid.

IX. Capillary Pumped Loops

The capillary pumped loop (CPL), like the heat pipe, is a two-phase heat transfer device that operates with no external pumping power. The CPL utilizes the surface tension forces developed in a wick locally positioned in the evaporator zone to circulate the working fluid. Capillary pumped loops encounter lower wick pressure losses compared to heat pipes. In the CPL, the liquid and vapor flows are confined to separate sections of the loop, unlike the countercurrent flow in heat pipes. Theoretical models and experimental studies on capillary pumped loops in the recent literature are briefly discussed in this section.

A review of the developments in capillary pumped loop technology since the late 1970s was presented by Ku [128]. A discussion of CPL designs aimed at enhancing overall system performance was presented. The design of high-temperature CPLs operating between 975 and 1075 K, with sodium as the working fluid, was described by Anderson [129]. These CPLs were capable of transferring 5300 W with a peak evaporator heat flux of 67.5 W/cm^2.

A conjugate analysis of a flat plate evaporator for CPLs with three-dimensional vapor flow was presented by Cao and Faghri [130]. The model analyzed flow and heat transfer in the porous wick, vapor flow in the grooves, and heat transfer in the cover plate, with the liquid and vapor flows being coupled through the interfacial mass flux. Water, Freon-11, and ammonia were used as the working fluids. In comparison with the three-dimensional model, it was found that relatively accurate results could be obtained using a two-dimensional model in the cases of Freon-11 and ammonia.

Experimental and analytical studies of a CPL at various power inputs and adverse tilts were presented by Dickey and Peterson [131]. The model showed good agreement with experimental results and indicated that the overall heat transport capacity of the CPL was significantly higher than that expected in conventional heat pipes. For small values of power input, the effective thermal resistance of the CPL was found to decrease drastically with increasing power input, as shown in Fig. 27.

Muraoka et al. [132] investigated a CPL with the conventional tube condenser replaced with one having a porous element inside. A mathematical model for this CPL was presented and experimentally validated. Boo and Chun [133] conducted experiments on a copper–ethanol CPL to study the thermal performance of a flat evaporator. Layers of coarse-screen wicks were utilized at the evaporator to provide irregular passages for vapor flow. The thermal resistance of the system was calculated as a function of the heat flux and condenser cooling rate. Bazzo et al. [134] presented a mathematical
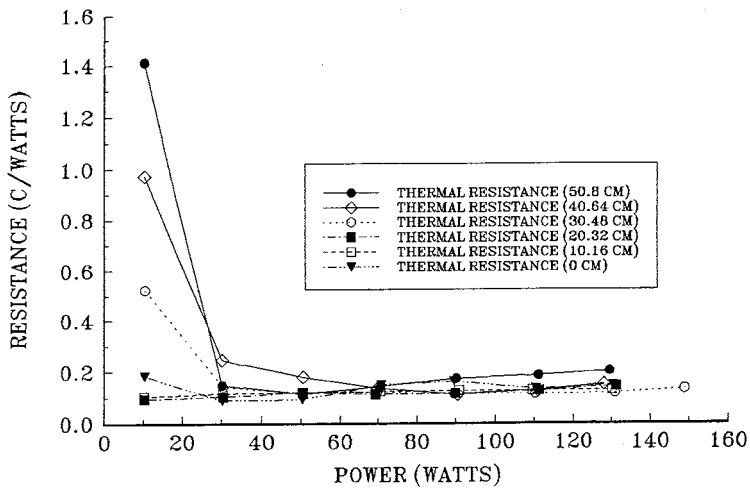
FIG. 27. Variation of the effective thermal resistance of a capillary pumped loop with heat input for different values of adverse height difference [131].

model to predict the hydrodynamic behavior and heat transport capability of a Freon-11 CPL. The startup behavior, heat transport limits, and repriming after dry-out were investigated. The model predictions were found to agree well with experiments.

Krotiuk [135] reported on the testing of a CPL thermal control system for the NASA EOS-AM spacecraft. Tests were performed at ambient conditions and under vacuum, with ammonia as the working fluid. Bugby *et al.* [136] presented experimental results for startup from a supercritical state and operation under adverse evaporator elevation for a cryogenic CPL using neon as the working fluid.

X. Inventions and Patents

A number of inventions based on new principles, designs, and applications of heat pipes have been reported. Although some of these deal with an improvement in the design of existing heat pipes and enhancement of their performance, most concentrate on the application of heat pipes to diverse fields. A search of the patents involving heat pipes awarded in the past decade was performed as part of this review, and results of the 159 U.S. patents collected are summarized in this section as evidence of the active and continued interest in heat pipe development.

The largest single category of patents, a total of 34, was related to electronics cooling. Twenty-eight inventions incorporated new designs in terms of principles, configurations, and shapes. Twenty-six patents were issued for new materials and methods in heat pipe manufacture. Applications of heat pipes to heat exchangers were the focus of 16 patents, while 11 dealt with space conditioning and refrigeration devices. Twelve others consisted of accessories and auxiliary equipment for heat pipe systems. Among the other major inventions, six dealt with the enhancement of heat pipe performance, and four offered heat pipe–based equipment for use in biomedical and human comfort applications.

In addition to the patents in the preceding categories, there were 22 additional inventions related to the use of heat pipes in equipment for specific and diverse applications, including vacuum processing chambers, vapor deposition systems, crystal growth apparatus, heat dissipating devices in spacecraft, cooling of electrical machines, thermal switches, ovens, microwave heating systems, thermal storage systems, cooling of enclosures, cryogenic heat transfer, cooling of laser heads, image-forming apparatus such as copiers and printers, inkjet apparatus, structural panels, asphalt road construction, roller with temperature sensors for photographic film development, metallurgy (reclaiming vaporized metals from smoke stacks), electromagnetic coupling apparatus, and hair styling.

XI. Closure

As seen from the discussion presented, research in heat pipes over the past decade may be grouped into several different thrust areas. One such area of focus has involved modeling of the transport processes in heat pipes to obtain the spatial and temporal distributions of the field variables. In general, the appropriate forms of the conservation equations have been solved in different regions, treating each region of the heat pipe individually, or using a single-domain approach. One of the more common simplifying assumptions has been to consider only conduction in the liquid-saturated wick, using appropriate models for thermal conductivity and diffusivity. In a number of studies, the wick has been modeled as a porous medium using Darcy's law. Only a few investigations have solved the complete set of transport equations in the wick. It is important that realistic models of heat pipe behavior include a detailed analysis of the flow and heat transport through the wick. Although some attempts at representing the transport problem in nondimensional terms have been reported, a general physics-based approach to the nondimensionalization scheme needs further attention.

Prediction of the various operating limits (capillary, boiling, entrainment) on heat transport in heat pipes has been another focus area of research. Theoretical predictions, visual observations, and temperature measurements have been used in identifying or verifying the predicted limiting conditions, both for the nonconventional designs discussed in this review and for micro heat pipes.

A third area of research has investigated specific designs of nonconventional heat pipes suited to particular applications, including special shapes (disk-shaped, annular core), geometries (helical grooves), and modes of operation (reciprocating, rotating, pumped liquid return). Novel approaches, such as application of an electric field to enhance the liquid flow, have also been explored. A majority of the results in this area have been obtained from numerical modeling.

Apart from these three broad categories of research, investigations into fundamental thermodynamic and fluid mechanics considerations in heat pipes have been reported. These include discussions of meniscus formation, liquid film behavior, and microchannel flow.

Miniaturization of heat pipes is a topic of great current interest and practical utility in the context of electronics cooling and is the focus of ongoing work in the authors' group. Although micro heat pipes have received much attention, less is known about scaling down wicked heat pipes to miniature size. The appropriate scaling methodology to arrive at smaller dimensions while still dissipating practically useful levels of heat presents an interesting area for further research. The operating limits of these miniaturized heat pipes need to be explored, as does a quantification of the dynamic pressure drop and the pressure recovery in the condenser for such heat pipes. Other approaches to miniaturization could include the reduction of the overall length of the heat pipe by employing internal surface enhancement at the evaporator and condenser sections.

Another topic that requires attention is the operation of heat pipes under partial load. A knowledge of the variation of the performance of the heat pipe operating at steady state but not under full heat load would find use in heat pipe applications. There is also a need for detailed local and transient measurements obtained through experimental studies; novel techniques could be used to carry out measurements *inside* the heat pipe such as for velocities and vapor temperatures. This would provide a database against which results from numerical programs may be benchmarked.

Acknowledgment

Nomenclature

A   Hamaker constant (J)

$\bar{A}$ Modified Hamaker constant (J) in Eq. (3), $[A/6\pi]$

A_{w} Cross-sectional area of working fluid in the wick (m²)

A_{eff} Effective cross-sectional area of the groove (m²)

A_{hp} Cross sectional area of the heat pipe (m²)

a_{r} Radial acceleration vector (m/s²)

C   Heat capacity per unit length (J/K m)

CCFL   Countercurrent flooding limit

D   Diameter (m)

D_{eff} Hydraulic diameter (m)

D_{h} Duct hydraulic diameter (m)

D_{r} Liquid loading, $[H/R_{o}]$

d_{1} Wire spacing (m) in Eq. (4)

d_{i} Inner surface diameter in Fig. 26

d_{2} Wire thickness (m) in Eq. (4)

Fr   Froude number, $[\Omega^2 R_{o}/g]$

F_{1} Liquid friction factor

f   Working frequency of heat pipe (s⁻¹)

FMHP   Flat miniature heat pipe

g   Gravitational acceleration (m/s²)

H   Average film thickness (m)

h_{fg} Latent heat of vaporization (J/kg)

h_{tr} Transition film thickness (m)

h_{c} Condensation heat transfer coefficient (W/m²K)

h_{v} Vapor phase thickness (m)

I_{m} Liquid impingement number, $[v_1 L/(r_c f A_{hp})]$

k_{eff} Effective thermal conductivity (W/mK)

k^* Effective thermal conductivity ratio, $[k_{eff}/k_{copper}]$

L   Length of the heat pipe (m)

L_{a} Length of adiabatic section (m)

L_{c} Length of condenser section (m)

L_{e} Length of evaporator section (m)

l_{e} Length of the evaporating section of the grooved plate (m)

l^+ Dimensionless length of the heat pipe

N   Rotational speed of the heat pipe (rpm)

N_{vi} Dimensionless viscosity number, $\left(\dfrac{\mu_1}{\sqrt{\rho_1 \sigma \lambda_c/2\pi}}\right)$

NZ   Axial node number

n′   Number of active sites per square centimeter for nucleate boiling

ΔP_{1} Overall liquid pressure drop along the length of the heat pipe (Pa)

ΔP_{v} Overall vapor pressure drop along the length of the heat pipe (Pa)

P_{o} Initial pressure (N/m²)

Pr   Prandtl number

P_{x} Local pressure value (N/m²)

Q   Heat transfer rate (W)

Q_{eff} Unit effective area heat transport (W/m²)

Q_{in} Input power (W)

Q_{max} Maximum axial heat flow through the heat pipe cross section (W)

R_{o} Radius of tube (m)

R_{th} Thermal resistance (K/W)

R_{v} Vapor core radius (m)

r   Radius of curvature of the intrinsic meniscus (m) in Eq. (3)

r   Radial coordinate for the disk-shaped heat pipe (m) in Fig. 10

r^* Nondimensional radius

r_{c} Radius of the engine crank (m)

Re_{ext} Film Reynolds number at evaporator exit $[4Q/(\pi d_i h_{fg} \mu_1)]$ in Fig. 26

Re_{n} Injection Reynolds number

Re_{v} Vapor Reynolds number

$Re_{h,l}$ Liquid Reynolds number based on hydraulic diameter

T   Temperature (K)

ΔT Temperature drop (K)

T_{a} Ambient temperature or initial temperature of the frozen heat pipe (K)

ΔT_{c} Critical interfacial temperature difference (K)

T_{HP} Temperature of heat pipe (K)

T_{m} Melting temperature of the working substance in Eq. (5)

T_m	Mean working temperature of the heat pipe (K) in Fig. 11	
T_v	Vapor temperature (K)	
ΔT_w	Sum of wall temperature drops on the evaporator and condenser (°C)	
t	Time (s)	
U	Longitudinal velocity (m/s)	
V^+	Fill ratio	
V_1	Liquid volume in heat pipe (m^3)	
V_{hp}	Heat pipe volume (m^3)	
We_{vc}	Critical Weber number	
X	Axial distance (mm)	
x^+	Dimensionless axial length	
x_g	Mole fraction of the noncondensible gas	
y	Transverse coordinate in the flat heat pipe	
y^*	Nondimensional transverse coordinate	
z	Axial coordinate (m)	
z^*	Nondimensional axial coordinate	

GREEK

δ	Wick thickness (m)
ε	Wick porosity
Φ	Geometric dimensions group (m^2) in Eq. (2)
ϕ	Channel half-angle (degrees)
φ	Heat pipe wick porosity in Eq. (5)
φ	Inclination angle from horizontal (deg) in Fig. 6
λ_c	Critical wavelength (m)
μ_1	Liquid viscosity (Ns m^{-2})
μ_v	Vapor viscosity (Ns m^{-2})
ν_1	Kinematic viscosity of liquid (m^2/s)
Θ	Thermophysical properties group (m^2) in Eq. (2)
ρ_v	Vapor density (kg/m^3)
ρ_1	Density of the liquid (kg/m^3)
σ	Surface tension (N/m)
Ω	Angular velocity (rad/s)
Ψ	Dimensionless number in Eq. (2)

References

1. Jang, J. H., Faghri, A., and Chang, W. S. (1991). Analysis of the one-dimensional transient compressible vapor flow in heat pipes. *Int. J. Heat Mass Transfer* **34**, 2029–2037.
2. Bowman, W. J. (1987). "Simulated Heat Pipe Vapor Dynamics. Ph.D. Dissertation, Air Force Institute of Technology.
3. Ivanovskii, M. N., Sorokin, V. P., and Yagodkin, I. V. (1982). *The Physical Principles of Heat Pipes*. Clarendon Press, Oxford.
4. Bowman, W. J., Winn, R. C., and Martin, H. L. (1992). Transient heat pipe modeling: A quasi-steady, incompressible vapor flow model. *AIAA J. Thermophys. Heat Transfer* **6**, 571–574.
5. Bowman, W. J., and Beran, P. S. (1994). Implicit heat pipe vapor model. *AIAA J. Thermophys. Heat Transfer* **8**, 187–190.
6. Issacci, F., Catton, I., and Ghoniem, N. M. (1991). Vapor dynamics of heat pipe start-up. *ASME J. Heat Transfer* **113**, 985–994.
7. Zuo, Z. J., and Faghri, A. (1997). Boundary element approach to transient heat pipe analysis. *Numer. Heat Transfer* **32A**, 205–220.
8. Cao., Y., and Faghri, A. (1990). Transient two-dimensional compressible analysis for high-temperature heat pipes with pulsed heat input. *Numer. Heat Transfer* **18**, 483–502.
9. Tournier, J. M., and El-Genk, M. S. (1994). A heat pipe transient analysis model. *Int. J. Heat Mass Transfer* **37**, 753–762.
10. Chang, M., and Chow, L. C. (1992). Transient response of liquid metal heat pipes—A comparison of numerical and experimental results. In *Proceedings of the 8th International Heat Pipe Conference, Beijing, China*, 139–147.
11. Yamamoto, T., Nagata, K., Katsuta, M., and Ikeda, Y. (1994). Experimental study of mercury heat pipe. *Exp. Thermal Fluid Sci.* **9**, 39–46.

12. El-Genk, M. S., and Huang, L. (1993). An experimental investigation of the transient response of a water heat pipe. *Int. J. Heat Mass Transfer* **36**, 3823–3830.

13. El-Genk, M. S., Huang, L., and Tournier, J. M. (1995). Transient experiments of an inclined copper–water heat pipe. *AIAA J. Thermophys. Heat Transfer* **9**, 109–116.

14. Huber, N. F., and Bowman, W. J. (1996). Longitudinal vibration effects on a copper/water heat pipe's capillary limit. *AIAA J. Thermophys. Heat Transfer* **10**, 90–96.

15. Wirsch, P. J., and Thomas, S. K. (1996). Performance characteristics of a stainless steel/ammonia loop heat pipe. *AIAA J. Thermophys. Heat Transfer* **10**, 326–333.

16. Kobayashi, Y., Ikeda, S., and Iwasa, M. (1996). Evaporative heat transfer at the evaporative section of a grooved heat pipe. *AIAA J. Thermophys. Heat Transfer* **10**, 83–89.

17. Vafai, K., and Wang, W. (1992). Analysis of flow and heat transfer characteristics of an asymmetrical flat plate heat pipe. *Int. J. Heat Mass Transfer* **35**, 2087–2009.

18. Zhu, N., and Vafai, K. (1998). Analytical modelling of the startup characteristics of asymmetrical flat-plate and disk-shaped heat pipes. *Int. J. Heat Mass Transfer* **41**, 2619–2637.

19. Unnikrishnan, V. V., and Sobhan, C. B. (1997). Finite difference analysis of the transient performance of a flat heat pipe. In *10th International Conference on Numerical Methods in Thermal Problems, Swansea, UK*, pp. 391–400.

20. Whitaker, S. (1986). Flow in porous media I: A theoretical derivation of Darcy's law. *Transport Porous Media* **1**, 3–25.

21. Sobhan, C. B., Garimella, S. V., and Unnikrishnan V. V. (2000). A computational model for the transient analysis of flat heat pipes. In *Procs. Inter Society Conference on Thermal and Thermomechanical Phenomena in Electronic Systems—ITHERM 2000, Las Vegas, NV*, pp. 106–113.

22. Vadakkan, U. V., Garimella, S. V., and Sobhan, C. B. (2000). Characterization of the Performance of Flat Heat Pipes for Electronics Applications. In *Emerging Cooling Technologies in Electronic Systems, IMECE 2000, Orlando, Florida*.

23. Khrustalev, D., and Faghri, A. (1996). Enhanced flat miniature axially grooved heat pipe. *ASME J. Heat Transfer* **118**, 261–264.

24. Um, J. Y., Chow, L. C., and Baker, K. (1994). An experimental investigation of flat plate heat pipe. In *Fundamentals of heat pipes*, ASME HTD-Vol. 278, pp. 21–26.

25. Faghri, A., and Thomas, S. (1989). Performance characteristics of a concentric annular heat pipe: Part I—Experimental prediction and analysis of the capillary limit. *ASME J. Heat Transfer* **111**, 844–850.

26. Faghri, A. (1989). Performance characteristics of a concentric annular heat pipe: Part II—Vapor flow analysis. *ASME J. Heat Transfer* **111**, 851–857.

27. Faghri, A., Gogineni, S, and Thomas, S. (1993). Vapor flow analysis of an axially rotating heat pipe. *Int. J. Heat Mass Transfer* **36**, 2293–2303.

28. Harley, C., and Faghri, A. (1995). Two-dimensional rotating heat pipe analysis. *ASME J. Heat Transfer* **117**, 202–208.

29. Lin, L., and Groll, M. (1996). Critical conditions for collapse of annular flow in a rotating heat pipe with a cylindrical wall. *Heat Transfer Eng.* **17**, 29–34.

30. Lin, L., and Faghri, A. (1997). Steady-state performance of rotating miniature heat pipe. *AIAA J. Thermophys. Heat Transfer* **11**, 513–518.

31. Lin, L., and Faghri, A. (1998). Condensation in rotating stepped wall heat pipes with hysteretic annular flow. *AIAA J. Thermophys. Heat Transfer* **12**, 94–99.

32. Lin, L., and Faghri, A. (1999). Heat transfer in micro region of a rotating miniature heat pipe. *Int. J. Heat Mass Transfer* **42**, 1363–1369.

33. Ponnappan, R., and He, Q. (1998). Test results of water and methanol high-speed rotating heat pipes. *AIAA J. Thermophys. Heat Transfer* **12**, 391–397.

34. Daniels, T. C., and Al-Jumaily, F. K. (1975). Investigations of the factors affecting the performance of a rotating heat pipe. *Int. J. Heat Mass Transfer* **18**, 961–973.

35. Vafai, K., Zhu, N., and Wang, W. (1995). Analysis of asymmetric disk-shaped and flat-plate heat pipes. *ASME J. Heat Transfer* **117**, 209–218.

36. Zhu, N., and Vafai, K. (1996). Optimization analysis of a disk-shaped heat pipe. *AIAA J. Thermophys. Heat Transfer* **10**, 179–182.

37. Zhu, N., and Vafai, K. (1997). Numerical and analytical investigation of vapor flow in a disk-shaped heat pipe incorporating secondary flow. *Int. J. Heat Mass Transfer* **40**, 2887–2900.

38. Cao, Y., and Wang, Q. (1995). Thermal analysis of a piston cooling system with reciprocating heat pipes. *Heat Transfer Eng.* **16**, 50–57.

39. Ling, J., Cao, Y., and Wang, Q. (1996). Experimental investigations and correlations for the performance of reciprocating heat pipes. *Heat Transfer Eng.* **17**, 34–45.

40. Peterson, P. F., and Tien, C. L. (1990). Mixed double-diffusive convection in gas-loaded heat pipes. *ASME J. Heat Transfer* **112**, 78–83.

41. Harley, C., and Faghri, A. (1994). Transient two-dimensional gas loaded heat pipe analysis. *ASME J. Heat Transfer* **116**, 716–723.

42. Ponnappan, R., and Chang, W. S. (1994). Startup performance of a liquid–metal heat pipe in near-vacuum and gas-loaded modes. *AIAA J. Thermophys. Heat Transfer* **8**, 164–171.

43. Chung, J. H., and Edwards, D. K (1996). Moving gas effects on heat pipe transient behavior. *AIAA J. Thermophys. Heat Transfer* **10**, 76–82.

44. Cao, Y., and Faghri, A. (1991). Transient multidimensional analysis of nonconventional heat pipes with uniform and nonuniform heat distributions. *ASME J. Heat Transfer* **113**, 995–1002.

45. Cao, Y., and Faghri, A. (1993). Conjugate modeling of high temperature nosecap and wing leading edge heat pipes. *ASME J. Heat Transfer* **115**, 819–822.

46. Thomas, S. K., Klasing, K. S., and Yerkes, K. L. (1998). The effects of transverse acceleration-induced body forces on the capillary limit of helically grooved heat pipes. *ASME J. Heat Transfer* **120**, 441–451.

47. Bryan, J. E., and Seyed-Yagoobi, J. (1997). Heat transport enhancement of monogroove heat pipe with electrohydrodynamic pumping. *AIAA J. Thermophys. Heat Transfer* **11**, 454–460.

48. Richter, R., and Gottschlich, J. M. (1994). Thermodynamics aspects of heat pipe operation. *AIAA J. Thermophys. Heat Transfer* **8**, 334–340.

49. Zuo, Z. J., and Faghri, A. (1998). A network thermodynamic analysis of the heat pipe. *Int. J. Heat Mass Transfer* **41**, 1473–1484.

50. Swanson, L. W., and Peterson, G. P. (1995). The interfacial thermodynamics of micro heat pipes. *ASME J. Heat Transfer* **117**, 195–201.

51. Khrustalev, D., and Faghri, A. (1995). Heat transfer during evaporation on capillary grooved structures of heat pipes. *ASME J. Heat Transfer* **117**, 740–747.

52. Schonberg, J. A., Dasgupta, S., and Wayner, P. C. (1995). An augmented Young–Laplace model of an evaporating meniscus in a microchannel with high heat flux. *Exp. Thermal Fluid Sci.* **10**, 163–170.

53. Pratt, D. M., Brown, J. R., and Halliman, K. P. (1998). Thermocapillary effects on the stability of a heated, curved meniscus. *ASME J. Heat Transfer* **120**, 220–226.

54. Ha, J. M., and Peterson, G. P. (1996). The interline heat transfer of evaporating thin films along a micro grooved surface. *ASME J. Heat Transfer* **118**, 747–755.

55. Ha, J. M., and Peterson, G. P. (1998). Capillary performance of evaporating flow in micro grooves: An analytical approach for very small tilt angles. *ASME J. Heat Transfer* **120**, 452–457.

56. Ma, H. B., Peterson, G. P., and Peng, X. F. (1996). Experimental investigation of countercurrent liquid–vapor interactions and their effect on the friction factor. *Exp. Thermal Fluid Sci.* **12**, 25–32.

57. Peterson, G. P., and Ma, H. B (1996). Analysis of countercurrent liquid–vapor interactions and the effect on the liquid friction factor. *Exp. Thermal Fluid Sci.* **12**, 13–24.

58. Peterson, G. P., and Ha, J. M. (1998). Capillary performance of evaporating flow in micro grooves: An approximate analytical approach and experimental investigation. *ASME J. Heat Transfer* **120**, 743–751.

59. Peng, X. F., Peterson, G. P., and Lu, X. J. (1993). Analysis of capillary induced rewetting in circular channels with internal grooves. *AIAA J. Thermophys. Heat Transfer* **7**, 334–339.

60. Ochterbeck, J. M., Peterson, G. P., and Ungar, E. K. (1995). Depriming/rewetting of arterial heat pipes: Comparison with Share-II flight experiment. *AIAA J. Thermophys. Heat Transfer* **9**, 101–108.

61. Kim, B. H., and Peterson, G. P. (1994). Theoretical and physical interpretation of entrainment phenomenon in capillary-driven heat pipes using hydrodynamic instability theories. *Int. J. Heat Mass Transfer* **37**, 2647–2660.

62. Kihm, K. D., Kim, B. H., and Peterson, G. P. (1994). Entrained sprays from meshed interface occurring in a heat pipe. *AIAA J. Thermophys. Heat Transfer* **8**, 184–187.

63. Kim, B. H., and Peterson, G. P. (1995). Analysis of the critical Weber number at the onset of liquid entrainment in capillary driven heat pipes. *Int. J. Heat Mass Transfer* **38**, 1427–1442.

64. Imura, H., Kozai, H., and Ikeda, Y. (1994). The effective pore radius of screen wicks. *Heat Transfer Eng.* **15**, 24–32.

65. McCreery, G. E. (1994). Liquid flow and vapor formation phenomena in a flat heat pipe. *Heat Transfer Eng.* **15**, 33–41.

66. Jang, J. H., Faghri, A., Chang, W. S., and Mahefkey, E. T. (1990). Mathematical modeling and analysis of heat pipe start-up from the frozen state. *ASME J. Heat Transfer* **112**, 586–594.

67. Ochterbeck, J. M., and Peterson, G. P. (1993). Freeze/thaw characteristics of a copper/water heat pipe: Effects of noncondensible gas charge. *AIAA J. Thermophys. Heat Transfer* **7**, 127–132.

68. Ochterbeck, J. M., and Peterson, G. P. (1995). Investigation of the freezing blowby phenomenon in heat pipes. *AIAA J. Thermophys. Heat Transfer* **9**, 314–320.

69. Tournier, J. M., and El-Genk, M. S. (1996). A vapor flow model for analysis of fluid–metal heat pipe startup from a frozen state. *Int. J. Heat Mass Transfer* **39**, 3767–3780.

70. Faghri, A., Buchko, M., and Cao, Y. (1991). A study of high-temperature heat pipes with multiple heat sources and sinks: Part I — Experimental methodology and frozen startup profiles. *ASME J. Heat Transfer* **113**, 1003–1009.

71. Faghri, A. (1992). Frozen start-up behavior of low-temperature heat pipes. *Int. J. Heat Mass Transfer* **35**, 1681–1694.

72. Cao, Y., and Faghri, A. (1992). Closed-form analytical solutions of high-temperature heat pipe startup and frozen startup limitation. *ASME J. Heat Transfer* **114**, 1028–1035.

73. Faghri, A., Buchko, M., and Cao, Y. (1991). A study of high-temperature heat pipes with multiple heat sources and sinks: Part II — Analysis of continuum transient and steady state experimental data with numerical predictions. *ASME J. Heat Transfer* **113**, 1010–1016.

74. Ponnappan, R. (1989). Studies on the startup transients and performance of a gas loaded sodium heat pipe. Technical Report, WRDC-TR-89-2046, Universal Energy Systems, Inc., Dayton, OH.

75. Cao, Y., and Faghri, A. (1993). Simulation of the early startup period of high-temperature heat pipes from the frozen state by a rarefied vapor self-diffusion model. *ASME J. Heat Transfer* **115**, 239–246.

76. Cao, Y., and Faghri, A. (1993). A numerical analysis of high-temperature heat pipe startup from the frozen state. *ASME J. Heat Transfer* **115**, 247–254.

77. Jang, J. H. (1995). Startup characteristics of a potassium heat pipe from the frozen state. *AIAA J. Thermophys. Heat Transfer* **9**, 117–122.

78. Faghri, A., and Buchko, M. (1991). Experimental and numerical analysis of low-temperature heat pipes with multiple heat sources. *ASME J. Heat Transfer* **113**, 728–734.

79. Schmalhofer, J., and Faghri, A. (1993). A study of circumferentially-heated and block-heated heat pipes—I. Experimental analysis and generalized analytical prediction of capillary limits. *Int. J. Heat Mass Transfer* **36**, 201–212.

80. Schmalhofer, J., and Faghri, A. (1993). A study of circumferentially-heated and block-heated heat pipes—II. Three-dimensional numerical modeling as a conjugate problem. *Int. J. Heat Mass Transfer* **36**, 213–226.

81. Tanaka, O., Koshino, H., Kuriki, J., Yohmatsu, Y., and Harada, O. (1995). Heat extraction from the ground in a volcanic zone using copper water heat pipes—experiment and analysis. *Exp. Thermal Fluid Sci.* **11**, 72–76.

82. McGuinness, M. J. (1996). Steady solution selection and existence in geothermal heat pipes—I. The convective case. *Int. J. Heat Mass Transfer* **39**, 259–274.

83. Schlitt, R. (1995). Performance characteristics of recently developed high-performance heat pipes. *Heat Transfer Engineering* **16**, 44–52.

84. Ambrose, J. H., Field, A. R., and Holmes, H. R. (1995). A pumped heat pipe cold plate for high-flux applications. *Exp. Thermal Fluid Sci.* **10**, 156–162.

85. Dickinson, T. J., Bowman, W. J., and Stoyanof, M. (1998). Performance of liquid metal heat pipes during a Space Shuttle flight. *AIAA J. Thermophys. Heat Transfer* **12**, 263–269.

86. Wei, J., Hijikata, K., and Inoue, T. (1997). Fin efficiency enhancement using a gravity assisted planar heat pipe. *Int. J. Heat Mass Transfer* **40**, 1045–1051.

87. Zhao, Z., and Avedisian, C. T. (1997). Enhancing forced air convection heat transfer from an array of parallel plate fins using a heat pipe. *Int. J. Heat Mass Transfer* **40**, 3135–3147.

88. Cao, Y., Faghri, A., and Mahefkey, E. T. (1993). Micro/miniature heat pipes and operating limitations. In *Heat Pipes and Capillary Pumped Loops*, ASME HTD-Vol. 236, 55–62.

89. Babin, B. R., Peterson, G. P., and Wu, D. (1990). Steady state modeling and testing of a micro heat pipe. *ASME J. Heat Transfer* **112**, 595–601.

90. Wu, D., and Peterson, G. P. (1991). Investigation of the transient characteristics of a micro heat pipe. *AIAA J. Thermophys. Heat Transfer* **5**, 129–134.

91. Collier, J. C. (1981). *Convective Boiling and Condensation*. McGraw-Hill, New York.

92. Wu, D., Peterson, G. P., and Chang, W. S. (1991). Transient experimental investigation of micro heat pipes. *AIAA J. Thermophys. Heat Transfer* **5**, 539–544.

93. Peterson, G. P., Duncan, A. B., and Ahmed, A. S. (1991). Experimental investigation of micro heat pipes in silicon wafers. In *Microchemical Sensors, Actuators, and Systems*, ASME DSC-Vol. 32, 341–348.

94. Peterson, G. P. (1992). Investigation of micro heat pipes fabricated as an integral part of silicon wafers. In *Proceedings of the 8th International Heat Pipe Conference, Beijing, China*, pp. 385–395.

95. Peterson, G. P., Duncan, A. B., and Weichold, M. H. (1993). Experimental investigation of micro heat pipes fabricated in silicon wafers. *ASME J. Heat Transfer* **115**, 751–756.

96. Mallik, A. K., Peterson, G. P., and Weichold, M. H. (1992). On the use of micro heat pipe as an integral part of semi-conductor devices. *ASME J. Electron. Packaging* **114**, 436–442.

97. Mallik, A. K., and Peterson, G. P. (1995). Steady-state investigation of vapor deposited micro heat pipe arrays. *ASME J. Electron. Packaging* **117**, 75–81.

98. Peterson, G. P., and Mallik, A. K. (1995). Transient response characteristics of vapor deposited micro heat pipe arrays. *ASME J. Electron. Packaging* **117**, 82–87.

99. Duncan, A. B., and Peterson, G. P. (1995). Charge optimization for a triangular-shaped etched micro heat pipe. *AIAA J. Thermophys. Heat Transfer* **9**, 365–368.

100. Hopkins, R., Faghri, A., and Khrustalev, D. (1999). Flat miniature heat pipes with micro capillary grooves. *ASME J. Heat Transfer* **121**, 102–109.

101. Khrustalev, D., and Faghri, A. (1993). Thermal analysis of a micro heat pipe. In *Heat Pipes and Capillary Pumped Loops*, ASME HTD-Vol. 236, 19–30.

102. Longtin, J. P., Badran, B., and Gerner, F. M. (1994). A one-dimensional model of a micro heat pipe during steady-state operation. *ASME J. Heat Transfer* **116**, 709–715.

103. Sobhan, C. B., Huang, X. Y., and Liu, C. Y. (2000). Investigations on transient and steady-state performance of a micro heat pipe. *AIAA J. Thermophys. Heat Transfer* **14**, 161–169.

104. Peterson, G. P., and Ma, H. B. (1996). Theoretical analysis of the maximum heat transport in triangular grooves: A study of idealized micro heat pipes. *ASME J. Heat Transfer* **118**, 731–739.

105. Ma, H. B., and Peterson, G. P. (1998). The minimum meniscus radius and capillary heat transport limit in micro heat pipes. *ASME J. Heat Transfer* **120**, 227–233.

106. Ma, H. B., and Peterson, G. P. (1996). Experimental investigation of the maximum heat transport in triangular grooves. *ASME J. Heat Transfer* **118**, 740–746.

107. Ha, J. M., and Peterson, G. P. (1998). The heat transport capacity of micro heat pipes. *ASME J. Heat Transfer* **120**, 1064–1071.

108. Cotter, T. P. (1984). Principles and prospects of the micro heat pipes. In *Proceedings of the 5th International Heat Pipe Conference, Tsukuba, Japan*, pp. 328–335.

109. Chen, H., Groll, M., and Rosler, S. (1992). Micro heat pipe: Experimental investigation and theoretical modelling. In *Proceedings of the 8th International Heat Pipe Conference, Beijing, China*, pp. 396–400.

110. Zhang, J., Wang, C., Yang, X., and Zhou, Z. (1992). Experimental investigation of the heat transfer characteristics of the micro heat pipes. In *Proceedings of the 8th International Heat Pipe Conference, Beijing, China*, pp. 416–420.

111. Zhou, J., Yao, Z., and Zhu, J. (1992). Experimental investigation of the application characteristics of micro heat pipe. In *Proceedings of the 8th International Heat Pipe Conference, Beijing, China*, pp. 421–424.

112. Bezrodny, M. K., and Podgoretskii, V. M. (1994). Flooding and heat transfer limits in horizontal and inclined two-phase thermosiphons. *Exp. Thermal Fluid Sci.* **9**, 345–355.

113. Shatto, D. P., Besly, J. A., and Peterson, G. P. (1997). Visualization study of flooding and entrainment in closed two-phase thermosyphon. *AIAA J. Thermophys. Heat Transfer* **11**, 579–582.

114. Zuo, Z. J., and Gunnerson, F. S. (1994). Numerical modeling of the steady-state two-phase closed thermosyphon. *Int. J. Heat Mass Transfer* **37**, 2715–2722.

115. Harley, C., and Faghri, A. (1994). Complete transient two dimensional analysis of two-phase closed thermosyphons including the falling condensate film. *ASME J. Heat Transfer* **116**, 418–426.

116. El-Genk, M. S., and Saber, H. H. (1999). Determination of operation envelope for closed, two-phase thermosyphons. *Int. J. Heat Mass Transfer* **42**, 889–903.

117. Zuo, Z. J., and Gunnerson, F. S. (1995). Heat transfer analysis of an inclined two-phase closed thermosyphon. *ASME J. Heat Transfer* **117**, 1073–1075.

118. Shiraishi, M., Terdtoon, P., and Murakami, M. (1995). Visual study on flow behavior in an inclined two-phase closed thermosyphon. *Heat Transfer Eng.* **16**, 53–59.

119. Peterson, P. F., Elkouh, N., Lee, K. W., and Tien, C. L. (1991). Flow instability and bifurcation in gas-loaded reflux thermosyphons. *ASME J. Heat Transfer* **113**, 158–165.

120. Zhou, X., and Collins, R. E. (1995). Condensation in a gas-loaded thermosyphon. *Int. J. Heat Mass Transfer* **38**, 1605–1617.

121. Kishimoto, T., and Harada, A. (1994). Two-phase thermosyphon cooling for high-power multichip modules. *IEICE Trans. Electron.* **E77–C**, 986–994.

122. Lock, G. S. H., and Fu, J. (1993). Observations on an evaporative, elbow thermosyphon. *ASME J. Heat Transfer* **115**, 501–503.

123. Lock, G. S. H., and Fu, J. (1993). Heat transfer characteristics of a cranked evaporative thermosyphon. *Int. J. Heat Mass Transfer* **36**, 1827–1832.

124. Lock, G. S. H., and Fu, J. (1993). Natural convection in the inclined, cranked thermosyphon. *ASME J. Heat Transfer* **115**, 166–172.

125. Lock, G. S. H. (1992). *The Tubular Thermosyphon.* Oxford University Press, Oxford.

126. Lin, L., Groll, M., and Rosler, S. (1996). One-dimensional analysis of maximum performance in a closed two-phase thermosyphon with a crossover flow separator. *Heat Transfer Eng.* **17**, 19–28.

127. Islam, M. A., Monde, M., Hasan, M. Z., and Mitsutake, Y. (1998). Experimental study of critical heat flux in concentric-tube open thermosyphon. *Int. J. Heat Mass Transfer* **41**, 3691–3704.

128. Ku, J. (1993). Overview of capillary pumped loop technology. In *Heat Pipes and Capillary Pumped Loops*, ASME HTD-Vol. 236, 1–17.

129. Anderson, W. G. (1993). High temperature capillary pumped loops. In *Heat Pipes and Capillary Pumped Loops*, ASME HTD-Vol. 236, 93–101.

130. Cao, Y., and Faghri, A. (1994). Conjugate analysis of a flat-plate type evaporator for capillary pumped loops with three-dimensional vapor flow in the groove. *Int. J. Heat Mass Transfer* **37**, 401–409.

131. Dickey, J. T., and Peterson, G. P. (1994). Experimental and analytical investigation of a capillary pumped loop. *AIAA J. Thermophys. Heat Transfer* **8**, 602–607.

132. Muraoka, I., Ramos, F. M., and Vlassov, V. V. (1998). Experimental and theoretical investigation of a capillary pumped loop with a porous element in the condenser. *Int. Commun. Heat Mass Transfer* **25**, 1085–1094.

133. Boo, J. H., and Chun, M. S. (1998). Effect of mesh size in a flat evaporator and condenser cooling capacity on the thermal performance of a capillary pumped loop. ASME HTD-Vol. 361-3, 121–127.

134. Bazzo, E., Colle, S., and Groll, M. (1999). Theoretical and experimental study of a CPL using Freon 11 as the working fluid. *J. Brazil. Soc. Mech. Sci.* **21**, 17–28.

135. Krotiuk, W. J. (1997). Engineering testing of the capillary pumped loop thermal control system for the NASA EOS-AM spacecraft. In *Proceedings of the 32nd Intersociety Energy Conversion Engineering Conference, Honolulu, HI*, Vol. 2(2), pp. 1463–1469.

136. Bugby, D. C., Kroliczek, E. J., Cullimore, B. A., and Baumann, J. E. (1997). Experimental investigation of a neon cryogenic capillary pumped loop. In *Proceedings of the 32nd Intersociety Energy Conversion Engineering Conference, Honolulu, HI*, Vol. 2(2), pp. 1403–1408.

AUTHOR INDEX

Numerals in parentheses following the page numbers refer to reference numbers cited in the text.

SUBJECT INDEX

A

ALENIA, 78
American Institute of Chemical Engineers, 4
American Society of Mechanical Engineers (ASME), 2–3, 4

B

Baffled shell-side configurations, 29–30
Ballistic rockets, 67
Batchelor-Stewartson controversy, 185
BDPU (bubble, drop, particle unit), 78, 79, 96, 153
Beam Warming finite difference method, 251
Biot number, fouling, 43–45
Blow-by phenomenon, 277–279
Boiling/Nukiyama curve
  critical heat flux, 72, 119–123, 158–161
  at earth gravity and microgravity, 69–76
  experiments, 76–81
  film, 73, 123–127
  heat transfer, Newton's law of, 69–70
  influence of gravity on correlations, 73–76
  nucleate, 70–72
  reverse order, 73
  saturated, 70, 88–106
  subcooling, 70, 106–119, 157–158
  transition, 72–73
Boiling heat transfer
  applications, 61–62, 165
  historical review, 60
  importance of fluid studies, 58–59
  pool, 62
Boiling heat transfer, saturated nucleate
  cylindrically symmetrical bubble boiling, 87–88
  GAS mission, 95
  KC-135 missions, 90–94, 101
  onset of boiling, 82–90
  plane plate surfaces, 101–106
  small surfaces, 96–101

TEXUS, 101–106
two-dimensional plane boiling, 87
wires as heating elements, 81–95
Boiling heat transfer, subcooled nucleate
  direct electrical heated flat plate, 111–119
  general observations, 106–107
  small surfaces, 108–111
  on wires, 107–108
Boltzmann constant, 131
Bond number, 62
Brinkman-Forchheimer extended Darcy flow model, 254
Bubbles
  capillary-adhesion flow, 132–136
  detachment by coalescence processes, 144–145
  detachment by residual gravity forces, 139–141
  detachment by ripeness, 143–144
  detachment in saturated liquids, 139–147
  detachment in space shuttle experiments, 141–143
  growth model, 128–136
  in homogeneous liquid, 136–139
  microwedge development, 128–132
  size of, and heat transfer, 161–162
  vapor transport, 145–147
Burnout point, 72
Bypass flow, shell-side, 27–28

C

Capillary-adhesion flow, 132–136
Capillary pumped loops (CPLs), 297–298
Clausius-Clapeyron equation, 131, 151, 254, 268, 296
Coalesce boiling region, 165
Colburn *j*-factor, 22
Compensation, principle of, 62–63
Concentric annular heat pipes, 259–261
Contrarotating isothermal sealed cavities, 198–206
Coriolis accelerations, 242